ISSN 1344-6320

2014

PHOTON FACTORY ACTIVITY REPORT

PART A : HIGHLIGHTS AND FACILITY REPORT #32

KEK Progress Report 2015-3

KEK Reports are available from:

Library and Archives
High Energy Accelerator Research Organization (KEK)
1-1 Oho, Tsukuba, Ibaraki, 305-0801
JAPAN

E-mail: irdlib@mail.kek.jp
URL: http://www.kek.jp/en/

#32

PHOTON FACTORY ACTIVITY REPORT

2014

April 2014 to March 2015

1 R. Sagayama
2 M. Kimura
3 T. Senda
4 K. Amemiya
5 K. Yamada
6 Y. Murakami
7 R. Kumai
8 S. Adachi
9 H. Kawata
10 Y. Kobayashi
11 N. Sakabe
12 K. Saito
13 K. Haga
14 N. Nakamura
15 T. Nogami
16 T. Kosuge
17 N. Nagata
18 K. Kuramochi
19 Ryukou Kato
20 K. Ikeda
21 N. Inami
22 K. Mase
23 K. Fukumoto
24 R. Fukaya
25 S. Nozawa
26 H. Sagayama
27 H. Nitani
28 H. Makio
29 S. Naito
30 Ta. Honda
31 Y. Yamada
32 N. Shimizu
33 H. Abe
34 T. Sato
35 K. Hirano
36 H. Matsubara
37 M. Senda
38 Y. Yamaguchi
39 S. Kishimoto
40 To. Honda
41 H. Sagehashi
42 K. Nigorikawa
43 H. Tanaka
44 R. Hashimoto
45 Yu. Takahashi
46 T. Takahashi
47 Y. Uchida
48 M. Adachi
49 A. Saito
50 D. Liebschner
51 C. Hamamatsu
52 H. Matsumaru
53 N. Funamori
54 Y. Kuramoto
55 Y. Takeichi
56 T. Oota
57 K. Hyodo
58 H. Ban
59 K. Horiba
60 M. Minohara
61 S. Yamamoto
62 R. Takai
63 A. Ueda
64 J. Adachi
65 T. Ueno
66 Yo. Takahashi
67 M. Igarashi
68 E. Utsuno
69 N. Yamano
70 M. Horiguchi
71 M. Ito
72 Y. Kakizawa
73 T. Zeniya
74 A. Kamijo
75 H. Toyama
76 M. Sakamaki
77 R. Haruki
78 S. Asaoka
79 H. Miyauchi
80 Y. Misumi
81 K. Nakajima
82 N. Suzuki
83 M. Kitamura
84 M. Shimada
85 O. Tanaka
86 K. Wada
87 K. Tsuchiya
88 S. Nagahashi
89 T. Yamasaki
90 T. Sudayama
91 K. Inoue
92 K. Takahashi
93 N. Igarashi
94 M. Mochida
95 K. Kimijima
96 S. Saijo
97 N. Adachi
98 K. Koiwai
99 Y. Nakashima
100 R. Yukawa
101 H. Ohshima
102 Y. Yamashita
103 H. Nakao
104 T. Matsuhashi
105 A. Hashimoto
106 N. Kuwabara
107 T. Koide
108 A. Tomita
109 K. Ichiyanagi
110 A. Koyama
111 Y. Kitajima

Editorial

This is the 32nd edition of the Photon Factory (PF) Activity Report (ACR2014), and covers scientific activities approximately in the period from April 2013 to March 2014. The report is composed of two parts: PART A and PART B. The former summarizes scientific highlights achieved using the PF, newly developed experimental facilities including beamlines and experimental apparatuses, and the organization and facts of the PF. PART B presents a number of users' short reports and a list of research proposals.

For the past several editions we have promoted the electronic distribution of the PF Activity Report, and all of ACR2014 can be obtained from the PF's website at http://pfwww.kek.jp/publications/acrpubl.html. The main part of PART A is published also in a printed version.

From 2013, we have accepted user reports for PART B throughout the year and upload them promptly after a quick check by our staff. Your timely submission of results obtained using the PF to ACR and scientific papers is of great importance to support the PF. Only users' support will enable us to continue to research new techniques, develop our facilities, and keep them open to the public for scientific and industrial activities.

Finally, we would like to express our sincere gratitude to all of those who have contributed to this volume of ACR2014.

Masao Kimura, Editor-in-Chief
Tsukuba
October 2015

CONTENTS

Awards, Theses and Publication List are available on the PF's website (http://pfwww.kek.jp/acr2014pdf/).

Introduction

Youichi Murakami

On behalf of the staff of the Photon Factory (PF) we are pleased to present Photon Factory Activity Report 2014. This report covers the research activities carried out in fiscal year 2014 (April 2014 – March 2015). Using the PF and PF-AR we have been conducting a variety of synchrotron radiation experiments including slow positron experiments in material and life sciences as an Inter-University Research Corporation. The PF is promoting inter-university collaboration to activate joint research projects. In FY2014 we had about 940 active approved proposals, 3,100 registered users and more than 600 publications. The inter-university research program has been going well and the activities are becoming increasingly important. The PF is also participating in large national projects of the Ministry of Education, Culture, Sports, Science and Technology (MEXT): “Elements Strategy Initiative to Form Core Research Center”, “Platform for Drug Discovery, Informatics, and Structural Life Science”, “Photon and Quantum Basic Research Coordinated Development Program”, “Cross-ministerial Strategic Innovation Promotion Program”, and “Impulsing Paradigm Change through Disruptive Technologies Program”. The PF is also serving as an administrative facility in the Photon Beam Platform to open new research fields of industrial use. Thus, the PF is working to solve a variety of challenges for sustainable human development as well as fundamental scientific problems.

Operation and upgrades of the PF and the PF-AR

The PF has actively been upgrading the beamlines to focus on important scientific areas over the past decade. We are operating two storage rings, the 2.5 GeV PF ring and the 6.5 GeV PF-AR. The PF ring has strong photon intensities in energy regions of vacuum ultraviolet (VUV) and soft X-ray (SX), while the PF-AR has a great advantage in the hard X-ray region. In the long straight sections of the PF ring we have installed new undulators and reconstructed the VUV and SX beamlines to capitalize on the PF ring’s strengths: BL-2A/B for surface and interface science, BL-13A/B for surface chemistry, BL-16A for surface spectroscopy with polarization switching, and BL-28A/B for strongly correlated electron science. Meanwhile, we have upgraded the hard X-ray beamlines to support the large number of X-ray users and gain long-term competitiveness in the field of X-ray science by installing short-gap undulators in the short straight sections of the PF ring: BL-1A for protein crystallography, BL-3A for structural science, BL-15A for XAFS and small-angle scattering, and BL-17A for protein crystallography. In the PF-AR we are focusing on hard X-ray activities such as high-pressure, time-resolved experiments. In the PF and PF-AR, competitive bending beamlines have been supported generously while beamlines with low productivity have been closed. We had almost reconstructed these beamlines successfully by the end of FY2014. Thanks to the systematic reconstruction of beamlines we succeeded in reducing the number of stations from 72 (FY2005) to 39 (FY2014) in the PF ring with no loss of productivity. The scrapping and building of beamlines has had a significant positive effect on manpower and budget shortages. Our user community has also played an important role in these improvements: six stations are managed by user groups and one station by a university.

In FY2014 we suffered a serious budget cut and an increase in electricity rates. As a result it was very difficult to secure the operating time of the PF and PF-AR. Finally, the user times of the PF and PF-AR were 2328 hours and 1992 hours, respectively, which are approximately half of the pre-quake level. It is most unfortunate that users’ research activities and graduate school education were seriously affected by this shortage of user time. In order to overcome the difficult situation, the PF cooperated with the PF user association (PF-UA) and communicated the difficulty to KEK and MEXT. At the request of the PF-UA, 28 chairpersons of scientific associations, 21 representatives of companies and eleven leaders of national projects gave their approval on a document requesting the securing of user time and submitted a formal request to KEK and MEXT. Thanks to this powerful appeal, we were able to promptly recapture budget for operating rings in FY2015, though it is still not sufficient. To overcome the crisis of beamtime shortage we are also developing ways for effectively using user time, including time-sharing by two groups.

We have been promoting the project for a direct injection path to the PF-AR. In this project we are constructing a tunnel for the injection path to achieve a good balance between the injections to PF-AR and Super KEKB. In future we will acquire the ability of top-up operation in the PF-AR with the completion of this tunnel. We have already completed building the tunnel, and construction of the accelerator and some facilities. We are planning to install the accelerator in early autumn 2016 and start the PF-AR again in winter.

The PF is conducting inter-university research programs using slow positron as well as synchrotron radiation. Recently, a technique to determine atomic positions on the top surface of a crystal using slow positrons was

developed in collaboration with the Japan Atomic Energy Agency and Nagoya University. They have refined the reflection high-energy positron diffraction (RHEPD) method to develop the total-reflection high-energy positron diffraction (TRHEPD) method, which have provided good evidence of the effectiveness of determining surface structure by observations of the reconstructed structure of a silicon surface and silicon structure on silver and so on.

Inter-university research program

The PF welcomes applications for research proposals from all over the world. There are various proposal categories: type G for general experiments, type P for preliminary experiments by novice users or feasibility studies for new types of experiments, Type S1 and S2 for high-level research projects, and type U for urgent and important experiments. In FY2014 we launched a new type of research proposal, type T, in collaboration with the PF-UA. This proposal supports research by PhD students for three years until they complete their doctoral course. The proposal is rigorously judged by documentary examination and interview. The PhD students have to make the proposal by themselves, conduct the experiments, and sometimes learn from their failure. Finally they are expected to mature as scientists who can make excellent use of synchrotron radiation. The corresponding PF staff member becomes a mentor of the student and leads various experiments in collaboration with a supervisor in a university.

The Institute of Materials Structure Science (IMSS), KEK started planning a new inter-university research program, called multi-probe experimental proposals, to promote researches using multiple quantum beams such as synchrotron light, neutron, muon, and slow positron beams. The proposals must be experimental ones using multi-probes. The proposals are expected to be a high-level research project, which requires the full use of multi-probes, with a validity period of three years. The proposals are also judged by documentary examination and interview by an ad hoc committee. We hope the projects will produce flagship science of the IMSS.

Collaboration among universities and institutes

The 32nd PF symposium, which is an annual meeting to communicate the present status of the PF to PF users, was held on March 18th, 2015. The PF symposium has joined in the IMSS Science Festa since 2012. On the first day we discuss quantum beam science with neutron, muon, and slow positron users, and on the second day specific issues are separately discussed by each side. The IMSS Science Festa has given PF users a valuable opportunity for communication with many researchers of different fields. 2015 in the PF symposium, after some reports from facilities and centers, we frankly discussed various issues about the operation, management, and future direction of the PF as well as photon science. In particular, there was serious discussion about the future plan. This issue has long been under discussion and is slowly but surely being resolved as described below.

The IMSS launched a special symposium to address the IMSS's identity or raison d'etre. In the past four symposiums we discussed various issues of the IMSS and tried to find solutions. We began with the mission and the installation purpose of the IMSS and then proceeded to the present status and future challenges. Finally we were trying to find solutions and make proposals in various directions such as communities, KEK, and government. The issues discussed include the IMSS's place in KEK and future plans for quantum beams and facilities. The final report will be written up this fiscal year.

We strongly support nanotechnology research and education in the Tsukuba area, namely the Tsukuba Innovation Arena for Nanotechnology (TIA-nano), which has been led by the National Institute of Advanced Industrial Science and Technology, the National Institute for Materials Science, University of Tsukuba, and KEK. In FY2014, TIA-nano and Kyoto University's Nanotechnology Hub established the Nanotech Career-up Alliance (Nanotech CUPAL) based on subsidized projects for fostering science and technology personnel. We aim to enhance the careers of nanotech researchers in Japan and to improve their mobility by conducting two projects: Nanotech Research Professional and Nanotech Innovation Professional projects.

Future plan of the PF

The KEK Roadmap 2013 was published in May 2013. In the Photon Science section of the Roadmap, it is described that KEK will construct and then operate the compact energy recovery linac (cERL) and will work toward construction of a 3 GeV ERL facility. After that, based on the opinions and discussions from the PF-UA, the Japanese Society for Synchrotron Radiation Research, and the international review committee of the Roadmap, KEK made the following additional statement in October 2013: While KEK is engaged in a long-term effort toward the construction of a 3 GeV ERL facility, KEK will play a leading role in the realization of a low-emittance storage ring as a high-brilliance light source in the mid-term. KEK is now beginning specific studies on this possibility with an eye on the value of the nationwide effort.

The IMSS Steering Committee established the "Committee for Future Plans of the PF" to consider carefully the relation between the low-emittance storage ring and the 3 GeV ERL project in the PF future plan. The Committee for Future Plans submitted the mid-term summary to the IMSS Steering Committee in July 2015. On the basis of discussions in the Steering Committee, the Committee for Future Plans will summarize a final report and submit it before the end of FY2015.

Youichi Murakami

Memorials 2014

April 14-20, 2014
Open House of PF in Science & Technology Week

The open house of KEK Tsukuba was held, and 570 visitors joined a tour of Photon Factory.

June 7, 2014
KEK Open Seminar: "The Cutting Edge of Science using Positrons"

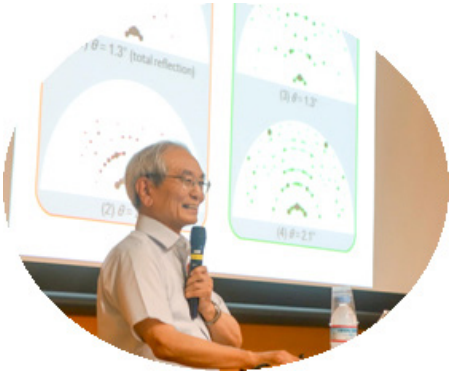

Professor Toshio Hyodo (Institute of Materials Structure Science, KEK) gave a lecture entitled "Positrons: the useful antiparticle, from diagnosis of cancer to structural analysis of solid surfaces"

July 11-12, 2014
PF Workshop "Science Performed by XAFS Experiments at the Next Light Source"

This PF workshop was held on July 11-12 at the Seminar Hall, 4th building. The invited speakers gave special talks on their research areas and prospects. Following topics were actively discussed; improvements in temporal and spatial resolution, operando measurements, observation of complex systems, new material development, heterogeneity, and surface/interface phenomena.

August 15-17, 2014
1st Training Course on Symmetry and Group Theory

These training courses were held for 3 days at KEK, Tsukuba to celebrate the International Year of Crystallography. The course was designed for researchers and students in order to improve their knowledge on symmetry and group theory in crystallography. The training program consisted of lectures and exercises. All lectures were given by Prof. Massimo NESPOLO, University of Lorraine. 2nd training course was held on March 9-13, 2015.

August 19-27, 2014
Summer Challenge

The 8th summer school on “Particle and nuclear physics” and “Material and biological science” was held at KEK. About 80 undergraduate students from 39 universities attended this school, which included lectures, students’ presentations, and facility tours.

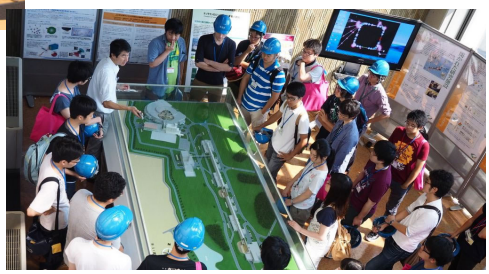

September 11, 2014
PF Workshop “Industrial Applications of Synchrotron X-Ray Imaging”

The first PF workshop on the industrial applications of SR imaging was held at KEK,Tsukuba. Over 50 researchers including private-sector researchers participated and actively discussed the industrial applications of conventional and phase-contrast imaging, topography, X-ray imaging detectors, and microscopes.

September 13, 2014
Open House

The open house of KEK Tsukuba was held and attracted about 3,500 visitors. They enjoyed special lectures on various topics and special events on the latest science concerning materials, biology and accelerators.

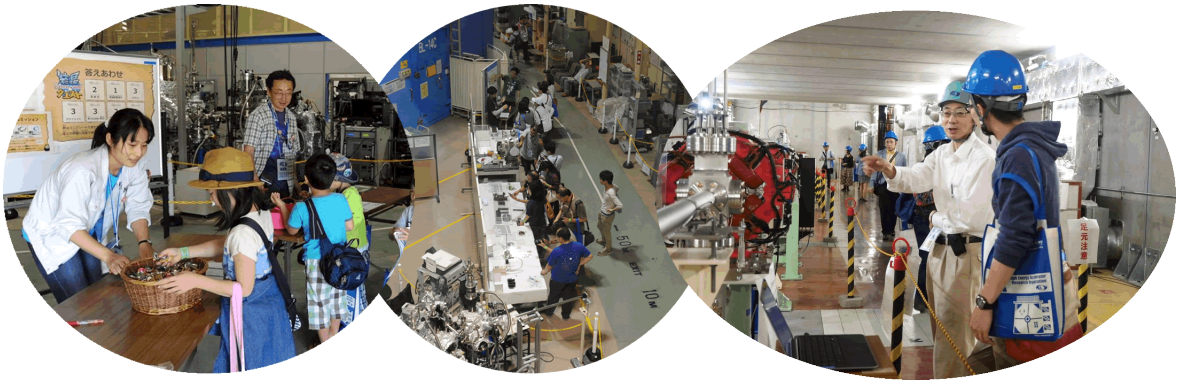

November, 2014
Installation of the Laser Compton Scattering X-Ray Beamline in cERL

The construction of the laser Compton scattering X-ray beamline and the production of X-rays were one of the most important activities of the cERL, whichi was a collaborative effort between KEK and JAEA. In November, the key component of the laser system was installed at the interaction point of the cERL accelerator, and the experimental station was completed in December 2014.

December 4-5, 2014
XAFS Short Course

To acquire new users, a short course on XAFS was held at the PF, including lectures and beamline practice during the two days. The 24 participants were mainly researchers from private companies.

December 6-7, 2014
Summer Challenge: Experimental Session

The students who had participated in the summer challenge in August joined this experimental session on the use of synchrotron radiation X-rays in the PF and PF-AR facilities.

February, 2015
Renewal of the Undulators for BL-13 and BL-28

New undulators (U#13 and U#28) were installed at BL-13 and BL-28, enabling these beamlines to provide bright light in the VUV-SX region with various polarizations.

February 17, 2015
Construction Team of the Compact ERL Received SUWA Award

The construction team of the compact ERL received the SUWA Award in 2014 presented by the Foundation for high energy Accelerator Science (FAS), Japan for their efforts to develop fundamental ERL accelerator technologies and investigative studies. This award is given to researchers, engineers, and teams who have contributed to the development of accelerator science.

February 18, 2015
Workshop on Chocolate Science

This workshop was held at six locations in Tsukuba and other areas and attracted many children and adults. Through experiments, participants learned and experienced how the molecular structure (polymorphism) of chocolate determines its taste.

March 17-18, 2015
The 3rd IMSS Science Festa

The 3rd IMSS Science Festa was held at Tsukuba, Japan in a joint conference with the 6th MLF symposium and the 32nd PF symposium, and was attended by about 570 participants from universities and research institutes from all over Japan. The main purpose of the conference is to promote complementary use of four types of quantum beams: synchrotron light, neutrons, muons and slow positrons offered by IMSS, KEK.

Highlights

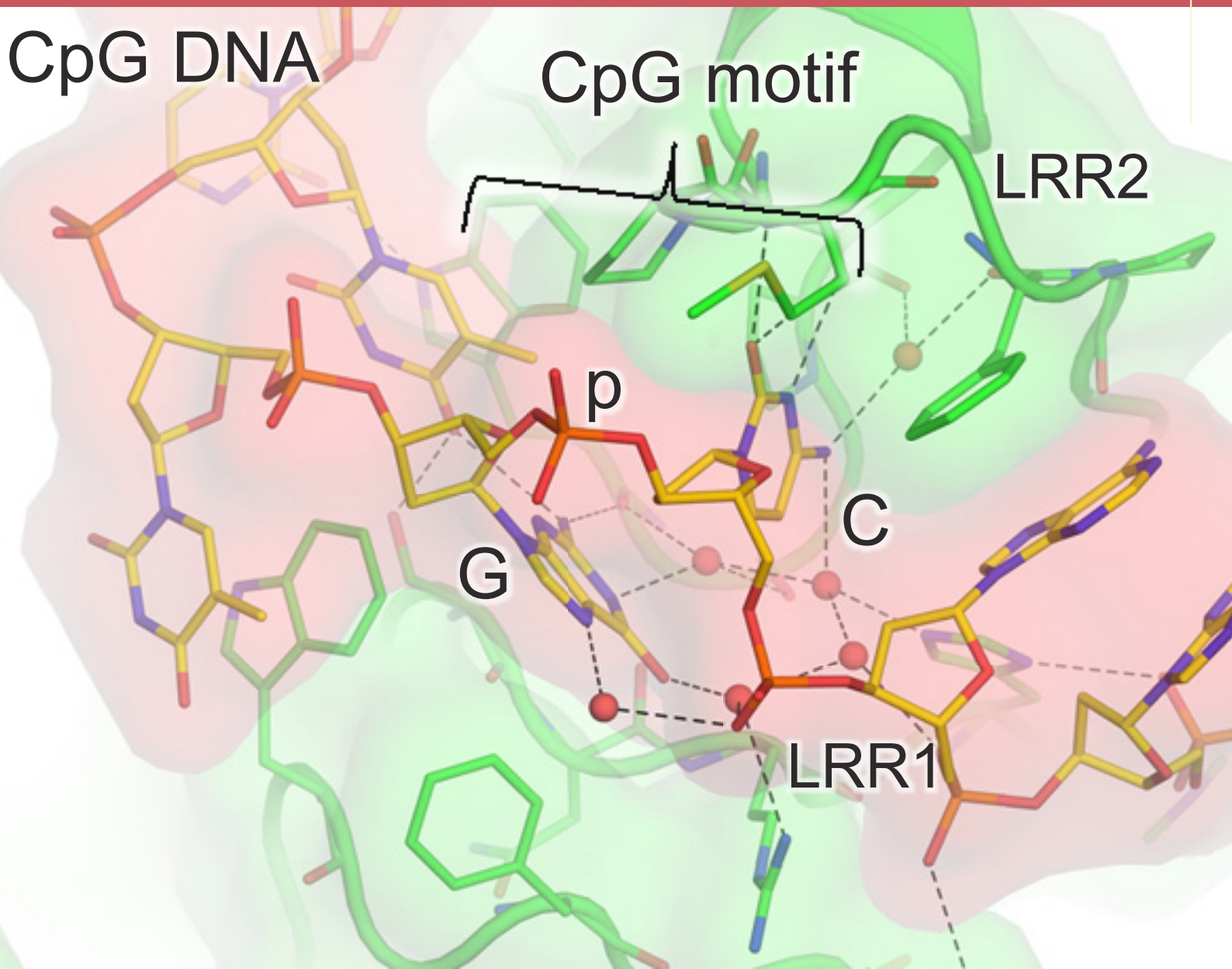

HIGHLIGHTS

Hydrogen Bonds can Switch Electrical Conductivity and Magnetism

Hydrogen-bonds (H-bonds) are one of the most fundamental and important non-covalent interactions in materials, thus attracting much attention in a wide range of scientific fields. Notably, H-bonded protons (or hydrogen atoms) can be thermally transferred or displaced within the H-bond. This unique dynamic behavior plays a crucial role in the (bio)chemical reactions/processes and certain kinds of functional solids/materials. Herein, a new kind of H-bond-dynamics-based phase transition in a purely organic conductor crystal is described. Interestingly, an interplay between the H-bond dynamics and organic π-electrons plays an essential role in this dynamic behavior with switching of physical properties.

Hydrogen bonds (H-bonds) are one of the most fundamental and important non-covalent interactions in materials, and as such have attracted significant attention in a wide range of scientific fields. Notably, H-bonded protons (or hydrogen atoms) can be thermally transferred or displaced within the H-bond. This unique dynamic behavior plays crucial roles in the (bio)chemical reactions/processes and some kinds of functional solids/materials, such as dielectrics and proton conductors. For example, in an H-bonded material, such a displacement varies the polarity not only of the H-bond part, but also the whole material, resulting in switching of the dielectric properties (i.e., the paraelectric-to-(anti) ferroelectric transition). The control and switching of such physical properties and functions utilizing H-bond dynamics is of great interest not just in the basic science but also from the perspective of the applied science and its practical applications. However, successful examples of such switching based on H-bonding are limited.

In 2014, we discovered unprecedented H-bond-dynamics-based switching of electrical conductivity and magnetism [1]. The material they focused on in this study is a purely organic conductor crystal, κ-H_3(Cat-EDT-TTF)$_2$ (abbreviated as κ-H), synthesized by the same research group in 2013 [2]. The κ-H conductor has a peculiar crystal structure, in which the conducting layers are connected by $[O\cdots H\cdots O]^-$ H-bonds (Fig. 1), suggesting the emergence of coupling between the π-electrons and H-bond dynamics that results in novel electronic properties and functionalities. In this study, the research group performed deuteration of the H-bonds of κ-H, to modulate the H-bond dynamics. As a result, a unique phase transition triggered by deuterium transfer accompanied by electron transfer occurred, leading to the switching of electrical conductivity and magnetism.

The present deuterated analogue, κ-D_3(Cat-EDT-TTF)$_2$ (abbreviated as κ-D), at room temperature is isostructural to the parent hydrogen crystal κ-H. The H-bonded molecular unit, shown in the top left of Fig. 2, is assembled [Fig. 1(a)] to form the two-dimensional conducting layer [Fig. 1(b)], in which the π-dimers with S = 1/2 spins are arranged in a triangular pattern. The temperature dependence of electrical resistivity ρ of κ-D exhibited semiconducting behavior similar to κ-H, cooling down to 185 K, and then rapidly increasing [blue circles in Fig. 3(a)]. Such an anomaly was also observed in the magnetic susceptibility χ_p of κ-D: After recording paramagnetic behavior similar to that of κ-H, χ_p of κ-D abruptly dropped at 185 K, to approach $\chi_p \sim 0.0$ emu mol^{-1} with decreasing temperature. This result suggests that spin-singlet pairs were formed upon the phase transition, which leads to a singlet ground state. This is in contrast to the fact that the hydrogen compound κ-H assumes a quantum spin liquid ground state [3].

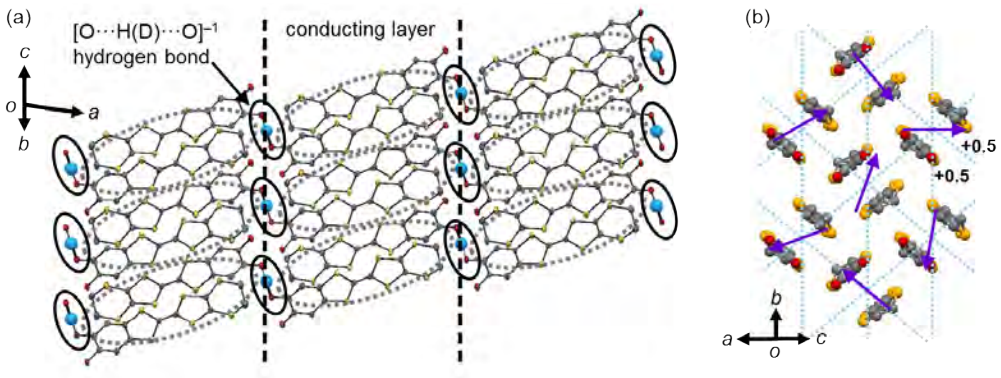

Figure 1: Crystal structures of κ-X_3(Cat-EDT-TTF)$_2$ (κ-H: X = H, κ-D: X = D) at room temperature. (a) H-bonding manner and (b) molecular arrangement in the conducting layer shown in (a). Purple arrows represent S = 1/2 spins.

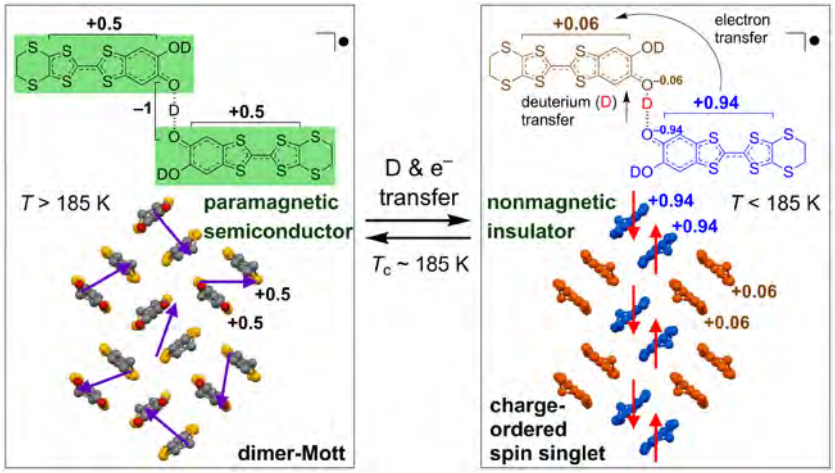

Figure 2: Schematic drawing of the phase transition of κ-D (top: H-bonded molecular unit, bottom: conducting layer). The chemical structures shown in green (top left) represent the Cat-EDT-TTF molecule. The black circles in top right of the top panels represent the fact that the H-bonded molecular unit has an unpaired electron.

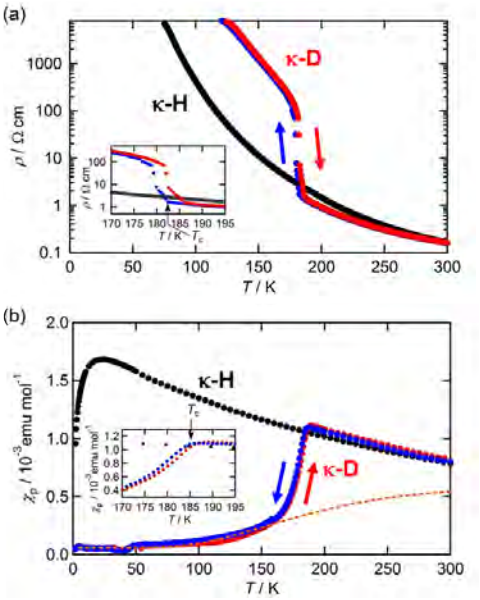

Figure 3: Temperature dependence of (a) electrical resistivity and (b) magnetic susceptibility of κ-D (the blue and red circles represent the cooling and heating processes, respectively) and κ-H (black circles).

Then, to reveal the origin of this phase transition, the temperature dependence of the X-ray crystal structure was examined by using synchrotron radiation at KEK-PF. As a result, it turned out that, below 185 K, the H-bonded deuterium is displaced from the center to one side between the two oxygen atoms, which induced an electron transfer between the Cat-EDT-TTF π-skeletons, to give a charge-disproportionated state composed of the +0.06 and +0.94 species (Fig. 2 top). Consequently, the high-temperature dimer-Mott state was transformed into a charge-ordered spin-singlet state, to give rise to the switching from the paramagnetic semiconductor to the nonmagnetic insulator (Fig. 2 bottom). Generally, charge ordering in molecular conductors is caused by the intermolecular Coulomb interactions. On the other hand, the present charge ordering is triggered by the H-bonded deuterium transfer. Specifically, the present system consists of a truly new type of molecular conductors, whose electronic structures and physical properties are coupled to the structural degree of freedom of hydrogen (deuterium) in H-bonds. In addition, it is also of interest that only κ-D exhibited the transition; this is qualitatively interpreted as a result of the combination of the geometrical and quantum isotope effects.

In summary, this study has demonstrated that the H-bond dynamics can switch electrical conductivity and magnetism in the crystal [1]. This switching or phase transition is an extremely rare event not only in the organic materials but also in the inorganic ones; thus, the further investigation of the mechanism and H/D isotope effect and application to organic electronic materials/devices with switching functionality is of great interest.

REFERENCES

[1] A. Ueda, S. Yamada, T. Isono, H. Kamo, A. Nakao, R. Kumai, H. Nakao, Y. Murakami, K. Yamamoto, Y. Nishio, and H. Mori, *J. Am. Chem. Soc.* **136**, 12184 (2014).
[2] T. Isono, H. Kamo, A. Ueda, K. Takahashi, A. Nakao, R. Kumai, H. Nakao, K. Kobayashi, Y. Murakami, and H. Mori, *Nat. Commun.* **4**, 1344 (2013).
[3] T. Isono, H. Kamo, A. Ueda, K. Takahashi, M. Kimata, H. Tajima, S. Tsuchiya, T. Terashima, S. Uji, and H. Mori, *Phys. Rev. Lett.* **112**, 177201 (2014).

BEAMLINE

BL-8A

A. Ueda[1, S], Yamada[1, 2], T. Isono[1], H. Kamo[1], A. Nakao[3], R. Kumai[4], H. Nakao[4], Y. Murakami[4], K. Yamamoto[5], Y. Nishio[2], and H. Mori[1] ([1]The Univ. of Tokyo, [2]Toho Univ., [3]CROSS, [4]KEKIMSS-PF/CMRC, [5]Okayama Univ. of Sci.)

Engineering Artificial Interface Dipoles at Oxide Heterointerfaces

In all contemporary electronic devices, the most fundamental design constraint is the band alignment between two materials at a heterointerface. A central focus of a wide range of fields and various disciplines is therefore the control of such energy bands to enhance the properties without affecting the bulk properties of the materials. While the insertion of interfacial charges has been utilized to control band offsets in conventional semiconductors and organic materials, here we show that the ionic nature of the complex oxides can be used to vastly enhance the degree and magnitude of band offset control. As a general experimental proof of principle, we use atomically controlled layers of positive and negative charge at a well-defined oxide metal/semiconductor Schottky junction, to produce an interface dipole that varies the barrier height over a range of 1.7 eV. This large control – representing a change of over 50% of the oxide semiconductor band gap – provides a compelling new tool for complex oxides in a wide range of applications.

Devices such as dye-sensitized solar cells, batteries, and solid-state electronic devices take advantage of interface electron transfer, in which interface dipoles (electric double layers) play an essential role. Although the functionality of these devices could be greatly enhanced by optimizing the magnitude of the dipoles at the dye/semiconductor interface, the electrode/electrolyte interface, or the solid/solid interface, dipole engineering is often problematic. For example, attempts to engineer the dipole at conventional metal/semiconductor interfaces, which form Schottky junctions, are hindered by the presence of broken covalent bonds at the edge of the semiconductor. These dangling bonds create interface states, pinning the interface chemical potential, and partially canceling out the interface dipole [1].

Ionic materials, on the other hand, are sometimes free from this pinning effect [2], facilitating the formation of dipoles simply by the accurate positioning of the required charges, one after another. Here, in oxides with strong ionic character, we succeeded in creating a huge electric dipole of the order of 1 eV by fabricating an artificial alignment of ions at a metal/semiconductor interface. By varying the sign and number of embedded ions, the band alignment at this interface was tuned in the range of 1.7 eV, as reflected in a systematic variation of the electric properties of the Schottky junctions. These results demonstrate the validity of using the ionic limit to model dipole engineering in oxides, and imply a larger freedom for structures in devices with ionic materials.

The (001)-oriented $SrRuO_3$/Nb:$SrTiO_3$ junction was chosen as the model interface to tune the Schottky barrier height (SBH) using interface dipole control [3]. The interface dipole was fabricated by inserting $LaTiO_3$ or $SrAlO_3$ at the interface [Fig. 1(a) and (b)]. In the resultant structures, Sr^{2+} is replaced by La^{3+} in the case of $LaTiO_3$ insertion, and Ti^{4+} by Al^{3+} in the case of $SrAlO_3$ insertion. This ionic replacement creates an effect charge with the positive and negative sign, respectively, which are nominally denoted by $(LaO)^+$ or $(AlO_2)^-$. This inserted charge induces a counter (screening) charge in the metal $SrRuO_3$ [Fig. 1(c) and (d)] to form an interface dipole. These interface dipoles create electrostatic potential offsets [Fig. 1(e) and (f)], which modify the SBHs [Fig. 1(g) and (h)].

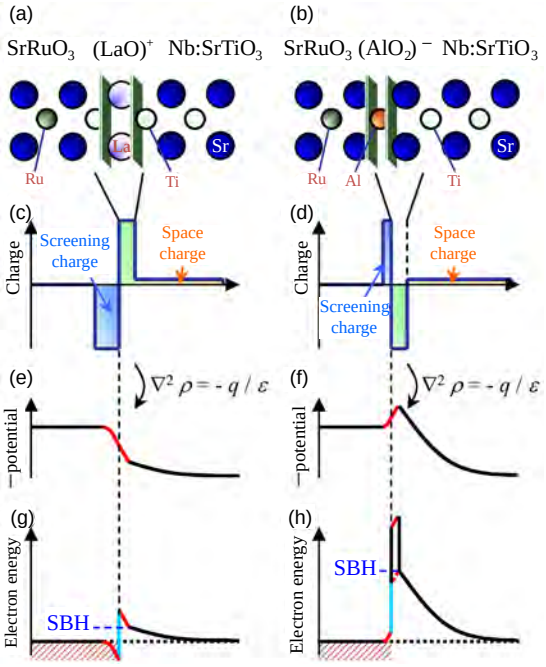

Figure 1: Schematic illustrations of two types of interface dipoles originated from the insertion of positive charge $(LaO)^+$ and negative charge $(AlO_2)^-$ in the $SrRuO_3$/Nb:$SrTiO_3$(001) Schottky junctions. Schematics show (a, b) atomic arrangements, (c, d) charge profiles, (e, f) (negative) potential profiles, and (g, h) band diagrams for each interface dipole.

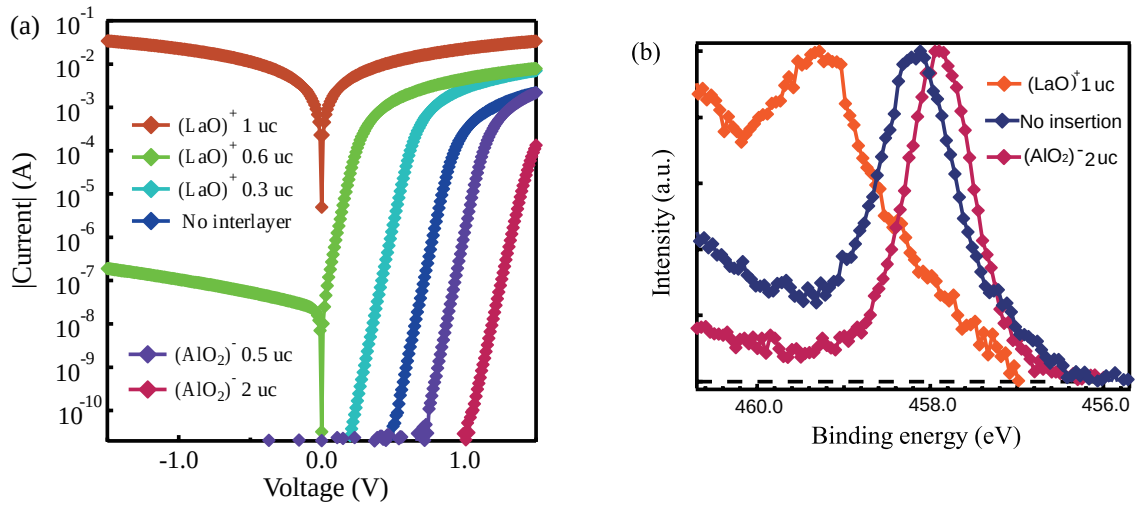

Figure 2: (a) Current-voltage characteristics and (b) Ti $2p_{3/2}$ photoelectron spectra of $SrRuO_3$ / Nb:$SrTiO_3$(001) Schottky junctions with various signs and magnitudes of interface dipoles.

The structures were fabricated by pulsed laser deposition using TiO_2-terminated 0.01 wt.% Nb:$SrTiO_3$ (001) substrates. After the $LaTiO_3$ or $SrAlO_3$ interlayer growth, 60 unit cells (uc) of $SrRuO_3$ were then deposited. The interlayer thickness was varied from 0 uc to 1 uc for $LaTiO_3$, and from 0 uc to 2 uc for $SrAlO_3$. The SBH was evaluated from electrical measurements as well as photoelectron spectroscopy.

As shown in Fig. 2(a), the current-voltage characteristics could be varied from Ohmic to rectifying (SBH = 1.7 eV), reflecting the SBH tuning by the interface dipole from the original $SrRuO_3$/Nb:$SrTiO_3$ junction with SBH = 1.3 eV. The sign of the interface dipole was consistent with the schematics shown in Fig. 1: the SBH was reduced by $(LaO)^+$, and increased by $(AlO_2)^-$. This systematic shift in the SBHs was also observed by photoelectron spectroscopy [Fig. 2(b)]. The binding energy of Ti $2p_{3/2}$ core level was shifted to higher energy for the $(LaO)^+$ insertion indicating the decrease in the SBH, and vice versa for the $(AlO_2)^-$ insertion.

Thus, dipole engineering was demonstrated using $SrRuO_3$/Nb:$SrTiO_3$ Schottky junctions, taking advantage of the ionic character of these oxides. The SBH, originally 1.3 eV, was tuned using the interface dipole in a broad range from 0 eV to 1.7 eV. In a simple electrostatic picture, these interface dipoles can be understood to be formed by the inserted $(LaO)^+$ or $(AlO_2)^-$ sheet charges and the counter (screening) charge in the metal $SrRuO_3$. Engineering interface dipoles in this manner has enormous potential for controlling the band alignments of junctions used in oxide electronics, as well as for improving the functionality of dye-sensitized solar cells and batteries.

REFERENCES

[1] H. Hasegawa, *Jpn. J. Appl. Phys*. **38**, 1098 (1999).
[2] S. Kurtin, T. C. McGill, and C. A. Mead, *Phys. Rev. Lett*. **22**, 1433 (1969).
[3] T. Yajima Y. Hikita, M. Minohara, C. Bell, J. A. Mundy, L. F. Kourkoutis, D. A. Muller, H. Kumigashira, M. Oshima, and H. Y. Hwang, *Nature Commun*. **6**, 6759 (2015).

BEAMLINE

BL-2C

T. Yajima[1, 2], Y. Hikita[1], M. Minohara[1, 3, 4], C. Bell[1], J. A. Mundy[5], L. Fitting Kourkoutis[5], D. A. Muller[5, 6], H. Kumigashira[4], M. Oshima[2], and H. Y. Hwang[1, 3]
([1]SLAC National Accelerator Laboratory, [2]The Univ. of Tokyo, [3]Stanford Univ., [4]KEK-IMSS-PF, [5]Cornell Univ, [6]Kavli Inst. at Cornell)

Structure Determination and Reaction Mechanisms of an Earth Abundant Sodium Battery Electrode

Sodium-ion batteries are becoming increasingly important due to the rapidly growing demand for electric energy storage technology. A new positive electrode material, sodium iron sulfate $Na_{2+2x}Fe_{2-x}(SO_4)_3$, has been developed, using only abundant elements in the Earth's crust. The compound shows a high working voltage of 3.8 V vs. Na/Na^+ with good high-rate capability. High-resolution powder diffraction revealed the crystal structure of the $Na_{2+2x}Fe_{2-x}(SO_4)_3$ through an *ab initio* structure determination procedure. This structure has two kinds of large one-dimensional tunnels, which are suitable for sodium ion transport. *In operando* diffraction of an $Na_{2+2x}Fe_{2-x}(SO_4)_3$//Na electrochemical cell clearly demonstrated continuous and smooth lattice volume change without any transitions during charge-discharge processes.

Technology for storing energy, especially electrical energy, is crucial to realize a greener society. The lithium-ion battery (LIB) caused a paradigm shift in the mobile storage of electrical energy owing to its high voltage and high energy density. Its applications are now growing from small and mobile devices toward larger-scale systems. In view of this trend, the sodium-ion battery (SIB) is a candidate for practical energy storage systems [1]. An intrinsic problem that has hindered the commercialization of the SIB is its lower voltage due to higher electrodeposition potential of Na/Na^+ than Li/Li^+ by *ca*. 0.3 V. This limits the potential of the negative electrode, and hence the cell voltage becomes lower. To overcome this issue, it is necessary to develop a positive electrode with a higher potential.

A new electrode material, $Na_{2+2x}Fe_{2-x}(SO_4)_3$ (NFS), has been found by exploring the binary sulfate Na_2SO_4-$FeSO_4$ system, which consists only of the abundant elements Na, Fe, S and O. Sulfate (sulfuric acid) is one of the most produced engineering chemicals. Electrochemical tests of NFS//Na cells show a high working voltage of 3.8 V vs. Na/Na^+, which is comparable with that of commercial LIBs. This corresponds to the highest Fe^{3+}/Fe^{2+} redox potential ever reported. Furthermore, the NFS electrode shows high-rate capability: reversible capacity exceeds 50% of the full capacity even at 3 minutes of charging/discharging.

The crystal structure of the NFS was determined by powder X-ray diffraction (XRD) at BL-4B2. High-resolution diffraction patterns were collected by a multi-detector system in which Ge(111) analyzers were installed for each detector to ensure sufficiently high angular resolution. The high-resolution data facilitates indexing and initial phase reconstruction from complex diffraction patterns for *ab initio* structure solution. The observed reflections were indexed by a C-centered monoclinic lattice and the initial structure was derived by the charge-flipping method. Figure 1(a) illustrates the crystal structure model of the NFS after subsequent Rietveld refinements. The structure is essentially isostructural to alluaudite, which is a kind of phosphate mineral [2]. Fe is surrounded by $[SO_4]^{2-}$ anions in a distorted octahedral geometry and forms a three-dimensional framework structure, where two kinds of large tunnels run parallel with the c-axis. The Na ions occupy three crystallographic positions: Na(1), Na(2) and Na(3). The Na(2) and Na(3) are in the two large tunnels, respectively. Spatial bond valence analysis revealed that the accessible space for Na is spread along the tunnel [3]. These structural features should contribute to high Na ionic conductivity.

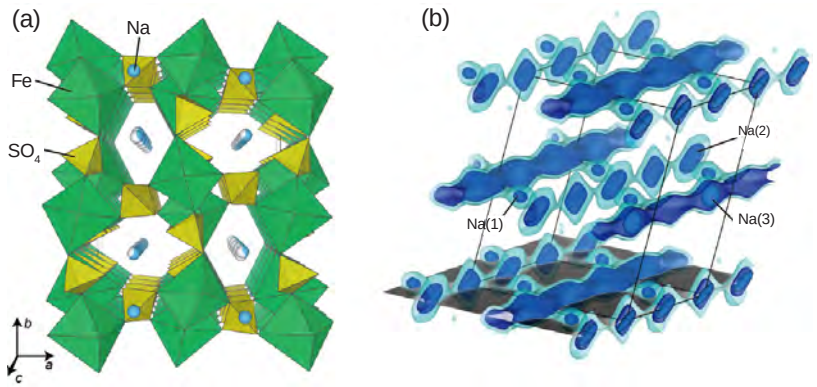

Figure 1: (a) Crystal structure of $Na_{2+2x}Fe_{2-x}(SO_4)_3$. (b) Bond-valence mismatch (ΔV) mapping. Blue and cyan equivalue surfaces represent 0.25 and 0.5, respectively.

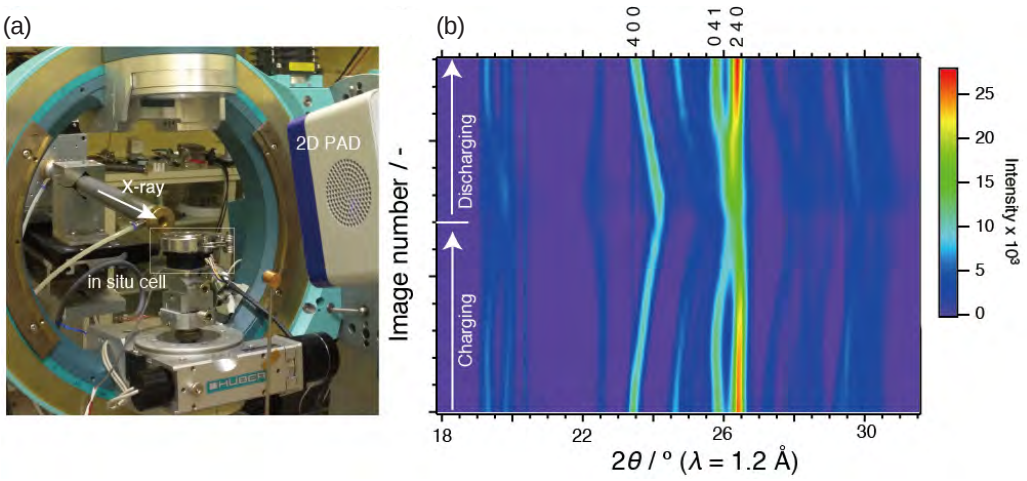

Figure 2: (a) Experiment setup for *in operando* XRD at BL-3A. (b) Two-dimensional representation of time series of *in operando* XRD patterns.

Changes in the crystal structure during the battery reaction were traced by *in operando* X-ray diffraction at BL-3A. The cell was set in a pseudo symmetric reflection geometry [Fig. 2(a)]. The scattered X-ray was detected by a two-dimensional pixel array detector (2D-PAD: PILATUS 100K, DECTRIS) within shutter-less exposure. Figure 2(b) shows a time series of the *in operando* XRD patterns, where the cell was operated in a galvanostatic (constant current) mode with 0.2 C rate (5 hours for charging and discharging, respectively). Each pattern was collected in an exposure time of 10 seconds. All the reflections show continuous shift during the operation. No additional reflections appeared. These results confirm that neither phase separations nor first-order phase transitions occur during the battery operation. This feature may contribute to stable cycling of the battery, since such drastic transitions frequently cause significant degradation of the electrode.

Synchrotron experiments at the Photon Factory provided critical information about the structure of the completely new electrode material [4]. These important findings will contribute to further improvement of the battery performance through further exploration and design of new materials with higher reaction voltage, faster ionic-electronic transport, larger reversible capacity, and so forth.

REFERENCES

[1] N. Yabuuchi, K. Kubota, M. Dahbi, and S. Komaba, *Chem. Rev*. **114**, 11636 (2014).
[2] P. B. Moore, *Am mineral.* **56**, 1955 (1971).
[3] S. Adams, *Acta Cryst*. B**57**, 278 (2001); S. Adams, *Solid State Ionics* **177**, 1625 (2006).
[4] P. Barpanda, G. Oyama, S. Nishimura, S. -C. Chung, and A. Yamada, *Nat. Commun*. **5**, 4358 (2014).

BEAMLINES

BL-3A and BL-4B2

S. Nishimura[1, 2], G. Oyama[1], and A. Yamada[1, 2] ([1]The Univ. of Tokyo, [2]ESICB-Kyoto Univ.)

Small-Angle X-Ray Scattering Study on Deformation Mechanism of Highly Stretchable Hydrogels Using Polyrotaxane Cross-linkers

Extremely stretchable and tough hydrogels are fabricated by incorporating a small amount of polyrotaxane cross-linker into polymer networks. Polyrotaxane is a necklace-like supramolecular assembly in which cyclic molecules are threaded on an axial linear chain, and the cyclic molecules can slide along the axial chain. By cross-linking cyclic molecules in polyrotaxanes with polymer networks, we can introduce slidable cross-links in the gels. The sliding motion of the cyclic molecules in the gels homogenizes the network structure, remarkably improving stretchability and toughness. We have performed small-angle X-ray scattering (SAXS) experiments on the gels containing polyrotaxane cross-linkers under deformation to characterize the homogeneity of the polymer network.

Hydrogels, which are polymer networks swollen in water, have been expected to be used as biomaterials such as artificial skin, artificial vessels, and joint prostheses because of their high biocompatibility. However, one of the problems for such biological applications is that conventional hydrogels are quite brittle. To improve the mechanical strength of hydrogels, various chemical designs of polymer networks have been proposed in the last two decades [1]. One promising strategy to toughen the gels is to connect polymer chains by slidable cross-links. Okumura and Ito developed a novel type of advanced polymer gel, called a “slide-ring (SR) gel” [2, 3]. SR gel is prepared from polyrotaxane (PR), which is a necklace-like molecule composed of an axial polymer chain and cyclic molecules. By cross-linking the cyclic molecules on different PRs, the linear polymers are interlocked by figure-of-eight cross-links composed of cyclic molecules. The cross-links can slide along the polymer chains to equalize the internal stress in SR gels just like pulleys. Due to the mobility of the cross-links, SR gels demonstrate remarkable properties such as high extensibility and a great degree of swelling.

Recently, Imran et al. reported that introducing slidable cross-links into conventional chemical gels changes drastically the mechanical toughness [4]. *N*-Isopropylacrylamide (NIPA) hydrogel is a well-known thermoresponsive gel that changes in volume in response to temperature. To improve the low mechanical strength of NIPA hydrogels, NIPA and sodium acrylic acid (AAcNa) monomers are polymerized by polyrotaxane cross-linkers in which cyclic molecules contain vinyl groups. The NIPA-AAcNa-PR hydrogels with slidable cross-linking points show excellent stretchability and toughness compared with conventional NIPA gels (Fig. 1). The mechanical toughness is thought to result from the mobility of the ring molecules like SR gels.

Figure 1: Schematic view of highly stretchable hydrogel containing polyrotaxane cross-linkers and photograph of deformed state of the gel. The figure was reproduced from ref. 4.

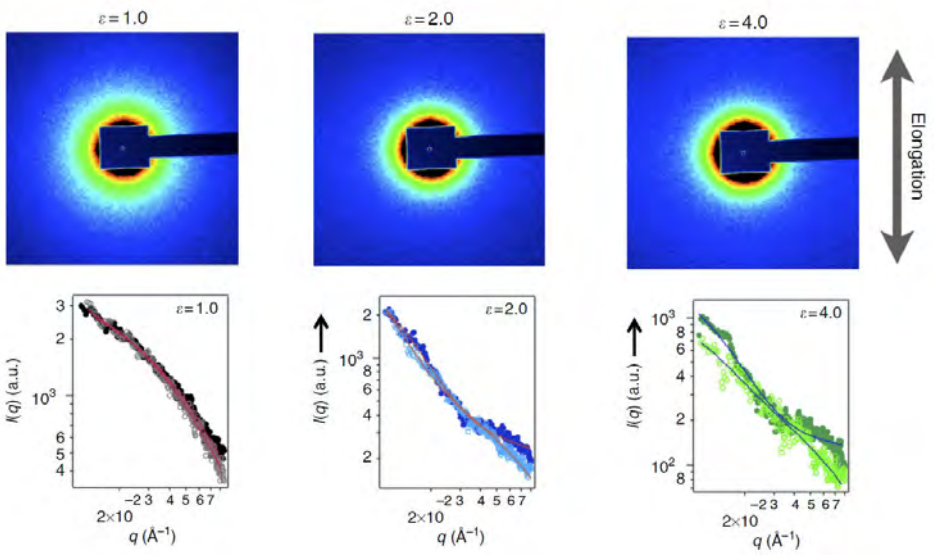

Figure 2: 2-D SAXS patterns and sector average of the 2-D patterns (open circles: the direction parallel to the elongation, closed circles: the direction perpendicular to the elongation) for the highly stretchable gels with polyrotaxane under deformation. ε is the stretching ratio. The figure was reproduced from ref. 4.

To confirm the pulley effect of the movable cross-links in the NIPA-AAcNa-PR hydrogels, we performed small-angle X-ray scattering (SAXS) experiments on deformed gels. When the conventional chemical gels are deformed, the inhomogeneity of the network structure is enhanced; the inhomogeneous structure has been observed by SAXS and small-angle neutron scattering (SANS) [1]. The two-dimensional (2D) X-ray or neutron scattering patterns of deformed chemical gels are elongated in the stretching direction. The anisotropic scattering patterns, called abnormal butterfly patterns, originate from the inhomogeneous network structure [1]. Figure 2 (top) shows 2D SAXS patterns of the NIPA-AAcNa-PR hydrogels under uniaxial deformation (stretching ratio ε = 1, 2, 4). The SAXS pattern of the hydrogel remains isotropic at high deformation ratios, which is consistent with the results for SR gels in a good solvent [3]. The isotropic SAXS patterns indicate that the mobility of the ring molecules in the PR cross-linkers suppresses the inhomogeneity of the network structure. We quantitatively evaluated the SAXS patterns by calculating the sector average of the intensity in the directions parallel and perpendicular to the stretching. Figure 2 (bottom) shows the sector-averaged scattering profiles of the hydrogel at elongation ratios ε = 1–4 in each direction. We can fit the scattering functions with the sum of two functions: a Lorentzian function that describes polymer concentration fluctuation, and a squared Lorentzian function that corresponds to excess scattering from spatial inhomogeneity. The correlation length ξ and Ξ for the Lorentzian and squared Lorentzian function remains almost constant for all deformation ratios, which suggests that the NIPA-AAcNa-PR hydrogels have a more homogenous structure than conventional chemical gels. Thus, the SAXS results prove that the movable cross-links in the gels homogenize the polymer network structure.

Using a small amount of polyrotaxane as a cross-linker in a polymer network leads to dramatic changes in the toughness. This method can be applied to various polymer networks to improve their mechanical strength. Developing hydrogels with good mechanical performance in a simple way at low cost will enable new applications of hydrogels in the fields of drug delivery systems, tissue engineering, and biomaterials.

REFERENCES

[1] M. Shibayama, *Polym. J.* **43**, 18 (2011).
[2] Y. Okumura and K. Ito, *Adv. Mater.* **13**, 485 (2001).
[3] K. Ito, *Polym. J.* **39**, 489 (2007).
[4] A. B. Imran, K. Esaki, H. Gotoh, T. Seki, K. Ito, Y. Sakai, and Y. Takeoka, *Nat. Commun.* **5**, 5124 (2014).

BEAMLINES

BL-6A, BL-10C, and BL-15A

K. Mayumi, H. Yokoyama, and K. Ito (The Univ. of Tokyo)

Structure Determination of the Gold Atomic Chain on Si(111) by Surface X-Ray Diffraction

Self-assembled metallic chains are attracting interest in a wide range of fields. Regular arrays of metal atomic chains can be fabricated on silicon surfaces by depositing sub-monolayer amounts of metals, offering a rich source of phenomena peculiar to one-dimensional conductors. The Si(111)-5×2-Au surface, the regular array of gold chains on the Si(111) surface, is a representative system discovered about half a century ago, but its complex atomic structure had not been solved. We determined the structure by using surface X-ray diffraction. The structure obtained from the model-free direct methods strongly supports the latest structural model predicted by the theory.

Structure determination is a necessary step for understanding the nature of a system. But, in the case of the regular array of one-dimensional (1D) chains on a surface, the structure determination is not straightforward due to the complexity such as a large unit cell with a low symmetry, a significant 1D reconstruction of the substrate surface that originally has a 2D structure, or an intrinsic incoherence in the chain-chain ordering. The Si(111)-5×2-Au surface is one of the most famous prototypes of a 1D metal on Si, and it and its relatives have been the subject of intensive experimental and theoretical studies [1]. However, the structure of Si(111)-5×2-Au remains controversial, although more than a dozen structure models have been proposed. Recently, two similar promising structure models were proposed from *ab-initio* calculations. One is called the EBH model consisting of three Au rows and the honeycomb chain structure of Si [2]. The other is called the KK model, a modified version of the EBH model [3]. It has an additional Au atom with respect to the EBH model as indicated by the dashed circle in Fig. 1(a). Indeed, the calculations suggest that the KK model is energetically stable, but it is quite difficult for the theory, on its own, to determine which of the two very similar models is correct. Therefore, experimental verification is indispensable to reach a final conclusion.

In order to reveal the structure of Si(111)-5×2-Au, we performed surface X-ray diffraction (SXRD) experiments [4] at beamline 15B2 of the Photon Factory at KEK. The surface was prepared in an ultrahigh vacuum chamber mounted on the 6-circle diffractometer which enabled *in-situ* SXRD experiments on the freshly prepared surfaces. We measured in-plane SXRD data of 1/5-order reflections (37 symmetrically inequivalent reflections) to obtain the 2D structure projected on the surface. For the out-of-plane structure analysis, intensity profiles along two 1/5-order diffraction rods and four integral-order rods (crystal truncation rod) were measured.

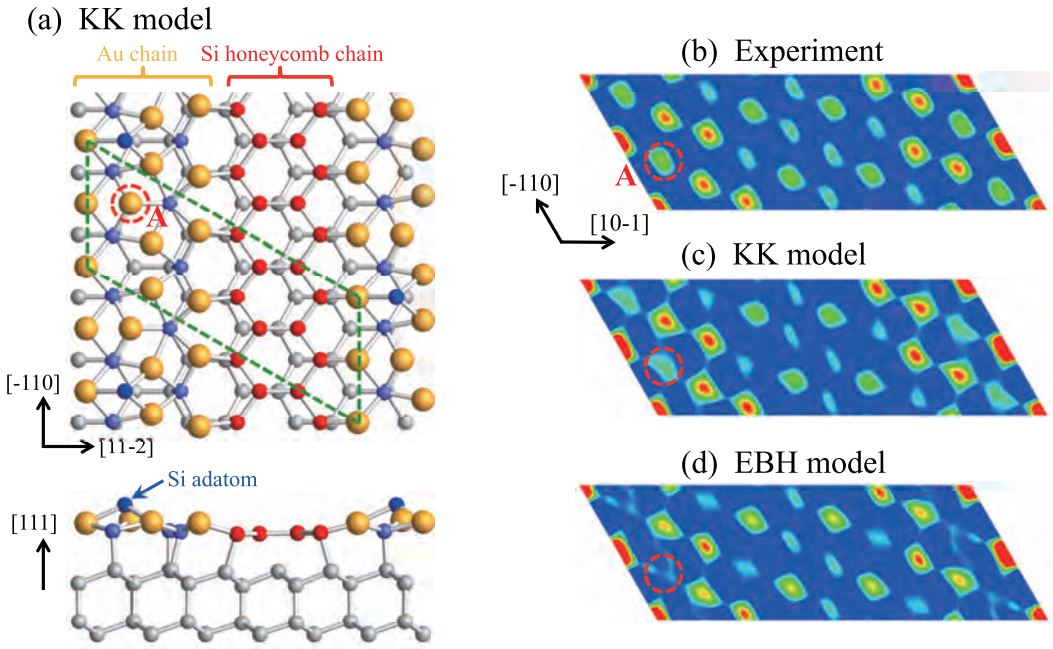

Figure 1: (a) Top and side views of the KK model of the Si(111)-5×2-Au surface [3]. The 5×2 unit cell is outlined by the dashed parallelogram. The larger spheres are Au atoms and the smaller ones are Si where the reconstructed atoms are highlighted. The dashed circle indicates the additional Au atom with respect to the EBH model [3]. (b) 2D Patterson map calculated from the in-plane SXRD data and simulated ones for (c) the KK model and (d) the EBH model. The dashed circle A indicates the peak that becomes stronger by the additional Au atom of the KK model. Note that since the half-order reflections are not included in the calculation [4], the essential unit cell of the Patterson map is 5×1 and the ×2-modulated structure is folded into the 5×1 unit cell.

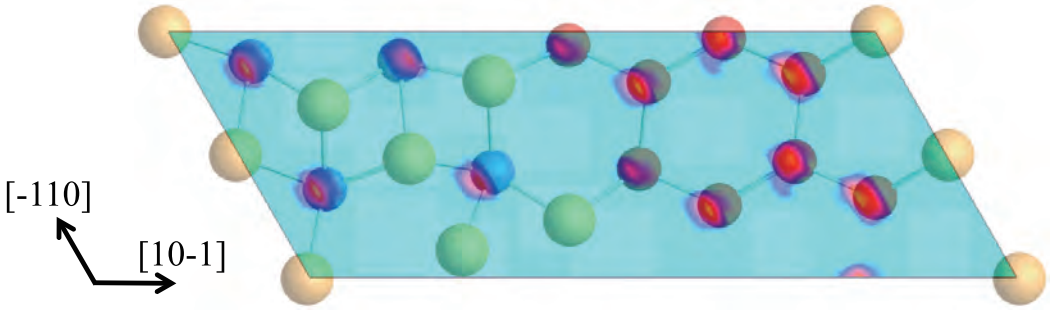

Figure 2: 2D holographic reconstruction of the surface Si atoms. The KK model is overlaid on the image. The arrangement of Au atoms, obtained from the Patterson map of Fig. 1(b), was used as the reference structure to image out the surface Si atoms. The space-inverted twin images and values of less than 35% with respect to the maximum value are omitted for clarity.

A promising way to solve such a complex structure without ambiguity is to derive structural information directly from measured diffraction data. First, we calculated the 2D Patterson map of the surface by Fourier transforming the in-plane reflection intensity data. The Patterson map is the autocorrelation function of the electron density. Therefore, the position of a peak corresponds to an interatomic vector between two atoms, and its intensity corresponds to the product of their electron densities. In the present case, since the electron density of Au is more than five times greater than that of Si, the Patterson map is dominated by the arrangement of Au atoms. Comparing the experimental Patterson map [Fig. 1(b)] to the simulated ones for the KK model [Fig. 1(c)] and EBH model [Fig. 1(d)], one can see that the KK model reproduces the experimental map very well, whereas the EBH model fails to reproduce the peak A indicated by the dashed circle, due to the lack of the additional Au atom.

Now, the arrangement of Au atoms is obtained from the Patterson map, but the positions of Si atoms cannot be solved due to their minor contribution. The arrangement of Si was imaged out directly from the in-plane SXRD data by using a holographic method [5]. The principle of this method is that the measured diffraction wave is regarded as the interference between the reference wave from a known structure with a major scattering contribution and the object wave from the unknown one with a minor contribution. In the present case, the arrangement of Au atoms obtained from the Patterson map is a good reference structure. Figure 2 shows the reconstructed image overlaid with the KK model. All the peaks agree well with the Si atoms of the KK model. Therefore, the direct structure analyses of the in-plane SXRD data support the KK model without ambiguity. Moreover, the atomic positions along the height direction determined from the out-of-plane SXRD data also agree with the KK model [4]. The experimental evidence strongly suggests that the properties of the Si(111)-5×2-Au surface should be reexamined in light of the KK model.

REFERENCES

[1] F. J. Himpsel, K. N. Altmann, R. Bennewitz, J. N. Crain, A. Kirakosian, J. -L. Lin, and J. L. McChesney, *J. Phys. Condens. Matter* **13**, 11097 (2001).
[2] S. C. Erwin, I. Barke, and F. J. Himpsel, *Phys. Rev. B* **80**, 155409 (2009).
[3] S. G. Kwon and M. H. Kang, *Phys. Rev. Lett.* **113**, 086101 (2014).
[4] T. Shirasawa, W. Voegeli, T. Nojima, Y. Iwasawa, Y. Yamaguchi, and T. Takahashi, *Phys. Rev. Lett*. **113**, 165501 (2014).
[5] T. Takahashi, K. Sumitani, and S. Kusano, *Surf. Sci.* **493**, 36 (2001).

BEAMLINE

BL-15B2

T. Shirasawa[1, 2] and T. Takahashi[1] ([1]The Univ. of Tokyo, [2]JST-PRESTO)

Chirality Fingerprinting and Geometrical Determination of Single-Walled Carbon Nanotubes

The recent development of a technique for purifying single-walled carbon nanotubes (SWCNTs) makes it possible to study the physical properties of 2nd and 3rd generation SWCNT solids, which are highly-enriched metallic (or semiconducting) and single-chirality SWCNT materials, respectively. However, the methods for characterizing their purity and structures are very limited. For example, the detailed structures, such as carbon–carbon bond lengths in a SWCNT, have not been fully clarified yet. Here, we demonstrate that a powder X-ray diffraction experiment is useful to fingerprint the chiralities of SWCNTs in a solid and examine the detailed structures.

Single-walled carbon nanotubes (SWCNTs) are quasi one-dimensional hollow cylinders with diameters ranging from less than one nanometer to a few nanometers [1]. The structure of SWCNTs is often hypothetically obtained by rolling up a graphene sheet, and is specified by a pair of integers (n, m) referred to as chiral indices. Although it has been almost 25 years since SWCNTs were discovered, their detailed structures and the intrinsic physical properties of bulk SWCNT solids remain to be fully elucidated. This is because the SWCNT materials usually contain SWCNTs with various chiralities. Very recently, however, the development of purification and separation techniques [2-4] has made it possible to study almost-pure metallic (or semiconducting) SWCNT materials as well as single-chirality SWCNT materials. These are referred to as 1st, 2nd, and 3rd generation SWCNT materials (see Fig. 1). However, existing methods for characterizing the purity of bulk samples and SWCNT structures are very limited. For example, electron diffraction [5] and optical absorption spectroscopy [6] suffer from weaknesses such as limitation of quantitative estimates, or insufficient accuracy or sensitivity.

In this work, we developed a powder X-ray diffraction (XRD) method to characterize the geometrical structures of SWCNTs and purity of bulk materials based on a simulation study of XRD patterns [7]. Here rolling-up structures of a graphene sheet, which consists of a honeycomb arrangement of carbon atoms, are used as default structures for the modeled SWCNTs. The calculations were performed using the Debye formula.

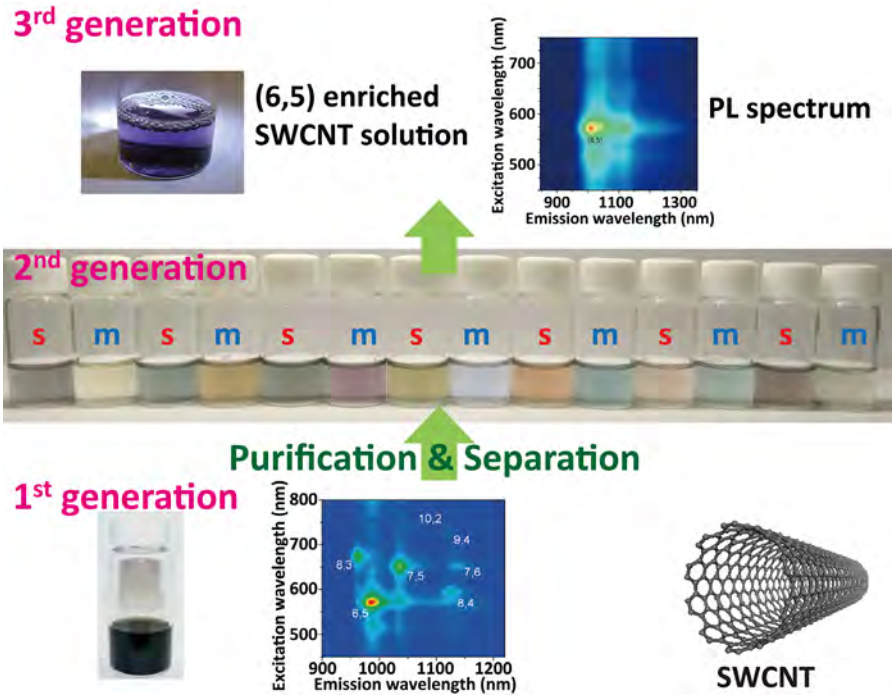

Figure 1: SWCNT solutions of the 1st, 2nd, and 3rd generation SWCNT materials. The 1st generation material contains SWCNTs with various chiralities. In the 3rd generation material, SWCNTs with a specific chirality are enriched, while the metallic or semiconducting SWCNTs are enriched in the 2nd generation materials. For the (6,5)-enriched sample, 2D maps of the photoluminescence excitation/emission peak intensities are shown before and after the enrichment. The metallic (semiconducting) solution is shown by "m (s)".

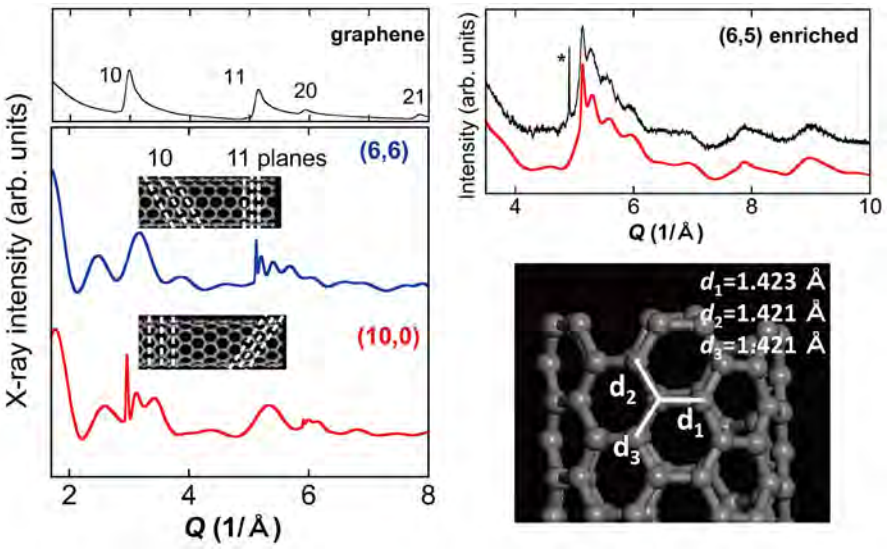

Figure 2: Left panel: calculated XRD patterns for graphene, (6,6) and (10,0) SWCNTs. Right panel: an observed XRD pattern (black solid line) of the (6,5)-enriched SWCNT sample and the simulated pattern (red solid line). Bottom: a schematic structure of a (6,5) SWCNT which is the rolled-up structure of a graphene sheet expanded by 1% along the radial direction.

We found that the XRD patterns sensitively depend on the chiralities of SWCNTs even for non-crystalline samples. An example is shown in the left panel of Fig. 2. SWCNTs with $m = n$ and $m \approx n$ exhibit distinct sharp peaks in the range Q = 5–6 Å^{-1}, or the 11 diffraction region of graphene. On the other hand, similar structures appear around Q = 3–4 Å^{-1}, or the 10 diffraction region of graphene, for $m = 0$ and $m \approx 0$ SWCNTs. These features reflect the arrangement of carbon atoms in a SWCNT. In other words, such fine structures in the XRD patterns can be used as a fingerprint for the chiral indices for a given sample. Besides, it was also shown that the XRD patterns depend sensitively on the detailed structures of SWCNTs such as the carbon–carbon bond length.

The proposed method was used to analyze observed XRD patterns of (6,5) enriched and metal-enriched SWCNT films (see the right panel in Fig. 2 for the (6,5) enriched sample). The measurements were carried out using synchrotron radiation with a wavelength of 1.00 Å at beamlines BL-8A and BL-8B of the Photon Factory in Japan. The observed pattern for the (6,5) enriched sample was well reproduced as the weighted sum of patterns for default SWCNTs with the different chiralities identified in the optical absorption spectra. It was also found that the metal-enriched sample contains (6,6) and (7,4) SWCNTs with a ratio of 42:58 as major SWCNTs. This information was first obtained from the present study; it was indistinguishable in an absorption spectrum.

To obtain more detailed structural information, the observed XRD patterns were analyzed based on a model in which a default structure is expanded or compressed by different degrees along the radial direction and the tube (axial) direction. As a result, a radial expansion of 0.9±0.3% was obtained for (6,5) SWCNTs with a negligible change along the tube axis compared to the rolled-up structure. The bottom right panel of Fig. 2 shows a schematic illustration of a (6,5) SWCNT with a radial expansion of 1%. The bond lengths d_2 and d_3 are nearly equal to those in graphite, while d_1 aligning almost perpendicular to the tube axis is slightly larger than that in graphite. The present results are in semi-quantitative agreement with those of first-principles calculations for armchair SWCNTs [8].

In summary, the present study demonstrated that powder XRD patterns can be used to fingerprint chiralities of SWCNTs present in the samples. Furthermore, it was found that the structure of SWCNTs substantially deviates from that of the ideal rolled-up graphene structure.

REFERENCES

[1] R. Saito, G. Dresselhaus, and M. S. Dresselhaus, *Physical Properties of Carbon Nanotubes*, Imperial College Press, London, 1998.
[2] M. S. Arnold, A. A Green, J. F. Hulvat, S. I. Stupp, and M. C. Hersam, *Nature Nanotech.* **1**, 60 (2006).
[3] K. Yanagi, Y. Miyata, and H. Kataura, *Applied Physics Express* **1**, 034001 (2008).
[4] H. Liu, D. Nishida, T. Tanaka, and H. Kataura, *Nature Commun.* **2**, 309 (2011).
[5] J. Zhang and J. M. Zuo, *Carbon* **47**, 3515 (2009).
[6] A. Hagen and T. Hertel, *Nano Lett.* **3**, 383 (2003).
[7] R. Mitsuyama, S. Tadera, H. Kyakuno, R. Suzuki, H. Ishii, Y. Nakai, Y. Miyata, K. Yanagi, H. Kataura, and Y. Maniwa, *Carbon* **75**, 299 (2014).
[8] K. Kato and S. Saito, *Physica E* **43**, 669 (2011).

BEAMLINES

BL-8A and BL-8B

H. Kyakuno and Y. Maniwa (Tokyo Metropolitan Univ.)

Two-Dimensional Electronic Structure of La and P Co-Doped $CaFe_2As_2$ Studied by ARPES

The relation between the occurrence of high-temperature superconductivity and the underlying electronic structure in iron-based superconductors is a major unresolved problem. We revealed the electronic structure of La and P co-doped $CaFe_2As_2$ superconductor with the critical temperature (T_c) = 45 K by angle-resolved photoemission spectroscopy. Its Fermi surface topology consists of nearly two-dimensional hole- and electron-like Fermi surfaces. Compared to other high-T_c iron-based superconductors, we discuss the relationship between the dimensionality of Fermi surface topology and the value of T_c.

The discovery of high critical temperature (high-T_c) superconductivity in $LaFeAsO_{1-x}F_x$ [1] has triggered intensive research on iron-based superconductors [2-4]. Density functional theory calculations for iron-based superconductors predict that Fermi Surfaces (FSs) in these materials are composed of nearly cylindrical (two-dimensional) hole- and electron-like FSs at the Brillouin zone center and corner, respectively, as shown in Fig. 1(a) [5, 6]. For the emergence of iron-based superconductivity, the FSs nesting that can enhance spin and/or orbital fluctuations has been believed to be important for realizing exotic Cooper pairing [5-8].

Experimentally, FS topology and its nesting condition for several iron-based superconductors have been directly studied by angle-resolved photoemission spectroscopy (ARPES) [9-22]. The FS topology for AFe_2As_2 (so-called 122-type bulk superconductors, where *A* represents alkali or alkali-earth metals) has revealed that high-T_c 122-type bulk superconductors have both hole- and electron-like FSs with the electron-like FSs in common [19-22]. However, the dimensionality of the FSs, especially hole-like FSs, shows marked material dependence: while in hole-doped $Ba_{1-x}K_xFe_2As_2$ (T_c = 38 K), all hole-like FSs have a cylindrical shape [Fig. 1(b)] [19, 20], in electron-doped $Ba(Fe_{1-x}Co_x)_2As_2$ (T_c = 25 K), two- and three-dimensional hole-like FSs are present [Fig. 1(c)] [21, 22]. Since the presence of such a three-dimensional FS is not favorable for superconductivity resulting from the FS nesting, the relationship between the FS nesting and superconductivity is still unclear in iron-based superconductors. In this regard, the recent discovery of electron-doped $CaFe_2As_2$ with T_c = 45 K, namely La and P co-doped $Ca_{1-x}La_xFe_2(As_{1-x}P_x)_2$ [23], may be of importance. This value of T_c is the highest yet reported among iron-based bulk superconductors that have been studied by ARPES. In order to check the characteristic FS topology for the emergence of high-T_c in iron-based superconductors, we performed ARPES measurements for $Ca_{0.82}La_{0.18}Fe_2(As_{0.94}P_{0.06})_2$ superconductor [24].

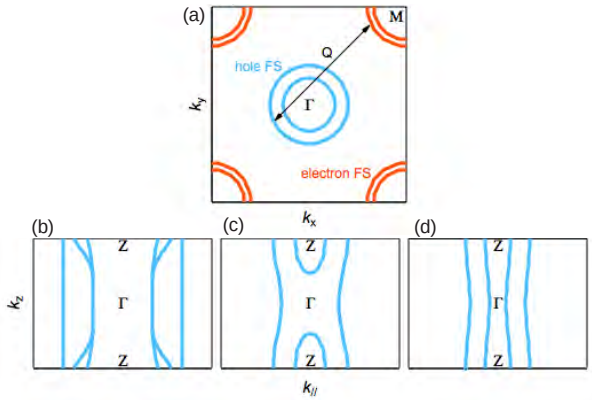

Figure 1: (a) Fermi surface (FS) and the nesting with nesting vector Q in the k_x-k_y plane for iron-based superconductors. The sky-blue and orange curved lines represent hole- and electron-like FSs, respectively. (b)-(d) Hole-like FSs in the k_z–$k_{//}$ plane for $Ba_{1-x}K_xFe_2As_2$, $Ba(Fe_{1-x}Co_x)_2As_2$, and $Ca_{0.82}La_{0.18}Fe_2(As_{0.94}P_{0.06})_2$ obtained from refs. 19, 21 and 24, respectively.

High-quality single crystals of $Ca_{0.82}La_{0.18}Fe_2(As_{0.94}P_{0.06})_2$ were grown as described elsewhere [23]. ARPES measurements were carried out at BL-28A of the Photon Factory using circularly polarized light ($h\nu$ = 40–86 eV) and at BL-9A of the Hiroshima Synchrotron Radiation Center using circularly and linear polarized light ($h\nu$ = 19–31 eV). The total energy resolution was set to 10–30 meV. Clean surfaces were obtained by *in situ* cleaving of crystal in a working vacuum better than 3×10^{-8} Pa and measured at 60 K (above T_c).

In Figs. 2(a) and (b), we show ARPES intensity plots taken along the Γ-X direction with *s*- and *p*-polarized light, respectively ($h\nu$ = 31 eV). We observed one hole-like band whose top is located around 30 meV below E_F (α_1) and two hole-like bands with crossing E_F (α_2 and β). In the *s*-pol data along the Z-X [Fig. 2(c)], we found that the top of the α_1 band is located around 10 meV below E_F, indicating that the α_1 band cannot form FS between the Γ and Z points. On the other hand, the α_2 and β bands cross E_F at Z, as seen in the *p*-pol data [Fig. 2(d)]. Since the position of the Fermi wave vector (k_F) of the α_2 and β bands has almost no k_z dependence [Fig. 2(h)], we find these bands form nearly two-dimensional hole-like FSs. Around the M and A points, we observed two electron-like bands (ε and δ) as seen in Figs. 2(e) and (f). These form elliptical electron-like FSs [Fig. 2(g)], and their k_F position shows sizeable undulation along the k_z direction [Fig. 2(i)] reflecting the elliptical shape of these FSs and the shape of the boundary in the body-centered tetragonal Brillouin zone. Figs. 2(g-i) show the shape of the four FSs (α_2, β, ε, δ) observed by our ARPES measurements [24]. The total carrier number deduced from the volume of FSs of

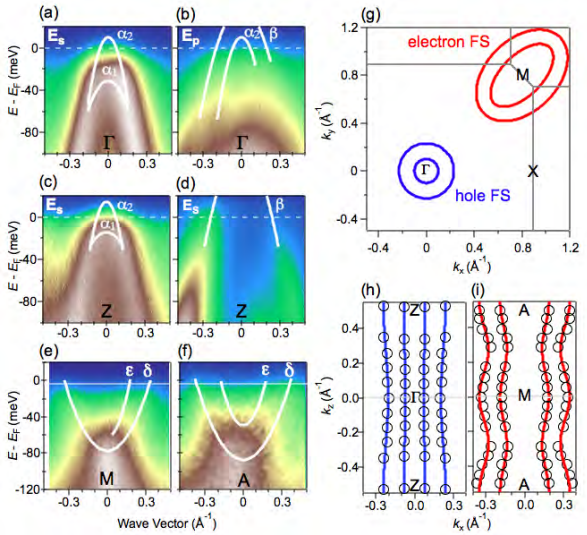

Figure 2: (a), (b) ARPES intensity plots taken along the Γ-X direction with *s*- and *p*-polarized light, respectively ($h\nu$ = 31 eV). (c), (d) are the same as (a), (b) but measured along the Z-X direction ($h\nu$ = 19 eV). (e), (f) ARPES intensity plots taken at M and A points, respectively ($h\nu$ = 69 eV and $h\nu$ = 86 eV). In (a)-(f), the white curves represent the band dispersion. (g) The FS topology in the k_x-k_y plane. The blue and red curved lines represent hole- and electron-like FSs, respectively. (h) and (i) The FS topology in the k_x-k_z plane. In (h) and (i), open circles show the positions of k_F deduced from the momentum distribution curve analysis of photon-energy dependent ARPES data [24].

0.12 ± 0.07 e/Fe agrees with the value expected from the chemical composition of 0.09 e/Fe.

Next we discuss the implications of the present ARPES results for iron-based superconductivity. As shown in Figs. 1(b) and (d), all hole-like FSs in hole-doped $Ba_{1-x}K_xFe_2As_2$ and electron-doped $Ca_{0.82}La_{0.18}Fe_2(As_{0.94}P_{0.06})_2$ have nearly a two-dimensional shape in common [19, 20]. From these results, we suggest that the two-dimensional FS topology, leading to the good FS nesting condition, is universal for high-T_c superconductivity regardless of the type of doped carrier. This supports the unconventional mechanisms for superconductivity in iron-based superconductors.

In summary, we investigated the three-dimensional electronic structure near E_F in electron-doped $Ca_{0.82}La_{0.18}Fe_2(As_{0.94}P_{0.06})_2$ (T_c = 45 K). We observed a nearly two-dimensional FS topology similar to that of $Ba_{1-x}K_xFe_2As_2$, demonstrating the common identity of the electronic structure to induce high-T_c in 122-type iron-based superconductors.

REFERENCES

[1] Y. Kamihara, T. Watanabe, M. Hirano, and H. Hosono, *J. Am. Chem. Soc.* **130**, 3296 (2008).
[2] K. Ishida, Y. Nakai, and H. Hosono, *J. Phys. Soc. Jpn*. **78**, 062001 (2009).
[3] I. I. Mazin and J. Schmalian, *Physica C* **469**, 614 (2009).
[4] F. Wang and D. -H. Lee, *Science* **332**, 200 (2011).
[5] I. I. Mazin, D. J. Singh, M. D. Johannes, and M. H. Du, *Phys. Rev. Lett.* **101**, 057003 (2008).
[6] K. Kuroki, S. Onari, R. Arita, H. Usui, Y. Tanaka, H. Kontani, and H. Aoki, *Phys. Rev. Lett*. **101**, 087004 (2008).
[7] H. Kontani and S. Onari, *Phys. Rev. Lett*. **104**, 157001 (2010).
[8] Y. Yanagi, Y. Yamakawa, and Y. Ōno, *Phys. Rev. B* **81**, 054518 (2010).
[9] P. Richard, T. Sato, K. Nakayama, T. Takahashi, and H. Ding, *Report on Progress in Physics* **74**, 124512 (2011).
[10] H. Ding, P. Richard, K. Nakayama, K. Sugawara, T. Arakane, Y. Sekiba, A. Takayama, S. Souma, T. Sato, T. Takahashi, Z. Wang, X. Dai, Z. Fang, G. F. Chen, J. L. Luo, and N. L. Wang, *Europhys. Lett.* **83**, 47001 (2008).
[11] K. Terashima, Y. Sekiba, J. H. Bowen, K. Nakayama, T. Kawahara, T. Sato, P. Richard, Y. -M. Xu, L. J. Li, G. H. Cao, Z. -A. Xu, H. Ding, and T. Takahashi, *Proc. Natl. Acad. Sci. U.S.A.* **106**, 7330 (2009).
[12] T. Yoshida, I. Nishi, S. Ideta, A. Fujimori, M. Kubota, K. Ono, S. Kasahara, T. Shibauchi, T. Terashima, Y. Matsuda, H. Ikeda, and R. Arita, *Phys. Rev. Lett.* **106**, 117001 (2011).
[13] D. H. Lu, M. Yi, S. -K. Mo, A. S. Erickson, J. Analytis, J. -H. Chu, D. J. Singh, Z. Hussain, T. H. Geballe, I. R. Fisher, and Z. -X. Shen, *Nature* **455**, 81 (2008).
[14] I. Nishi, M. Ishikado, S. Ideta, W. Malaeb, T. Yoshida, A. Fujimori, Y. Kotani, M. Kubota, K. Ono, M. Yi, D. H. Lu, R. Moore, Z. -X. Shen, A. Iyo, K. Kihou, H. Kito, H. Eisaki, S. Shamoto, and R. Arita, *Phys. Rev. B* **84**, 014504 (2011).
[15] T. Hajiri, T. Ito, R. Niwa, M. Matsunami, B. H. Min, Y. S. Kwon, and S. Kimura, *Phys. Rev. B* **85**, 094509 (2012).
[16] K. Nakayama, T. Sato, P. Richard, T. Kawahara, Y. Sekiba, T. Qian, G. F. Chen, J. L. Luo, N. L. Wang, H. Ding, and T. Takahashi, *Phys. Rev. Lett*. **105**, 197001 (2010).
[17] T. Qian, N. Xu, Y. -B. Shi, K. Nakayama, P. Richard, T. Kawahara, T. Sato, T. Takahashi, M. Neupane, Y. -M. Xu, X. -P. Wang, G. Xu, X. Dai, Z. Fang, P. Cheng, H. -H. Wen, and H. Ding, *Phys. Rev. B* **83**, 140513 (2011).
[18] D. Mou, S. Liu, X. Jia, J. He, Y. Peng, L. Zhao, L. Yu, G. Liu, S. He, X. Dong, J. Zhang, H. Wang, C. Dong, M. Fang, X. Wang, Q. Peng, Z. Wang, S. Zhang, F. Yang, Z. Xu, C. Chen, and X. J. Zhou, *Phys. Rev. Lett*. **106**, 107001 (2011).
[19] Y. Zhang, L. X. Yang, F. Chen, B. Zhou, X. F. Wang, X. H. Chen, M. Arita, K. Shimada, H. Namatame, M. Taniguchi, J. P. Hu, B. P. Xie, and D. L. Feng, *Phys. Rev. Lett*. **105**, 117003 (2010).
[20] Y. -M. Xu, Y. -B. Huang, X. -Y. Cui, E. Razzoli, M. Radovic, M. Shi, G. -F. Chen, P. Zheng, N. -L. Wang, C. -L. Zhang, P. -C. Dai, J. -P. Hu, Z. Wang, and H. Ding, *Nat. Phys.* **7**, 198 (2011).
[21] C. Liu, A. D. Palczewski, R. S. Dhaka, T. Kondo, R. M. Fernandes, E. D. Mun, H. Hodovanets, A. N. Thaler, J. Schmalian, S. L. Bud'ko, P. C. Canfield, and A. Kaminski, *Phys. Rev. B* **84**, 020509 (2011).
[22] W. Malaeb, T. Yoshida, A. Fujimori, M. Kubota, K. Ono, K. Kihou, P. M. Shirage, H. Kito, A. Iyo, H. Eisaki, Y. Nakajima, T. Tamegai, and R. Arita, *J. Phys. Soc. Jpn*. **78**, 123706 (2009).
[23] K. Kudo, K. Iba, M. Takasuga, Y. Kitahama, J. Matsumura, M. Danura, Y. Nogamia, and M. Nohara, *Sci. Rep*. **3**, 1478 (2013).
[24] M. Sunagawa, T. Ishiga, K. Tsubota, T. Jabuchi, J. Sonoyama, K. Iba, K. Kudo, M. Nohara, K. Ono, H. Kumigashira, T. Matsushita, M. Arita, K. Shimada, H. Namatame, M. Taniguchi, T. Wakita, Y. Muraoka, and T. Yokoya, *Sci. Rep*. **4**, 4381 (2014).

BEAMLINE

BL-28A

M. Sunagawa[1], T. Ishiga[1], K. Tsubota[1], T. Jabuchi[1], J. Sonoyama[1], K. Iba[1], K. Kudo[1], M. Nohara[1], K. Ono[2], H. Kumigashira[2], T. Matsushita[3], M. Arita[4], K. Shimada[4], H. Namatame[4], M. Taniguchi[4], T. Wakita[1], Y. Muraoka[1], and T. Yokoya[1] ([1]Okayama Univ., [2]KEK-IMSS-PF, [3]JASRI-SPring-8, [4]Hiroshima Univ.)

The Extreme Surface Sensitivity of TRHEPD Demonstrated

This work shows that total-reflection high-energy positron diffraction (TRHEPD), the positron counterpart of reflection high-energy electron diffraction (RHEED), is extremely sensitive to the structure (atomic configuration) of the topmost surface and the immediate sub-surface. The total reflection happens when the positrons are directed to a surface with a glancing angle smaller than a critical value; the TRHEPD patterns in this condition depend only on the surface atoms. When the glancing angle is larger than the critical value, the positrons penetrate the crystal making it possible to obtain information about the immediate subsurface. These features are demonstrated using the TRHEPD patterns from a Si(111)-(7×7) surface.

Crystal structure determination by X-ray diffraction has played a crucial role in the materials research and the life sciences. For the surface science, however, an equally effective single method to determine the top- and near-surface atomic configurations has yet to be established. This work shows that total-reflection high-energy positron diffraction (TRHEPD) is the ideal technique for this purpose [1]. The method is the positron counterpart of reflection high-energy electron diffraction (RHEED) and formerly called reflection high-energy positron diffraction (RHEPD). But now it has been renamed as TRHEPD with an intention to emphasize the important role of the total-reflection in this unique method.

Many aspects of the positron diffraction are superior to those of its electron counterpart. The only possible drawback with using positrons, that is, the difficulty in obtaining a beam of high intensity, has been resolved by using the high-intensity slow positron beam at the Slow Positron Facility (SPF) of the Institute of Materials Structure Science.

First proposed in 1992 [2], TRHEPD (then called RHEPD) uses positrons with energy of around 10 keV and directs them to a crystal surface with a glancing angle smaller than about 5°. The usefulness of this technique was proven in 1998 [3], with an apparatus using a ^{22}Na positron source to provide a beam of 10^3-10^4 slow-positrons/s.

The total reflection of the positrons takes place when the positron beam is directed to a material surface with a glancing angle smaller than a certain critical value because the crystal potential in every crystal is positive. When the glancing angle is larger than the critical value, the positrons penetrate the crystal, being refracted toward the surface. In contrast, the electrons penetrate the crystal being refracted off the surface regardless of the value of the glancing angle.

Recently a TRHEPD station was developed at the SPF in collaboration with the researchers of Japan Atomic Energy Agency [4]. The intense slow positron beam of the SPF is produced using a dedicated electron linac (55 MeV, 600 W) and a production unit consisting of a Ta target and a W foil moderator. A transmission-type brightness enhancement unit was installed upstream of the TRHEPD chamber, providing a beam of 5×10^5 slow-positrons/s.

The present study shows that the TRHEPD patterns from a Si(111)-(7×7) surface in the total reflection condition actually contain contributions only from atoms on the topmost surface. The critical glancing angle for the total reflection of 10 keV positrons from Si(111)-(7×7) surface is 2.0°. Figure 1 is a schematic drawing of this surface, in which the circles indicate Si atoms. It shows (a) the arrangement of the adatoms (colored red), (b) the adatoms and the first surface layer (colored green), and (c) down to the second surface layer (colored blue). Figure 1(d) shows the side view of this surface structure.

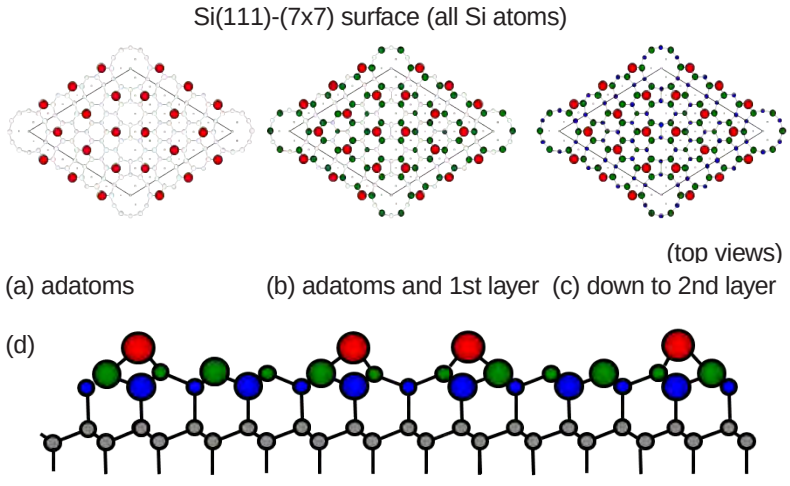

Figure 1: Schematic diagram of the Si(111)-(7×7) structure. The circles indicate silicon atoms.

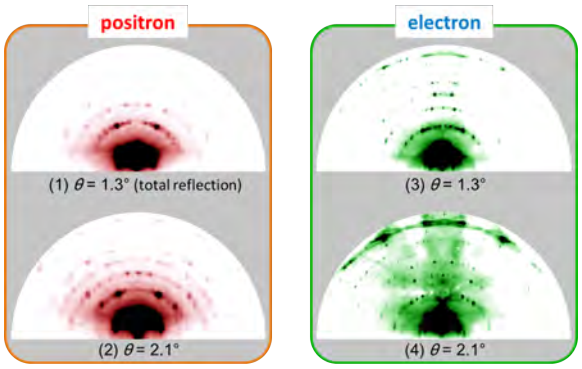

Figure 2. RHEPD (positron) and RHEED (electron) patterns of Si(111)-(7×7) surface for galncing angles θ =1.3° and 2.1°. The critical glancing angle for the total reflection of the positron is 2.0°.

Figure 2 shows the TRHEPD patterns observed for (1) a glancing angle, θ, of 1.3° (within the total reflection condition) and (2) 2.1° (slightly off the total reflection condition). The results of RHEED at the same energy and glancing angles, θ =1.3° (3) and 2.1° (4), are also shown. The TRHEPD and RHEED patterns are quite different for both angles. This is explained by the different depth of crystal penetration by the positrons and the electrons.

Figure 3(1-d) shows the calculated TRHEPD pattern for θ =1.3°. The established detailed positions of the atoms of this surface were assumed in the calculation. It can be clearly seen that the agreement of Fig. 3(1-d) with the experimental data for θ=1.3° in Fig. 2(1) is good. Figure 3(1-a) shows the TRHEPD pattern expected for a two-dimensional single sheet of the Si(111)-(7×7) adatom configuration [Fig. 1(a)]. Such a sheet cannot support itself in reality, but it is possible to assume its existence for the purpose of calculation. This calculated pattern already displays most of the features of Fig. 3(1-d) and Fig. 2(1) and strongly indicates that the main features of the latters for the whole sample are essentially determined by the contribution from the adatoms on the surface. If we look more closely at Fig. 3(1-a), (1-b), and (1-d), the inclusion of the contributions from the atoms in the first surface layer provides a better agreement. This is reasonably understood because the distribution of the Si adatoms in the 7×7 super structure is rather sparse, so that most of the atoms in the first surface layer (colored green) are also exposed, as it can be seen in Fig. 1(b and d). Fig. 3(1-c) is indistinguishable from (1-b) and (1-d), indicating that the atoms in the second surface layer make almost no contribution.

Figure 3(2) shows similar results for a glancing angle of θ = 2.1°. This indicates that the pattern at this glancing angle includes contributions also from the second layer, but no more. In contrast, the results of the calculations for RHEED at θ = 1.3° and θ = 2.1° shown in Fig. 3(3, 4) indicate that the pattern from the bulk

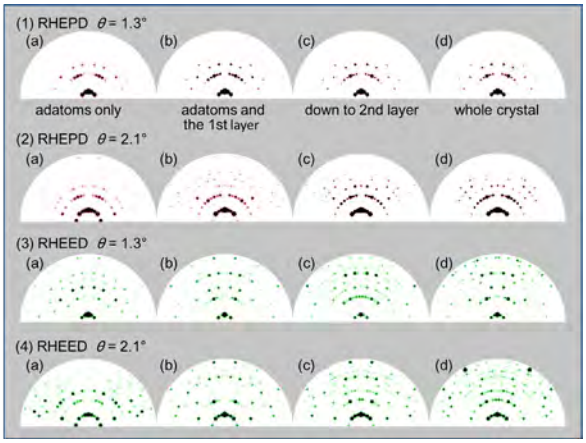

Figure 3. TRHEPD and RHEED patterns for glancing angles θ = 1.3° and θ = 2.1° calculated on the basis of the dynamical diffraction theory. The results are shown for the assumed two-dimensional crystal sheet of the Si adatoms (a), as in Fig. 1(a); the set of the sheets of adatoms and the first surface layers (b), as in Fig. 1(b); the set of sheets of layers down to the second layer (c), as in Fig. 1(c); and for the whole crystal (d).

sample does not include only the exposed atoms on the surface, nor down to the second layer surface – a feature that is expected from the positive crystal potential, which leads to negative potential energy of the electron in the bulk.

The conclusion is that the TRHEPD pattern in the total reflection condition for the Si(111)-7×7 surface *observed from a bulk sample* includes only the contributions from *the atoms exposed on the surface*. Surface science now has a method of observing a diffraction pattern formed only by the atoms on the surface by means of a straightforward measurement on a bulk sample. Moreover, analyzing TRHEPD patterns with increasing glancing angle across the critical angle for total reflection provides a powerful technique to characterize the surface and the near-surface crystal structure from the top downwards.

We expect the application of this technique to play a role as significant in surface science as the one played by the X-ray diffraction in the solid state physics and molecular biology.

REFERENCES

[1] Y. Fukaya, M. Maekawa, A. Kawasuso, I. Mochizuki, K. Wada, T. Shidara, A. Ichimiya and T. Hyodo, *Appl. Phys. Express* **7**, 056601 (2014).
[2] A. Ichimiya, Solid State Phenom. **28/29**, 143 (1992).
[3] Kawasuso, A. & Okada, S., Phys. Rev. Lett. **81**, 2695 (1998).
[4] M. Maekawa, K. Wada, Y. Fukaya, A. Kawasuso, I. Mochizuki, T. Shidara, T. Hyodo, *Eur. Phys. J. D* **68**,165 (2014).

BEAMLINE

SPF-A3

T. Hyodo (KEK-IMSS-PF)

Direct Observation of Gold-Gold Bond Formation in Solution

Bond making and bond breaking are essential processes in chemistry, but visualizing the track of atomic rearrangement is challenging and often requires a technique with high temporal and spatial resolutions. Visualizing the bond formation in the solution phase is especially elusive, because the synchronization of the meet-up of two reactants with ultrafast time resolution is mandatory. Here, we investigate the photo-induced formation of gold-gold (Au-Au) covalent bonds among weakly bound Au atoms in a gold trimer complex. Based on time-resolved X-ray scattering data, we visualize subtle structural changes of the metal complex in real time in the form of Au-Au interatomic distances in real space.

For several decades, ultrafast bond-breaking processes of many molecular systems have been studied intensively using various time-resolved techniques. In contrast, the dynamics of bond making, particularly in solution, have been rarely studied because bond making is a bimolecular process limited by slow diffusion through the solvent, making it difficult to initiate and follow the process with ultrafast time resolution.

In order to overcome the difficulty in capturing bond formation, a gold complex, $[Au(CN)_2^-]_n$, plays as an ideal model system [1]. Au atoms in $[Au(CN)_2^-]_n$ exhibit an interatomic interaction caused by the relativistic effect, which is often called as aurophilicity or aurophilic interactions [1]. Due to this unique interactions, Au atoms are weakly bound to each other, forming an aggregated complex $[Au(CN)_2^-]_n$ even in the ground state. Upon photoexcitation of the complex, an electron is excited from antibonding to bonding orbital, resulting in formation of strong Au-Au covalent bonds. Since Au atoms belong to the same solvent cage in the ground state of the $[Au(CN)_2^-]_n$ complex, the formation of Au-Au covalent bonds occurs without being limited by slow diffusion through the solvent.

Recently, ultrafast Au-Au bond formation in a gold trimer complex, $[Au(CN)_2^-]_3$, was investigated using transient absorption (TA) spectroscopy [2], and the transient changes of absorption were observed on the time scales of 500 fs, 2 ps and 2 ns. The first two time constants, 500 fs and 2 ps, were ascribed to the changes of molecular structure leading to the formation of Au-Au covalent bonds, that is, (i) contraction of Au-Au bonds and (ii) conformational change from bent to linear structure, respectively. However, because the TA signal is not directly related to the molecular structure, those structural assignments were solely based on the assumption of theoretical TA spectra of model structures. In this work, we applied time-resolved X-ray solution scattering (TRXSS) (Fig.1) to directly elucidate the ultrafast structural dynamics of Au-Au bond formation in $[Au(CN)_2^-]_3$ [3].

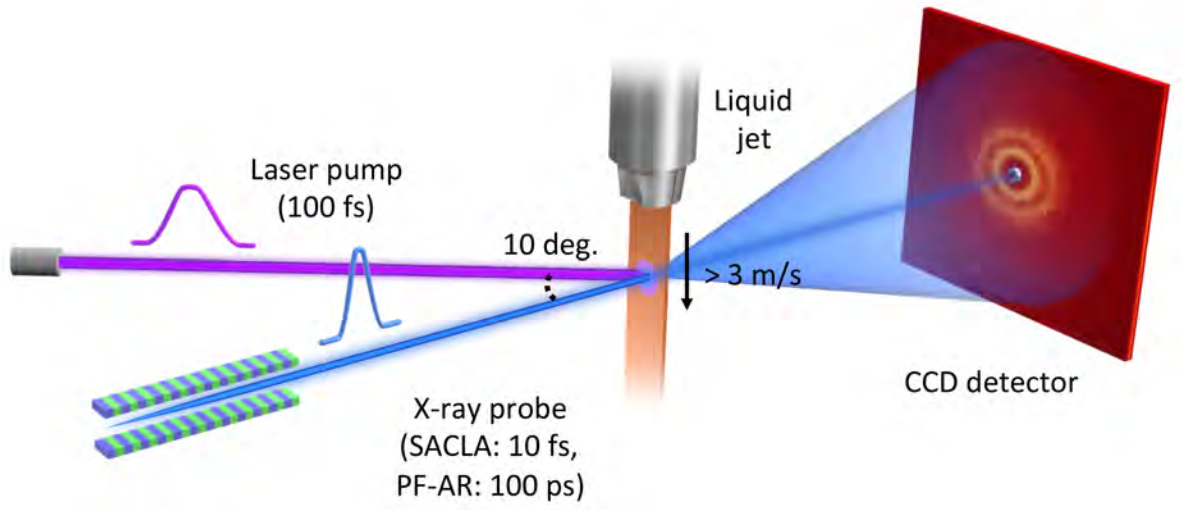

Figure 1: Schematic view of the experimental setup of time-resolved X-ray solution scattering (TRXSS). The sample solution is circulated and injected into the sample position by the liquid jet system to avoid sample damage caused by intense X-ray and optical laser pulses.

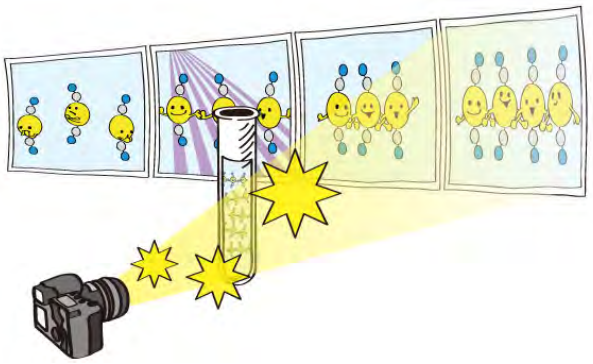

Figure 2: Schematic view of capturing the “molecular movie” of photochemical reaction dynamics by TRXSS

TRXSS is a powerful method for probing photoinduced structural changes of molecules in solution and has been used for revealing the dynamics and mechanism of many molecular reaction systems ranging from small molecules to biological macromolecules. The recent development of X-ray free electron lasers (XFELs), which generate ultrashort (~10 fs duration) X-ray pulses with ~10^{12} photons per pulse made it possible to explore chemical processes occurring down to sub-ps time scale using TRXSS. By performing the TRXSS experiment at PF-AR (KEK) and SACLA (RIKEN) facilities complementally, structural dynamics of bond formation of $[Au(CN)_2^-]_3$ in solution was elucidated from femtosecond to nanosecond time domain (Fig.2) [3].

The initial photo-induced formation of Au-Au covalent bonds among weakly bound Au atoms in a gold trimer complex, $[Au(CN)_2^-]_3$ was investigated by using femtosecond TRXSS at SACLA. Based on the TRXSS data, subtle structural changes of the metal complex were visualized in real time and real space. Upon photoexcitation, the trimer with an asymmetric bent structure and weakly bound Au atoms (3.3 Å and 3.9 Å Au-Au distances) in the ground (S_0) state rapidly converted into a symmetric and linear structure in the electronic excited (S_1) state where stronger Au-Au bonds (2.8 Å Au-Au distances) are formed (Fig. 3). Subsequently, the S_1 state transforms to the T_1 state with 1.6 ps time constant while accompanying further contraction of Au-Au bonds by 0.1 Å. Later, the T_1 state of the trimer converts to a tetramer on nanosecond time scale. Finally, the bond lengths and bond angles of the reactant (S_0 of the trimer), the transient species (S_1 and T_1 of the trimer) and the final product (the tetramer) was successfully determined with sub-angstrom spatial resolution.

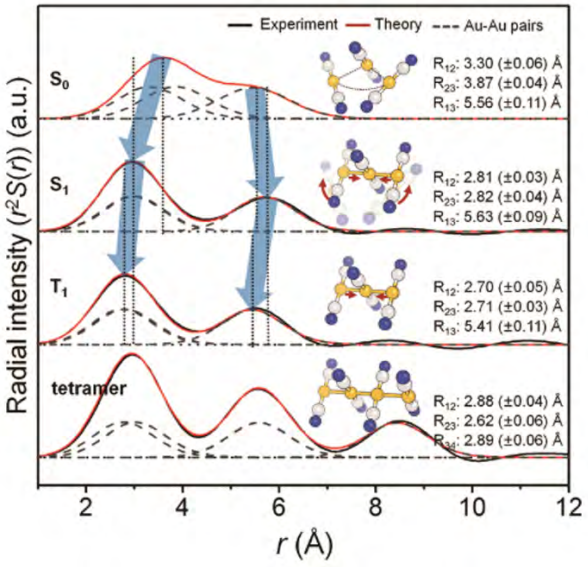

Figure 3: Time-dependent modulation of the radial distribution functions directly reflecting time-dependent change of molecular structure of gold complex. Yellow, white, and blue atoms represent gold, carbon, and nitrogen atoms, respectively.

The TRXSS method offers a means of visualizing the whole processes of photo-induced reactions in real time and real space, and will be used as a fundamental tool to study the reaction dynamics of chemical and biological systems, such as artificial and natural photosynthetic reactions.

REFERENCES

[1] M. A. Rawashdeh-Omary, M. A. Omary, and H. H. Patterson, *J. Am. Chem. Soc*. **122**, 10371 (2000).
[2] M. Iwamura, K. Nozaki, S. Takeuchi, and T. Tahara, *J. Am. Chem. Soc*. **135**, 538 (2013).
[3] K. H. Kim, J. G. Kim, S. Nozawa, T. Sato, K. Y. Oang, T. W. Kim, H. Ki, J. Jo, S. Park, C. Song, T. Sato, K. Ogawa, T. Togashi, K. Tono, M. Yabashi, T. Ishikawa, J. Kim, R. Ryoo, J. Kim, H. Ihee, and S. Adachi, *Nature*, **518**, 385 (2015).

BEAMLINE

AR-NW14A

K. H. Kim[1, 2], J. G. Kim[1, 2], S. Nozawa[3], T. Sato[3], K. Y. Oang[1, 2], T. W. Kim[1, 2], H. Ki[1, 2], J. Jo[1, 2], S. Park[1, 2], C. Song[4], T. Sato[4], K. Ogawa[4], T. Togashi[5], K. Tono[5], M. Yabashi[4], T. Ishikawa[4], J. Kim[6], R. Ryoo[1, 2], J. Kimi[7], H. Ihee[1, 2], and S. Adachi[3, 8] ([1]Center for Nanomaterials and Chemical Reactions, [2]KAIST, [3]KEK-IMSS-PF, [4]RIKEN SPring-8 Center, [5]JASRI, [6]The Catholic Univ. of Korea, [7]Inha Univ., [8]SOKENDAI / The Graduate Univ. for Advanced Studies)

Unprecedented Single-Layered Rhodium Nanosheets: Metallene

Despite significant advances in the fabrication of two-dimensional materials, the preparation of single-layered metal materials remains a challenge. We report a solvothermal synthesis of novel single-layered rhodium nanosheets (Rh NSs) with large dimensions. Atomic force microscopy shows that the Rh NS is less than 4 Å thick. Electron diffraction and X-ray absorption spectroscopy measurements suggest that the ultrathin Rh NS has only a single-atom layer. Density functional theory (DFT) studies reveal that the single-layered Rh NS possesses a unique δ-bonding framework formed via Rh 4d orbitals that stabilizes the ultrathin structure. Similar to graphene, we propose to call the single-layered metal nanosheet "metallene".

The discovery of ultrathin materials, such as graphene [1], molybdenum disulfide, and boron nitride [2], has aroused considerable research interest due to their fascinating properties, such as high electron mobility, quantum Hall effects, extraordinary thermal conduction, magnetic resonant mode, and superconductivity. Up to now, the fabrication of ultrathin materials has mainly relied on the strong intra-layer chemical bonding and weak inter-layer interactions. In contrast, metal atoms have strong preferences for three-dimensional close-packed structures, making it challenging to prepare ultrathin metallic materials.

Herein, we report the fabrication of single-layered rhodium nanosheets (Rh NSs) with an edge length of ca. 500–600 nm by using a simple solvothermal synthetic approach [3]. These semi-transparent Rh NSs are highly sensitive to electron beam irradiation in high-resolution transmission electron microscopy (HRTEM), suggesting an ultrathin structure. Aberration-corrected electron microscopy, atomic force microscopy (AFM), and X-ray adsorption spectroscopy further reveal that the Rh NSs are composed of planar single-atom-layer sheets of Rh atoms. As shown in Fig. 1, AFM visualization and the corresponding height profiles display a large sheet-like morphology with a height of ca. 4 Å, in accordance with the diameter of a Rh atom of 3.46 Å, suggesting that the as-prepared Rh NSs are layers of only one atom in thickness. Taking advantage of its ability to provide statistical significance, extended X-ray absorption fine structure (EXAFS) was used to elucidate the local coordination environment of Rh atoms and to determine the thickness of Rh NSs. As shown in Table 1, the coordination number (CN) for close-packed nanoparticles (NPs) is 10.4 ± 0.8, in agreement with the expected value for normal nanoparticles. In contrast, a much smaller CN value of 6.4 ± 0.7 is obtained for the Rh NSs, fitting well with the CN of a single-layered structure. Additionally, the average Rh–Rh bond length in Rh NSs is estimated as 2.692 ± 0.004 Å from the EXAFS spectra, which is similar to that of Rh foil (2.687 ± 0.003 Å), indicating that the single-layered Rh NSs consist of close-packed Rh atoms.

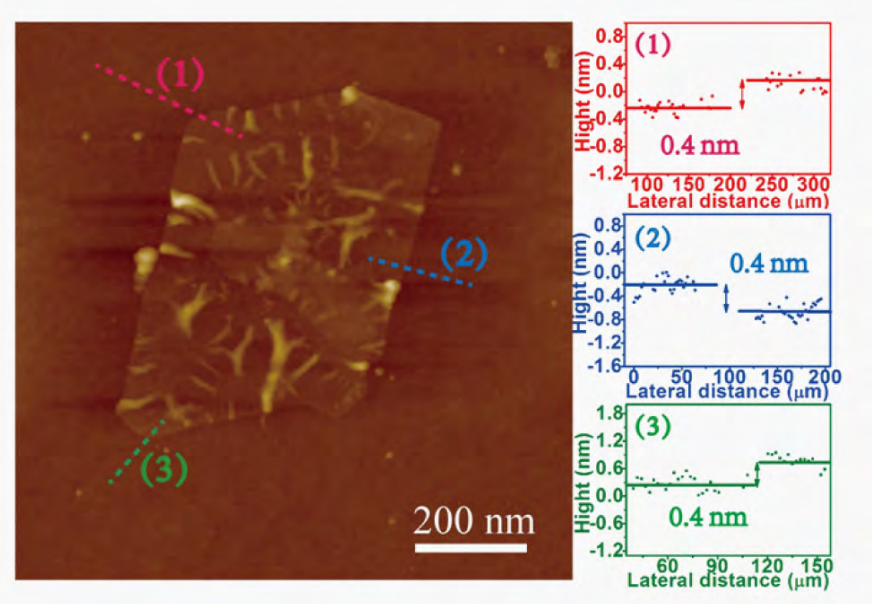

Figure 1: Atomic force microscope image of an individual rhodium nanosheet with height profiles for three different areas.

Table 1: Structural parameters obtained from the curve fitting analysis of the EXAFS spectra
[a]X-ray absorbing and scattering atoms, [b]Coordination number, [c]Atomic distance, [d]Mean-square disorder in the distribution of inter-atomic distances, [e]defined; Range Δk = 2–13 Å^{-1}, ΔR = 1.8–2.8 Å.

Sample	Ab−Sc[a]	C.N.[b]	r^c/Å	σ^{2d}	R factor
Rh foil	Rh–Rh	12[e]	2.687 ± 0.003	0.0038 ± 0.0004	0.0019
Rh NPs	Rh–Rh	10.4 ± 0.8	2.687 ± 0.003	0.0045 ± 0.0004	0.0015
ultrathin Rh sheets	Rh–Rh	6.4 ± 0.7	2.692 ± 0.004	0.0063 ± 0.0006	0.0041

To elucidate the nature of the unexpected stability of the Rh NSs, theoretical studies were carried out by using density functional theory (DFT) and *ab initio* molecular dynamics (AIMD) simulations. It is shown that the single-layered Rh NSs possess a delocalized δ-bonding framework, constructed from $4d_{z^2}$–5s hybrid orbitals of Rh atoms, which stabilizes the single-layered structure together with the external poly(vinylpyrrolidone) ligands. The δ-bonding in single-layered Rh NSs has high similarity with the π-bonding in graphene. As shown in Fig. 2(a), Rh 4d orbitals split into e_{2g} (d_{xy}, $d_{x^2-y^2}$), e_{1g} (d_{xz}, d_{yz}), and a_{1g} (d_{z^2}) species upon interacting with six peripheral Rh atoms in a Rh_7 (D_{6h}) cluster. The highest half-filled a_{1g} orbital forms the shoulder-to-shoulder δ-bonding framework. In contrast, in graphene, each C atom has half-filled $(sp^2)^3$ hybrid orbitals that form the σ-skeleton and a $(p_z)^1$ orbital that forms the delocalized π-bonding framework. Based on the analogy with graphene, we have chosen to call the Rh NSs "metallene". AIMD simulations at 21 ps show that the structure of single-layered Rh is stable even at T = 300 K [Fig. 2(b)].

To investigate the catalytic properties of ultrathin Rh NSs, hydrogenation processes of phenol and hydroformylation of 1-octene were employed as probe reactions. Commercial Rh/C and Rh NPs were chosen as the benchmark catalysts. In the hydrogenation of phenol, the best performance was achieved with ultrathin Rh NSs, which gave >99.9% conversion within 4 h near room temperature (30°C) under low H_2 pressure (1.0 MPa) and showed an activity that was, respectively, four and seven times greater than those of commercial Rh/C and Rh NPs (based on conversion at 1 h). In the hydroformylation of 1-octene, ultrathin Rh NSs were found to give both superior catalytic activity and selectivity towards the target product (aldehyde) compared with commercial Rh/C and Rh NPs. The high performance of Rh NSs in catalysis is attributed to the 100% proportion of surface atoms, which is not possible in commercial Rh/C or Rh NPs.

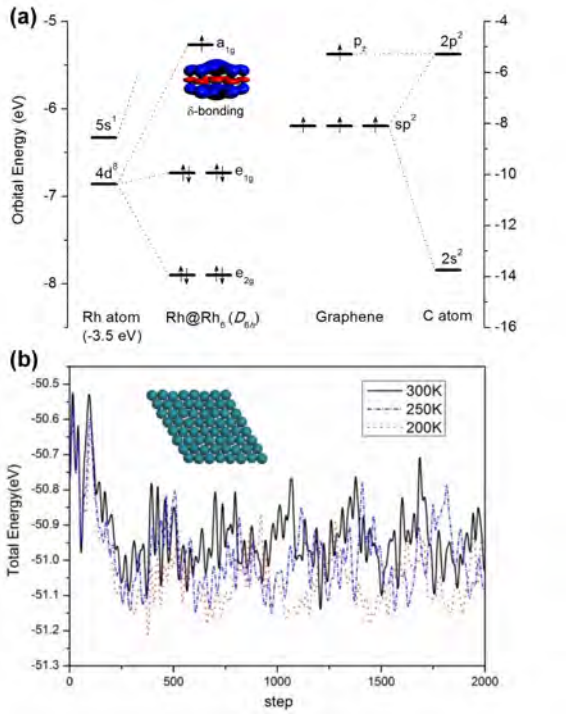

Figure 2: (a) Molecular orbitals of Rh_7 (D_{6h}) cluster constructed by central Rh atom and peripheral Rh_6 frame (left) and schematic molecular orbitals of change to graphene (right). (b) Total energies of a single-layered Rh of the last 6 ps of AIMD simulations at 200, 250 and 300 K.

REFERENCES

[1] K. S. Novoselov, A. K. Geim, S. V. Morozov, D. Jiang, Y. Zhang, S. V. Dubonos, I. V. Grigorieva, and A. A. Firsov, *Science* **306**, 666 (2004).
[2] K. S. Novoselov, D. Jiang, F. Schedin, T. J. Booth, V. V. Khotkevich, S. V. Morozov, and A. K. Geim, *Proc. Natl. Acad. Sci. U. S. A.* **102**, 10451 (2005).
[3] H. Duan, N. Yan, R. Yu, C. -R. Chang, G. Zhou, H. -S. Hu, H. Rong, Z. Niu, J. Mao, H. Asakura, T. Tanaka, P. J. Dyson, J. Li, and Y. Li, *Nat. Commun*. **5**, 3093(2014).

BEAMLINE

AR-NW10A

H. Duan, C.-R. Chang, J. Li, and Y. Li (Tsinghua Univ.)

Scanning Transmission X-Ray Microscopic Investigation of Bulk-heterojunction Organic Solar Cell

Organic solar cells (OSCs) with a bulk-heterojunction (BHJ) are promising energy conversion devices, because they are flexible and environment-friendly, and can be fabricated by a low-cost roll-to-roll process. Using scanning transmission X-ray microscopy (STXM), we investigated the fullerene mixing ($\Phi_{Fullerene}$) of the active layer in OSCs based on films of poly-(9,9-dioctylfluorene-co-bithiophene) (F8T2) / [6,6]-phenyl C_{71}-butyric acid methyl ester ($PC_{71}BM$) blend annealed at various temperatures (T_{an}). We found that the $\Phi_{Fullerene}$ value in the polymer matrix decreases with increase in T_{an}, which suppresses the power conversion efficiency (PCE) of OCS.

The bulk-heterojunction (BHJ) active layer of organic solar cell (OSC) is easily fabricated by thermal annealing after spin-coating of the organic solvent of donor (D) polymer and acceptor (A) fullerene. The active layer consists of phase-separated nano-size domains of the polymer and fullerene. The power conversion efficiency (PCE) is optimized by chemical admixture into the solvent and/or the annealing temperature (T_{an}) via modification of the morphology of the active layer. The energy conversion process of the OSC is realized by the combination of the carrier formation and transfer processes. In the former process, the photo-created exciton migrates to the D/A interface and separates into an electron and hole pair. The nano-size structure is essential for efficient carrier formation, because the length of exciton migration is ~3 nm. In the latter process, the carriers transfer to the collector electrode and are collected as photocurrent. Thus, it is essential to clarify the film morphology in order to truly understand the OSC device.

Scanning transmission X-ray microscopy (STXM) around the carbon K-edge is a powerful tool to clarify the molecular mixing as well as the domain structure in the BHJ active layer [1, 2], because it can distinguish the fullerene carbon from the polymer carbon. Collins *et al*. [1] revealed the fullerene mixing ($\Phi_{Fullerene}$) in the polymer matrix of PTB7/$PC_{71}BM$ blend film. Due to the low spatial resolution (~ several tens of nm) of STXM, however, the domain size had to be enlarged by chemical admixture [1] or high-temperature annealing [2]. Here, we selected the F8T2/$PC_{71}BM$ system, because the blend films form periodic large domains (~ several hundreds of nm) independent of T_{an}. We clarify the interrelation between $\Phi_{Fullerene}$ and T_{an}, and discuss the effect of molecular mixing on photovoltaic performance.

Figure 1 shows an STXM image of the F8T2/$PC_{71}BM$ blend films annealed at T_{an} = 190°C at 284.4 eV. The photon energy (284.4 eV) was at the π^*-resonance absorption of the fullerene framework [1, 3, 4]. Therefore, the bright regions correspond to the fullerene-rich domains, while the dark regions the polymer-rich domains. The length scale (~ 230 nm) of the fullerene domain was evaluated by two-dimensional Fourier transformation.

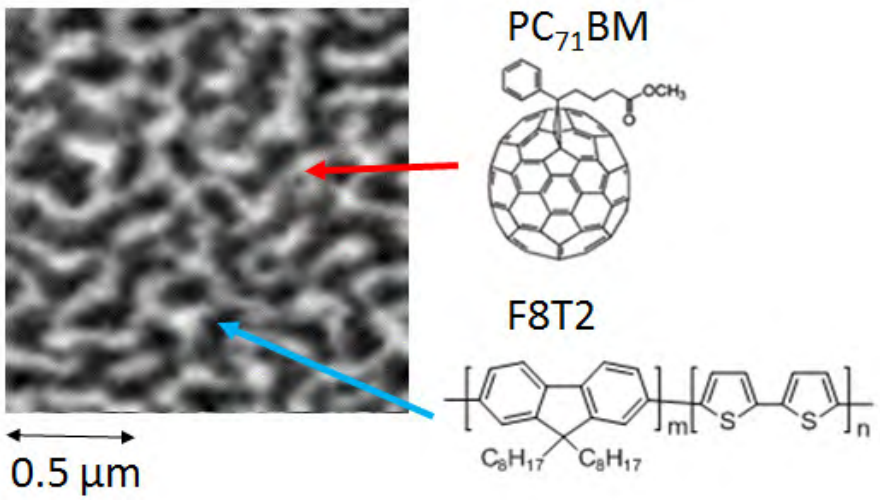

Figure 1: STXM image of F8T2/$PC_{71}BM$ blend films at 284.4 eV. The bright regions correspond to the $PC_{71}BM$-rich domains, while the dark regions the F8T2-rich domains.

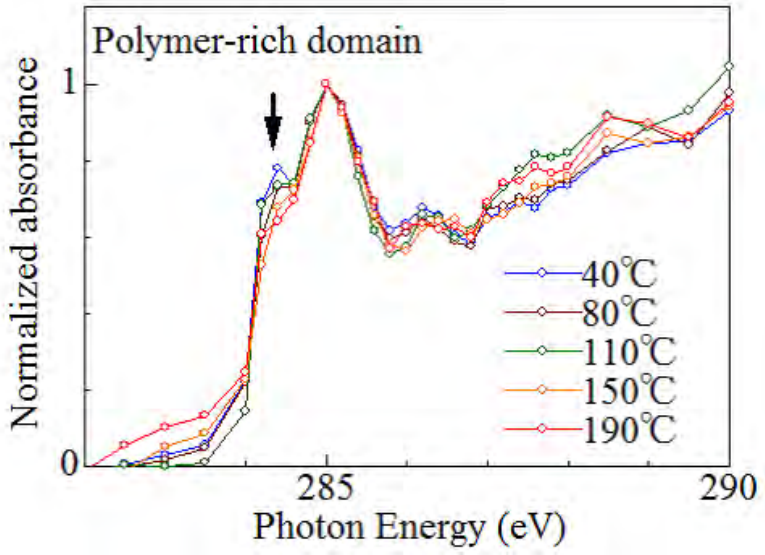

Figure 2: Carbon K-edge absorption spectra in the polymer-rich domain against T_{an}. The spectra are normalized at 285.0 eV. A downward arrow indicates the first π-resonance of fullerene carbon. The data were replotted from Ref. [4].

Figure 2 shows carbon K-edge absorption spectra in the polymer-rich domain against T_{an}. The spectral feature is characteristic to the F8T2 polymer [3] except for the shoulder structure at 284.4 eV. The structure is ascribed to the first π-resonance of fullerene carbon. Importantly, the relative intensity of the fullerene peak at 284.4 eV systematically decreases with T_{an}. This indicates that the $\Phi_{Fullerene}$ value in the polymer-rich domain decreases with increase in T_{an}. The decrease in $\Phi_{Fullerene}$ is reasonable, because the thermal annealing at higher T_{an} accelerates the phase-separation into more pure domains.

The reduction of $\Phi_{Fullerene}$ causes the suppression of the PCE of the OSC. Yasuda *et al*. [5] systematically investigated the photovoltaic properties of the OSCs based on films of F8T2/PC_{71}BM (33 : 67 wt.%) blend annealed at various T_{an}. They found that the PCE systematically decreases from the optimal value (= 2.28%) at T_{an} = 80°C to 0.81% at 240°C. Thus, the annealing process at higher temperature deteriorates the photovoltaic performance. We evaluated the length scales of the fullerene domain against T_{an} by two-dimensional Fourier transformation. We found that the domain size (~ 230 nm) is nearly independent of T_{an}. This indicates that the T_{an} dependence of the PCE cannot be ascribed to the domain size effects in our F8T2/PC_{71}BM system. As seen in Fig. 2, the $\Phi_{Fullerene}$ value in the polymer-rich domain decreases with increase in T_{an}. We consider that the mixed fullerene within the polymer-rich domain works as a reaction site for the charge separation, because the domain size (~ 230 nm) of our F8T2/PC_{71}BM system is too large for excitons to reach the domain boundary. Therefore, the reduction of $\Phi_{Fullerene}$ suppresses the efficiency of carrier formation within the polymer domains, even though domain purification may be advantageous for carrier transfer efficiency.

REFERENCES

[1] B. A. Collins, Z. Li, J. R. Tumbleston, E. Gann, C. R. McNeill, and H. Ade, *Adv. Energy Matter*. **3**, 65 (2013).
[2] W. Ma, J. R. Tumbleston, M. Wang, E. Gann, F. Huang, and H. Ade, *Adv. Energy Mater*. **3**, 864 (2013).
[3] Y. Moritomo, T. Sakurai, T. Yasuda, Y. Takeichi, K. Yonezawa, H. Kamioka, H. Suga, Y. Takahashi, Y. Yoshida, N. Inami, K. Mase, and K. Ono, *Appl. Phys. Express* **7**, 052302 (2014).
[4] Y. Moritomo, T. Yasuda, K. Yonezawa, T. Sakurai, Y. Takeichi, H. Suga, Y. Takahashi, N. Inami, K. Mase, and K. Ono, *Sci. Rep*., **5**, 9483 (2015).
[5] T. Yasuda, K. Yonezawa, M. Ito, H. Kamioka, L. Han, and Y. Moritomo, *J. Photopolym. Sci. Technol*., **25**, 271 (2011).

BEAMLINE

BL-13A

Y. Moritomo[1], T. Yasuda[2], K. Yonezawa[1], T. Sakurai[1], Y. Takeichi[3], H. Suga[4], Y. Takahashi[3, 5], N. Inami[3], K. Mase[3], and K. Ono[3] ([1]Univ. of Tsukuba, [2]NIMS, [3]KEK-IMSS-PF, [4]Hiroshima Univ., [5]The Univ. of Tokyo)

Comparative Crystal Chemistry of Perovskite-to-Postperovskite Transitions in Germanates under High Pressure

Postperovskite with the $CaIrO_3$ structure in (Mg, Fe)SiO_3 characterizes the D″ layer in the lowermost mantle of the Earth. Because of the scarcity of examples of postperovskites in analogue compounds, it is difficult to investigate the criteria for crystallization of the postperovskite structure. One solution is to explain the transition to the $CaIrO_3$-type postperovskite structure by the extrapolated compressive behavior of the $GdFeO_3$-type orthorhombic perovskite. Therefore, we conducted in situ X-ray diffraction experiments to follow the structural change of germanate perovskites. Based on the crystallographic data of $AGeO_3$ (A = Mn, Zn, and Mg), we developed a comparative crystal chemistry approach to stabilize the $CaIrO_3$ structure.

Postperovskite phase transition to the $CaIrO_3$-type structure in magnesium silicates characterizes the structure of the D″ layer in the lowermost mantle of the Earth [1]. Although the change in density for the perovskite-to-postperovskite transition is less than a few percent, the structural change from a corner sharing framework to a layered structure explains the anisotropy in the seismic data of the D″ layer.

Since postperovskite has been found in $MgSiO_3$, many ABO_3 compounds have been tested for transformation to the postperovskite phase. However, it is difficult to investigate the criteria for transformation to the $CaIrO_3$-type structure. One of the reasons is that the $CaIrO_3$ structure is not a typical structure of most ABO_3 perovskites, except for the related compounds of $CaIrO_3$, such as $CaRhO_3$ [2], $CaPtO_3$ [3], and $CaRuO_3$ [4]. In fact, postperovskites are not found in silicate except for $MgSiO_3$. Moreover, titanate perovskites, such as $FeTiO_3$ [5], $MnTiO_3$ [6], $CaTiO_3$ [7], and $ZnTiO_3$ [8], prefer to decompose to dense oxide compounds rather than to crystallize in the $CaIrO_3$ structure. However, multiple germanate compounds have been reported to crystallize in the $CaIrO_3$ structure. Perovskite–postperovskite transitions of $MgGeO_3$ [9] and $MnGeO_3$ [10] have been confirmed to occur at 55 and 65 GPa. Recently, using the in situ X-ray diffraction method with a laser-heated diamond anvil cell, we found that the perovskite–postperovskite transition in $ZnGeO_3$ occurs above 110–130 GPa [11]. Considering the similarity of the cationic radius of Zn^{2+} with those of Mg^{2+} and Mn^{2+}, the transition pressure was unexpectedly high compared with the transition pressure in other germanate compounds.

Theoretical calculations suggest that distortion of $GdFeO_3$-type orthorhombic perovskite could trigger the postperovskite transition [12]. It is well-known that the Goldschmidt tolerance factor represents the distortion in ABO_3 perovskites [13]. However, the tolerance factor based on the ionic radii only reflects the distortion at atmospheric pressure. Because the orthorhombic distortion is derived from the rotation of the BO_6 octahedra, the rotation angle Φ, which is calculated from the lattice parameters as $\Phi = \cos^{-1}(\sqrt{2}c^2/ab)$, is a useful indicator of the distortion to the postperovskite transition [14]. Our recent studies of fluoride perovskite with sodium fluorides, such as $NaCoF_3$, $NaNiF_3$ and $NaZnF_3$, indicated that the transition starts at Φ_{tr} = 24–27°. Irrespective of the octahedral constituent cations, other known postperovskites in $MgSiO_3$ and $MgGeO_3$ also

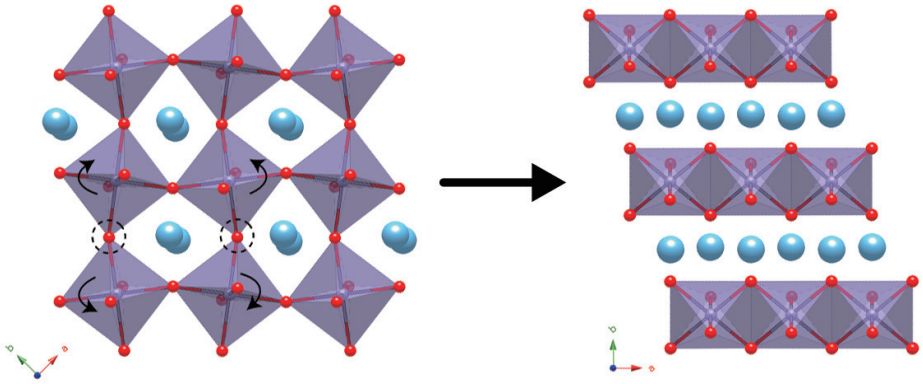

Figure 1: Schematic illustrations of the phase transition from the perovskite (left) to the postperovskite phase (right).

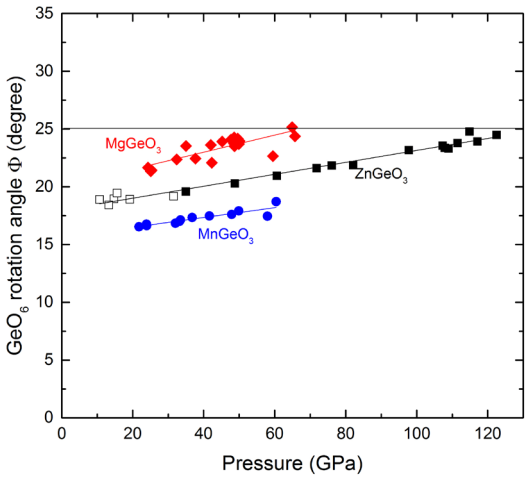

Figure 2: GeO_6 rotation angle (Φ) in perovskites as a function of pressure. Diamonds, squares, and circles represent the Φ values of $MgGeO_3$, $ZnGeO_3$, and $MnGeO_3$, respectively.

exhibit a transition at around Φ_{tr} = 25°. The above example suggests that $\Phi_{tr} \approx$ 25° would be a critical angle to induce the phase transition to postperovskite. The transformation scheme is shown in Fig. 1. To examine the Φ value in the present germanate compositions, the lattice parameters of the perovskite and postperovskite phases of $ZnGeO_3$ and $MnGeO_3$ were determined under high pressure with careful annealing with a laser beam to reduce the full-width at half maximum of the X-ray diffraction peaks. Figure 2 shows Φ of $ZnGeO_3$ and $MnGeO_3$ with pressure change. In this figure, Φ of $MgGeO_3$, which is calculated from literature data [15], is included for comparison. The gradient of Φ is almost independent of the divalent cation species. Interestingly, Φ_{tr} of $ZnGeO_3$ is also located at around Φ_{tr} = 25°. Therefore, a rather high transition pressure in $ZnGeO_3$ is reasonable with respect to the rotation of the GeO_6 octahedra. Instead, according to Φ_{tr}, the low value of $MnGeO_3$ (Φ_{tr} = 18°) might be an exception. The ionic radius of Mn^{2+} (0.96 Å) is significantly larger than the radii of Mg^{2+} (0.89 Å) and Zn^{2+} (0.90 Å). Therefore, in perovskites with large divalent cations, the corner-sharing GeO_6 frameworks cannot generate sufficient space to incorporate the cations by increasing the tilting angle. These frameworks likely decompose to form the postperovskite structure without a large rotation of the GeO_6 octahedra. Furthermore, in view of the geometry of the $CaIrO_3$ structure, the *b* axis should be the most sensitive to the divalent cationic radius because divalent cations incorporate into the GeO_6 layered structure. In fact, the *b* axis of $MnGeO_3$ is considerably longer than the *b* axes of other germanates. This can be attributed to the ability of the postperovskite structure to incorporate large divalent cations.

REFERENCES

[1] M. Murakami, K. Hirose, K. Kawamura, N. Sata, and Y. Ohishi, *Science* **304**, 855 (2004).
[2] Y. Shirako, H. Kojitani, M. Akaogi, K. Yamaura, and E. T. -Muromachi, *Phys. Chem. Miner.* **36**, 455 (2009).
[3] K. Ohgushi, Y. Matsushita, N. Miyajima, Y. Katsuya, M. Tanaka, F. Izumi, H. Gotou, Y. Ueda, and T. Yagi, *Phys. Chem. Miner.* **35**, 189 (2008).
[4] H. Kojitani, Y. Shirako, and M. Akaogi, *Phys. Earth Planet. Inter.* **165**, 127 (2007).
[5] D. N. -Hamane, M. G. Zhang, T. Yagi, and Y. M. Ma, *Am. Mineral.* **97**, 568 (2012).
[6] T. Okada, T. Yagi, and D. N. -Hamane, *Phys. Chem. Miner.* 38, 251 (2011).
[7] D. Hamane and T. Yagi, *Review of High Pressure Science and Technology* **22**, 246 (2012).
[8] M. Akaogi, K. Abe, H. Yusa, H. Kojitani, D. Mori, and Y. Inaguma, *Phys. Chem. Miner.* **42**, 421 (2015).
[9] E. Ito, D. Yamazaki, T. Yoshino, H. Fukui, S. M. Zhai, A. Shatzkiy, T. Katsura, Y. Tange, and K. Funakoshi, *Earth. Planet. Sci. Lett.* **293**, 84 (2010).
[10] D. Yamazaki, E. Ito, T. Katsura, T. Yoshino, S. M. Zhai, H. Fukui, A. Shatskiy, X. Z. Guo, S. M. Shan, T. Okuchi, Y. Tange, Y. Higo, and K. Funakoshi, *Am. Mineral.* **96**, 89 (2011).
[11] H. Yusa, T. Tsuchiya, M. Akaogi, H. Kojitani, D. Yamazaki, N. Hirao, Y. Ohishi, and T. Kikegawa, *Inorg. Chem.* **53**, 11732 (2014).
[12] T. Tsuchiya, J. Tsuchiya, K. Umemoto, and R. M. Wentzcovitch, *Earth. Planet. Sci. Lett.* **224**, 241 (2004).
[13] V. M. Goldschmidt, *Naturwissenschaften* **14**, 477 (1926).
[14] M. O'keeffe, B. G. Hyde, and J. O. Bovin, *Phys. Chem. Miner.* **4**, 299 (1979).
[15] C. E. Runge, A. Kubo, B. Kiefer, Y. Meng, V. B. Prakapenka, G. Shen, R. J. Cava, and T. S. Duffy, *Phys. Chem. Miner.* **33**. 699 (2006).

BEAMLINE

AR-NE1A

H. Yusa[1] and T. Kikegawa[2] ([1]NIMS, [2]KEK-IMSS-PF)

The Change in the Intermediate-Range Network Structure Plays a Key Role in the Migration of Magma in the Earth's Upper Mantle

We have found the occurrence of shear flow in usually brittle SiO_2 glass when compressed uniaxially in a diamond-anvil cell at room temperature. We have also measured the microscopic differential strain with a radial X-ray diffraction technique and clarified that SiO_2 glass transforms to a high-density low-viscosity phase by reconstructing the intermediate-range network consisting of SiO_4 tetrahedra. These results suggest that anomalous pressure dependence of the two important physical properties, density and viscosity, of silicate melts at the pressure range of the Earth's upper mantle can be attributed to the change in the intermediate-range order.

Numerous studies have long been conducted on the high-pressure behavior of glasses at room temperature because of their remarkable structural similarity to melts at high temperatures. In particular, it has been emphasized that the increase in coordination number of silicon takes place in silicate melts in the Earth's deep mantle, based on the observations in SiO_2 and other silicate glasses [1]. At the same time, SiO_2 glass has long been known for the phenomenon referred to as permanent densification [2]. This phenomenon is not related to the increase in coordination number but to the reconstruction of the intermediate-range network consisting of SiO_4 tetrahedra [3]. Our analyses have revealed that the anomalous pressure dependence of density of silicate melts at the pressure range of the upper mantle can be well explained by assuming the phase-transition-like structural change in the intermediate-range order [4, 5]. Structural changes are also expected to have strong effects on the viscosity of melts. In this study, uniaxial-compression experiments on SiO_2 glass were conducted to discuss the effects of the structural change in the intermediate-range order on the plasticity of glasses and hence the viscosity of melts.

Two types of high-pressure uniaxial-compression experiment, macroscopic-strain and microscopic-strain measurements, were conducted with a diamond-anvil cell at room temperature. In the former, the change in size of disk-shaped SiO_2 glass was measured with an optical microscope [Fig. 1(a)] [6]. In the latter, the azimuth-angle dependence of the first sharp diffraction peak (FSDP) of SiO_2 glass (at Q ~2 $Å^{-1}$) was measured with a radial X-ray diffraction technique, in which X-ray irradiated the sample from a direction perpendicular to the compression axis [Fig. 2(a)] [7]. The FSDP has been considered to be associated with the periodicity of the intermediate-range network. Radial X-ray diffraction measurements were also conducted on the recovered sample to obtain more complete structural information (up to Q ~15 $Å^{-1}$) [6].

The optical-microscope observations revealed that a large shear flow began at around 8–10 GPa, which is the onset-pressure condition of permanent densification, and continued at least up to 20 GPa [Fig. 1(b)]. Note that SiO_2 glass is usually considered to be a brittle material. The radial X-ray diffraction measurements showed significant anisotropy in the intermediate-range

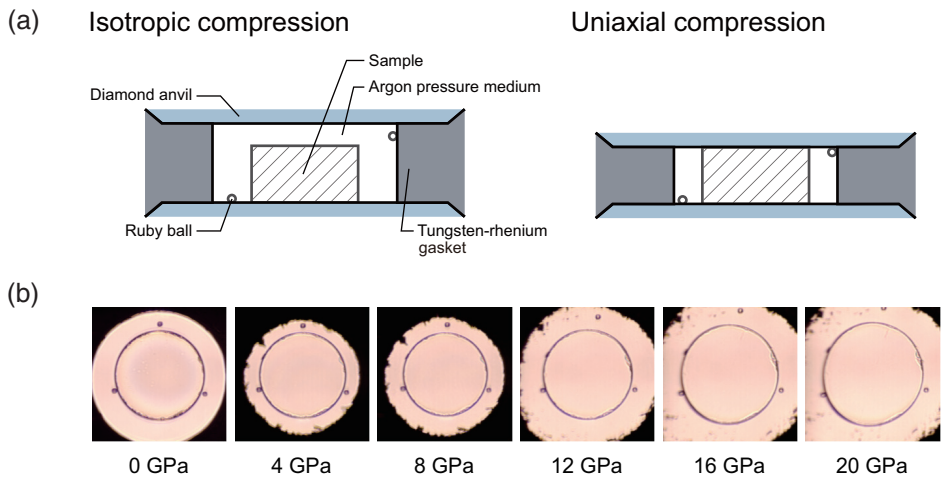

Figure 1: (a) Schematic illustrations of the cross section of the sample chamber and (b) optical-microscope images in high-pressure deformation experiments. The disk-shaped sample having an initial diameter of ~150 μm was compressed isotropically up to 6–8 GPa and its size decreased with increasing pressure. The sample was pinched directly by the two anvils and compressed uniaxially at higher pressures and its size in the radial direction increased with increasing pressure.

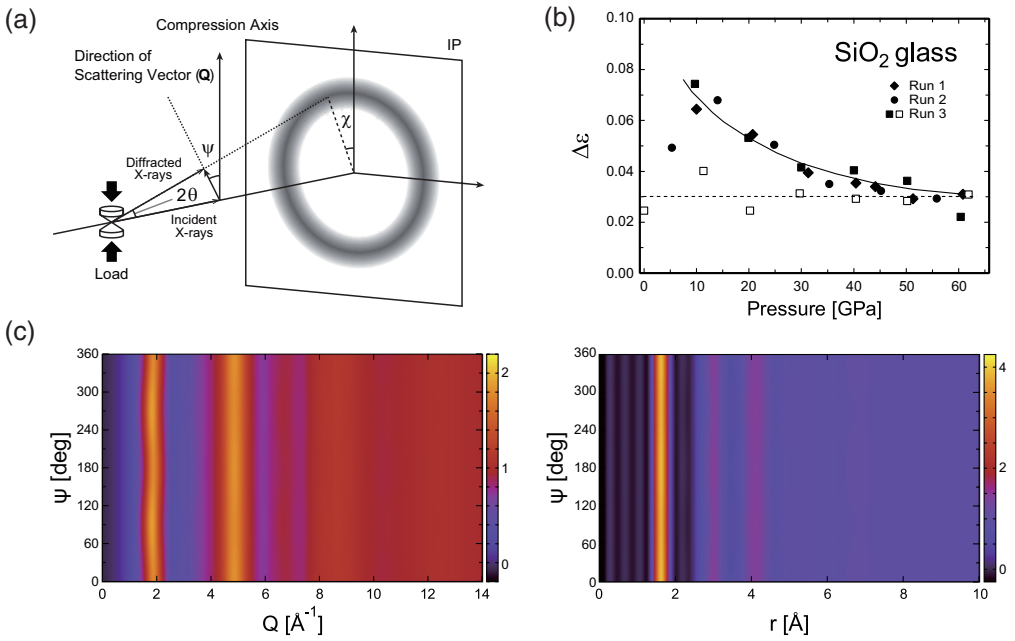

Figure 2: (a) Schematic illustration of the radial X-ray diffraction geometry. (b) Pressure dependence of the microscopic differential strain calculated from the azimuth-angle dependence of the FSDP of SiO_2 glass. Black and white symbols represent the data on compression and decompression, respectively. The solid and broken lines are to guide the eye. A large differential strain of ~3% remained after decompression. (c) Azimuth-angle dependence of the structure factor and pair distribution function of the recovered sample. Again, the FSDP showed significant anisotropy. The structure factor at a higher-Q range and the first peak of the pair distribution function (corresponding to the Si-O bond) did not show any significant anisotropy, indicating that differential strain did not remain in the basic unit of the SiO_4 tetrahedron.

network at high pressures [Fig. 2(b)]. Measurements on the recovered sample suggested that the plastically deformed sample was in the fully densified state (~20% increase in density) and, very surprisingly, a large differential strain of ~3% (equivalent to ~2 GPa in differential stress) remained in the intermediate-range order [Fig. 2(c)]. However, this large residual strain (or anisotropic permanent densification) cannot directly explain the macroscopic differential strain (or shear flow) that is about an order of magnitude larger. The weakening of the Si-O-Si bond with the densification is supposed to facilitate the rearrangement of the network and make a large shear flow possible.

The density and viscosity of silicate melt are very important for understanding the dynamics of the Earth and planetary interiors. The density contrast between silicate melts and crystals and the viscosity of silicate melts are directly related to the migration of magma as the driving and resisting forces, respectively. Here, we discuss the pressure dependence of viscosity of silicate melt on the basis of our experimental results on the plasticity of SiO_2 glass. The viscosity of SiO_2-rich melts has been reported to decrease with increasing pressure [8]. This anomalous decrease in viscosity has often been explained by a model in which the increase in the coordination number of aluminum plays a key role. Several other models have also been proposed. However, none of these models can explain our experimental results on SiO_2 glass. It seems to be more appropriate to introduce a model in which the change in intermediate-range order plays a key role. The pressure dependence of viscosity is supposed to be determined by a balance between two competing effects: the negative effect due to the weakening of the Si-O-Si bond (caused by the change in intermediate-range order) and the positive effect due to the decrease in free volume. The anomalous pressure dependence of the two important physical properties, density and viscosity, of silicate melts at the pressure range of the Earth's upper mantle can be attributed to the change in the intermediate-range network structure.

REFERENCES

[1] N. Funamori and T. Sato, *Earth Planet. Sci. Lett.* **295** (2010) 435.
[2] P. W. Bridgman and I. Šimon, *J. Appl. Phys.* **24** (1953) 405.
[3] D. Wakabayashi, N. Funamori, T. Sato, and T. Taniguchi, *Phys. Rev. B* **84** (2011) 144103.
[4] D. Wakabayashi and N. Funamori, *Phys. Chem. Mineral.* **40** (2013) 299.
[5] D. Wakabayashi, N. Funamori, T. Sato, and T. Sekine, *Geophys. Res. Lett.* **41** (2014) 50.
[6] D. Wakabayashi, N. Funamori, and T. Sato, *Phys. Rev. B* **91** (2015) 014106.
[7] T. Sato, N. Funamori, and T. Yagi, *J. Appl. Phys.* **114** (2013) 103509.
[8] I. Kushiro, H. S. Yoder Jr., and B. O. Mysen, *J. Geophys. Res.* **81** (1976) 6351.

BEAMLINES

BL-18C and AR-NE1A

D. Wakabayashi[1], N. Funamori[1], and T. Sato[2] ([1]KEK-IMSS-PF [2]Hiroshima Univ.)

Blocking Effect of Natural Organic Matter on the Adsorption of Cesium in Particulate Matter Recovered from the Pripyat River in Chernobyl

Cesium (Cs) is adsorbed into the interlayer of clay minerals as an inner-sphere complex. Natural organic matter (NOM) in the environment can inhibit the adsorption of Cs by an NOM covering on the clay minerals. This blocking effect of NOM can increase the dissolved fraction of Cs in river water, leading to an increase of Cs incorporation in the ecosystem. The blocking effect, however, has not been shown by direct observation of natural samples. Using scanning transmission X-ray microscopy (STXM), we confirmed a coating of humic substances on clay minerals in particulate matter obtained from the Pripyat River, and revealed that the blocking effect occurs in natural samples.

The behavior of radioactive cesium (RCs) emitted by nuclear power plant accidents [1, 2] differed between the Abukuma (Fukushima) and Pripyat (Chernobyl) Rivers. Previous studies showed that more than 70% of Cs was dissolved in the Pripyat River [3]. Conversely, Cs in particulate matter (PM) accounted for more than 70% of total Cs in the Abukuma River (dissolved fraction was less than 30%) [4]. Although Cs is generally adsorbed into the interlayer of clay minerals as an inner-sphere complex [5], laboratory adsorption experiments suggested that the different RCs behavior between Chernobyl and Fukushima may be related to the blocking effect by the coating of natural organic matter (NOM) on clay minerals [6]. This blocking effect of NOM, however, has not been shown by direct observation of natural samples in terms of morphological images and characterization of NOM responsible for the effect. Therefore, the aim of this study was to investigate the blocking effect in the environment (especially at Chernobyl) including characterization of the blocking organic matter.

In the Pripyat River, water sample was filtered initially by a membrane filter to recover river PM (> 0.45 μm). Dissolved organic carbon (DOC) content was 18 mg/L in the Pripyat River, which is 10 times higher than that in the Abukuma River (= 0.9–1.3 mg/L).

We examined Cs L_{III}-edge EXAFS to study Cs species adsorbed on PM collected from the Pripyat River and on the PM treated by hydrogen peroxide (H_2O_2) to decompose organic matter [6]. The samples for Cs-EXAFS were prepared as follows: a PM sample was equilibrated with 0.76 mol/L CsCl, washed repeatedly with Milli-Q water to remove the excess CsCl solution, and then sealed in polyethylene bags [6]. The EXAFS spectra of the Cs on PM were measured at BL-9A and BL-12C.

Figure 1(b) shows radial structural functions (RSF; phase shift uncorrected) of Cs L_{III}-edge EXAFS spectra for Cs adsorbed on Chernobyl PM before and after the removal of NOM [7]. As references, spectra of hydrated Cs^+ in water and Cs adsorbed on clay minerals are shown. The first and second peaks at R+ΔR = 2.3–2.7 Å and 3.3–3.7 Å are ascribed to Cs bonding to oxygen in hydrated water and the direct bonding of Cs to a siloxane layer in a 2:1 phyllosilicate mineral, respectively. As to the PM from Chernobyl, the RSF for the original sample exhibits a larger first peak than the second one. On the other hand, the magnitude of the second peak became similar to that of the first peak after the removal of NOM. These results suggest that PM has the potential to form an inner-sphere complex with Cs, the contri-

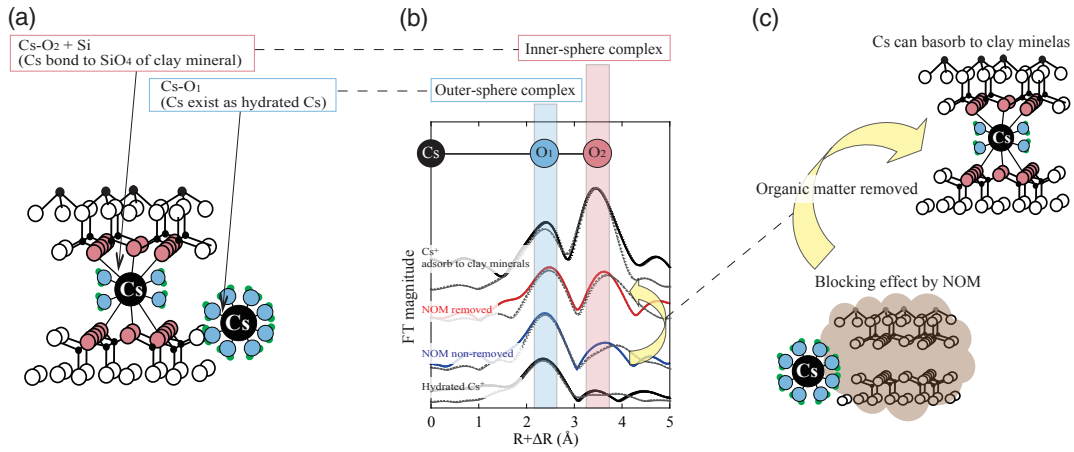

Figure 1: (a) Cs adsorption model of inner-sphere and outer-sphere complex. (b) RSF of Cs L_{III}-edge EXAFS of Cs adsorption on clay minerals, NOM removed sample, NOM non-removed sample, and hydrated Cs. (c) The model of the blocking effect, and relationship between organic matter and Cs adsorption behavior.

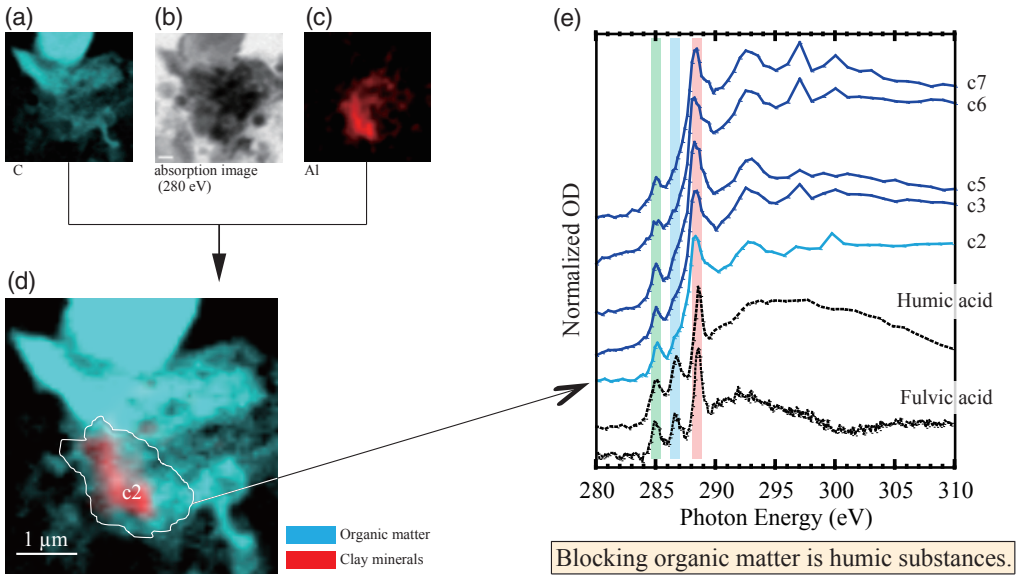

Figure 2: (a), (b), and (c) are the carbon image, absorption image at 280 eV as the morphological image, and aluminum image, respectively. (d) Composite image of (a) and (c), clearly showed that organic matter covering the clay minerals. (e) C-XANES extracted from the area of interest in (d) and that of other PM, which revealed that the blocking organic matter is humic substances. The first, second, and third peak indicate aromatic, phenolic or ketonic, and carboxylic carbon, respectively.

bution of which is larger in the sample after the removal of organic matter [6]. The second peak, however, was attenuated for Cs adsorbed on the original PM, which suggests that the NOM inhibits the formation of the inner-sphere complex because of the blocking effect. The coating of NOM results in the reduction of K_d (solid-water distribution coefficient), or the decrease of Cs adsorption onto the PM [7].

Subsequently, association of NOM and clay minerals in the PM and characterization of NOM were conducted by scanning transmission X-ray microscopy (STXM) coupled with C *K*-edge XANES for the area of interest within the STXM image [7] using a compact STXM [8], newly developed at BL-13A. Figure 2 shows the absorption image at 280 eV as a morphological image (b), carbon image (a), and aluminum image (c) of PM [7]. Figure 2 (d) clearly shows that organic matter covered the clay minerals, and carbon *K*-edge XANES [Fig. 2(e)] indicated that humic substances, mainly composed of humic and fulvic acids [9, 10], were the main components that induced the blocking effect in the Pripyat River.

Based on these Cs EXAFS and C XANES results, it is confirmed that the blocking effect can occur in the Pripyat River, which is caused by the covering of humic substances on clay minerals [7]. It was also found that K_d of Cs decreases with the increase of organic content in the PM, possibly due to the blocking effect. Hence, we conclude that the association of NOM and clay minerals can control the distribution of RCs into the aqueous phase, which in turn governs its incorporation into aquatic ecosystems.

REFERENCES

[1] P. H. Santschl, S. Bollhalder, K. Farrenkothen, A. Lueck, S. Zlngg, and M. Sturm, *Environ. Sci. Technol.* **22**, 510 (1988).
[2] N. Yoshida and Y. Takahashi, *Elements* **8**, 201 (2012).
[3] U. Sansone, M. Belli, O. V. Voitesekovitch, and V. V. Kanivets, *Sci. Total. Environ* **186**, 257 (1996).
[4] A. Sakaguchi, K. Tanaka, H. Iwatani, H. Chiga, Q. H. Fan, Y. Onda, and Y. Takahashi, *J. Environ. Radioact.* **139**, 379 (2015).
[5] H. Qin, Y. Yokoyama, Q. H. Fan, H. Iwatani, K. Tanaka, A. Sakaguchi, Y. Kanai, J. Zhu, Y. Onda, and Y. Takahashi, *Geochem. J.* **46**, 297 (2012).
[6] Q. H. Fan, M. Tanaka, K. Tanaka, A. Sakaguchi, and Y. Takahashi, *Geochim. Cosmochim. Act.* **135**, 49 (2014).
[7] H. Suga, Q. Fan, Y. Takeichi, K. Tanaka, H. Kondo, V. V. Kanivets, A. Sakaguchi, K. Kato, N. Inami, K. Mase, K. Ono, and Y. Takahashi, *Chem. Lett.* **43**, 1128 (2014).
[8] Y. Takeichi, N. Inami, H. Suga, K. Ono, and Y. Takahashi, *Chem. Lett.* **43**, 373 (2014).
[9] A. Rigol, M. Vidal, G. Rauret, C. A. Shand, and M. V. Cheshire, *Environ. Sci. Technol.* **32**, 663 (1998).
[10] T. Schäfer, G. Buckau, R. Artinger, J. I. Kim, S. Geyer, M. Wolf, W. F. Bleam, S. Wirick, and C. Jacobsen, *Org. Geochem.* **36**, 567 (2005).

BEAMLINES

BL-9A, BL-12C, and BL-13A

H. Suga[1, 2], Q. H. Fan[3], Y. Takeichi[2, 4], K. Tanaka[1], H. Kondo[1], A. Sakaguchi[5], N. Inami[2], K. Mase[2, 4], K. Ono[2, 4], and Y. Takahashi[2, 6] ([1]Hiroshima Univ., [2]KEK-IMSS-PF, [3]Chinese Academy of Sciences, [4]SOKENDAI, [5]Univ. of Tsukuba, [6]The Univ. of Tokyo)

Structural Study of Core Complex Cascade in the CRISPR-Cas Immune System

Clustered regularly interspaced short palindromic repeats (CRISPR) together with CRISPR-associated (cas) proteins form the CRISPR-Cas system to defend against foreign nucleic acids of bacterial and archaeal origin. In the I-E subtype CRISPR/Cas system, 11 subunits from five Cas proteins ($CasA_1B_2C_6D_1E_1$) assemble along a crRNA to form the Cascade complex. We reported on the 3.05 Å crystal structure of the 405-kDa *E. coli* Cascade complex, which provides molecular details beyond those available from earlier lower-resolution cryo-EM structures.

In recent years, a novel adaptive immune system called the CRISPR-Cas system has been found in approximately half of bacteria and almost all archaea [1, 2]. CRISPR-Cas immune systems depend the invading nucleic acid by three steps. The first step is spacer acquisition, in which new spacers are acquired from the foreign nucleic acid into the CRISPR locus. The second step is CRISPR-Cas expression, in which CRISPR arrays are transcribed and processed into small interfering crRNAs. The final step is interference, in which mature crRNAs assemble with Cas proteins into a surveillance complex that targets DNA for degradation, thereby preventing the propagation of viruses and plasmids. The hallmark of the type I CRISPR-Cas system is the assembly of the large Cascade surveillance complex that uses crRNA to recognize DNA targets. Previous studies indicated that Cascade is a 405-kDa complex packaged by five essential proteins with different numbers of copies ($CasA_1B_2C_6D_1E_1$) and a 61-nucleotide crRNA (Fig. 1a). Despite comprehensive functional and structural characterizations, the high-resolution structure of Cascade at the atomic level is needed to clarify the molecular mechanism of its reconstitution and targeting DNA.

We determined the crystal structure of *Escherichia coli* Cascade complex using diffraction data collected at the Photon Factory (Fig. 1b) [3]. This structure provides molecular details beyond those available from earlier lower-resolution cryo-electron microscopy structures. Overall, this complex exhibits a sea-horse-shaped architecture. Instead of forming a simple, compact structure, the 11 subunits are assembled into two structural layers. Six CasC proteins, together with CasD and CasE, tightly pack to form the outer layer. The inner layer consists of CasA and CasB dimer. With the perfect electron density map, we observed all 61 nucleotides of the crRNA and subsequently analyzed its interactions with different Cas proteins. Specifically, the 3'-end of crRNA adopts a stem loop-fold and the stem makes extensive contact with the positively charged area in the CasE C-terminal, whereas the 5'-end of crRNA takes on a hook-like shape, and is embedded in a "pocket" formed by CasD, CasA, and CasC6. The crRNA consists of a 32-nucleotide spacer flanked by two end repeats. Interestingly, the spacer fragment is not continuously stacked, with five kinks present at regular intervals, namely at the positions of the 6^{th}, 12^{th}, 18^{th}, 24^{th}, and 30^{th} nucleotides. The kinked positions precisely co-localize and interact with the five beta-hairpins projecting from CasC2-CasC6. Consequently, the bases of the kinked nucleotides are flipped out and do not participate in DNA binding. Subsequent mutagenesis and biochemical experiments showed that the mutations of the kinked nucleotides had no obvious effect on target DNA recognition and confirmed the discovery from the structure.

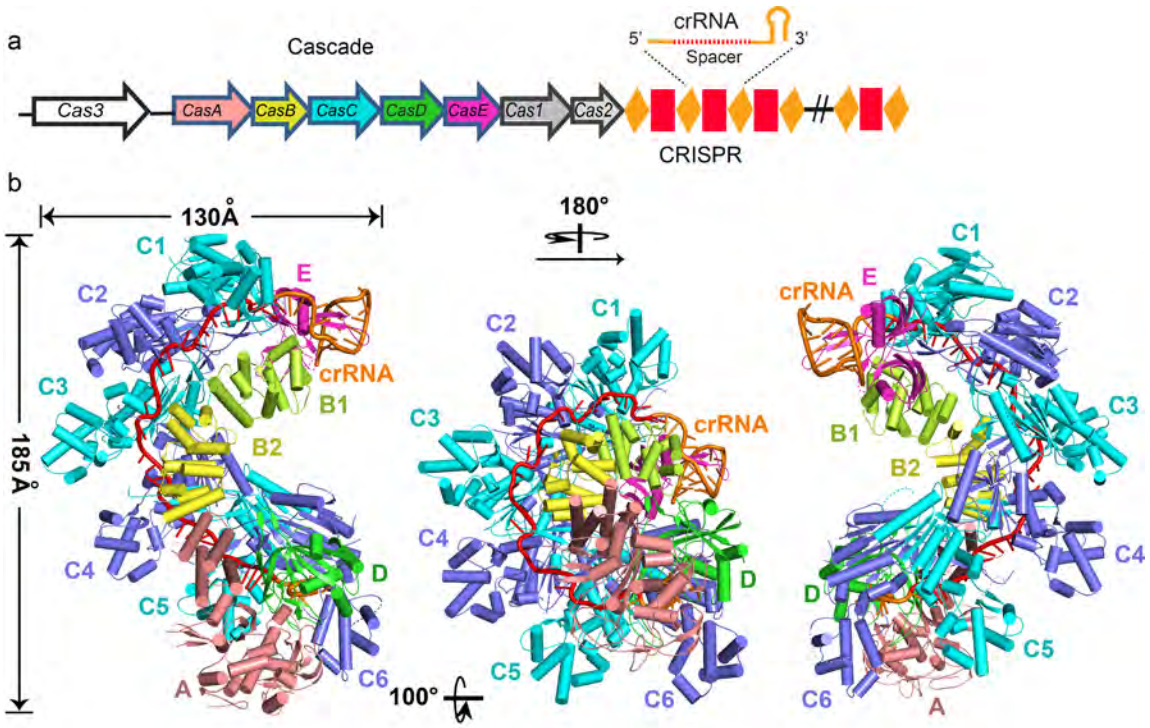

Figure 1: Crystal structure of the Cascade complex from *E. coli.* a, The I-E subtype CRISPR system in *E. coli* (K12) consists of eight Cas proteins and the CRISPR locus. b, Overall structure of the Cascade complex. Reprinted with permission from the Nature.

In conclusion, these structural studies have provided insights into both the assembly and target recognition of the Cascade complex. The results also revealed that crRNA plays an essential role not only in target recognition, but also in Cascade complex formation. Furthermore, the elongated beta-hairpin loop from Cas protein represents a multifunctional element that plays a critical role in spacer RNA stabilization, CasC helix formation, and CasA–CasD as well as CasC–CasA and CasC–CasB interactions.

REFERENCES

[1] B. Wiedenheft, S. H. Sternberg, and J. A. Doudna, *Nature* **482**, 331 (2012).
[2] B. Wiedenheft, S. H. Sternberg, and J. A. Dounda, *Science* **315**, 1709 (2007).
[3] H. Zhao, G. Sheng, J. Wang, M. Wang, G. Bunkoczi, W. Gong, Z. Wei, and Y. Wang, *Nature* **515**, 147 (2014).

BEAMLINES

BL-1A, BL-5A, and BL-17A

H. Zhao and Y. Wang (Chinese Academy of Sciences)

Crystal Structure of Marburg Virus GP Bound to a Cross-Reactive Antibody from a Human Survivor

Filoviruses, including Marburg and Ebola viruses, cause hemorrhagic fever with up to 90% mortality in humans. Despite its potential availability, no cross-reactive antibody has been reported against filovirus glycoproteins (GPs). Here, we present the structure of a cross-reactive antibody MR78, derived from a human survivor, in complex with Marburg virus (MARV) GP. The conformational epitope recognized by MR78 is shown to overlap with the receptor binding site on GP, and is highly conserved among all filoviruses. The GP and Fab complex structure provides a clue for structure-based vaccine designs.

Marburg virus (MARV) and Ebola virus (EBOV), members of the family *Filoviridae*, cause highly lethal hemorrhagic fever in humans. EBOV reemerged and caused the biggest outbreak of a filovirus in Western Africa, mainly in Guinea, Liberia, and Sierra Leone, in 2014 [1]. MARV also caused the biggest outbreak in Angola in 2004–2005, which exhibited ~90% mortality [2, 3]. Currently, no licensed therapeutic agents or vaccines are available. Filoviruses possess a sole GP on their envelope (lipid bilayer membrane), which is mainly comprised of the highly glycosylated GP1, responsible for receptor attachment, and the GP2, mediating membrane fusion. To enter a cell, a filovirus is initially internalized by macropinocytosis. Next, cathepsin cleavage of GPs exposes the receptor-binding site (RBS) fully for the Niemann Pick C1 (NPC1) receptor in the endosome.

Therapeutic antibodies are expected to be a highly effective treatment not only for infectious diseases but also for various other diseases. Recently, broadly cross-reactive antibodies have been elicited against the glycoproteins of HIV and Influenza virus (Flu) as potentially therapeutic agents, and the structural basis for the broad cross reactivity has also been solved [4-6]. So far, however, little has been known about cross-reactive antibodies against MARV and EBOV. Especially, structural information for such monoclonal antibodies (mAbs) is lacking in filovirus research, in contrast to those of HIV and Flu. Here, we report the structures of the cross-reactive antibody, MR78, in complex with MARV GP. Our structural study sheds light on the humoral response and vaccine development by revealing how MR78 provides cross reactivity against filovirus GPs [7, 8].

For a structural understanding of the cross reactivity by MR78, we determined the crystal structure of the antigen-binding fragment (Fab) MR78 in complex with MARV GP (Fig. 1). The GP was in its supposed metastable, prefusion conformation. Diffraction to 3.6 Å resolution was obtained from the cocrystal of MARV GP and Fab MR78, which contained four complexes in the asymmetric unit. The overall structure of MR78 and MARV GP exhibited inverted tripod-like binding modes [Fig. 1(a)]. Although MARV and EBOV differ in the whole GP sequences by ~70%, MR78 recognizes the same regions on both viruses. The epitope recognized by MR78 is located only on the GP1 subunit. This is different from previously reported ebolavirus GP-binding antibodies, KZ52, 16F6, 2G4 and 4G7, which bind both GP1 and GP2 subunits [Fig. 1(b)] [9-12]. Unlike ebolavirus GP-binding antibodies, MR78 could absolutely inhibit domain binding of the NPC1 domain C. The binding site of MR78 would be on or close to the putative RBS.

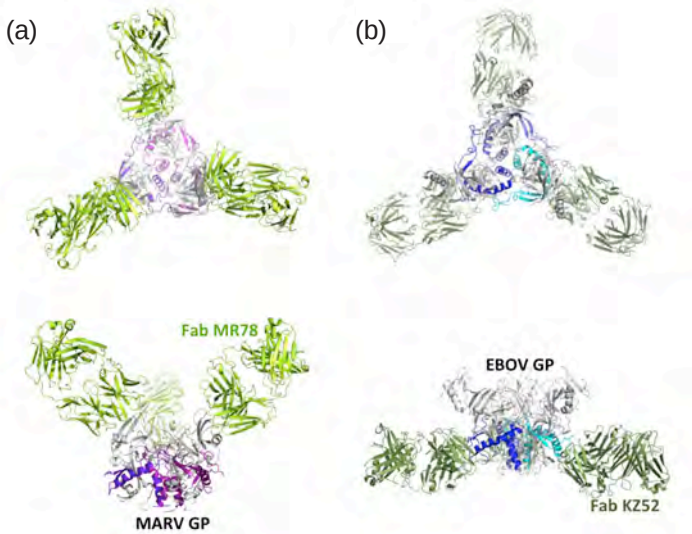

Figure 1: Crystal structures of filovirus GPs and antibodies. Top view (top) and side view (bottom). (a) MARV GP and Fab MR78 (light green). (b) EBOV GP and Fab KZ52 (dark green).

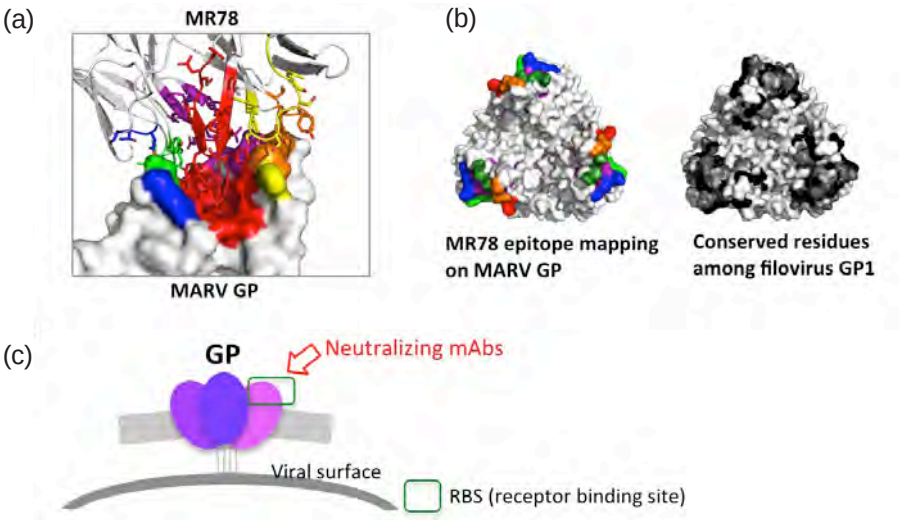

Figure 2: Binding site of MR78 and MARV GP. (a) The interaction between Fab MR78 (ribbon model) and MARV GP (surface). CDR-L1 (green), CDR-L2 (blue), CDR-L3 (purple), CDR-H1 (yellow), CDR-H2 (orange), CDR-H3 (red). (b) The epitope recognized by MR78 and the conserved residues (indicating by black, dark gray and gray depending on the level of conservation) on filovirus GP trimer. (c) Schematic presentation of MARV GP and its neutralizing antibodies.

To assess the MR78-epitope conservation among filovirus GPs, the protein sequence alignment was performed in ebolaviruses (*Zaire, Sudan, Reston, Taï Forest, Bundibugyo*), marburgviruses (Musoke, Angola, Popp, Ci67, DRC1999, Ravn), and cuevaviruses (Lloviu). As a result, 85% of the residues comprising the MR78 epitope showed similarity among filoviruses. Especially, the highly conserved residues on GP were found to interact with both heavy and light chains, however, the major interaction is comprised of the residues in the third complementarity-determining region of the heavy chain (CDR-H3) of Fab MR78 [Fig. 2(a)]. By contrast, the difference is ~70% in the whole GPs between MARV and EBOV as described above. These results explain why MR78 shows cross reactivity between MARV and EBOV. It is thus suggested that MR78 might bind to all filovirus GPs and inhibit the NPC1 binding [Fig. 2(b)].

The highly conserved MR78 epitope provided the structural basis for the cross reactivity against MARV and EBOV. However, no pan-reactive anti-filovirus antibodies have yet been reported from immunization using EBOV GP. MARV GP might be a better antigen to elicit cross-reactive mAbs against all filoviruses. The anti-RBS antibodies, like MR78, would be promising therapeutic candidates, because the escape mutants from anti-RBS antibodies would lose the receptor binding ability and then not be able to survive [Fig. 2(c)].

REFERENCES

[1] WHO E. R. Team, *The New England journal of medicine* **371**, 1481 (2014).
[2] J. S. Towner, M. L. Khristova, T. K. Sealy, M. J. Vincent, B. R. Erickson, D. A. Bawiec, A. L. Hartman, J. A. Comer, S. R. Zaki, U. Stroher, F. G. da Silva, F. del Castillo, P. E. Rollin, T. G. Ksiazek, and S. T. Nichol, *Journal of virology* **80**, 6497 (2006).
[3] T. W. Geisbert, K. M. D. -DiCaprio, J. B. Geisbert, H. A. Young, P. Formenty, E. A. Fritz, T. Larsen, and L. E. Hensley, *The Journal of infectious diseases* **196** Suppl 2, S372 (2007).
[4] D. R. Burton, R. Ahmed, D. H. Barouch, S. T. Butera, S. Crotty, A. Godzik, D. E. Kaufmann, M. J. McElrath, M. C. Nussenzweig, B. Pulendran, C. N. Scanlan, W. R. Schief, G. Silvestri, H. Streeck, B. D. Walker, L. M. Walker, A. B. Ward, I. A. Wilson, and R. Wyatt, *Cell host & microbe* **12**, 396 (2012).
[5] D. C. Ekiert, A. K. Kashyap, J. Steel, A. Rubrum, G. Bhabha, R. Khayat, J. H. Lee, M. A. Dillon, R. E. O'Neil, A. M. Faynboym, M. Horowitz, L. Horowitz, A. B. Ward, P. Palese, R. Webby, R. A. Lerner, R. R. Bhatt, and I. A. Wilson, *Nature* **489**, 526 (2012).
[6] R. H. Friesen, P. S. Lee, E. J. Stoop, R. M. Hoffman, D. C. Ekiert, G. Bhabha, W. Yu, J. Juraszek, W. Koudstaal, M. Jongeneelen, H. J. Korse, C. Ophorst, E. C. B. -van der Linden, M. Throsby, M. J. Kwakkenbos, A. Q. Bakker, T. Beaumont, H. Spits, T. Kwaks, R. Vogels, A. B. Ward, J. Goudsmit, and I. A. Wilson, *Proceedings of the National Academy of Sciences of the United States of America* **111**, 445 (2014).
[7] A. I. Flyak, P. A. Ilinykh, C. D. Murin, T. Garron, X. Shen, M. L. Fusco, T. Hashiguchi, Z. A. Bornholdt, J. C. Slaughter, G. Sapparapu, C. Klages, T. G. Ksiazek, A. B. Ward, E. O. Saphire, A. Bukreyev, and J. E. Crowe, Jr., *Cell* **160**, 893 (2015).
[8] T. Hashiguchi, M. L. Fusco, Z. A. Bornholdt, J. E. Lee, A. I. Flyak, R. Matsuoka, D. Kohda, Y. Yanagi, M. Hammel, J. E. Crowe, and Jr., E. O. Saphire, *Cell* **160**, 904 (2015).
[9] J. E. Lee, M. L. Fusco, A. J. Hessell, W. B. Oswald, D. R. Burton, and E. O. Saphire. *Nature* **454**, 177 (2008).
[10] J. M. Dias, A. I. Kuehne, D. M. Abelson, S. Bale, A. C. Wong, P. Halfmann, M. A. Muhammad, M. L. Fusco, S. E. Zak, E. Kang, Y. Kawaoka, K. Chandran, J. M. Dye, and E. O. Saphire, *Nat Struct Mol Biol* **18**, 1424 (2011).
[11] S. Bale, J. M. Dias, M. L. Fusco, T. Hashiguchi, A. C. Wong, T. Liu, A. I. Keuhne, S. Li, V. L. Woods Jr., K. Chandran, J. M. Dye, and E. O. Saphire. *Viruses* **4**, 447 (2012).
[12] C. D. Murin, M. L. Fusco, Z. A. Bornholdt, X. Qiu, G. G. Olinger, L. Zeitlin, G. P. Kobinger, A. B. Ward, and E. O. Saphire. P*roceedings of the National Academy of Sciences of the United States of America* **111**, 17182 (2014).

BEAMLINE

BL-1A

T. Hashiguchi (Kyushu Univ.)

Crystal Structure of Innate Immune Toll-Like Receptor 9 Recognizing Bacterial CpG DNA

Toll-like receptor 9 (TLR9) recognizes microbial DNA containing CpG motifs and activates innate immune responses. We determined the crystal structures of three TLR9 forms: unliganded, bound to agonistic CpG-DNA, and bound to inhibitory DNA (iDNA). Agonistic CpG-DNA–bound TLR9 formed a symmetric TLR9/CpG-DNA complex with 2:2 stoichiometry, whereas iDNA-bound TLR9 was a monomer. CpG-DNA was recognized by both protomers in the dimer, specifically by the N-terminal fragment from one protomer and the C-terminal fragment from the other. The iDNA, which forms a stem-loop structure suitable for binding by intramolecular base pairing, binds to the concave surface of TLR9.

Our bodies often face dangers from bacterial and viral invasions. The immune system is a defense against the infections, which eliminates pathogenic microorganisms. The innate immune system provides the first line of defense by detecting certain kinds of microbial products as a sign of danger and activating the downstream immune response. The toll-like receptor (TLR) is one of the best-known receptors in the innate immune system that recognizes a wide variety of microbial products. Dr. Beutler and Dr. Hoffmann won the Nobel Prize in Physiology or Medicine 2011 for their discovery concerning the activation of innate immunity by TLRs [1, 2]. TLR is a type I transmembrane receptor consisting of extracellular leucine-rich repeat (LRR) domain, transmembrane domain, and intracellular Toll/IL-1 receptor (TIR) domain. The LRR and TIR domains are responsible for the ligand recognition and signaling, respectively. In humans, ten members of TLRs (TLR1 to TLR10) are identified and each TLR recognizes different ligand. TLR9 recognizes CpG DNA, a DNA sequence with Cytosine-phosphate-Guanine dinucleotide (CpG) motif that is specific to bacterial and viral DNA [3, 4]. The activation of TLR9 by CpG DNA leads to the release of interferon and inflammatory cytokines. TLR9 thereby has a potential to be a target for the vaccine adjuvant or therapeutic agents for viral infections and allergy diseases. Although TLR9 has been studied extensively since its discovery in 2000, the way it functions, especially from a structural point of view, remains unknown.

We determined the crystal structures of the LRR domain of TLR9 in three forms: unliganded, inhibitory DNA bound, and CpG DNA bound forms [5].

The ring-shaped monomer structure of TLR9, where its N- and C-termini directly interact (Fig. 1A) is similar to that of TLR8 [6], the other member of TLRs that recognizes single stranded RNA, however, the ligand

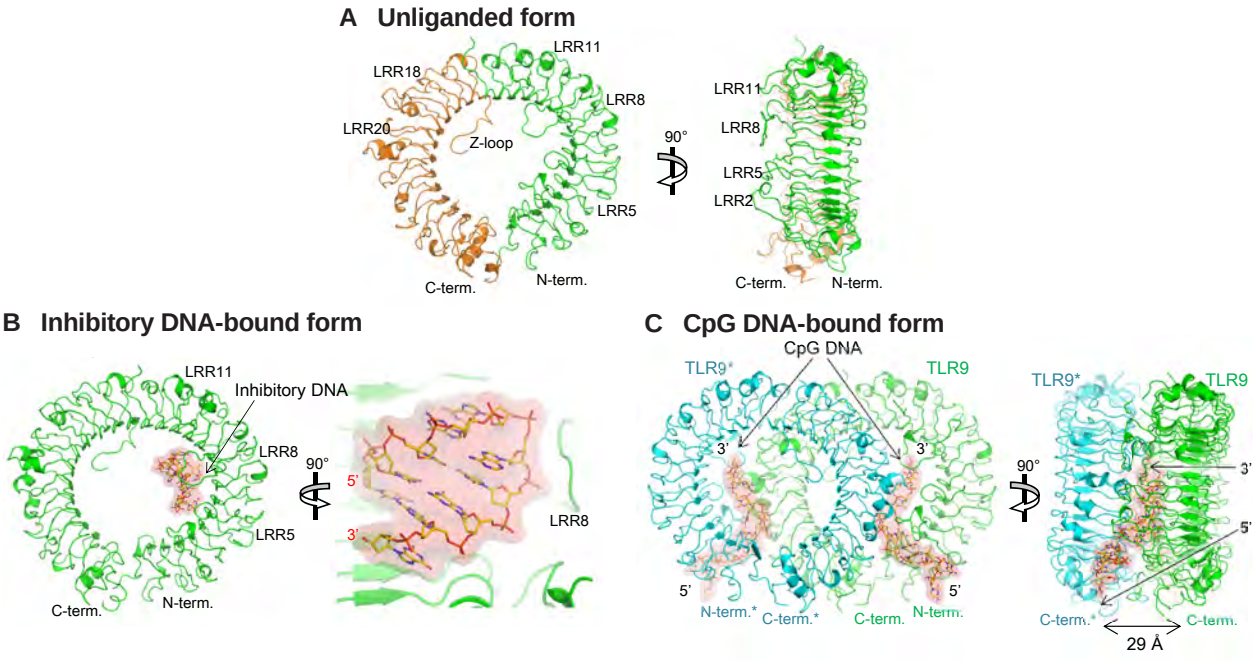

Figure 1: Structures of TLR9 in the unliganded (A), inhibitory DNA bound (B), and CpG DNA bound (C) forms. Bound DNAs are shown in sticks with semi-transparent surface representations in magenta. The N- and C-terminal halves of TLR9 are shown in green and brown, respectively in (A). The two protomers in the dimer are shown in green and cyan in (C).

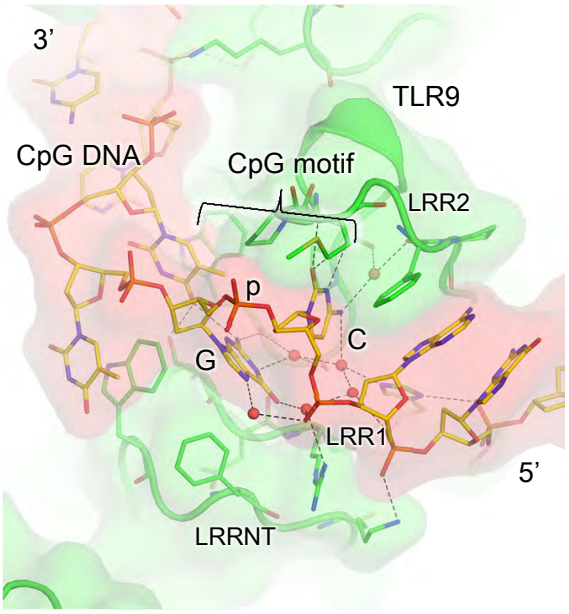

Figure 2: CpG motif binding mode of TLR9. CpG DNA and residues of TLR9 interacting with DNA are shown in sticks with semi-transparent surface representations in magenta (CpG DNA) and green (TLR9). Hydrogen-bonds are indicated with dashed lines.

binding modes are strikingly different between the two. In the crystal structures, the unliganded and inhibitory DNA bound forms of TLR9 are monomeric (Fig. 1A and 1B) while the agonistic CpG DNA bound form of TLR9 is dimeric (Fig. 1C), thus representing inactivated and activated forms, respectively. The dimerization of TLR9 brings the two C-termini in close proximity and would induce the association of the intracellular TIR domain, leading to the activation (Fig. 1C).

The agonistic CpG DNA in an extended conformation is recognized by both protomers in the dimer (Fig. 1C). The CpG DNA binds to the groove formed at the lateral face of the ring structure near the N-terminus in one protomer and simultaneously to the lateral face of the C-terminal side of the other protomer, thus act as a molecular glue to bridge the two TLR9 molecules and induce the activated form. The core hexamer regions of CpG DNA, including the CpG motif, are mainly recognized by TLR9 (Fig. 2). The bases of the CpG motif are accommodated in the groove and engage in multiple specific interactions with TLR9, which defines the specificity of the TLR9 toward CpG dinucleotide (Fig. 2). In addition, the flanking regions of the CpG motif further strengthen the interaction between TLR9 and CpG DNA.

The inhibitory DNA binds to the concave surface of TLR9 forming stem-loop structures with intramolecular three or four base-pairs (Fig. 1B). The high affinity of the inhibitory DNA is achieved mainly through the recognition of the backbone of the stem-loop structures. Since the binding site for the inhibitory DNA partially overlaps with that for agonistic CpG DNA, inhibitory DNA competes for the binding site with agonistic CpG DNA and thereby inhibits the TLR9 activation.

These structural analyses enable us to understand the detailed CpG DNA and inhibitory DNA recognition and activation mechanism of TLR9 and also open a new avenue for developing the novel therapeutic agents targeting TLR9.

REFERENCES

[1] A. Poltorak, X. He, I. Smirnova, M. -Y. Liu, C. V. Huffel, X. Du, D. Birdwell, E. Alejos, M. Silva, C. Galanos, M. Freudenberg, P. R. -Castagnoli, B. Layton, and B. Beutler, *Science* **282**, 2085 (1998).
[2] B. Lemaitre, E. Nicolas, L. Michaut, J. M. Reichhart, and J. A. Hoffmann, Cell 86, 973 (1996).
[3] H. Hemmi, O. Takeuchi, T. Kawai, T. Kaisho, S. Sato, H. Sanjo, M. Matsumoto, K. Hoshino, H. Wagner, K. Takeda, and S.Akira, *Nature* **408**, 740 (2000).
[4] S. Bauer, C. J. Kirschning, H. Hacker, V. Redecke, S. Hausmann, S. Akira, H. Wagner, and G. B. Lipford, *Proc. Natl. Acad. Sci. U.S.A.* **98**, 9237 (2001).
[5] U. Ohto, T. Shibata, H. Tanji, H. Ishida, E. Krayukhina, S. Uchiyama, K. Miyake, and T. Shimizu, *Nature* (2015).
[6] H. Tanji, U. Ohto, T. Shibata, M. Taoka, Y. Yamauchi, T. Isobe, K. Miyake, and T. Shimizu, *Nat. Struct. Mol. Biol.* **22**, 109 (2015).

BEAMLINES

BL-17A and AR-NE3A

U. Ohto, Hi. Tanji, and T. Shimizu (The Univ. of Tokyo)

Complete Snapshots of the Hemoglobin Allosteric Transition in a Single Crystal Form

Hemoglobin was one of the first protein structures ever to be solved by X-ray crystallography. Two crystal structures of hemoglobin, tense (T) and relaxed (R), have shaped our view of protein allostery, but it is increasingly clear that the hemoglobin allosteric transition cannot be adequately described by just these two states. We determined a wide range of nine hemoglobin quaternary structures including previously unidentified intermediates by using a novel crystal form in which hemoglobin is free to adopt any structure, depending on the conditions. Our findings give a comprehensive picture of the equilibrium conformers and transition pathway for hemoglobin.

Human hemoglobin, an $(\alpha\beta)_2$ tetrameric hemoprotein (see Fig. 1, top), acts as an efficient O_2 carrier by changing its affinity for O_2 more than 100-fold during the four successive binding steps [1]. Such a cooperative interaction is generally thought to be attributed to an allosteric transition from a tense (T) to a relaxed (R) state that binds O_2 more strongly [2]. Earlier crystallographic studies on the deoxy unliganded T state and fully liganded R state of hemoglobin provided a simple view of this transition, which involves a rotation of one $\alpha\beta$ dimer ($\alpha1\beta1$) relative to the other ($\alpha2\beta2$) by approximately 15° [Fig. 1(a)] [3]. In contrast to this textbook description, later studies argued that there may be intermediate states in this transition, but capturing those structures proved difficult [4-6]. Thus, significant debate continues as to the sequence and nature of the allosteric transition.

We recently succeeded in fully capturing the hemoglobin allosteric transition by using three isomorphous hemoglobin crystals [Fig. 1(b)] [7]. We used metal substitution [8], a variety of conditions, and interdimer chemical cross-linking [9] to generate three kinds of hemoglobin crystals, namely, half-CO-liganded hemoglobin crystals with and without phosphate (referred to as HL+ and HL−, respectively) and fully-H_2O-liganded met-hemoglobin crystal with phosphate (referred to as FL+) [Fig. 2(a)]. Using X-ray crystallography, we found that each crystal contains three tetramers (A, B, and C) with different quaternary structures [Fig. 2(a)]. We also found that the conformational set of this crystal form varies with the samples, and thus we could identify nine distinct conformations in a single crystal form. Since the structure of the $\alpha1\beta1$ (or $\alpha2\beta2$) dimer remains nearly the same in all the tetramer conformations, each quaternary structure was characterized by a movement of its $\alpha2\beta2$ dimer as a whole (an RMSD in the Cα atoms in the $\alpha2\beta2$ dimer) with respect to the $\alpha2\beta2$ dimer of R-state hemoglobin after superposing the $\alpha1\beta1$ dimers of both structures [Fig. 2(b)], and also by a difference distance matrix of the $\alpha1\beta2$ subunits using R as a reference [Fig. 2(c)]. Significantly, the nine snapshot structures cover the entire conformational space of hemoglobin, ranging from T to R2 (the second relaxed quaternary structure) through R [Fig. 1(b) and Fig. 2(b), (c)].

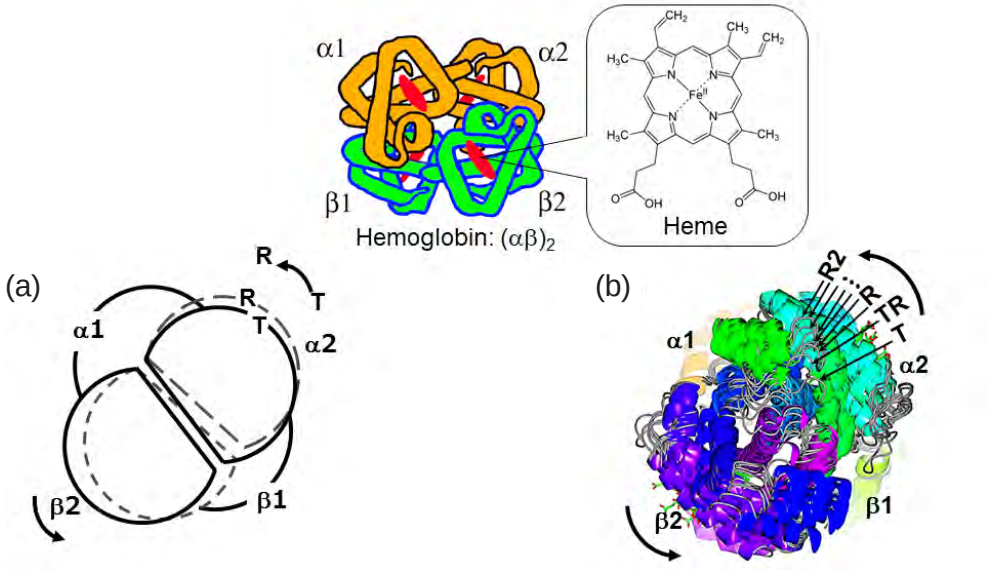

Figure 1: Hemoglobin allosteric transition. (a) Textbook description. (b) Our new view.

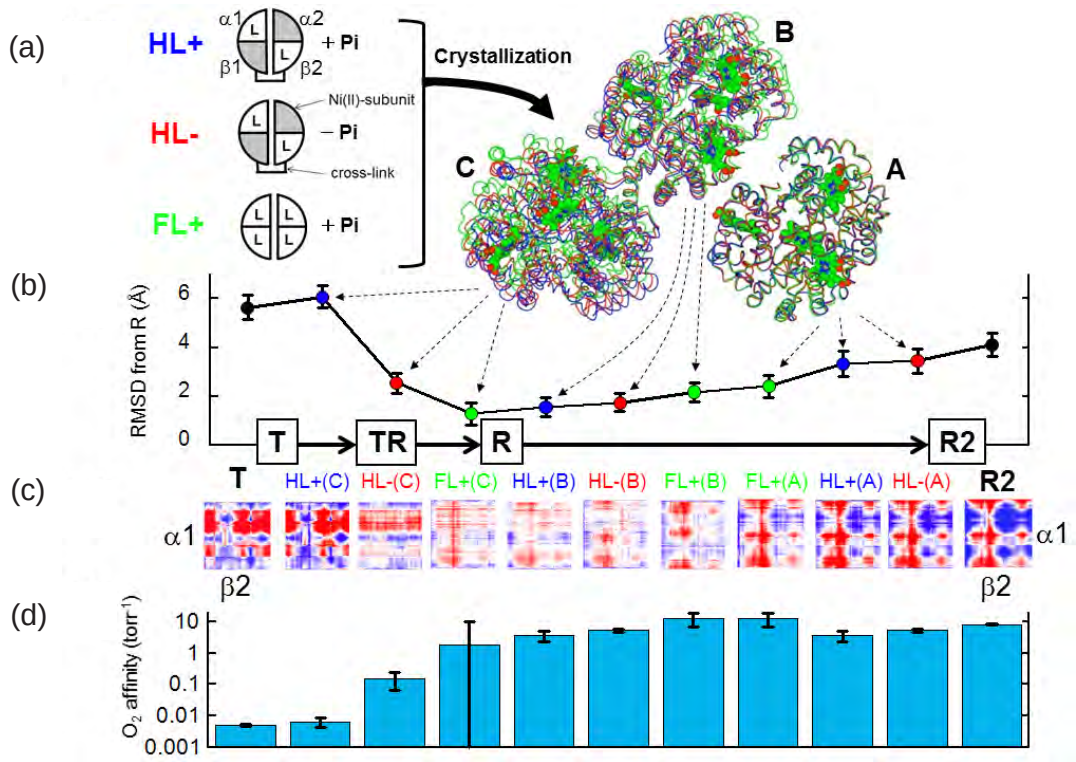

Figure 2: Nine hemoglobin structures in a single crystal form. (a) Three samples (HL+, HL−, and FL+) that crystallize in the same crystal form, each capturing three tetramers (A, B, and C) with different structures. (b) RMSD of the $\alpha 2\beta 2$ dimers after superposing the $\alpha 1\beta 1$ dimers of each structure and R. (c) Difference distance matrices of the $\alpha 1\beta 2$ subunits using R as a reference (red indicates closer than R and blue indicates the opposite). (d) O_2 affinity in the crystals.

Using microspectrophotometry, we next measured the O_2 equilibrium curves in the crystals to assess the O_2 affinity of each of the nine quaternary structures [Fig. 2(d)] [7]. As shown in Fig. 2, hemoglobin can assume various relaxed states from classical R to R2, all of which have a loosely packed dimer-dimer interface and bind O_2 with a similar high affinity to the isolated $\alpha\beta$ dimer, confirming the central role of quaternary (inter-dimer) constraints in the cooperativity of tetrameric hemoglobin. More importantly, we discovered a previously unidentified intermediate between T and R (called TR) with a truly intermediate O_2 affinity (Fig. 2), which has been sought by many research groups for a couple of decades [4-6]. While the O_2 affinity of deoxyhemoglobin is known to vary widely with solution conditions [1], so far all known deoxy T crystals contain essentially the same T quaternary structure [10] with a very low affinity for O_2 [11], suggesting that there is an as yet unidentified allosteric state with intermediate O_2 affinity. We now identify TR as a candidate for this new allosteric state, which may represent the missing link between hemoglobin structure and function that has remained elusive for several decades.

Our results illustrate the hemoglobin allosteric transition with a stepwise pattern in moving from the more tense-like state (classical T state) to the new intermediate TR to the relaxed-like states [Fig. 1(b) and see details in Fig. 2]. The results strongly suggest that hemoglobin exists in pre-existing equilibrium between multiple, not only two, conformations, providing an important reminder that allosteric proteins may have multiple quaternary structures that are structurally and functionally different.

REFERENCES

[1] K. Imai, *J. Mol. Biol*. **133**, 233 (1979).
[2] J. Monod, J. Wyman, and J. P. Changeux, *J. Mol. Biol.* **12**, 88 (1965).
[3] J. Baldwin and C. Chothia, *J. Mol. Biol*. **129**, 175 (1979).
[4] A. P. Minton and K. Imai, *Proc. Natl. Acad. Sci. USA* **71**, 1418 (1974).
[5] M. F. Colombo and F. A. V. Seixas, *Biochemistry* **38**, 11741 (1999).
[6] N. Shibayama and S. Saigo, *FEBS Lett*. **492**, 50 (2001).
[7] N. Shibayama, K. Sugiyama, J. R. H. Tame, and S. -Y. Park, *J. Am. Chem. Soc*. **136**, 5097 (2014).
[8] N. Shibayama, K. Imai, H. Morimoto, and S. Saigo, *Biochemistry* **34**, 4773 (1995).
[9] N. Shibayama, K. Imai, H. Hirata, H. Hiraiwa, H. Morimoto, and S. Saigo, *Biochemistry* **30**, 8158 (1991).
[10] Z. Ren, *PLoS One* **8**, e77141 (2013).
[11] A. Mozzarelli, C. Rivetti, G. L. Rossi, E. R Henry, and W. A. Eaton, *Nature* **351**, 416 (1991).

BEAMLINE

BL-17A

N. Shibayama[1] and S. -Y. Park[2] ([1]Jichi Medical Univ., [2]Yokohama City Univ.)

Pore Formation Mechanism of Staphylococcal Pore-forming Toxin

Pathogenic bacteria express pore-forming toxins (PFTs) to attack host cells. PFTs are expressed as soluble monomeric proteins, which assemble to prepore oligomer on the target cells. After forming prepore, conformational change occurs, and then the pore is formed. Although the crystal structures of monomer and pore have been determined, the detailed mechanism was unclear because the high-resolution structure of prepore was unknown. In this study, we determined the crystal structure of the prepore of staphylococcal PFTs, which showed an invisible transmembrane region with rigid other parts. Based on the structural information and biochemical data, we propose a two-step transmembrane pore formation mechanism.

PFTs are important proteins universally used in a wide range of organisms to attack target cells. Eukaryotes use PFTs as immune proteins [1], whereas pathogenic bacteria secrete them to kill blood cells [2]. PFTs are expressed as water-soluble monomeric proteins, which assemble on the target cell membranes to form a ring-shaped nonlytic oligomeric intermediate, called prepore [3]. At the prepore stage, the transmembrane pore is not yet formed. After forming the prepore, a marked structural change occurs to form membrane-inserted pores.

PFTs secreted by *Staphylococcus aureus*, a major cause of hospital- and community-acquired infections, are the best studied PFTs. Most of the staphylococcal PFTs consist of two different polypeptides, in which four molecules of each component alternately assemble in a circular pattern. The crystal structures of the monomer and the pore have been determined, and a structural model of the prepore was constructed by superposing the structure of the monomer onto that of the pore [4-6]. Based on these structures, a feasible pore formation mechanism was proposed. However, the mechanism had a serious drawback, i.e., protomers of the prepore model show steric hindrance. Therefore, the actual prepore structure should differ from the model, and it was necessary to determine the practical structure of prepore to elucidate the mechanism of β-barrel pore formation. However, since prepore is unstable and it proceeds immediately to form the pore, crystallization of prepore was considered to be impossible.

In the present study, we successfully determined the crystal structure of the prepore-state oligomer of staphylococcal PFT using a mutant which forms stable prepore [7]. The revealed structure was octamer as observed for the previous pore structure, in which two components alternately and circularly assemble. However, the β-barrel region showed a striking difference, i.e., the bottom half of the β-barrel corresponding to the transmembrane region was completely invisible, whereas the upper half showed clear electron density (Fig. 1). No significant structural differences were observed in other regions. These observations indicate that, in prepore, only the transmembrane region is disordered, whereas an octameric assembly similar to the pore is formed. The stem region, which crashed into the adjacent protomer in the previous prepore structure model, extruded to form the upper half of the β-barrel. Consequently, the revealed prepore neatly avoided the steric hindrance.

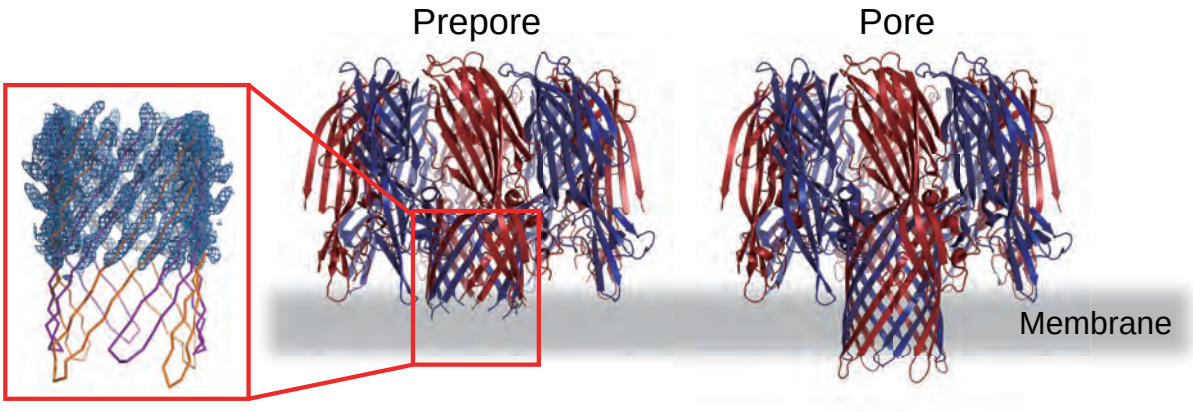

Figure 1: Structure of prepore and pore. The electron density of the β-barrel region of prepore is also shown.

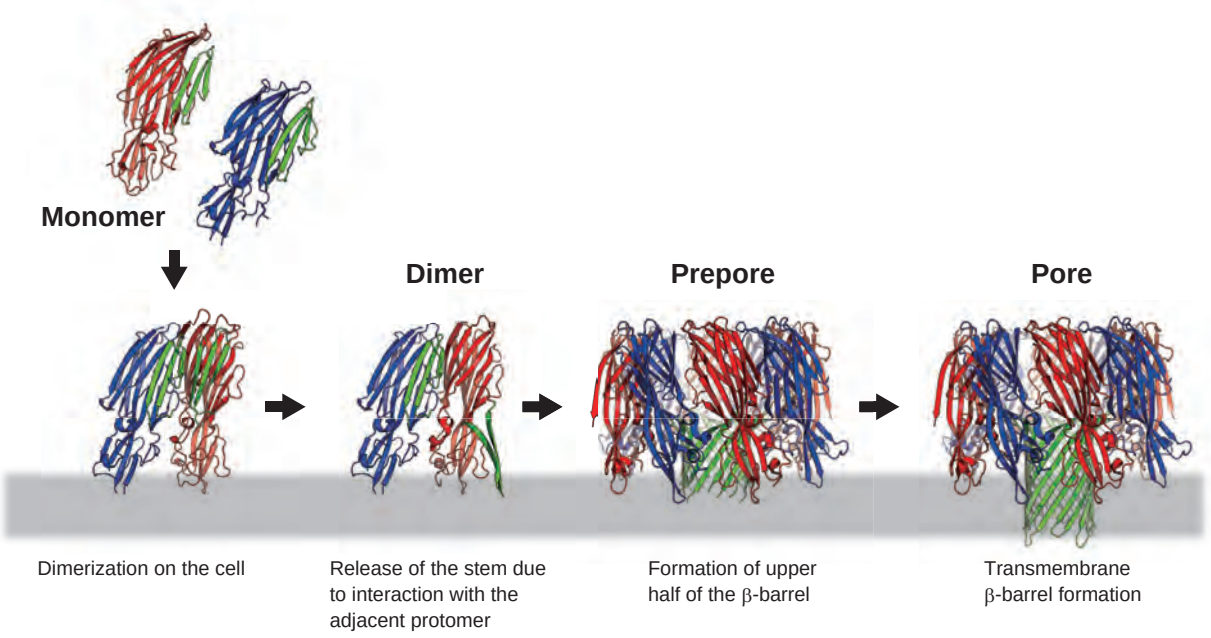

Figure 2: Pore formation mechanism revealed by this study.

To confirm that the observed structural change occurs on erythrocytes, we constructed six cysteine mutants of the β-barrel region, and fluorescence emission spectra of the fluorescent dye conjugated on the introduced cysteine were measured. The results showed that the difference between prepore and pore is the environment around the bottom half of the β-barrel, which is highly consistent with the results of crystal structure analysis.

The flexible transmembrane region had a glycine-rich sequence. To evaluate the role of these glycine residues on the flexibility of this region, several mutants with substitution of Pro for Gly were constructed and their hemolytic activities were compared. The results showed that flexibility at the junction between the trans- and extramembrane regions plays a pivotal role for a marked conformation change between monomer to pore.

From all these observations, we propose the following two-step β-barrel pore formation mechanism (Fig. 2). First, soluble monomers assemble to dimer on the cell membrane. Then, the stem region of one protomer is extruded due to the approach of the adjacent protomer. Next, four dimers assemble to octameric prepore, in which the upper extramembrane half of the β-barrel is formed. In this state, the bottom transmembrane half is not yet formed. Finally, the flexible transmembrane half folds into a rigid membrane-spanning pore. The β-barrel of staphylococcal PFTs is commonly quite stable, and was considered as a rigid structure unit. Therefore, it is surprising that extra- and transmembrane halves of the β-barrel are formed independently. Owing to the structure analysis of the prepore in this study, the atomic structures of monomer, prepore and pore of staphylococcal PFTs were revealed. The two-step β-barrel pore formation mechanism based on these actual structures reasonably explains the pore formation process with no stereochemical discrepancies.

REFERENCES

[1] M. C. Peitsch and J Tschopp, *Curr Opin Cell Biol* **3**, 710 (1991).
[2] I. Iacovache, F. G van der Goot, and L Pernot, *Biochim Biophys Acta* **1778**, 1611 (2008).
[3] V. T. Nguyen, H. Higuchi, and Y. Kamio, *Mol Microbiol* **45**, 1485 (2002).
[4] R. Olson, H. Nariya, K. Yokota, Y. Kamio, and E. Gouaux, *Nat Struct Biol* **6**, 134 (1999).
[5] K. Yamashita, Y. Kawai, Y. Tanaka, N. Hirano, J. Kaneko, N. Tomita, M. Ohta, Y. Kamio, M. Yao, and I. Tanaka, *Proceedings of the National Academy of Sciences of the United States of America* **108**, 17314 (2011).
[6] L. Song, M. R. Hobaugh, C. Shustak, S. Cheley, H. Bayley, and J. E. Gouaux, *Science* **274**, 1859 (1996).
[7] D. Yamashita, T. Sugawara, M. Takeshita, J. Kaneko, Y. Kamio, I. Tanaka, Y. Tanaka, and M. Yao, *Nat Commun* **5**, 4897 (2014).

BEAMLINE

BL-1A

Y. Tanaka and M. Yao (Hokkaido Univ.)

Crystal Structure of PILRα bound with *O*-Glycan and its Attached Peptide

Herpes simplex virus-1 (HSV-1) is the prototype of the Herpesviridae family and causes mucocutaneous lesions as well as lethal encephalitis. Recently, an entry receptor for one of the essential HSV-1 surface proteins, glycoprotein B, has been identified to be human paired immunoglobulin(Ig)-like type 2 receptor a (PILRα). We have revealed that a sialylated *O*-linked sugar attached peptide of HSV-gB (SnT-T(GPA)PAP) is an essential unit for PILRα-HSV-gB recognition and determined the free and the ligand bound structures, showing that PILRα recognizes both a sialic acid of the *O*-glycan and HSV-gB peptide sequence, and notably, exhibited large conformational rearrangements.

HSV-1 is well known for its extreme difficulty of complete elimination, because it can be latent in ganglia after infection and the reduction of immune responses can potentially induce the recurrence of herpes. To date, some reports showed that several viral envelope proteins are prerequisite for entry and infection. Among them, glycoprotein D (gD) is known to recognize herpes virus entry mediator (HVEM) and nectin-1. On the other hand, recently it was shown that human paired immunoglobulin-like type 2 receptor α (PILRα) associates with gB of HSV-1 and mediates membrane fusion during HSV-1 infection [1] (Fig. 1).

To gain structural insights for HSV-gB-PILRα recognition relevant to HSV-1 infection, we prepared the recombinant human PILRα protein comprising the critical V-set Ig-like domain (residues 13-131, hereafter designated as PILRα) and successfully crystallized the protein [2]. We determined the crystal structure of free PILRα at 1.4-Å resolution [3]. To calculate the experimental phases, iodide-anion derivative crystals were made by soaking in cryoprotectant solution including 1 M KI for 30 seconds and 1.8-Å SAD data were collected at beamline BL-17A. The PILRα ectodomain harbors a V-set Ig-like β-sandwich fold [Fig. 2(a)]. A DALI search identified sialoadhesin/Siglec(sialic-acid-binding-immunoglobulin-like-lectin)-1 [4] as the closest structure of PILRα (r.m.s.d. = 1.6 Å for 97 Cα atoms (PDB ID: 1URL)). The PILRα structure exhibits a similar structure and topology to the reported structures of members (Siglec-1, -5 and -7) of the Siglec family [5, 6], which consists of 14 Siglecs in humans. Furthermore, we successfully crystallized and determined the structure of the complex of PILRα with a sialylated *O*-linked sugar (sialyl T antigen, sTn) attached to a peptide of HSV-gB protein (residues 50-56), NH_2-GPAT(sTn)PAP-CO_2H, as described above [7]. The overall structure of the complex state was similar to the free form and the omit map of electron densities for the HSV-gB peptide was clearly identified [Fig. 2(b)]. However, PILRα unexpectedly induced large structural rearrangements to confer the simultaneous binding sites for both sugar and peptide regions of this *O*-glycosylated HSV-gB peptide [Fig. 2(b)].

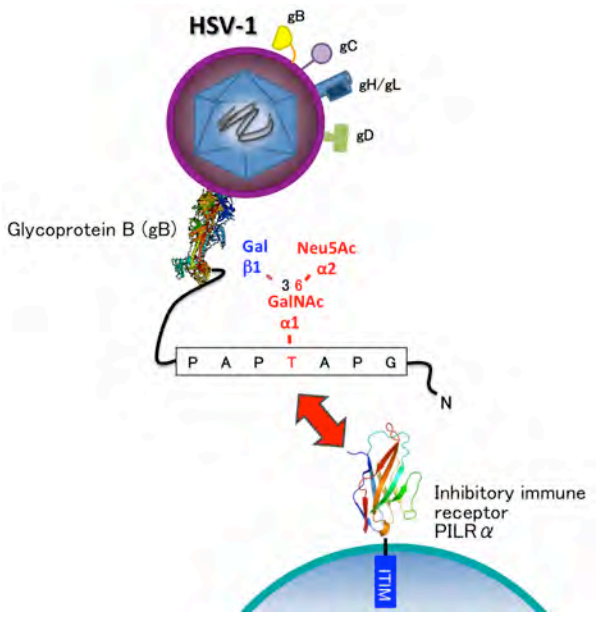

Figure 1: Schematic depiction of the interaction between gB from HSV-1 and PILRα. The *O*-linked GalNAc-(Gal)-Neu5Ac and attached N-terminal loop region of gB used in this study are highlighted.

Our structural analysis revealed the molecular details of protein-*O*-glycosylated peptide recognition, which is not well understood, with another example of the complex structure of P-selection (the polypeptide alpha-*N*-acetylgalactosaminyltransferase (pp-GalNAc-T10) complexed with GalNAc-*O*-Ser was crystallized but its structure unfortunately demonstrated no electron density for the serine residue) [8]. The PILRα residues that are contacting with the sialylated *O*-linked sugar as well as the Pro-rich peptide are essential in forming the unique compact conformation of the HSV-1 gB sTn peptide. They are highly conserved in human and

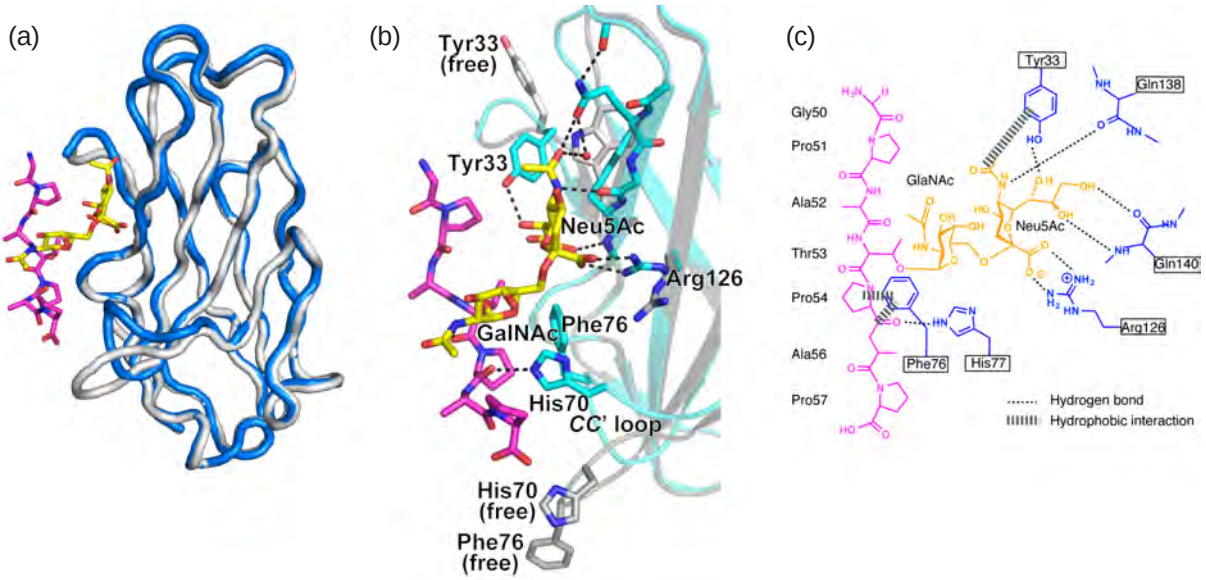

Figure 2: Interaction between SnT-T(GPA)PAP from HSV-1 and PILRα. (a) Superposition of the PILRα–sTn peptide complex (dark blue) with the free form of PILRα (gray) is shown in the tube model. The sTn-T(GPA)PAP peptide is shown as a stick model. The glycopeptides are colored yellow (sugar) and magenta (peptide), respectively. (b) Detailed view of the interaction between PILRα (cyan, stick and cartoon). The free form of PILRα (gray) is also presented. The glycopeptides are colored as (a). (c) Schematic representation of the simultaneous recognition by PILRα of the *O*-glycan and the attached peptide of the sTn peptide. Sialic acid (yellow), GalNAc (yellow), the peptide region (magenta), and PILRα residues (blue) are shown.

mouse PILRs, suggesting that this mode of sialylated O-glycosylated peptide recognition is maintained in species even though some distinct specificities exist. The way the PILRα contacts the sugar peptide is radically different from the previous descriptions of Siglecs in complex with sialylated sugar molecules. Tyr33 and Trp139 recognizing the glycerol group of a sialic acid are not well structurally conserved in the Siglec family members, possibly ensuring the adaptability of the recognition toward distinct sugar structures. Furthermore, the *CC*' loop of PILRα was significantly changed to fit both sugar-peptide connection and peptide regions, but those of other Siglec family members were basically not affected by the sugar binding. PILRα thus has a wider range of binding interface to simultaneously recognize both the *O*-linked sugar and its peptide [Fig. 2(c)].

The complex formation accompanied a wide range of conformational changes, which are possibly one of the largest ones among Ig-like domains, emphasizing that the ligand bound structure is essential for designing anti-HSV-1 entry inhibitor drugs. Importantly, the ligand specificity of PILRα seemed to be determined by the Thr53-Pro54-Ala55-Pro56, because the N-terminal GPA peptide region was not largely involved in the PILRα complex formation.

HSV-1 is difficult to eliminate completely, and dampened immune responses induce herpes recurrence [9]. HSV-1 seems to have evolved to utilize PILRα as an entry receptor for gB, as well as to suppress broad immune responses. The gB-PILRα interaction is crucial for HSV-1 to infect PILR-expressing cells, such as monocytes. Importantly, the sTn peptide definitely inhibited the entry of HSV-1 and thus can serve an initial frame for a potential therapeutic compound which may contribute to the rational design of antiviral drugs.

REFERENCES

[1] T. Satoh, J. Arii, T. Suenaga, J. Wang, A. Kogure, J. Uehori, N. Arase, I. Shiratori, S. Tanaka, Y. Kawaguchi, P. G. Spear, L. L. Lanier, and H. Arase. *Cell* **132**, 935 (2008).
[2] S. Tabata, K. Kuroki, N. Maita, J. Wang, I. Shiratori, H. Arase, D. Kohda, and K. Maenaka, *Acta crystallographica. Section F, Structural biology and crystallization communications* **64**, 44 (2008).
[3] K. Kuroki, J. Wang, T. Ose, M. Yamaguchi, S. Tabata, N. Maita, S. Nakamura, M. Kajikawa, A. Kogure, T. Satoh, H. Arase, and K. Maenaka, *Proc Natl Acad Sci USA* **111**, 8877-8882.
[4] A. P. May, R. C. Robinson, M. Vinson, P. R. Crocker, and E. Y. Jones, *Molecular cell* **1**, 719 (1998).
[5] A. Varki, *Nature* **446**, 1023 (2007).
[6] P. R. Crocker, J. C. Paulson, and A. Varki, *Nature reviews. Immunology* **7**, 255 (2007).
[7] J. Wang, Q. Fan, T. Satoh, J. Arii, L. L. Lanier, P. G. Spear, Y. Kawaguchi, and H. Arase, *J. of virology* **83**, 13042 (2009).
[8] T. Kubota, T. Shiba, S. Sugioka, S. Furukawa, H. Sawaki, R. Kato, S. Wakatsuki, and H. Narimatsu, *J Mol Biol* **359**, 708 (2006).
[9] R. J. Whitley and B. Roizman, *Lancet* **357**, 1513 (2001).

BEAMLINE

BL-17A

T. Ose, K. Kuroki, and K. Maenaka (Hokkaido Univ.)

Structural Basis for the Coevolution of Tomato Mosaic Virus and the Resistance Protein Tm-1

The tomato mosaic virus (ToMV) resistance protein Tm-1 binds the helicase domain of ToMV replication proteins (ToMV-Hel) and thereby inhibits RNA replication. Herein, we report crystal structures for the complex between the N-terminal inhibitory domains of Tm-1 and ToMV-Hel. The complex contains a Tm-1 dimer and two ToMV-Hel monomers, with the interfaces between them bridged by an ATP. Residues in ToMV-Hel and Tm-1 involved in antagonistic coevolution are also found at the interface. The crystal structures gave us an atomic view of the step-by-step coevolutionary arms race between a plant resistance protein and a viral protein.

Viruses evolve so rapidly that they can escape host defense systems. To counter rapidly evolving viruses, the sequences of many host restriction factor genes are subject to positive selection and, consequently, rapidly mutate [1, 2]. Molecular evolutionary approaches have revealed residues important for resistance in host defense protein sequences. The use of such information in conjunction with the tertiary structures of related proteins greatly facilitates our understanding of virus–host evolutionary arms races [3].

We previously found that tomato mosaic virus (ToMV) and the resistance gene *Tm-1* have coevolved [4]. Here, we report atomic details of the coevolutionary arms race between them as deduced from several crystal structures and molecular dynamics simulations [5]. The ToMV resistance protein Tm-1 is a 754-amino acid protein that binds ToMV replication protein and inhibits ToMV RNA replication [6]. Tm-1 protein contains at least two domains: an uncharacterized N-terminal region (M1-K431) and a TIM barrel-like C-terminal domain. An *Escherichia coli*-expressed N-terminal fragment of Tm-1 (residues 1–431; Tm-1(431)) inhibits ToMV RNA replication *in vitro* [7]. We first determined the crystal structure of Tm-1(431) [Fig. 1(a)]. Tm-1(431) is a dimer and the residues T79–D112, which were under positive selection meaning that the sequences have rapidly changed [4], are exposed to the surface of the molecule and form a flexible loop and an α-helix [5]. A *Tm-1*-resistance-breaking ToMV mutant LT1 harbors mutations that cause Q979 to E and H984 to Y substitutions in the helicase domain of replication proteins (ToMV-Hel) [4]. We also determined the crystal structure of ToMV-Hel [Fig. 1(b)]. Q979 and E984 of ToMV-Hel are also exposed to the surface [8], where Tm-1 presumably targets.

We then crystallized a complex of Tm-1(431) and ToMV-Hel [Fig. 1(c)]. Since ATP is required for the ToMV-Hel–Tm-1(431) complex formation [5] but is also hydrolyzed by ToMV-Hel [9], ATPγS was supplied for crystallization. The asymmetric unit of the crystal contains a tetrameric complex with a 2:2 stoichiometry consisting of a Tm-1(431) homodimer and two monomeric ToMV-Hel molecules [5]. Each interface of ToMV-Hel and Tm-1(431) consists of the N-terminal region of the Tm-1 NN domain and two regions of ToMV-Hel, i.e., I1094–Y1109 in the C-terminal region and H975–M986, which forms a loop and an α-helix connecting the 1A and 2A domains. At least 21 residues in Tm-1(431) and 23 residues in ToMV-Hel directly contact each other. Residues involved in the antagonistic coevolution such as E979 and H984 of ToMV-Hel and T79–D112 of Tm-1(431) are found in the interface. Notably, an ATPγS molecule is found in each ToMV-Hel–Tm-1(431) interface, in addition to those found in the two ToMV-Hel NTPase active sites. Additional biochemical experiments suggested that the ATP molecule in the interface is necessary for the interaction between ToMV-Hel and Tm-1(431).

A naturally occurring amino acid change (I91 to T) in Tm-1 makes it a stronger inhibitor of ToMV RNA replication, which enables it to inhibit the replication of LT1 [4]. We also solved the structure of the ToMV-Hel–Tm-1(431/I91T) complex crystallized in the presence of ATPγS [5]. The overall structure of this complex is very similar to that of the ToMV-Hel–Tm-1(431) complex. In the ToMV-Hel–Tm-1(431/I91T) structure, T91 is positioned at the center of the interface with ToMV-Hel and is involved in a hydrogen bond network containing water molecules. The structural information reasonably explains how the I91 to T substitution strengthens the inhibitory activity of Tm-1.

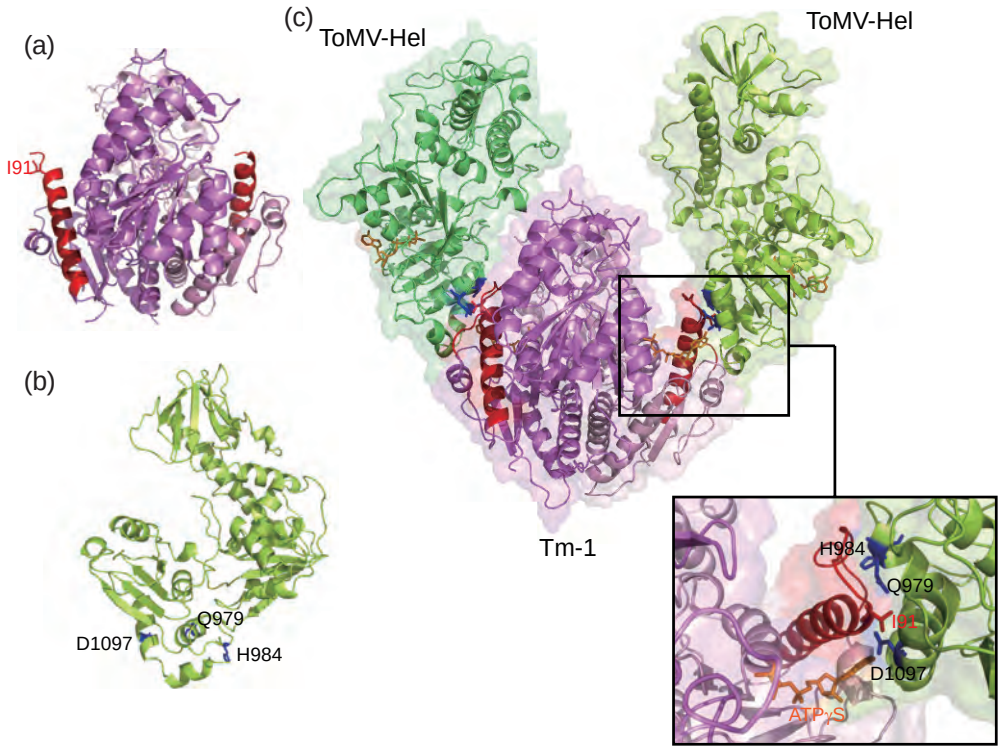

Figure 1: Crystal structures of ToMV-Hel and Tm-1(431). (a) Crystal structure of Tm-1(431). Residues T79-D112, which are under positive selection, are colored red. (b) Crystal structure of ToMV-Hel. The residues that are mutated in resistance-breaking mutants are shown as blue sticks. (c) Crystal structure of ToMV-Hel and Tm-1(431) complex. A close-up view of the interaction interface between ToMV-Hel and Tm-1 is shown on the lower right.

ToMV-LT1-derived mutants which additionally have E979 to K (LT1(E979K)) or D1097 to Y (LT1(D1097Y)) substitution in the replication proteins escape from the inhibition by Tm-1(I91T) [4]. Together with molecular dynamics simulations, we showed how viral mutations in LT1 (Q979 to E and H984 to Y) affect the interaction with Tm-1, and those in LT1(E979K) and LT1(D1097Y) affect the interaction with Tm-1(I91T). All of these substitutions compromised the interaction with Tm-1 or Tm-1(I91T). Taken together, we could visualize the molecular arms race between ToMV and Tm-1, comprising (i) inhibition by host, (ii) viral escape from the inhibition, (iii) acquisition of stronger inhibitory ability to inhibit the escaped virus mutants, and (iv) further viral escape from the inhibition.

REFERENCES

[1] N. K. Duggal and M. Emerman, *Nat. Rev. Immunol.* **12**, 687 (2012).
[2] W. Johnson, *Intrinsic Immunity, Current Topics in Microbiology and Immunology*, ed Cullen B. R. (Springer Berlin Heidelberg), **371**, 123 (2013).
[3] M. D. Daugherty and H. S. Malik Annu. *Rev. Genet*. **46**, 677 (2012).
[4] K. Ishibashi, N. Mawatari, S. Miyashita, H. Kishino, T. Meshi, and M. Ishikawa, *PLoS Pathog*. **8**, e1002975 (2012).
[5] K. Ishibashi, Y. Kezuka, C. Kobayashi, M. Kato, T. Inoue, T. Nonaka, M. Ishikawa, H. Matsumura, and E. Katoh, *Proc. Natl. Acad. Sci. USA* **111**, e3486 (2014).
[6] K. Ishibashi, K. Masuda, S. Naito, T. Meshi, and M. Ishikawa, *Proc. Natl. Acad. Sci. USA* **104**, 13833 (2007).
[7] M. Kato, K. Ishibashi, C. Kobayashi, M. Ishikawa, and E. Katoh, *Protein Expr. Purif*. **89**, 1 (2013).
[8] M. Nishikiori, S. Sugiyama, H. Xiang, M. Niiyama, K. Ishibashi, T. Inoue, M. Ishikawa, H. Matsumura, and E. Katoh, *J. Virol*. **86**, 7565 (2012).
[9] H. Xiang, K. Ishibashi, M. Nishikiori, M. C. Jaudal, M. Ishikawa, and E. Katoh, *Protein Expr. Purif*. **81**, 89 (2012).

BEAMLINES

BL-5A, BL-17A, and AR-NW12A

E. Katoh and K. Ishibashi (NIAS)

Novel Mechanism for DNA Duplex Unwinding by a Single Protein

Duplex DNA is generally unwound by protein oligomers prior to replication. The Rep protein of plasmid ColE2-P9 is an essential initiator for plasmid DNA replication. This protein binds the replication origin (Ori) in a sequence-specific manner as a monomer and unwinds DNA. The crystal structure of the DNA-binding domain of ColE2-P9 Rep in complex with Ori DNA unveiled the basis for Ori-specific recognition by the protein and also revealed that it unwinds DNA by the concerted actions of its three contiguous structural modules. A novel mechanism for DNA unwinding by a single protein has been proposed here.

Since a DNA molecule in cells usually forms a stable double-helix structure, the protein machineries acting on single-stranded DNA must separate the paired DNA strands before their actions take an effect. Many DNA-binding proteins enlarge the contact areas, contributing to the interaction with DNA, by increasing their molecular size, including multimer formation and/or complex formation with other cooperative proteins, so that binding specificity and affinity are strong enough to disrupt the stable double-helix structure of DNA. One of those machineries, which initiate double-stranded DNA replication, is protein-based.

DNA replication is the universal process for transmitting genetic information. The process is initiated from a specific region called replication origin. To initiate DNA replication, initiator proteins specifically bind to the origins in the chromosomal DNA. A number of eukaryotic and prokaryotic initiator proteins bind to the origins and form higher order structures consisting of multiple proteins to unwind locally the double-helix structure of DNA. Subsequently, the replication proteins, such as helicase, primase, and DNA polymerase, are loaded onto the unwound region.

The replication initiation of most plasmids, a small DNA molecule in a cell that is physically separated from the host chromosomal DNA and can replicate independently, requires a specific initiator protein, Rep, encoded by each plasmid. Multiple Rep molecules specifically bind to the cognate replication origin (Ori) and recruit host replication proteins. DNA unwinding often relies on the host initiation protein, and DNA replication initiates more or less similarly to the host chromosomal DNA replication.

The Rep of the *Escherichia coli* plasmid ColE2-P9 is unique, because this initiator binds to Ori of the plasmid in a sequence-specific manner as a monomer and unwinds locally its double-helix structure. Furthermore, the Rep exhibits Ori-specific primase activity; synthesizes the primer RNA necessary for the DNA chain synthesis by DNA polymerase. Thus, the replication of the plasmid ColE2-P9 initiates without host replication proteins, except for DNA polymerase I. Although the Rep of ColE2-P9 exhibits multiple functions necessary to initiate DNA replication, this protein is relatively small (34 kDa), and its C-terminal DNA-binding domain (E2Rep-DBD, 14 kDa) is sufficient only for specific binding to Ori of ColE2-P9 and its unwinding. How does this small molecule ensure binding specificity and affinity to DNA and how does it disrupt its double-helix structure?

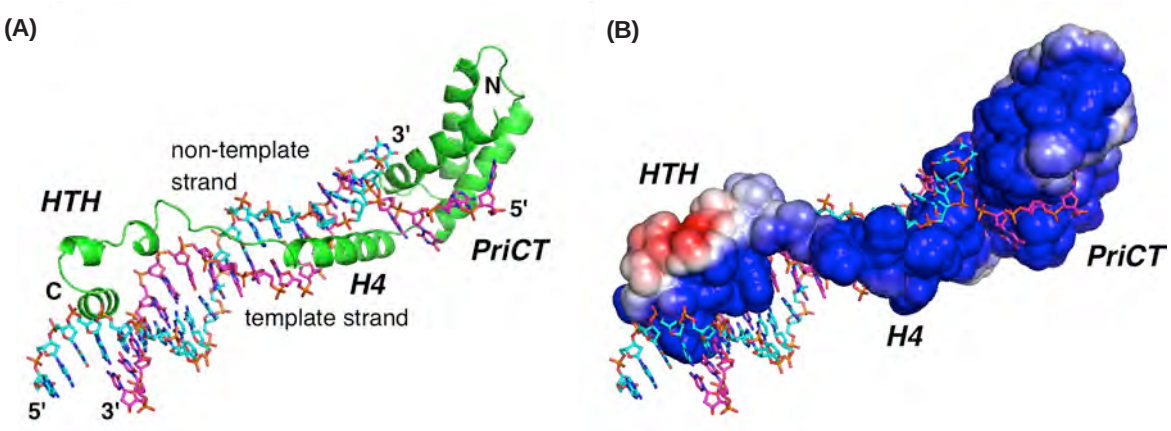

Figure 1: The representation of the crystal structure of the E2Rep-DBD in complex with Ori DNA. Combined with the results of the biochemical and genetic analyses, the structure is shown to represent the snapshot during the DNA unwinding process uniquely facilitated by a single protein molecule.(A) Overall view of the complex. The green ribbon shows E2Rep-DBD, and the magenta and cyan stick models show the template strand for the primer RNA synthesis and the non-template strand of DNA, respectively. (B) Surface charge representation of E2Rep-DBD. The viewpoint is the same as that of panel A. The blue and red colors on the molecular surface show the positively and negatively charged regions, respectively.

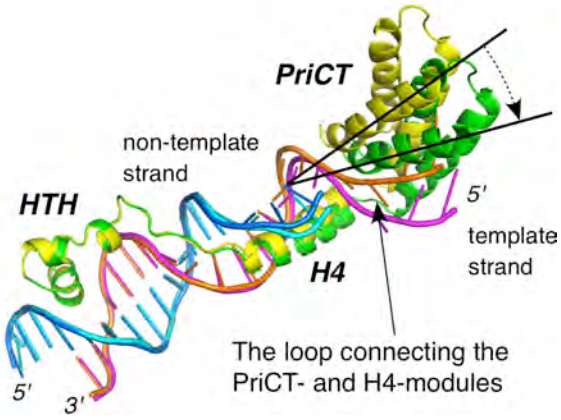

Figure 2: Comparison of the two complex molecules (the proteins are drawn in green and yellow) in the crystallographic asymmetric unit and the result of mutational analysis suggested that the structural flexibility between the H4 and PriCT-modules and the shift in position of the PriCT-module relative to the other modules is important for the unwinding of DNA.

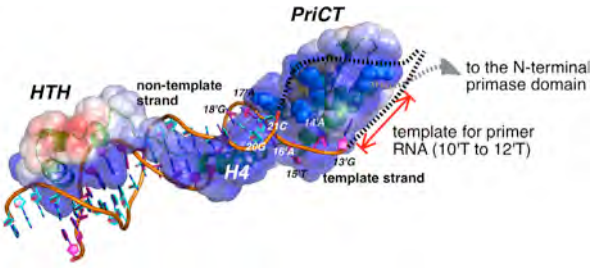

Figure 3: Model for unwinding of the complete Ori by Rep. Black dashed lines indicate the supposed trajectory of each of the DNA strands. The PriCT-module works as a wedge separating the DNA strands, and presumably also as a platform during the RNA primer synthesis by the primase domain. The N-terminal domain of Rep has been supposed to be the primase domain, and the trajectory of the linker connecting the primase domain to E2Rep-DBD is indicated with gray dashed lines.

A research group at the National Institute of Genetics determined the crystal structure of E2Rep-DBD in complex with Ori DNA of ColE2-P9 and revealed the molecular mechanism, using the data collected at the structural biology beam lines in the Photon Factory, KEK [1]. The crystal structure showed that E2Rep-DBD comprises three structural modules (PriCT, H4, and HTH), connected with flexible linker regions, and forms an elongated fold (Fig. 1). As E2Rep-DBD binds to DNA along with the molecule, this protein is capable of interacting with a long region of DNA. One third of the surface area of the molecule is used for interaction with DNA, and the area is comparable with that of the DNA-binding protein complex that is more than twice larger than the E2Rep-DBD molecule. The tight binding of the C-terminal HTH-module and the H4-module of E2Rep-DBD induces distortion of the double-helix structure of Ori DNA. The N-terminal PriCT-module separates the DNA strands, and the module holds the single-stranded DNA to stabilize the unwounded conformation (Fig. 2). The structural study showed that the E2Rep-DBD binds specifically to Ori and unwinds its double-helix structure by the concerted actions of its three contiguous structural modules. The study also suggested that the PriCT-module works as a platform to hold the template strand during the subsequent RNA primer synthesis by the primase domain, because the template region for the RNA primer locates immediate downstream of the bases specifically bound by the PriCT-module (Fig. 3). Although the PriCT domain is conserved in the C-termini of some archaeo-eukaryotic primases, its function has been unknown. The structural study showed that the PriCT domain of the ColE2-P9 Rep plays a central role in DNA unwinding and the stabilization of the unwound structure. The conservation of the domain indicates that it likely plays a similar role in the other proteins. The study is the first report providing the structural basis for the functional importance of the conserved PriCT domain and also reveals a novel mechanism for DNA unwinding by a single protein.

REFERENCE

[1] H. Itou, M. Yagura, Y. Shirakihara, and T. Itoh, *J. Biol. Chem.* **290**, 3601 (2015).

BEAMLINE

BL-17A and AR-NE3A

H. Itou (National Inst. of Genetics)

Genomic Instability to Risk of Cancer in Normal Human Cells Induced by Low-Dose X-Rays

Non-targeted radiobiological effects, such as genomic instability and the bystander effect, have important implications for estimating the risk of cancer induced by low-dose/low-dose-rate irradiation, especially chronic low-dose electromagnetic radiation from cesium 137 such as caused by the accident at the Fukushima Daiichi Nuclear Power Plants. However, there have been more studies, both quantitative and qualitative, on radiation-induced non-targeted effects using high-LET(linear energy transfer) radiation than those using low-LET electromagnetic radiation. Using highly precise controlled X-ray microbeams produced by synchrotron radiation, we have been examining how genomic instability leads to biological late effects in order to identify the risk of cancer.

A central paradigm in radiobiology, which is the study of the action of ionizing radiation on living things, has been that energy deposition from radiation tracks into a cell and/or water molecules causes either direct ionization or indirect ionization by hydroxyl radicals, eliciting radiobiological effects. This implies that the radiobiological consequences only affect the cells irradiated directly by the radiation and/or water radicals such as H radical, OH radical and e^-_{aq}, and that non-irradiated cells do not contribute to radiobiological effects. This paradigm is one basis for the current system of risk estimation from radiation, and the risk of radiation-induced cancer after high and moderate doses is relatively well known, based on data from detailed epidemiological studies of Japanese atomic bomb survivors in Hiroshima and Nagasaki [1]. However, the current system of risk estimation has recently been challenged by so-called non-targeted effects, such as the bystander effect (Fig. 1). The radiation-induced bystander effect can be explained as the ability of cells affected by some factors to convey manifestations of cellular damage to neighboring cells not directly hit by radiation. There are many reports regarding the bystander effect after exposure to low-fluence a particles from a plutonium-238 source or helium-ion microbeams. However, few studies have examined the gap-junction mediated bystander effect after exposure to comparatively low-LET electromagnetic radiation such as X- or γ-rays.

Radiation-induced genomic instability can be observed in cells in later generations after irradiation (Fig. 2). Compared with the direct effects of radiation, in which the effects are directly induced as a consequence of direct energy deposition in cells, radiation-induced genomic instability may include non-targeted effects, in which radiobiological effects are seen in cells that are not subject to a direct hit by radiation. In such instances, radiation may have hit cells and a response is communicated from direct-hit cells to non-hit cells, eliciting radiobiological effects (“bystander effect”). Such radiation-induced genomic instability may have important implications for risk evaluation of cancer by low-dose/low-dose-rate irradiation from terrestrial radiation, especially chronic low-dose electromagnetic radiation from cesium 137 such as caused by the accident at the Fukushima Daiichi Nuclear Power Plants, to identify the bystander effect induced by comparatively low-LET electromagnetic radiation.

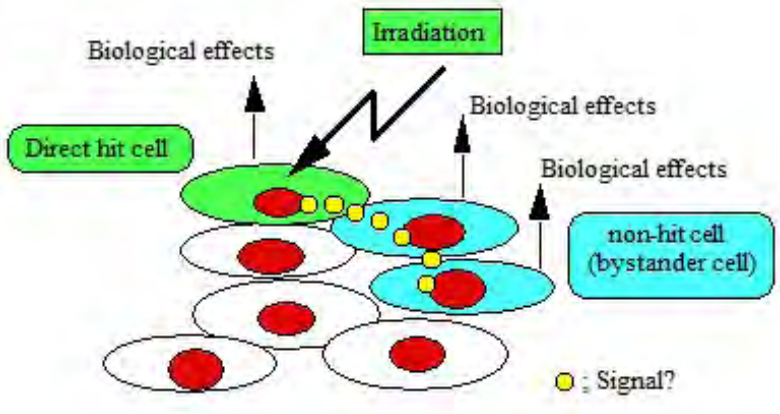

Figure 1: The concept of the radiation-induced bystander effect mediated by cell-cell communication.

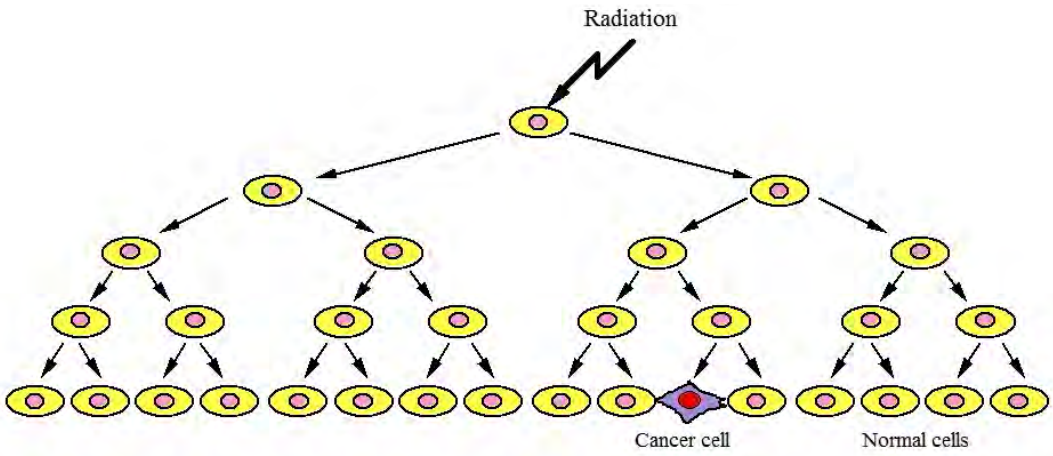

Figure 2: A hypothetical schematic of radiation-induced genomic instability.
A single cell survives after irradiation and is clonally expanded cell generations. During clonal expansion, instability events can occur in the progeny of the irradiated cell.

To identify genomic instability and the bystander effect induced by electromagnetic radiation for estimating risk of cancer, we have been examining gene mutation, as one of the indicators of biological late effects, in normal human cells. A very low number of cells of around 0.04% of the total cell population were irradiated with monochromatic (5.35 keV) X-ray microbeams and the subsequent 20-cell generations were assayed for gene mutation at the hypoxanthine-guanine phosphoribosyl transferase (*HPRT*) locus, which is mapped on the human chromosome X. The mutation frequency of the population was around 50 times higher than that of the non-irradiated control population. When we conducted the same experiment using high-LET carbon-ion microbeams, the mutation frequency was almost the same level as that of the control population. Although acute biological effects caused by comparatively low-LET electromagnetic radiation are less effective than those by high-LET radiation, there is clear evidence that low-LET X-rays can induce late biological effects, such as gene mutation, more frequently than high-LET heavy ions.

To examine the relationship between genomic instability and bystander effect via gap-junction mediated cell-cell communication, we added a specific inhibitor of gap-junction communication (18-α-glycyrrhetinic acid) to the cell population during X-ray-microbeam irradiation. The result showed that the mutation frequency at 20-cell generations after irradiation in the inhibitor-treated cell population was reduced compared to that in the non-treated cell population. The data provides evidence that gap-junction mediated cell-cell communication plays an important role in inducing genomic instability by X-rays. Although no gap-junction mediated bystander effects were observed in acute cellular effects by X-rays using our experimental cell system [2], we conjecture that genomic instability detected with gene mutation occurs in future generations by the bystander effect via gap-junction mediated cell-cell communication as one of the early events immediately after irradiation.

Our study suggests that we must carefully investigate biological late effects and evaluate radiation risks, such as risk of cancer, induced by low-LET electromagnetic radiation such as caused by the accident at the Fukushima Daiichi Nuclear Power Plants.

REFERENCES

[1] D. A. Pierce and D. L. Preston, *Radiat. Res.* **154**, 178 (2000).
[2] N. Autsavapromporn, M. Suzuki, T. Funayama, N. Usami, I. Plante, Y. Yokota, Y. Mutou, H. Ikeda, K. Kobayashi, Y. Kobayashi, Y. Uchihori, T. K. Hei, E. I. Azzam, and T. Murakami, *Radiat. Res.* **180**, 367 (2013).

BEAMLINE

BL-27B

M. Suzuki[1], N. Autsavapromporn[1], and N. Usami[2] ([1]NIRS, [2]KEK-IMSS-PF)

Storage Performance and Structural Characteristics of Natural Gas Hydrate

Natural gas hydrate (NGH) pellets are one candidate for a natural gas storage and transportation medium due to their high gas density and much easier storage method compared to liquefied natural gas (LNG) and compressed natural gas (CNG). More than 80% of natural gas stored within NGH pellets with different particle sizes from 0.50 mm to 30 mm was maintained for two weeks at 253 K under ambient pressure. The internal texture of the NGH pellets was investigated using phase contrast X-ray CT by diffraction enhanced imaging (DEI), revealing that the outer surface of the pellet was covered with an ice film and NGH was well preserved inside.

The production of natural gas from both conventional and unconventional fields is increasing because of the expanding worldwide demand for natural gas. Therefore, energy transportation systems have diversified not only to pipelines and LNG, but also new means such as gas to liquids (GTL), natural gas liquids (NGL), natural gas hydrate (NGH) [1-6]. NGH is a clathrate crystal that consists of water and natural gases such as CH_4, C_2H_6, and C_3H_8, with natural compositions. NGHs are usually stable at high pressure and low temperature, and can contain natural gas of approximately 170 times their own volume. It is known that CH_4 and CO_2 hydrates are preserved just below the freezing point of water under atmospheric pressure, though the conditions are outside the thermodynamically stable zone of CH_4 and CO_2 hydrates [7-11]; this is called the self-preservation phenomenon [7]. The surfaces of self-preserved CH_4 and CO_2 hydrates are covered with ice [9-12], so the distribution of ice film is thought to be important for the preservation of gas hydrate. NGH also shows the self-preservation phenomenon below the ice point. Especially, NGH in the form of pellets is well preserved under the conditions of 253 K and atmospheric pressure while powdered NGH does not show the preservation phenomenon [13]. In this study, we focused on how the small size of NGH pellets showed the self-preservation phenomenon, and then phase contrast X-ray computed tomography by diffraction enhanced imaging (DEI) measurements were carried out to prove that the original surface of the NGH pellet was covered with ice [14].

NGH pellets containing simulated natural gas (89.8% CH_4, 5.6% C_2H_6, 3.1% C_3H_8, 0.6% iso-C_4H_{10}, 0.8% n-C_4H_{10}, and under 0.1% iso-C_5H_{12}) were formed using a semi-batch system [13], and then they were divided into φ33 × 30, 10–20, 4.0–6.7, 1.0–4.0, and 0.50–1.0 mm. The mass fraction of NGH was 75 wt%, and that of ice was 25 wt% for the sample of φ33 × 30 mm. The others were 72 wt% for 10–20 mm, 59 wt% for 4.0–6.7 mm, 34 wt% for 1.0–4.0 mm, and 19 wt% for 0.50–1.0 mm (Fig. 1). The pellets were stored for two weeks at 253 K under ambient pressure to investigate their storage performance. After two weeks, the mass fraction of each NGH was 74 wt%, 67 wt%, 57 wt%, 32 wt%, and 16 wt% in descending order. In other words, the ratios of weight loss between the initial and final mass fraction of NGH in the storage test were 0.76 wt%, 6.9 wt%, 3.3 wt%, 6.7 wt%, and 17 wt% from largest to smallest. This result showed that smaller NGH samples had lower NGH fractions at the start of the storage test and were likely to dissociate during the storage period. This is because the smaller NGH particles have larger specific surface areas. Thus, larger particles of over approximately 10 mm in diameter of NGH pellets are more favorable than smaller ones from the viewpoint of gas storage.

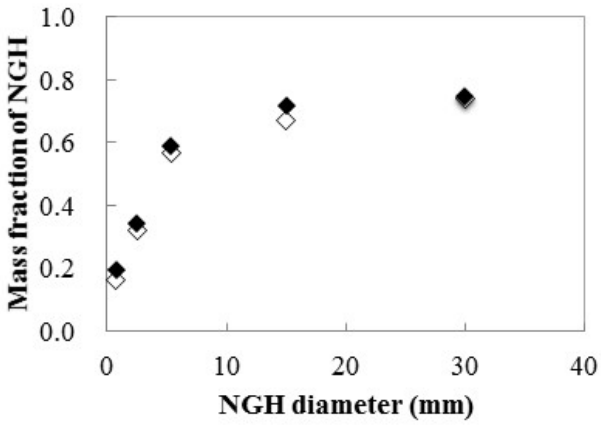

Figure 1: Change of mass fraction of NGH for each diameter. Solid diamonds represent starting mass fraction of NGH and open diamonds represent that of NGH after two weeks' storage.

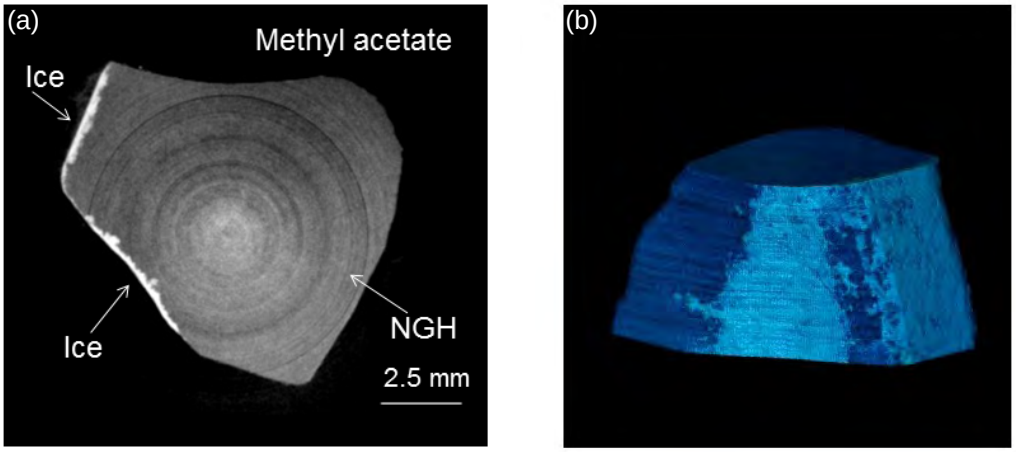

Figure 2: Cross-section image (a) and 3D image (b) of NGH particle with ice film obtained from DEI. Ring patterns in the cross-section image are artifact of X-ray CT imaging.

Non-destructive measurement by DEI was performed on the NGH pellets to visualize the internal distribution of NGH and ice with a spatial resolution of 0.040 mm. A 35-keV monochromatic synchrotron X-ray at a vertical wiggler beam was irradiated to an NGH pellet that was immersed in methyl acetate at 193 K ± 1 K to eliminate artifacts caused by the outer surface of the pellet [12, 13]. Phase map images were obtained by detecting the X-ray beam that diffracted after passing through the sample using the analyzer crystal. The sample was scanned at 11 positions with the scanning time of one second for each position, and the number of projections was 500. An internal image of the NGH pellet is shown in Fig. 2. The difference in density of the NGH pellet is reflected in the gray scale [Fig. 2(a)]. The white region shows ice whose density was lower than that of the surroundings, and the gray and black areas were NGH and methyl acetate, respectively. The observed result showed that only some part of the surface was covered with ice film [Fig. 2(b)]. But this is due to that the sample was shaved at a temperature below 150 K, a condition which suppressed NGH dissociation, to suitable size for the DEI measurement. Considering the good storage performance as shown in Fig.1 and its similarity with CH_4 hydrates, the NGH pellet in common state was undoubtedly thought to be fully covered with ice film. An ice film with a thickness of approximately 0.30 mm was observed on the pellet, and the inside of the pellet was dense with NGH without ice grains or pore spaces. Consequently, the formed NGH pellet that maintained natural gases under mild storage conditions was proved to be stabilized by the surface thin ice film.

REFERENCES

[1] Exxon Mobil Corporation, *The Outlook for Energy: A View to 2040* (2015).
[2] D. A. Wooda, C. Nwaohab, and B. F. Towlerc, *J. Natural Gas Sci. and Engineer*. **9**, 196 (2012).
[3] S. Thomas and R. A. Dawe, *Energy* **28**, 1461 (2003).
[4] H. Najibi, R. Rezaei, J. Javanmardi, K. Nasrifar, and M. Moshfeghian, *Appl. Therm. Eng*. **29**, 2009 (2009).
[5] S. P. Santos, J. E. Leal, and F. Oliveira, *Energy Policy* **39**, 4774 (2011).
[6] Y. Tamsilian, A. N. Ebrahimi, and A. Ramazani, *J. Dispr. Sci. Technol*. **34**, 259 (2013).
[7] V. S. Yakushev and V. A. Istomin, *Physics and Chemistry of Ice*, Hokkaido University Press, **136** (1992).
[8] L. A. Stern, S. Circone, S. H. Kirby, and W. B. Durham, *J. Phys. Chem. B* **105**, 1756 (2001).
[9] W. F. Kuhs, G. Genov, D. K. Satykova, and T. Hansen, *Phys. Chem. Chem. Phys*. **6**, 4917 (2004).
[10] W. Shimada, S. Takeya, Y. Kamata, T. Uchida, J. Nagao, T. Ebinuma, and H. Narita, *J. Phys. Chem. B* **109**, 5802 (2005).
[11] A. Falenty and W. F. Kuhs, *J. Phys. Chem. B* **113**, 15975 (2009).
[12] S. Takeya, A. Yoneyama, K. Ueda, K. Hyodo, T. Takeda, H. Mimachi, M. Takahashi, T. Iwasaki, K. Sano, H. Yamawaki, and Y. Gotoh, *J. Phys. Chem. C* **115**, 16193 (2011).
[13] S. Takeya, A. Yoneyama, K. Ueda, H. Mimachi, M. Takahashi, K. Sano, K. Hyodo, T. Takeda, and Y. Gotoh, *J. Phys. Chem. C* **116**, 13842 (2012).
[14] H. Mimachi, S. Takeya, A. Yoneyama, K. Hyodo, T. Takeda, Y. Gotoh, and T. Murayama, *Chem. Eng. Sci*. **118**, 208 (2014).

BEAMLINE

BL-14C

H. Mimachi[1], S. Takeya[2], A. Yoneyama[3], K. Hyodo[4], T. Takeda[5], Y. Gotoh[2], and T. Murayama[1] ([1]Mitsui Engineering and Shipbuilding Co. Ltd., [2]AIST, [3]Hitachi Ltd., [4]KEK-IMSS-PF, [5]Kitasato Univ.)

Development and Application of Variable-Magnification X-Ray Bragg Optics

A novel X-ray Bragg optics has been developed for variable-magnification of an X-ray beam at the vertical-wiggler beamline BL-14B. Our X-ray Bragg optics is composed of two magnifiers in a crossed arrangement, and the magnification factor, *M*, is controlled through the azimuth angle of each magnifier. We could successfully control the magnification factor between 0.1 and 10 at the wavelength of 0.112 nm. At various magnification factors, X-ray images of a nylon mesh were observed with an air-cooled X-ray CCD camera. Not only absorption-contrast but also edge-contrast due to Fresnel diffraction was observed in the magnified images.

The X-ray Bragg magnifier based on asymmetric diffraction at a nearly-perfect crystal [1] is a useful optical element for X-ray radiology and microscopy, and has been used at synchrotron facilities, for example, for X-ray microtomography (μ-CT), analyzer-based phase-contrast imaging [2] and inline holography. One of the most striking features of the X-ray Bragg magnifier is that it can cover a wide range of resolution from submicrometer up to submillimeter, thus filling the gap between X-ray microscopy and radiology. Another attractive feature is that it can be combined with X-ray single-photon-counting detectors such as PILATUS and Medipix, opening up a new possibility for high-resolution, wide-dynamic-range, high-sensitivity and fast X-ray imaging.

In the conventional X-ray Bragg magnifiers, however, it was difficult to change the magnification factor. In order to solve this problem, we developed a variable-magnification X-ray Bragg optics [3, 4]. Thanks to the tunability of the magnification factor, we can locate a region-of-interest (ROI) in a sample under low magnification, and then observe the details of the ROI under an optimized magnification. Our X-ray Bragg optics consists of two magnifier crystals in a crossed arrangement as schematically shown in Fig. 1. The first crystal magnifies the incident beam in the horizontal direction while the second crystal does so in the vertical direction. The glancing angle of each crystal, θ_j, is set at the Bragg condition. Here, the subscript *j* is 1 for the first magnifier and 2 for the second magnifier. The $\hat{\phi}_j$ -axis is perpendicular to the diffracting lattice planes of the *j*-th crystal, and we can scan the azimuth angle, ϕ_j, while keeping the Bragg condition. The magnification factor of each magnifier is given by

$$M_j(\phi_j) = \frac{\cos\alpha_j \sin\theta_{Bj} + \sin\alpha_j \cos\theta_{Bj} \sin\phi_j}{\cos\alpha_j \sin\theta_{Bj} - \sin\alpha_j \cos\theta_{Bj} \sin\phi_j} ,$$

where α_j is the asymmetric angle and θ_{Bj} is the Bragg angle. For example, calculations show that the magnification factor is tunable between 0.01 and 100 through the azimuth angle, ϕ_j, under the conditions of $\theta_{B1} = \theta_{B2} = 16.96^o$ and $\alpha_1 = \alpha_2 = 16.7^o$. Although the magnified image is usually deformed as shown in the inset of Fig. 1, this image deformation can be corrected by the 2×2 transformation matrix and bilinear interpolation method.

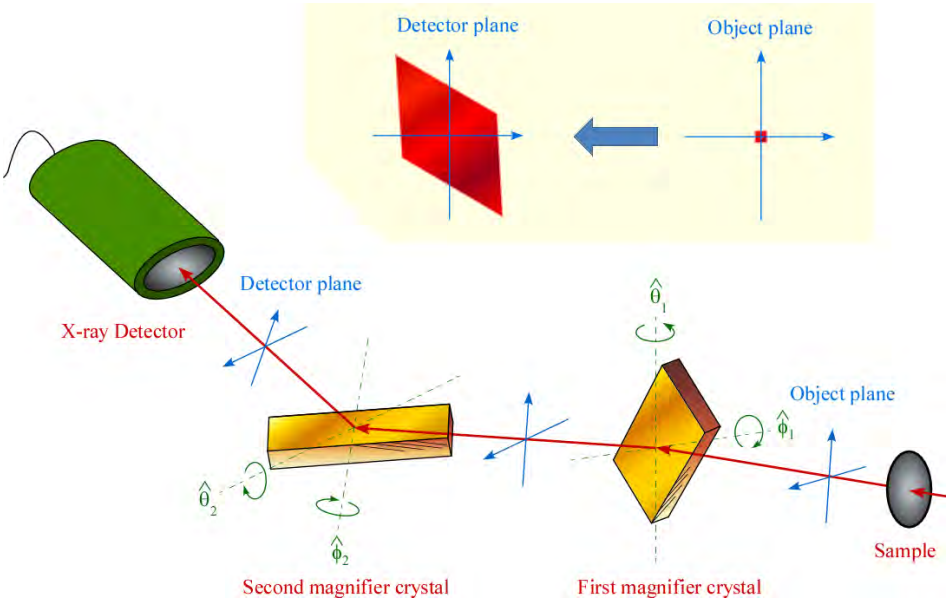

Figure 1: Variable-magnification X-ray Bragg optics.

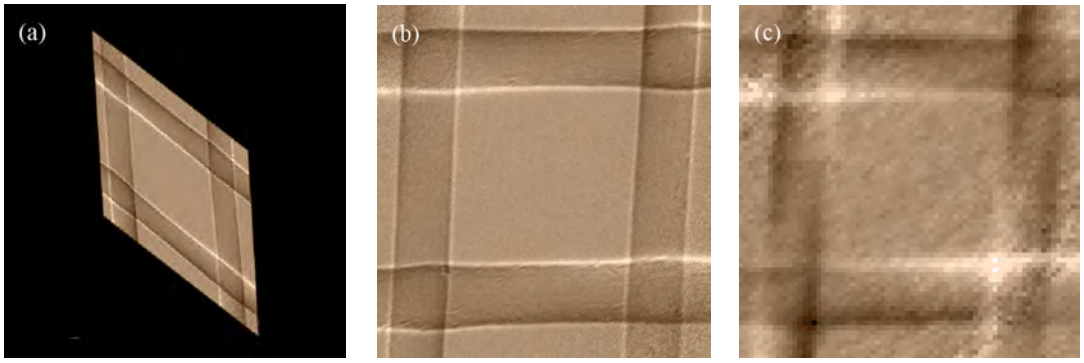

Figure 2: (a) Deformed magnified image and (b) corrected magnified image of the nylon mesh obtained at $\phi_1 = \phi_2 = 60^o$ ($M_1 = M_2 = 5.9$). (c) Corrected image obtained at $\phi_1 = \phi_2 = 0^o$ ($M_1 = M_2 = 1$). The period of the nylon mesh was about 1.1 mm in both the horizontal and vertical directions.

In order to verify the feasibility of our variable-magnification X-ray Bragg optics, we performed experiments at the vertical-wiggler beamline BL-14B. The white beam from the light source was monochromated at 0.112 nm by a Si(111) double-crystal monochromator. For magnifiers, we used asymmetric Si(220) crystals ($\theta_{B1} = \theta_{B2} = 16.96^o$, $\alpha_1 = \alpha_2 = 14°$) made of non-doped float-zone silicon crystal ($\rho \geq 2000\ \Omega{\cdot}cm$). Magnified X-ray images were observed by a fiber-coupled X-ray CCD camera (Photonic Science Ltd., X-ray Coolview FDI 40mm). The pixel size was 23 μm (H) × 23 μm (V) and the number of pixels was 1384 (H) × 1032 (V).

First, we estimated the spatial resolution of the optics at several magnification factors using MTF (Modulation Transfer Function) charts. For example, the spatial resolution was estimated to be about 15 μm in the vertical direction and 20 μm in the horizontal direction at $\phi_1 = \phi_2 = 60^o$ ($M_1 = M_2 = 5.9$). We found that the main determining factors of the spatial resolution were the pixel size of the X-ray CCD camera and the penumbral blurring. Then we observed a nylon mesh as a sample. The period of the mesh was about 1.1 mm in both the horizontal and vertical directions. Figure 2(a) shows a raw image observed at $\phi_1 = \phi_2 = 60^o$ ($M_1 = M_2 = 5.9$) with the exposure time of 4 sec. Figure 2(b) shows a corrected image. For comparison, Fig. 2(c) shows an image obtained at $\phi_1 = \phi_2 = 0^o$ ($M_1 = M_2 = 1$). It is worth noting that not only absorption-contrast but also edge-contrast due to Fresnel diffraction is observed in Figs. 2(b) and (c).

In the experiment we could control the magnification factor from 1.0 up to 10 with reasonable throughput even at a second-generation synchrotron radiation facility such as the Photon Factory. In fact, the exposure time was as short as 10 sec at the maximum magnification factor ($M_1 = M_2 = 10$). A much wider range of magnification factor will be realized at third-generation synchrotron radiation facilities where submicrometer resolutions have already been achieved with the conventional fixed-magnification X-ray Bragg optics. We expect that the performance of our variable-magnification X-ray Bragg optics will be maximized at linac-based X-ray sources such as X-ray free-electron lasers (XFEL) and energy recovery linacs (ERL), which can produce diffraction-limited X-rays in both the horizontal and vertical directions.

REFERENCES

[1] K. Kohra, in *Proceedings of the Sixth International Conference on X-Ray Optics and Microscopy*, edited by G. Shinoda, K. Kohra, and T. Ichinokawa (Univ. of Tokyo Press, Tokyo, 1972), pp. 35-45.
[2] K. Hirano, *Jpn. J. Appl. Phys.* **50**, 026402 (2011).
[3] K. Hirano, Y. Takahashi, and H. Sugiyama, *Nucl. Instrum. Methods Phys. Res. A* **741**, 78 (2014).
[4] K. Hirano, Y. Takahashi, and H. Sugiyama, *Jpn. J. Appl. Phys.* **53**, 040302 (2014).

BEAMLINE

BL-14B

K. Hirano[1], Y. Takahashi[1], H. Sugiyama[1], and Y. Yamashita[2]
([1]KEK-IMSS-PF, [2]RIKEN SPring-8 Center)

Development of Fast Scintillation Materials for High-Energy X-Ray Detection

We successfully developed fast scintillation materials for high-energy X-ray detection using two approaches. One is based on plastic scintillators; the detection efficiency of plastic scintillators for high-energy X-ray photons was significantly enhanced by loading Hf-based oxide nanoparticles. The other is the use of Auger-free luminescence in halide crystals. Among those, we found that Cs_2ZnCl_4 exhibits relatively efficient Auger-free luminescence and a negligible long scintillation component. These materials can be used for high-energy X-ray detection in the case that detection signals having fast decay and no long tail (afterglow) are desired.

There is an increasing demand for fast detectors for high-energy X-ray detection. For X-rays whose energy is on the order of several tens of keV, scintillation detectors equipped with fast scintillators would meet such demand. Among several approaches to develop such fast scintillation materials, we introduce the development of scintillation materials based on two approaches.

One is based on plastic scintillators; plastic scintillators are known to exhibit fast scintillation whose decay time constant is on the order of nanoseconds. However, a disadvantage of plastic scintillators is low atomic numbers of constituent elements, leading to a low interaction probability with X-rays or gamma-rays. The low interaction probabilities result in low detection efficiency. Loading of high atomic number elements is an effective method to enhance the average atomic number and thus the detection efficiency for high-energy photons. The conventional method is to load organometallic molecules containing heavy elements. However, such molecules often act as quenching centers, and loading a small amount of such molecules severely degrades the light yield. We have developed an alternative approach to enhance the average atomic number: loading of metal oxide nanoparticles [1, 2]. Here, we introduce the development of plastic scintillators loaded with Hf-based oxide nanoparticles [2]. Figure 1(a) shows the TEM image of plastic scintillator loaded with Hf-based oxide nanoparticles at 10 wt%. The particle size was less than 300 nm. The size of the nanoparticles was smaller than the wavelength of scintillation photons of ~400 nm. Thus, the scintillator was transparent to the scintillation photons. Figure 2(b) shows the temporal profile of scintillation of the plastic scintillator loaded with Hf-based oxide nanoparticles. The decay time constant of the scintillation was 2.5 ns, which is comparable to that of generic plastic scintillators. In addition, long scintillation components were negligible. The detection efficiency for 67.4 keV X-ray photons was twice that of a commercial plastic scintillator for high-energy photon detection, NE-142 (loaded with Pb at 5 wt%). Furthermore, the light yield was 1.2 times higher than that of NE-142. Based on these results, we successfully enhanced the detection efficiency of Hf-based oxide nanoparticles without degrading the light yield and excellent timing property.

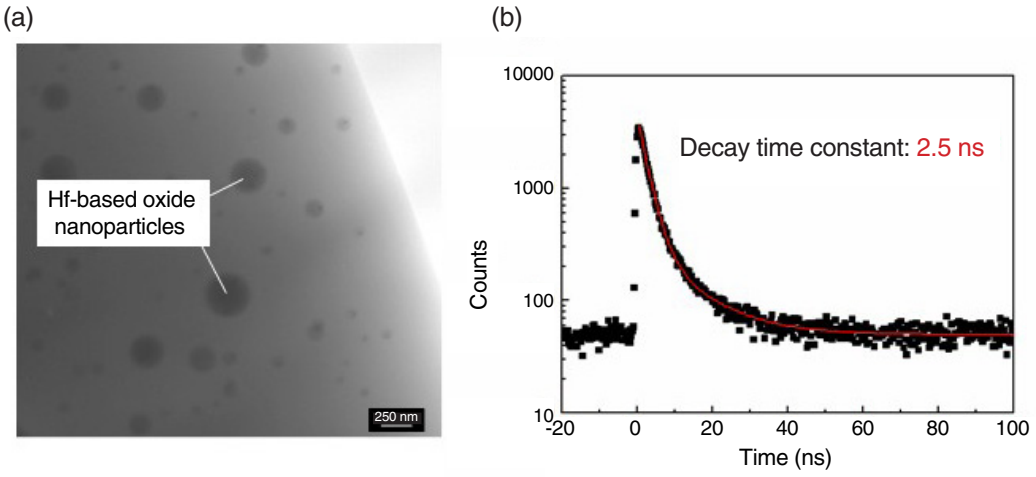

Figure 1: (a) TEM image of plastic scintillator loaded with Hf-based oxide nanoparticles. (b) Temporal profile of scintillation of the plastic scintillator loaded with Hf-based oxide nanoparticles.

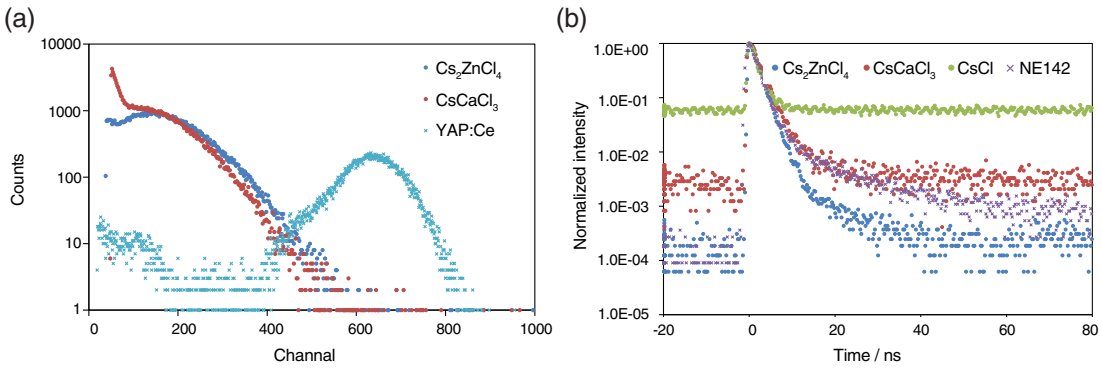

Figure 2: (a) Pulse height spectra of Cs_2ZnCl_4, $CsCaCl_3$, and YAP:Ce. The amplifier gain for Cs_2ZnCl_4 and $CsCaCl_3$ was five times that of YAP:Ce. (b) Temporal profiles of Cs_2ZnCl_4 and other similar compounds. The temporal profile of NE-142 is also shown.

The other approach is based on the Auger-free luminescence, which is a radiative process between the valence band and the outermost core level. In most insulators, holes at the outermost core level decay via the Auger process, in which the recombination energy between the core hole and a valence electron is deposited to another valence electron, i.e., an Auger electron. In contrast, in some insulators, the Auger process is prohibited owing to the band structure, and the recombination energy is released via photon emission, and this photon emission process is the Auger-free luminescence. The decay time constant of the Auger-free luminescence is subnanosecond to nanosecond, making it suitable for fast scintillation. A well-known scintillator exhibiting the Auger-free luminescence is BaF_2. However, BaF_2 has a disadvantage that it also exhibits a slow scintillation component with a decay time constant of 600 ns. We searched for insulators exhibiting the Auger-free luminescence without such long component, and developed several scintillators exhibiting Auger-free luminescence [3, 4]. Among them, we found that Cs_2ZnCl_4 exhibits relatively efficient scintillation due to the Auger-free luminescence and negligible long components [4]. Figure 2(a) shows the pulse height spectra of Cs_2ZnCl_4, $CsCaCl_3$, and YAP:Ce. The amplifier gain for Cs_2ZnCl_4 and $CsCaCl_3$ was five times that of YAP:Ce. Based on the peak positions and the wavelength-dependent sensitivity of the photomultiplier tube, the light yield of Cs_2ZnCl_4 was estimated to be 630 photons/MeV. The light yield of $CsCaCl_3$ is estimated to be quite similar to that of Cs_2ZnCl_4. Figure 2(b) shows the temporal profiles of Cs_2ZnCl_4 and other similar compounds. The temporal profile of NE-142 is also shown. The contribution of components having a decay time constant longer than the period of successive pulses in the single bunch oparation mode of the Photon factory (624 ns) can be seen as the time-independent component. It is clearly seen that Cs_2ZnCl_4 had a much lower contribution of long component than those of other scintillators. The main component of Cs_2ZnCl_4 had a decay time constant of 1.9 ns.

REFERENCES

[1] Y. Araya, M. Koshimizu, R. Haruki, F. Nishikido, S. Kishimoto, and K. Asai, *Sensors and Materials* **27**, 255 (2015).
[2] Y. Sun, M. Koshimizu, N. Yahaba, F. Nishikido, S. Kishimoto, R. Haruki, and K. *Asai, Appl. Phys. Lett.* **104**, 174104 (2014).
[3] M. Koshimizu, N. Yahaba, R. Haruki, F. Nishikido, S. Kishimoto, and K. Asai, *Opt. Mater.* **36**, 1930 (2014).
[4] N. Yahaba, M. Koshimizu, Y. Sun, T. Yanagida, Y. Fujimoto, R. Haruki, F. Nishikido, S. Kishimoto, and K. Asai, *Appl. Phys. Express* **7**, 062602 (2014).

BEAMLINES

BL-14A and AR-NE7A

M. Koshimizu[1], Y. Sun[1], N. Yahaba[1], R. Haruki[2], F. Nishikido[3], S. Kishimoto[2], T. Yanagida[4], Y. Fujimoto[1], and K. Asai[1] ([1]Tohoku Univ., [2]KEK-IMSS-PF, [3]NIRS, [4]NAIST)

Facility Report

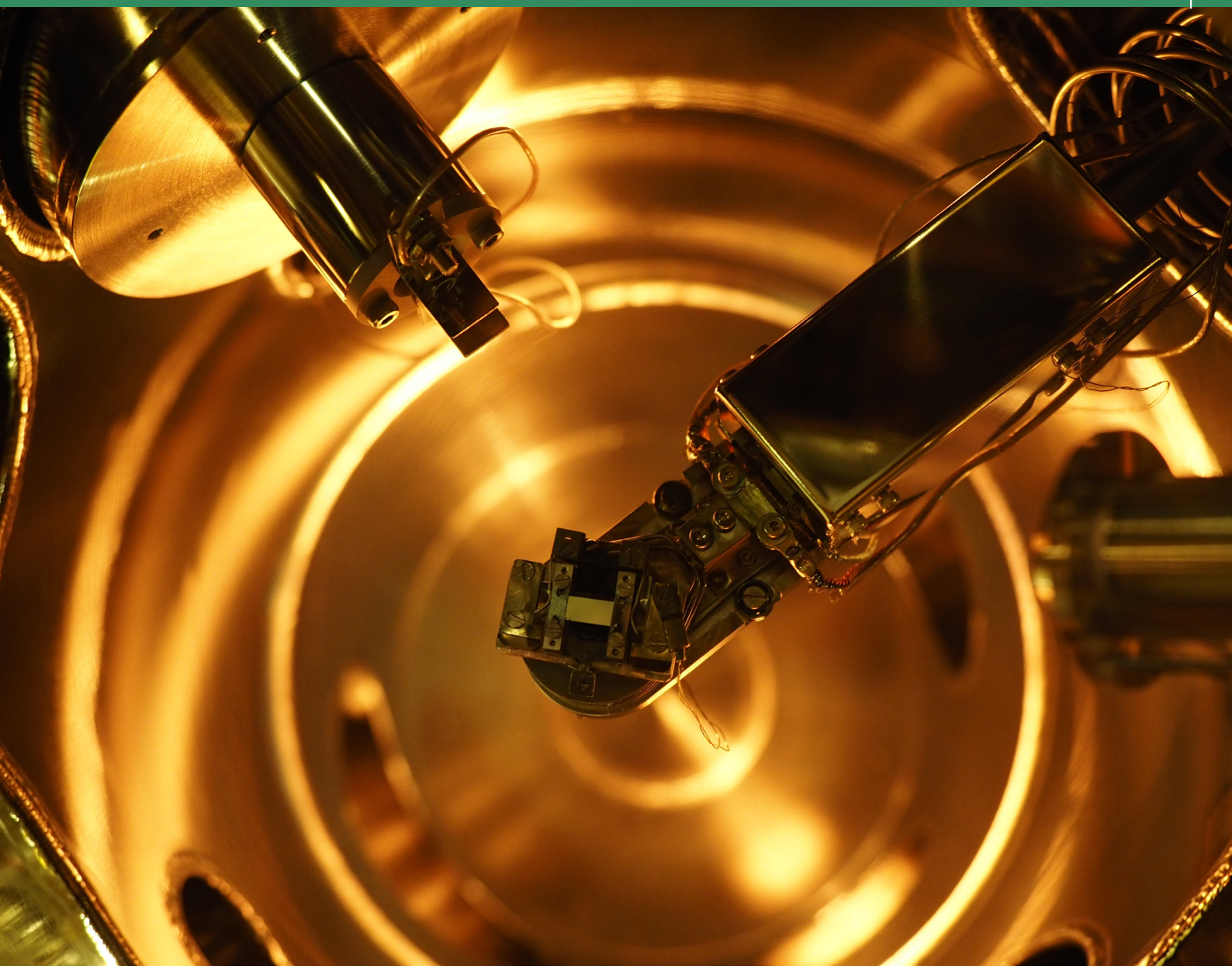

Facility Report

1 Facility Status

1-1 Accelerators

Two electron storage rings, the PF-ring and the PF-AR, as dedicated light sources were stably operated at the Photon Factory. The KEK linear accelerator with maximum electron energy of 8 GeV is employed to inject the electron beam into the rings. The full energy injection of 2.5 GeV is carried out at the PF-ring, while it is required to increase the energy from the injection energy of 3 GeV to the operation energy of 6.5 GeV at the PF-AR.

The machine parameters of the rings and the calculated spectral performances are listed in Table 1 and Table 2, respectively. The spectral distributions of synchrotron radiation (SR) from the bending magnets and the insertion devices are shown in Fig. 1

Table 1: Principal beam parameters of the PF ring and PF-AR.

	PF	PF-AR
Energy	2.5 GeV	6.5 GeV
Natural emittance	34.6 nm rad	293 nm rad
Circumference	187 m	377 m
RF frequency	500.1 MHz	508.6 MHz
Bending radius	8.66 m	23.2 m
Energy loss per turn	0.4 MeV	6.66 MeV
Damping time		
Vertical	7.8 ms	2.5 ms
Longitudinal	3.9 ms	1.2 ms
Natural bunch length	10 mm	18.6 mm
Momentum compaction factor	0.00644	0.0129
Natural chromaticity		
Horizontal	12.9	-14.3
Vertical	-17.3	-13.1
Stored current	450 mA	60 mA
Number of bunches	252	1
Beam lifetime	20-25 h (at 450 mA)	20-25 h (at 60 mA)

Table 2: Calculated spectral performances of the bend source and all the insertion devices at the PF ring (2.5 GeV, 450 mA) and the PF-AR (6.5 GeV, 60 mA). λ_u: period length, *N*: number of the periods, *L*: length of undulator or wiggler, $G_y(G_x)$: minimum vertical (horizontal) gap height, $B_y(B_x)$: maximum vertical (horizontal) magnetic field, Type of magnet, H: hybrid configuration, S.C.: super conducting magnet, σ_x,σ_y: horizontal or vertical beam size, σ_x',σ_y': horizontal or vertical beam divergence, $K_y(K_x)$: vertical (horizontal) deflection parameter, *D*: photon flux density (photons/sec/mrad^2/0.1%b.w.), *B*: brilliance (photons/sec/mm^2/mrad^2/0.1%b.w.), P_T:total radiated power. Different operating modes of undulator and wiggler are denoted by -U and -W, respectively

Name	E/I	λ_u	N	L	$G_y(G_x)$	$B_y(B_x)$	Type of magnet	σ_x	σ_y	$\sigma_{x'}$	$\sigma_{y'}$	$K_y(K_x)$	$\varepsilon_1/\varepsilon_c$	D	B	P_T
	GeV/mA	cm		m	cm	T		mm	mm	mrad	mrad		keV			kW
PF	**2.5/450**															
Bend								0.41	0.059	0.178	0.012		4	5.38E+13	3.48E+14	
SGU#01		1.2	39	0.5	0.4	0.7	P(NdFeB)	0.6	0.012	0.088	0.029	0.78		4.56E+16	9.90E+17	0.4
U#02-1		6	60	3.6	2.8	0.4	H(NdFeB)	0.65	0.042	0.054	0.008	2.3		2.73E+17	1.55E+18	1.07
U#02-2		16	17	2.72	2.6	0.33(0.33)	P(NdFeB)	0.65	0.042	0.054	0.008	4.93(4.93)		9.53E+15	4.58E+16	0.53
SGU#03		1.8	26	0.5	0.4	1	P(NdFeB)	0.6	0.012	0.088	0.029	1.68		2.50E+16	5.44E+17	0.82
MPW#05-W		12	21	2.5	2.64	1.4	H(NdFeB)	0.71	0.045	0.078	0.009	16	5.9	2.22E+15	1.10E+16	8.83
U#13		7.6	47	3.6	2.3	0.74(0.51)	P(NdFeB)	0.74	0.02	0.094	0.019	5.28(3.65)		4.46E+16	3.10E+17	3.53
VW#14					5	5	S.C.	0.53	0.045	0.128	0.008		20.8	5.42E+13	3.59E+14	
SGU#15		1.76	27	0.5	0.4	0.97	P(NdFeB)	0.6	0.012	0.088	0.029	1.37		4.38E+15	9.44E+16	0.75
U#16-1 & 16-2		5.6	44	2.5	2.1	0.6(0.38)	P(NdFeB)	0.654	0.042	0.055	0.008	3(2)		1.03E+18	1.82E+17	0.88
SGU#17		1.6	29	0.5	0.4	0.92	P(NdFeB)	0.6	0.012	0.088	0.029	1.37		7.88E+15	1.71E+17	0.69
Revolver#19-B		7.2	32	3.6	2.8	0.4	H(NdFeB)	0.7	0.045	0.078	0.009	2.7		7.17E+16	3.52E+17	0.63
U#28		16	22	3.52	2.7	0.33(0.33)	P(NdFeB)	0.53	0.045	0.127	0.008	4.93(4.93)		1.39E+16	6.59E+16	1.36
PF-AR	**6.5/60**															
Bend								1	0.2	0.593	0.036		26	3.90E+13	3.11E+13	
EMPW#NE01-W		16	21	3.36	3(11)	1(0.2)	P(NdFeB)	1.07	1.07	0.268	0.032	15(3)	28(90%)	1.84E+15	2.54E+15	5.52
U#NE03		4	90	3.6	1	0.8	P(NdFeB)	1.57	0.17	0.312	0.029	3		1.29E+16	7.66E+15	3.708
U#NW02		4	90	3.6	1	0.8	P(NdFeB)	1.57	0.17	0.312	0.029	3		1.29E+16	7.66E+15	3.708
U#NW12		4	95	3.8	1	0.8	P(NdFeB)	1.57	0.17	0.312	0.029	3		1.29E+16	7.66E+15	3.912
U#NW14-36		3.6	79	2.8	1	0.8	P(NdFeB)	1.35	0.14	0.338	0.036	2.8		7.69E+15	6.49E+15	3.12
U#NW14-20		2	75	1.5	0.8	0.63	P(NdFeB)	0.75	0.07	0.383	0.038	1.17		7.69E+15	6.49E+15	0.936

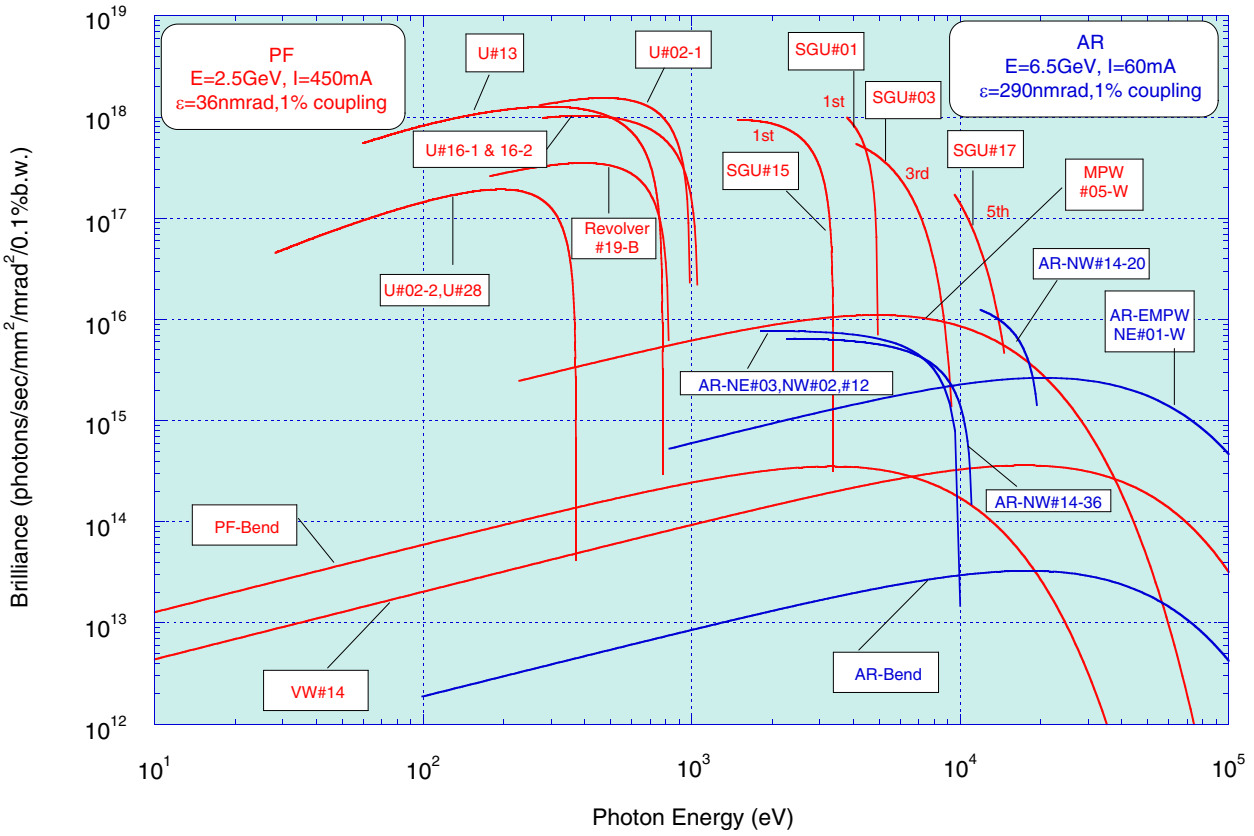

Figure 1: Synchrotron radiation spectra available at the PF Storage Ring (2.5 GeV) and the PF-AR (6.5 GeV). Brilliance of the radiation vs. photon energy are denoted by red curves for the insertion devices, SGU#01, U#02-1 & 02-2, SGU#03, MPW#05, U#13, VW#14, SGU#15, U#16-1 & 16-2, SGU#17, Revolver#19-B and U#28, and bending magnets (PF-Bend) at the PF Storage Ring. Blue curves denote those for the insertion devices, EMPW#NE01, U#NE03, U#NW02, U#NW12, U#NW14-36 and U#NW14-20, and the bending magnets (AR-Bend) at the PF-AR. The name of each source is assigned in Table 2. The spectral curve of each undulator (or undulator mode of multipole wiggler) is a locus of the peak of the first harmonic within the allowance range of K parameter. For SGU#01 and SGU#15, the fi rst harmonic regions are shown. For SGU#03, the third harmonic region is shown. For SGU#17, the fifth harmonic region is shown. Spectra of Revolver#19 for surface B are shown.

1-2 Experimental Stations

Fifty-two experimental stations are operated at the PF storage ring, the PF-AR and the slow positron facility (SPF), as shown in Figs. 2, 3, and 4. Thirty-five stations are dedicated to research using hard X-rays, 14 stations for studies in the VUV and soft X-ray energy regions, and 3 stations for studies using slow positrons. Tables 3, 4, and 5 summarize the areas of research carried out at the experimental stations at the PF storage ring, PF-AR and SPF. The specifications in terms of the optics and performance of each experimental station differ according to experimental requirements and methodology. Tables 6, 7, and 8 list the details of the optics of the hard X-ray stations, the soft X-ray/VUV stations and the slow positron stations. The principal performance parameters, including energy range, energy resolution, beam-spot size, and photon flux at the sample position for the PF and PF-AR, and energy range, pulse width, frequency, and positron flux for the SPF are shown.

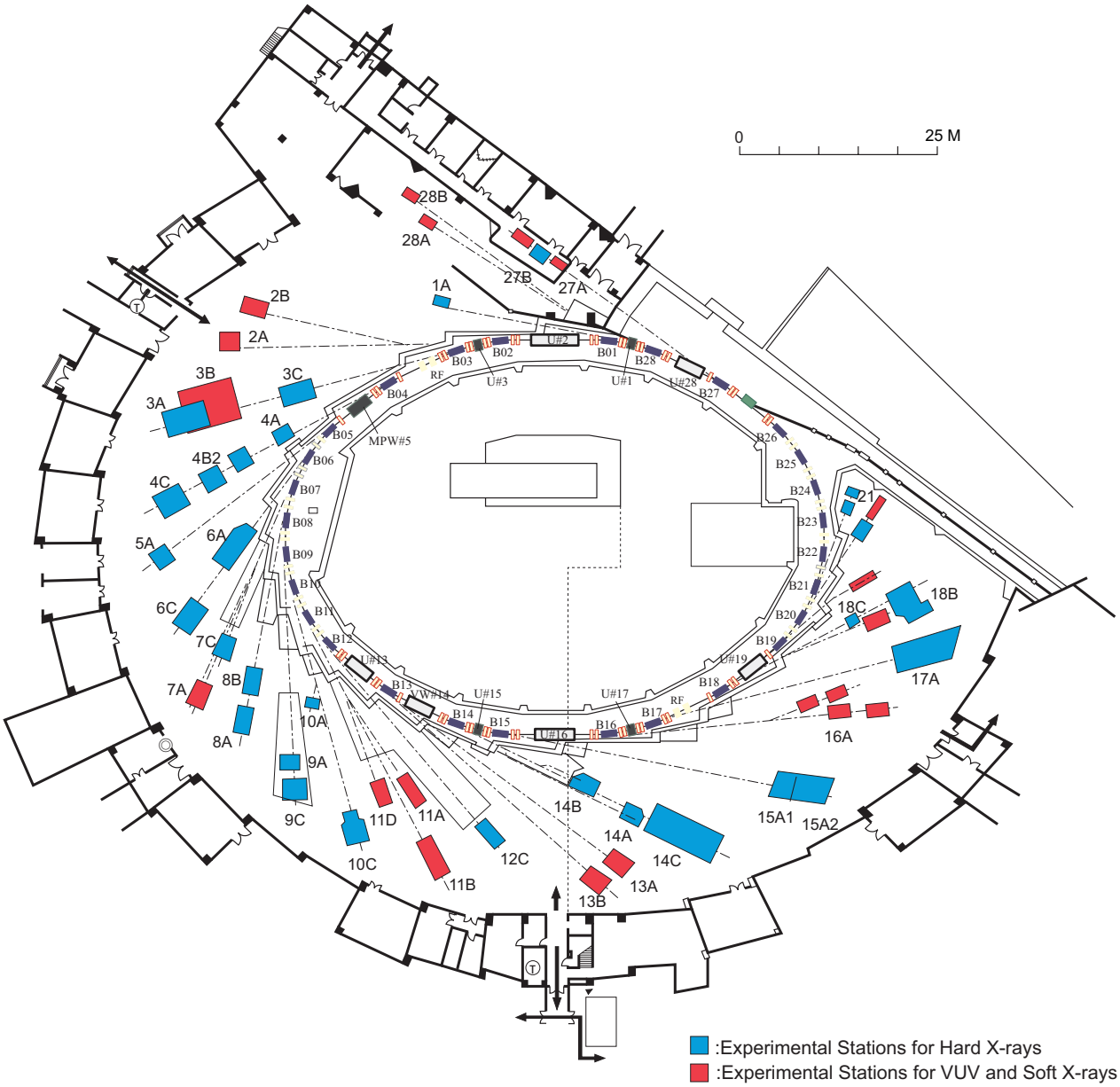

Figure 2: Plan view of the PF experimental hall, showing hard X-ray experimental stations (blue), and VUV and soft X-ray experimental stations (red).

Table 3: List of experimental stations available for users at the PF storage ring.

Experimental Station		Person in Charge
BL-1	(Short Gap Undulator)	
A	Macromolecular crystallography	N. Matsugaki
BL-2	(Undulator)	
A*	Soft X-ray spectroscopy	K. Amemiya
B*	Soft X-ray spectroscopy	K. Amemiya
BL-3	(A: Short Gap Undulator)	
A	X-ray diffraction and scattering station for materials science	H. Nakao
B	VUV and soft X-ray spectroscopy(◊)	H. Kato [Hirosaki Univ.], A. Yagishita
C	Characterization of X-ray optical elements/White X-ray magnetic diffraction	K. Hirano
BL-4		
A	Trace element analysis, X-ray microprobe	Y. Takahashi [The Univ. Tokyo], M. Kimura, Y. Niwa
B2	High resolution powder diffraction (♠)	T. Ida [Nagoya Inst. Tech.], H. Nakao
C	X-ray diffraction and scattering	H. Nakao
BL-5	(Multipole Wiggler)	
A	Macromolecular crystallography	N. Matsugaki
BL-6		
A	Small-angle X-ray scattering	N. Igarashi
C	Macromolecular crystallography	S. Sasaki [Tokyo Inst. Tech.], H. Kawata
BL-7		
A	Soft X-ray spectroscopy(♦)	J. Okabayashi [RCS], K. Amemiya
C	X-ray spectroscopy and diffraction	H. Sugiyama
BL-8		
A	Weissenberg camera for powder/Single-crystal measurements under extreme conditions	H. Sagayama
B	Weissenberg camera for powder/Single-crystal measurements under extreme conditions	H. Sagayama
BL-9		
A	XAFS	H. Abe
C	XAFS	H. Abe
BL-10		
A	X-ray diffraction and scattering(♠)	A. Yoshiasa [Kumamoto Univ.], R. Kumai
C	Small-angle X-ray Scattering	N. Shimizu
BL-11		
A	Soft X-ray spectroscopy	Y. Kitajima
B	Soft X-ray spectroscopy	Y. Kitajima
D	Characterization of optical elements used in the VSX region♠	K. Mase
BL-12		
C	XAFS	H. Nitani

Experimental Station		Person in Charge
BL-13	(Undulator)	
A/B	VUV and soft X-ray spectroscopies	K. Mase
BL-14	(Vertical Wiggler)	
A	Crystal structure analysis and detector development	S. Kishimoto
B	High-precision X-ray optics	K. Hirano
C	Medical applications and general purpose (X-ray)	K. Hyodo
BL-15	(Short Gap Undulator)	
A1	Semi-microbeam XAFS	H. Nitani
A2	High brilliance small-angle X-ray scattering	N. Shimizu
BL-16	(Variable Polarization Undulator)	
A	Soft X-ray spectroscopies with circular and linear polarization	K. Amemiya
BL-17	(Short Gap Undulator)	
A	Macromolecular crystallography	Y. Yamada
BL-18		
B	Multipurpose monochromatic hard X-ray station(♦)	A. Bhattacharyya [India,Saha Institute],R. Kumai
C	High pressure X-ray powder diffraction (DAC)(♠)	S. Nakano [NIMS], T. Kikegawa
BL-20		
A	VUV spectroscopy(◊)	N. Kouchi [Tokyo Inst. Tech], J. Adachi
B	White & monochromatic X-ray topography and X-ray diffraction experiment	H. Sugiyama
BL-27		
A	(Beamline for radioactive samples) Radiation biology, soft X-ray photoelectron spectroscopy	N. Usami
B	Radiation biology, XAFS	N. Usami
BL-28	(Elliptical / Helical Undulator)	
A	High-resolution VUV-SX beamline for angle-resolved photoemission	K. Ono
B	High-resolution VUV-SX spectroscopy	K. Ono

♠	User group operated beamline
♦	External beamline
◊	Operated by University
*	Under reconstruction
RCS:	Research Center for Spectrochemistry, the University of Tokyo
NIMS:	National Institute for Materials Science

Table 4: List of experimental stations at the PF-AR.

Experimental Station		Person in Charge
AR-NE1 A	(Multipole Wiggler) Laser-heating high pressure X-ray diffraction and nuclear resonant scattering (DAC)	T. Kikegawa
AR-NE3 A	(Undulator) Macromolecular crystallography	Y. Yamada
AR-NE5 C	High pressure and high temperature X-ray diffraction (MAX-80)	T. Kikegawa
AR-NE7 A	High pressure and high temperature X-ray diffraction (MAX-III), X-ray imaging	K. Hyodo
AR-NW2 A	(Undulator) Time-resolved Dispersive XAFS/XAFS/X-ray Diffraction	Y. Niwa
AR-NW10 A	XAFS	H. Nitani
AR-NW12 A	(Undulator) Macromolecular crystallography	Y. Yamada
AR-NW14 A	(Undulator) Time-resolved X-ray diffraction, scattering and absorption	S. Nozawa

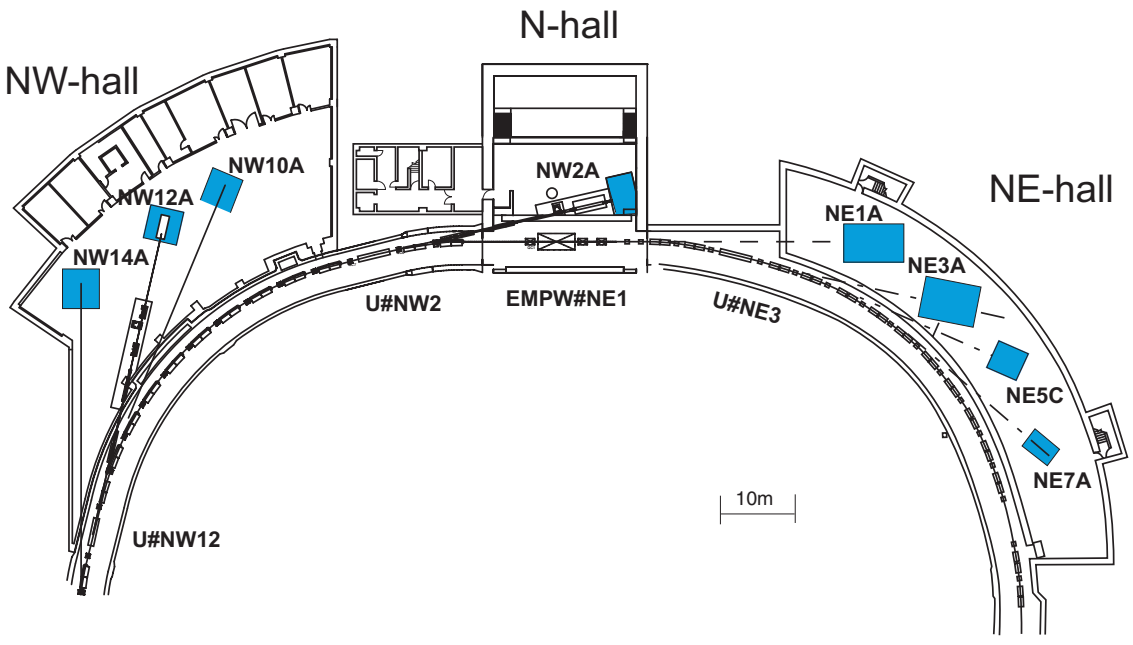

Figure 3: Plan view of beamlines in the PF-AR north-east, north, and north-west experimental halls.

Table 5: List of experimental stations at the Slow Positron Facility.

Experimental Station		Person in Charge
SPF-A3*	Total-reflection high-energy positron diffraction	T. Hyodo
SPF-B1	General purpose (Positronium negative ion)	T. Hyodo
SPF-B1	Positronium time-of-flight	T. Hyodo

* Under reconstruction

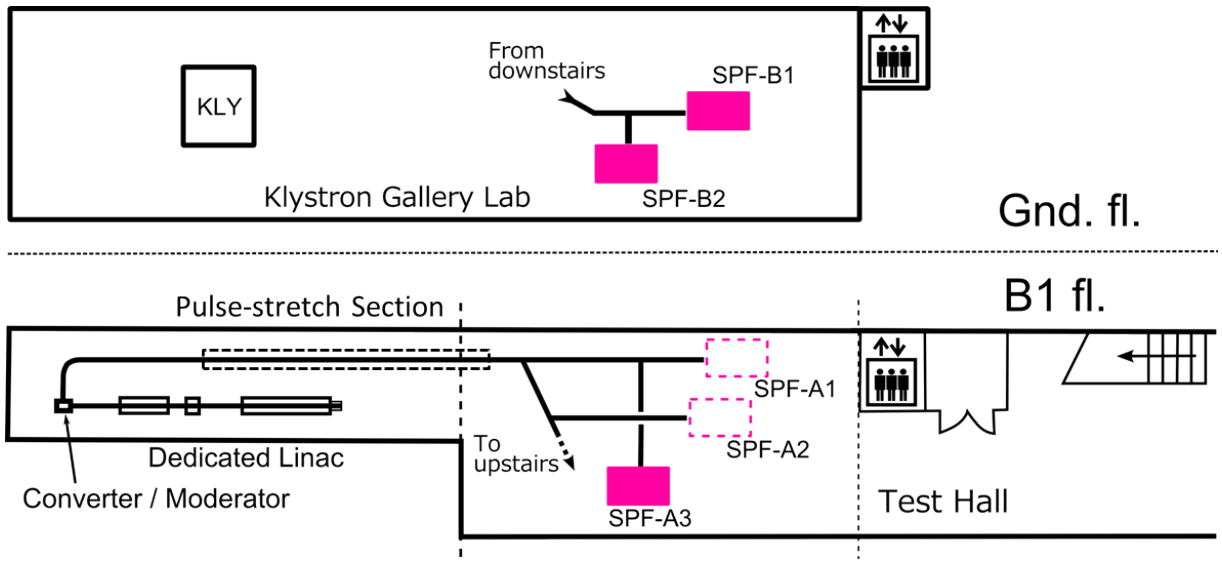

Figure 4: View of beamlines in the Slow Positron Facility.

Table 6: Specifications of X-ray beamline optics.

Branch Beamline	Horizontal Acceptance (mrad)	Type of Monochromator	Mirror	Photon Energy (keV)	Beam Size (H×V) (mm)	Photon Flux at Sample Position (/s)	Energy Resolution ($\Delta E/E$)×10^{-4}	Reference
BL-1A	0.15	Channel-Cut Si(111) Liquid N_2 Cooling	Bimorph Si Rh-Coated Si Rh-Coated	3.7 ~ 4.5 11.2 ~ 12.9	0.05×0.01	4×10^{11}@11.2 keV (0.025×0.01mm^2)	~2	
BL-3A	1	Flat Double Crystal Si(111)	Bent Cylinder	4 ~ 14	0.7×0.2	6×10^{12}	~5	1, 2
BL-3C	1.75	Double Crystal Si(111)	None	4 ~ 20 or white	20×6(mono) 0.1x0.1(white)		~2	
BL-4A	6	Double Crystal Si(111)	KB mirror polycapillary	4 ~ 20	0.005×0.005 0.03×0.03		~2	3
BL-4B2	4.5	Flat Double Crystal Si(111)	Bent Cylinder	6 ~ 20	13×2		~2	4, 5
BL-4C	2	Flat Double Crystal Si(111)	Bent Cylinder	5 ~ 19	0.7×0.5		~5	6, 7
BL-5A	0.5	Micro-Channel Double Crystal Si(111)	Bent Plane Si Rh-Coated Bent Cylinder Si Rh-Coated	6.5 ~ 17	1.2×0.4	3×10^{11} (0.2×0.2mm^2)	~2	
BL-6A	2	Bent Crystal Ge(111) (α = 8.0°)	Bent Cylinder ULE	8.3 (fixed)	0.5×0.2	1.0×10^{12}/mm^2 (Slit full-open)	~10	8
BL-6C	2	Flat Double Crystal Si(111)	Bent Cylinder	5 ~ 20 (~25 non-Focus)	0.5×0.3			
BL-7C	4	Double Crystal Si(111) Sagittal Focusing	Double Mirror Fused Quartz Focusing	4 ~ 20 (4 ~ 13)	5×1	1×10^{10}/6mm^2 (8keV, 300mA) (1×10^{11} when focused)	~2	9 - 11
BL-8A	2.22	Flat Double Crystal Si(111)	Bent Cylinder	5 ~ 19	0.82×0.52	3.2×10^{11} (12.4keV, 400mA)	~5	12
BL-8B	2.21	Flat Double Crystal Si(111)	Bent Cylinder	5 ~ 19	0.75×0.45	2.2×10^{11} (12.4keV, 400mA)	~5	12
BL-9A	3	Double Crystal Si(111)	Collimating and Focusing Bent Conical Mirrors Rh-Coated Double Flat Mirror Ni-Coated		0.5×0.3	6×10^{11}(7keV, 450mA)	2	13,14
BL-9C	3.5	Double Crystal Si(111)	Bent Cylinder Rh-Coated Si	4 ~ 23		1×10^{11}(8keV, 450mA)	~2	

Branch Beamline	Horizontal Acceptance (mrad)	Type of Monochromator	Mirror	Photon Energy (keV)	Beam Size (H×V) (mm)	Photon Flux at Sample Position (/s)	Energy Resolution ($\Delta E/E \times 10^{-4}$)	Reference
BL-10A	1	Si(111),Si(311) Quartz(100) PG(002) Curved Si(111) (α~ 4°, 8°)	Plane Pt Coated Fused Quartz	5 ~ 25	10×3		10 -5	15
BL-10C	2.1	Fix-Exit Double Crystal Si(111)	Bent Cylinder Rh-Coated	6 ~ 14	0.63×0.18	1.5×10^{11} (8 keV)	2	
BL-12C	2	Double Crystal Si(111)	Bent Cylinder Double Flat Mirror Ni-Coated	4 ~ 23	0.6×0.6	9×10^{10} (8 keV,450mA)	-2	16
BL-14A	1.28 (Vertical)	Double Crystal Si(111) Si(311) Si(553)	Bent Cylinder Rh-Coated Fused Quartz	5.1 ~ 19.1 9.9 ~ 35.6 22.7 ~ 84.5	2×1 at focus 5×38		2	17
BL-14B	2.2 (Vertical)	Flat Double Crystal Si(111)	None	10 ~ 57	5×14		2	18
BL-14C	1.96 (Vertical)	Double Crystal Si(111),Si(220)	None	5 ~ 100 or white	6×70		2	19,20
BL-15A1	0.2	Double Crystal Si(111) Liquid N_2 Cooling	Horizontal: Bent Plane Si Bimorph Silica Rh-Coated Vertical: Bent Plane Si Rh-Coated Double Flat Si Ni-Coated	2.1 ~ 15	0.02×0.02	3.5×10^{11} (7.5 keV, 450mA)	-2	21
BL-15A2					0.6×0.04			
BL-17A	0.1 ~ 0.2	Double Crystal Si(111) Liquid N_2 Cooling	Bent Plane Si Rh-Coated Bent Plane Si Rh-Coated	6 ~ 13	0.25×0.04	10^{10} (12.4 keV,450mA, 0.02×0.02mm^2)	-2	22 - 24
BL-18B [India, DST]	2	Double Crystal Si(111)	Plane and Bent Cylinder	6 ~ 20			-2	
BL-18C	1	Double Crystal Si(111)	Cylinder Fused Quartz Pt-Coated	6 ~ 25	0.07×0.04		-2	
BL-20B	2	Double Crystal Si(111)	None	5 ~ 25 or white	26×5	$1x\ 10^{11}$ (12 keV,450mA)	-2	
BL-27B	4	Double Crystal Si(111)	None	4 ~ 20	100×6		-2	25

Branch Beamline	Horizontal Acceptance (mrad)	Type of Monochromator	Mirror	Photon Energy (keV)	Beam Size (H×V) (mm)	Photon Flux at Sample Position (/s)	Energy Resolution ($\Delta E/E \times 10^{-4}$)	Reference
AR-NE1A	0.28	Micro-Channel Double Crystal Si(111), High-Resolution Channel Cut Si(4,2,2)&(12,2,2)	Bent Plane W/C Multilayer Coated Si	6~ 50	0.8×0.2	8×10^{11} ($0.2\times0.2mm^2$)	-2	
AR-NE3A	H:0.2 V:0.1	Double Crystal Si(111) Liquid N_2 Cooling	Pre-Mirror Bent Flat Si Rh-Coated Post-Mirror Bent Cylinder Fused Quartz Rh-Coated	6.5 ~ 17	0.8×0.2	8×10^{11} ($0.2\times0.2mm^2$)	-2	26, 27
AR-NE5C	3	Double Crystal Si(111)	None	30 ~ 100 or white	60×5		5	28
AR-NE7A	4			25 ~ 50 or white	80×3		5	
AR-NW2A	H:1.0 V:0.2	Double Crystal Si(111) Liquid N_2 Cooling	Bent Cylinder Si Rh-Coated Bent Flat Si Rh-Coated	5 ~ 25 or white	0.6×0.2 ~10×0.06	6×10^{12} (12keV, 60mA)	-2	29 - 31
AR-NW10A	1.2	Si(311)	Pt-Coated Bent Cylinder Double Flat Mirror Rh-Coated	8 ~ 42	2.2×0.5	1×10^{10} (12keV, 60mA)	-1	32
AR-NW12A	H:0.3 V:0.1	Double Crystal Si(111) Liquid N_2 Cooling	Pre-Mirror Bent Flat Si Rh-Coated Post-Mirror Bent Cylinder Si Rh-Coated	6.5 ~ 17	1.3×0.3	2×10^{11} ($0.2\times0.2mm^2$)	-2	33 - 35
AR-NW14A	H:0.3 V:0.1	Double Crystal Si(111) Liquid N_2 Cooling	Bent Cylinder Rh-Coated Bent Flat Rh-Coated	4.9 ~ 25	0.45×0.25	1×10^{12}	-2	36

India DST: Department of Science & Technology

REFERENCES

[1] *Photon Factory Activity Report 2006*, **#24**, A 64 (2008).
[2] *Photon Factory Activity Report 2006*, **#24**, A 104 (2008).
[3] A. Iida et *al., Rev. Sci. Instrum.* **66**, 1373 (1995).
[4] Powder Diffraction User Group, KEK Report **94-11** (1995).
[5] H. Toraya, H. Hibino, and K. Ohsumi, *J. Synchrotron Rad.* **3**, 75 (1996).
[6] H. Iwasaki *et al., Rev. Sci. Instrum.* **60**, 2406 (1989).
[7] *Photon Factory Activity Report 1995* **#13**, E-1 (1996).
[8] N. Shimizu *et al., J. Phys.: Conf. Ser.* **425**, 202008 (2013).
[9] M. Nomura and A.Koyama, *KEK Internal*, **93-1** (1993).
[10] M. Nomura *et al., KEK Report*, **91-1** (1991).
[11] M.Nomura and A.Koyama, in *"X-ray Absorption Fine Structure"*, ed. by S. S. Hasnain, Ellis Horwood, Chichester, **667** (1991).
[12] A. Nakao *et al., AIP Conf. Proc.* **1234**, 367 (2010).
[13] M. Nomura and A. Koyama, *J. Synchrotron Rad.* **6**, 182 (1999).
[14] M. Nomura and A. Koyama, *Nucl. Instrum. Meth.* **A467-468**, 733(2001).
[15] S. Sasaki, *Rev. Sci. Instrum.* **60**, 2417 (1989).
[16] M. Nomura and A. Koyama, *KEK Report,* **95-15** (1996).
[17] Y. Satow and Y. Iitaka, *Rev. Sci. Instrum.* **60**, 2390 (1989).
[18] M. Ando *et al., Nucl. Instrum. Meth.* **A246**, 144 (1986).
[19] *Photon Factory Activity Report 1999*, **#17**, A 92 (2000).
[20] *Photon Factory Activity Report 1999*, **#17**, A 103 (2000).
[21] N. Igarashi *et al., J. Phys.: Conf. Ser.* **425**, 072016 (2013).
[22] N. Igarashi *et al., AIP Conf. Proc.* **879**, 812 (2007).
[23] N. Igarashi *et al., J. Synchrotron Rad.* **15**, 292 (2008).
[24] Y. Yamada *et al., J. Synchrotron Rad.* **20**, 938 (2013).
[25] H. Konishi *et al., Nucl. Instrum. Meth.* **A372**, 322 (1996).
[26] Y. Yamada *et al., AIP Conf. Proc.* **1234**, 415 (2010).
[27] M. Hiraki *et al., AIP Conf. Proc.* **1234**, 673 (2010).
[28] T. Kikegawa *et al., Rev. Sci. Instrum.* **66**, 1335 (1995).
[29] T. Mori *et al., AIP Conf. Proc.* **705**, 255 (2004).
[30] H. Kawata *et al., AIP Conf. Proc.* **705**, 663 (2004).
[31] Y. Inada *et al., AIP Conf. Proc.* **879**, 1230 (2007).
[32] M. Nomura *et al., AIP Conf. Proc.* **882**, 896 (2007).
[33] L. M. G. Chavas *et al., J. Synchrotron Rad.* **19**, 450 (2012).
[34] L. M. G. Chavas *et al., J. Phys.: Conf. Ser.* **425**, 012008 (2013).
[35] L. M. G. Chavas *et al., J. Synchrotron Rad.* **20**, 838 (2013).
[36] S. Nozawa *et al., J. Synchrotron Rad.* **14**, 313 (2007).

Table 7: Specifications of VUV and soft X-ray beamline optics.

Branch Beamline	Acceptance H × V (mrad) or Undulator Parameters	Type of Monochromator	Groove Density (/mm)	Energy Range (eV)	Beam Size H × V (mm)	Resolving Power (E/ΔE) Photon Flux (photons/s)	Reference
BL-2A* Undulator	ID02: K_{max} = 2.3, λ_u = 6 cm ID022: K_{max} = 5.0, λ_u = 16 cm	Variable-Included-Angle Varied-Line-Spacing Plane Grating	400 600 1000	30 ~ 2000	~0.5 × 0.1	2000 ~ 20000 10^{13} ~ 10^{11}	1
BL-2B* Undulator	ID02: K_{max} = 2.3, λ_u = 6 cm ID022: K_{max} = 5.0, λ_u = 16 cm	Variable-Included-Angle Varied-Line-Spacing Plane Grating Double Crystal InSb(111), Ge(111), Si(111)	400 600 1000	30 ~ 4000	~0.5 × 0.1	2000 ~ 20000 10^{13} ~ 10^{11}	1
BL-3B	10 × 2	Grazing Incidence R = 24 m α+β = 165° 1800	200 600	10 ~ 280	< 2ϕ	200 ~ 3000 10^{12} ~ 10^{9}	2, 3
BL-7A [RCS]	6 × 1	Varied-Line-Space Plane Grating	150 300 650	50 ~ 1300	2.5 × 0.5	1000 ~ 9000 10^{12} ~ 10^{9}	4
BL-11A	5 × 1	Varied-Included-Angle Varied-Line-Spacing Plane Grating	600 1200	70 ~ 1900	2 × 1	500 ~ 5000 10^{12} ~ 10^{9}	
BL-11B	4 × 0.6	Double Crystal InSb (111), Si (111)		1724 ~ 5000	5 × 2	2000 10^{10}	5 - 7
BL-11D	4 × 2	Grazing Incidence Varied Deviation-Angle On-Blaze Mount R_1 = 52.5 m R_3 = 22.5 m	2400	60 ~ 245 200 ~ 900	1 × 0.1	2000 10^{11}	8, 9
BL-13A/B Undulator	K_{max} = 8 λ_u = 18 cm	Variable-Included-Angle Varied-Line-Spacing Plane Grating	300 1000	30 ~ 330 100 ~ 1600	~0.2 × 0.04	4000 ~ 10000 10^{12} ~ 10^{9}	10 - 12
BL-16A Undulator	K_{max} = 2.37 (Circular Polarization) K_{max} = 3.12 (Horizontal Linear Polarization) K_{max} = 1.98 (Vertical Linear Polarization) K_{max} = 1.73 (45-deg Linear Polarization) λ_u = 5.6 cm	Variable-Included-Angle Varied-Line-Spacing Plane Grating	500 1000	250 ~ 1500	~0.2 × 0.1	4000 ~ 8000 10^{12} ~ 10^{11}	13, 14
BL-19B Revolver Undulator	K = 0.5 ~ 1.25 λ_u = 5 cm	Varied-Line-Space Plane Grating	800 2400	200 ~ 1200	1 × 0.5	4000 ~ 8000 10^{12} ~ 10^{11}	15 - 17
BL-20A	28 × 5	3m Normal Incidence	1200 2400	5 ~ 40	2 × 1	300 ~ 30000 10^{12} ~ 10^{8}	18
BL-27A	5 × 0.5	Double Crystal InSb (111)		1800 ~ 4000		2000	19
BL-28A/B Helical Undulator	K_x = 0.23 ~ 3 K_y = 0.23 ~ 6 K_y = 0.23 ~ 6	Varied-Line-Space Plane Grating	400	30 ~ 300	0.15 × 0.05	30000 10^{12}	1

* Under reconstruction

RCS: Research Center for Spectrochemistry, the University of Tokyo

REFERENCES

[1] K. Amemiya and T. Ohta, *J. Synchrotron Rad.* **11**, 171 (2004).
[2] A. Yagishita *et al., Nucl. Instrum. Meth.* **A306**, 578 (1991).
[3] S. Masui *et al., Rev. Sci. Instrum.* **63**, 1330 (1992).
[4] K. Amemiya *et al., J. Elec. Spectrosc. Relat. Phenom.* **124**, 151 (2002).
[5] T. Ohta *et al., Nucl. Instrum. Meth.* **A246**, 373 (1986).
[6] M. Funabashi *et al., Rev. Sci. Instrum.* **60**, 1983 (1989).
[7] T. Iwazumi *et al., Rev. Sci. Instrum.* **66**, 1691 (1995).
[8] *Photon Factory Activity Report 1997* **#15**, A 101 (1998).
[9] T. Hatano and S. Aihara, *J. Phys.: Conf. Ser.* **425**, 152018 (2013).
[10] K. Mase *et al., AIP Conf. Proc.* **1234**, 709 (2010).
[11] A. Toyoshima *et al., J. Vac. Soc. Jpn.* **54**, 580 (2011).
[12] A. Toyoshima *et al., J. Phys.: Conf. Ser.* **425**, 152019 (2013).
[13] K. Amemiya *et al., AIP Conf. Proc.* **1234**, 295 (2010).
[14] K. Amemiya *et al., J. Phys.: Conf. Ser.* **425**, 152015 (2013).
[15] S. Suzuki *et al., Activity Report of SRL-ISSP* **60**, (1989).
[16] A. Kakizaki *et al., Rev. Sci. Instrum.* **60**, 1893 (1989).
[17] A. Kakizaki *et al., Rev. Sci. Instrum.* **63**, 367 (1992).
[18] K. Ito *et al., Rev. Sci. Instrum.* **66**, 2119 (1995).
[19] H. Konishi *et al., Nucl. Instrum. Meth.* **A372**, 322 (1996).

Table 8: Specifications of the beamlines at Slow Positron Facility.

Beamline	Beam Energy	Pulse Width	Frequency	Intensity	Reference
SPF-A3*	100eV - 35keV	1μs	≤ 50Hz	$5x10^7$ e+/s ($5x10^6$ e+/s after brightness enhancement)	3,4
SPF-B1	100eV - 35keV	1-10ns	≤ 50Hz	$5x10^6$ e+/s	1,2,3,4
SPF-B2	100eV - 35keV	1-10ns	≤ 50Hz	$5x10^6$ e+/s	5,6

* Under reconstruction

REFERENCES

[1] T. Tachibana, *et. al., Nucl. Instrum. Methods Phys. Res., Sect.* **A 621**, 670 (2010).
[2] K. Michishio, *et al., Phys. Rev. Lett.* **106**, 153401 (2011).
[3] K. Wada, *et al., Eur. Phys. J. D* **66**, 37 (2012).
[4] K. Michishio, *et al., Appl. Phys. Lett.* **100**, 254102 (2012).
[5] K. Wada, *et al., J. Phys.: Conf. Ser.* **443**, 012082 (2013).
[6] H. Terabe, S. Iida, K. Wada, T. Hyodo, A. Yagishita, and Y. Nagashima, *J. Phys.: Conf. Ser.* **443**, 012075 (2013).

2 Operation and Proposals

2-1 Operation Summary

In FY2014, the machine operation schedule of the PF ring and PF-AR was not like in past years as shown in Fig. 1. The PF ring and PF-AR did not deliver beams to users during the winter term from January to March 2015. This was due to a reduction in operation funding and higher electricity charges. As a result, the total user beam time of the PF ring was 2,317 hours, and that of the PF-AR was 1,955 hours, which are about half of the user beam time in the past (~4,000 hours). This situation seriously affected the allocation of beam time to users, which was evidenced by a much higher oversubscription ratio than usual at the highly popular insertion-device and bending-magnet beamlines. Both the facility staff and user community (PF-User Association, PF-UA) worked to resolve this situation in FY2014 by launching a campaign for collecting signatures from other academic communities (physics, chemistry, biology, engineering, etc.) and industrial companies in which synchrotron radiation users have been actively involved. Thanks to these comprehensive efforts by facility staff and users, the user beam time in FY2015 is expected to recover partly to ~3,000 hours. We deeply appreciate all the efforts and actions by the user community to support and maintain the activities of the PF. The operational statistics for the PF ring and PF-AR are summarized in Table 1. The statistics of the accelerator's operation for more than twenty years are shown in Fig. 2 for the PF ring and in Fig. 3 for the PF-AR.

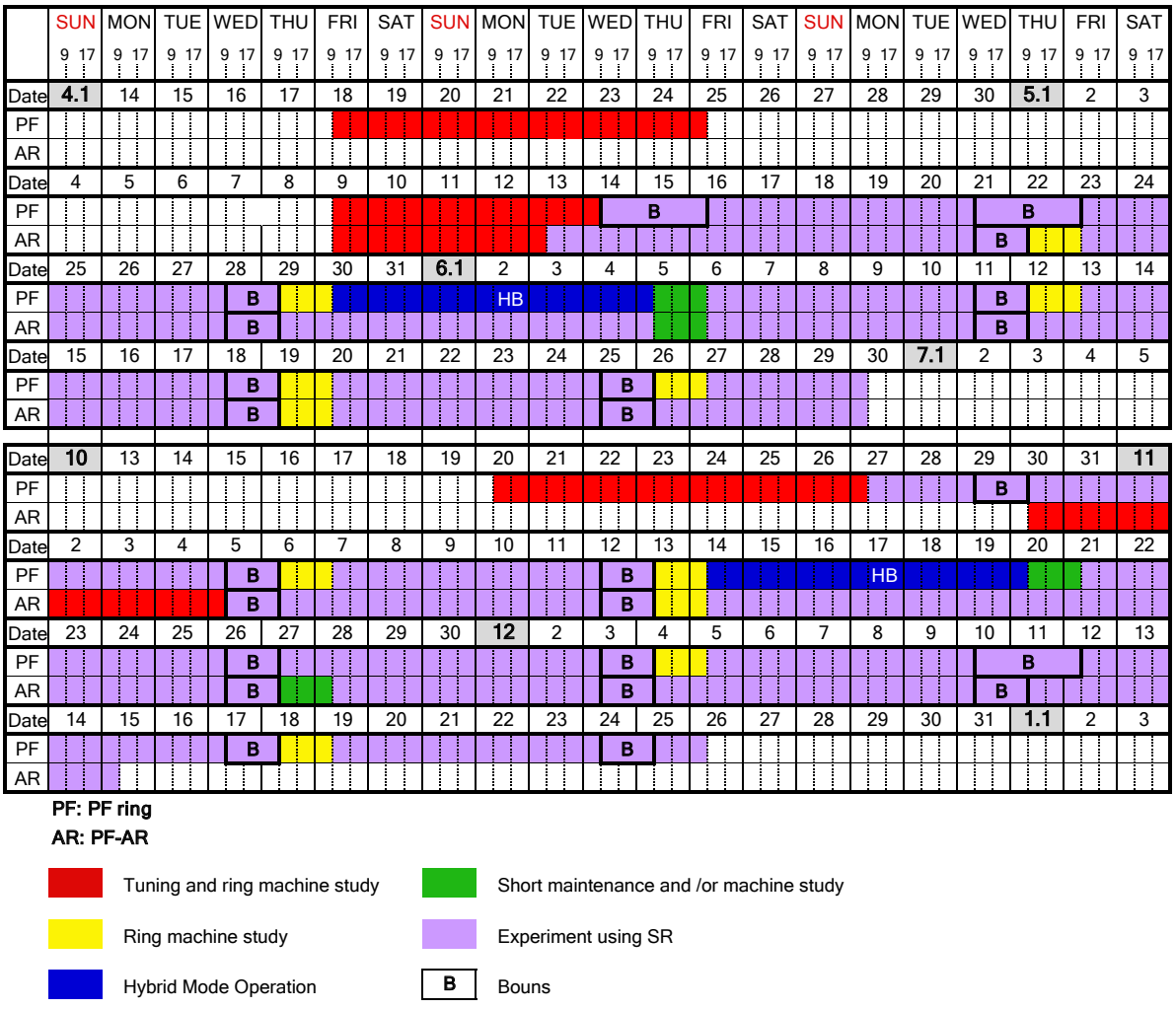

Figure 1: Timetable for PF ring and PF-AR operations in FY2014.

Table1: Operation statistics for PF ring and PF-AR in FY2014.

	PF- ring	PF-AR
Ring operation time (h)	3024.0	2352.0
Actual user time (h)	2316.6	1955
Machine adjustment time (h)	696.0	360.0
Failure time (h)	11.4	37.0

To demonstrate the good performance of the PF ring, the failure rates as a percentage of the total operation time are shown in Fig. 4.

In the PF ring, the user operation was delayed by one week from the primary schedule due to a leak of the gate valve with RF contacts, which was installed just upstream of undulator #02-2. Except for this accident, the operation has been smooth, although beamline #14 was closed till June 2014 due to a problem with the superconducting wiggler.

The numbers of failures in the PF-AR from FY2005 to FY2014 are listed by component in Table 2, and the downtimes in FY2014 are classified by component as a pie chart in Fig. 5.

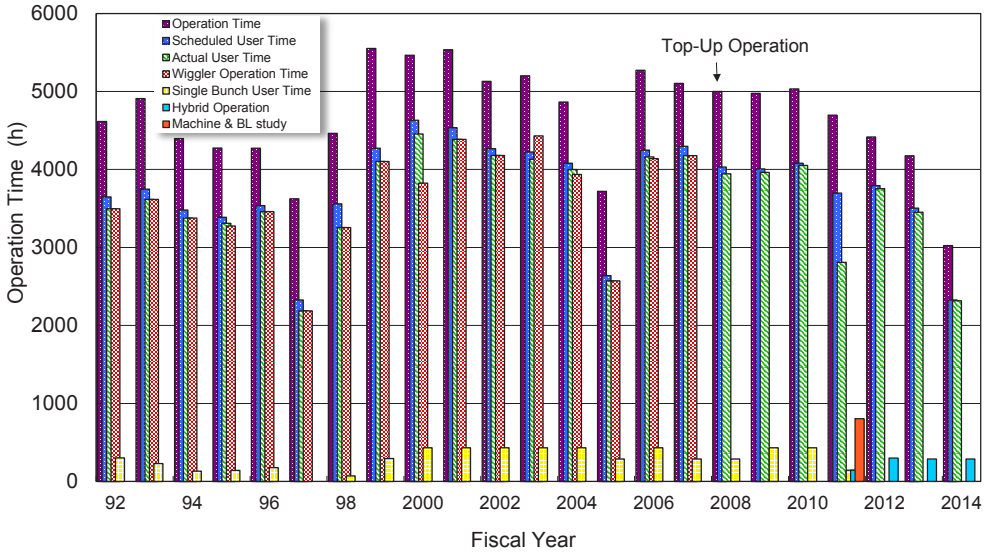

Figure 2: Total operation, scheduled user, actual user, and single-bunch user time for PF ring.

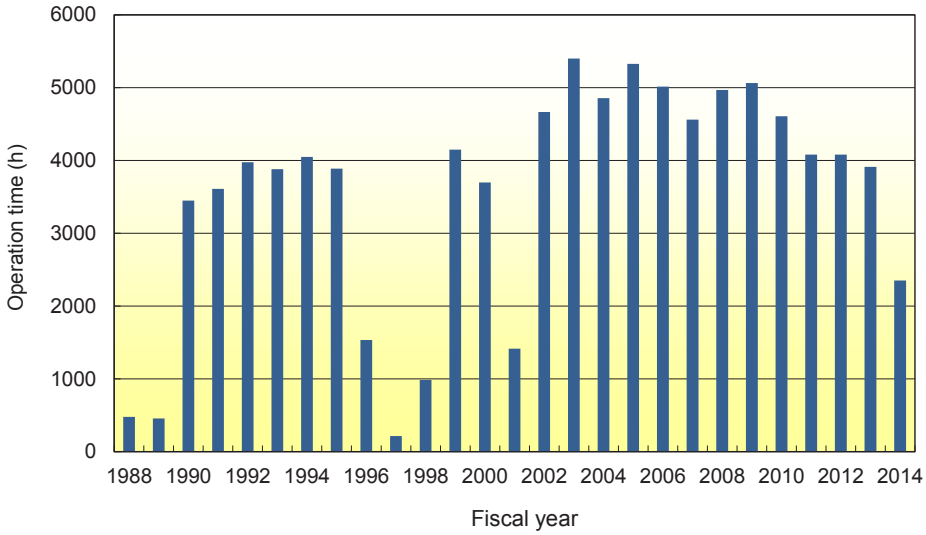

Figure 3: Total operation time for PF-AR.

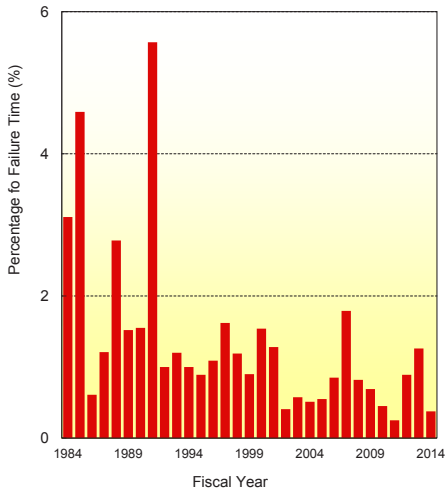

Figure 4: Failure rate for PF ring.

Table 2: The numbers of failures in the PF-AR from FY2005 to FY2014.

Fiscal year	2005	2006	2007	2008	2009	2010	2011	2012	2013	2014
RF	12	10	1	4	8	10	5	4	5	2
Magnet	4	1	1	2	2	10	8	3	4	9
Injection	4	3	8	9	1	6	4	3	18	7
Vacuum	2	6	2	0	2	1	0	1	0	0
Dust trap	37	24	39	15	16	24	20	13	3	2
Insertion devices	0	1	0	0	0	0	0	0	0	0
Control / Monitor	4	0	1	1	1	2	1	2	8	0
Cooling water	5	1	0	3	4	4	1	0	2	0
Safety / Beamline	9	4	5	5	7	17	3	4	3	1
Earthquake	2	0	1	0	0	0	5	3	1	0
Electricity	0	1	2	1	0	0	2	0	3	1
Total	79	51	60	40	41	74	49	33	47	22

Fiscal year	2005	2006	2007	2008	2009	2010	2011	2012	2013	2014
Total operation time (h)	5313	5016	4561	4969	5063	4608	4080	4080	3912	2352
Scheduled user time (h)	4456	4032	3624	4344	4392	4032	2904	3672	3478	1992
Ratio of user time (%)	83.9	80.4	79.5	87.4	86.7	87.5	71.2	90.0	88.9	84.7
Number of failures	79	51	60	40	41	74	49	33	47	22
Total down time (h)	69.3	55.1	45.2	41.7	91.0	73.7	38.7	29.7	99.6	37.0
Failure rate (%)	1.6	1.4	1.2	1.0	2.1	1.8	1.3	0.8	2.9	1.9
MTBF (h)	56.4	79.1	60.4	108.6	107.1	54.5	59.3	111.3	74.0	90.5
Mean down time (h)	0.9	1.1	0.8	1.0	2.2	1.0	0.8	0.9	2.1	1.7

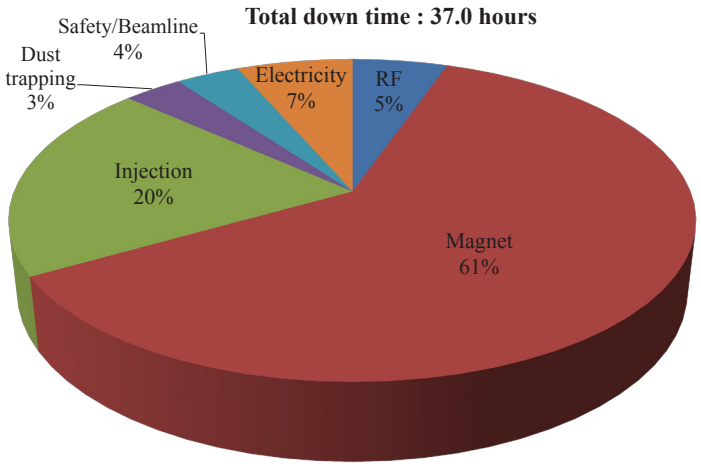

Figure 5: Pie chart of the down time in FY2014 of PF-AR.

2-2 Scientific Proposals

The Photon Factory accepts experimental proposals submitted by researchers mainly at universities and research institutes inside and outside Japan. The PF Program Advisory Committee (PF-PAC) reviews the proposals, and the Advisory Committee for the Institute of Materials Structure Science formally approves those that are favorably recommended. The number of accepted proposals over the period 2003–2014 is shown in Table 3, where S1/S2, U, G, and P denote Special, Urgent, General and Preliminary proposals, respectively. Category T is a new type of proposal for supporting researches by PhD students. The number of current G-type proposals each year has exceeded 800 for the past few years. A full list of the proposals effective in FY2014 and their scientific output can be found in Part B of this volume.

Table 3: Number of proposals accepted for the period 2003–2014.

Category	FY2003	2004	2005	2006	2007	2008	2009	2010	2011	2012	2013	2014
S1	1	1	0	1	0	0	0	0	0	0	0	0
S2	2	0	3	6	1	4	6	3	2	4	5	4
U	2	4	0	1	7	3	2	2	0	4	1	0
G	318	382	310	386	403	402	397	407	415	454	447	407
P	9	13	10	22	14	14	14	16	11	18	18	5
T												6

Table 4: List of S-type proposals effective in FY2014.

Proposal No.	Spokesperson	Title
2014S2-001	R. Kumai KEK-PF	Structural sciences for the understanding of the origin of physical properties and optimization of functions in the organic molecular assemblies
2014S2-003	H. Sawa Nagoya Univ.	Study of the new quantum lattice liquid system by crystal field analysis
2014S2-004	Y. Fukaya JAEA	Topmost surface structure determination using total reflection high-energy positron diffraction
2014S2-006	S. Nozawa KEK-PF	Dynamic study for optical functional materials by high-efficiency time-resolved XAFS
2013S2-001	T. Matsushita KEK-PF	Development of Time-Resolved X-Ray Reflectometory and its applications
2013S2-002	Y. Murakami KEK-PF	Synchrotron radiation research on element strategy project_electronic materials:The study of functionalities in lightelement anion systems
2013S2-003	Y. Takahashi The Univ. of Tokyo	Development of sustainable science by scanning transmission X-ray microscopy (STXM)
2013S2-004	K. Amemiya KEK-PF	Complementary studies on magnetic thin films aiming at control of their properties by external factors mainly by means of soft X-ray XMCD
2013S2-005	Y. Nagashima Tokyo Univ. of Sci.	New developments of the Ps- photodetachment experiment and applications of the energy tunable Ps beam
2012S2-001	T. Takahashi Tohoku Univ.	Quantum phenomena of Dirac fermion systems studied by highresolution angle-resolved photoemission spectroscopy
2012S2-004	A. Waseda AIST	Crystal evaluation of silicon crystals for the determination of the Avogadro constant
2012S2-005	H. Nakao KEK-PF	Materials structure science by resonant soft x-ray scattering under external field
2012S2-006	J. Yoshinobu The Univ. of Tokyo	Physical chemistry at surface and interface of energy-conversion materials using VUV/SX SR spectroscopies
2011S2-003	M. Oshima The Univ. of Tokyo	Operando analysis of green nano-device structures by high-resolution electron spectroscopy

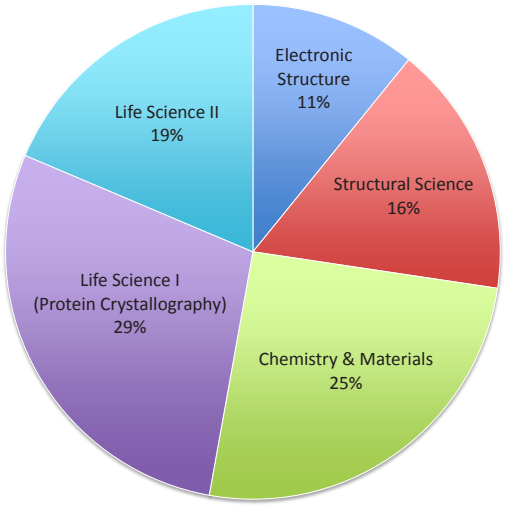

Figure 6: Distribution by scientific field of experimental proposals accepted in FY2014.

S-type proposals consist of two categories, S1 and S2. S1 proposals are self-contained projects of excellent scientific quality, and include projects such as the construction and improvement of beamlines and experimental stations which will be available for general users after the completion of the project. S2 proposals are superior-grade projects that require the full use of synchrotron radiation or long-term beam time. Table 4 lists the S-type projects effective in FY2014. The proposers are requested to report the current status and results to date of S1 and S2 proposals at the PF Symposium held at the end of every Japanese fiscal year. The scientific output of S1 and S2 proposals is presented in the Highlights of Part A and in the Users' Reports of Part B of this volume.

Proposals are categorized into five scientific disciplines, and reviewed by the five subcommittees of PF-PAC: 1) electronic structure, 2) structural science, 3) chemistry and new materials, 4) life science I (protein crystallography), and 5) life science II (including soft matter science). Figure 6 shows the distribution by research field of the proposals accepted by the subcommittees in FY2014.

2-3 Industrial Proposals

Proposals by users in industries can be accepted in the following categories:

Trial use: Only for users who have not used the PF in the field of analytical methods such as X-ray absorption fine structures (XAFS), topography, imaging, X-ray photoelectron spectroscopy (XPS), X-ray diffraction (XRD), and small-angle scattering (SAXS).

Time-designated proposal: A certain amount of beam time can be used for a fee. The experimental results can be kept confidential.

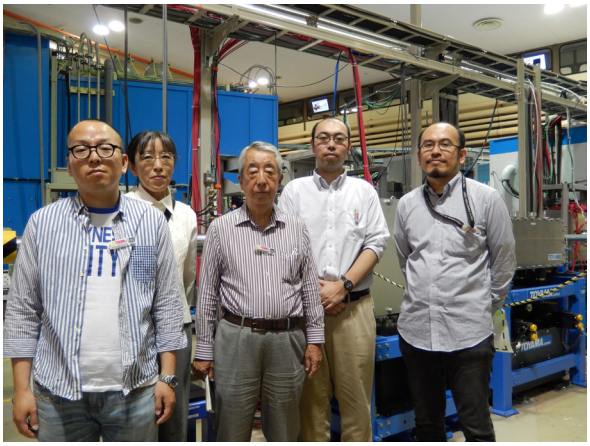

Figure 7: A group photo of technical support staff for the trial-use program.

Collaborative research: A certain amount of beam time can be used for collaborative research between an industrial organization and a research group in PF, IMSS or KEK for a fee.

(A) Trial use: Sixteen trial-use programs for industrial applications were carried out with the financial support of a MEXT project, the Open Advanced Research Facilities Initiative. Among these, twelve were newly approved and four were continued from FY2013. A total of six staff members, including the five persons shown in Fig. 7, supported these research activities. After ending the trial-use program in FY2012, a nonproprietary collaborative study was performed in FY2014.

(B) Time-designated proposal: In 2014 we accepted 22 proposals from industrial organizations at beamlines for various fields such as XAFS, XPS, and SAXS.

(C) Collaborative research: In 2014 we accepted 20 proposals from industrial organizations at beamlines. Topics in collaborative research cover a wide range of fields, from materials science to biochemistry.

2-4 Statistics of the Proposals

The number of users, for all types of proposals, has reached 3,074. Although the number of experimental stations has decreased, the approved scientific proposals and number of users have increased annually, as shown in Fig. 8. This indicates a high and increasing demand for synchrotron radiation and can be attributed to continuous improvements in the storage rings, beamlines, and experimental stations. The synchrotron has become one of the most important research tools for carrying out advanced science experiments and development. About 22% of the proposals are conducted by new spokespersons, which indicates that the Photon Factory is open to public academic scientists. Figure 9 shows the distribution of users by institution and position. About three-quarters of the users belong to universities, with approximately 73% of the users associated

with national universities. Over two-thirds of the national university users are graduate and undergraduate students; this indicates that the Photon Factory plays an important role in both research and education. The geographical distribution of the Photon Factory users is shown in Fig. 10 and Fig. 11, which also indicates the immense contribution of the Photon Factory to research and education throughout Japan. The registered number of papers published in 2014 based on experiments at the PF was 531 at the time of this writing and is expected to exceed 590. In addition, 11 doctoral and 45 master theses have been presented.

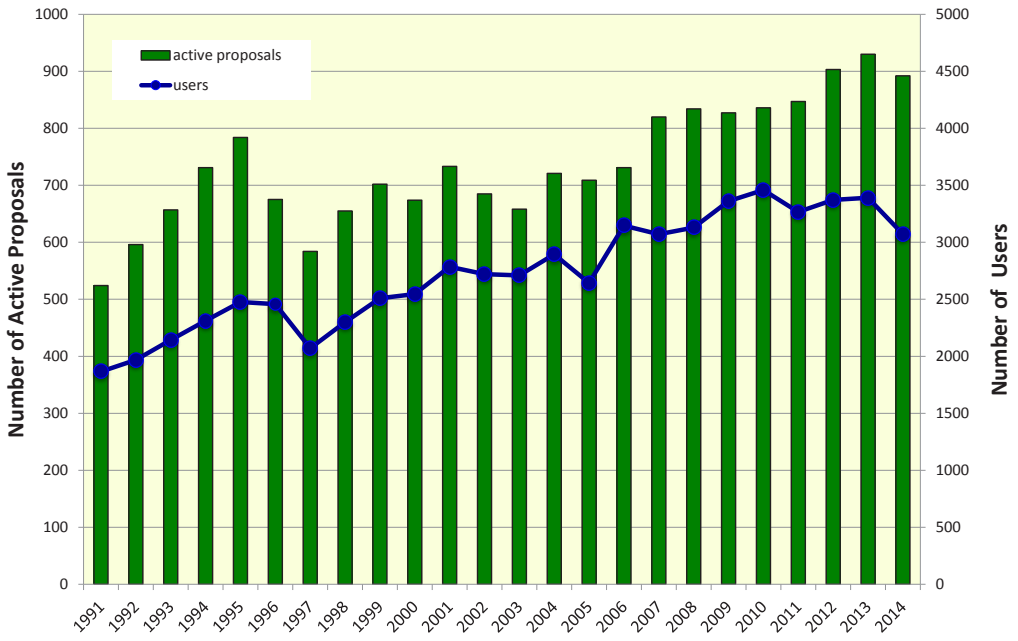

Figure 8: Number of registered PF users and scientific proposals over the period 1991–2014.

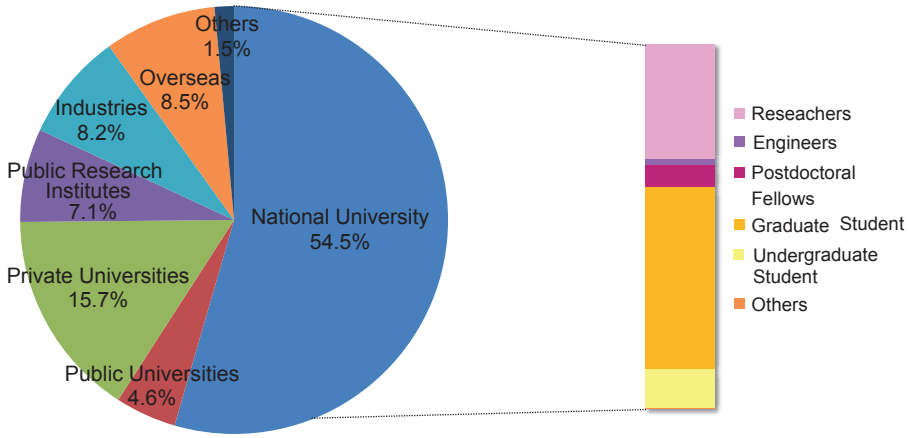

Figure 9: Distribution of users by institution and position.

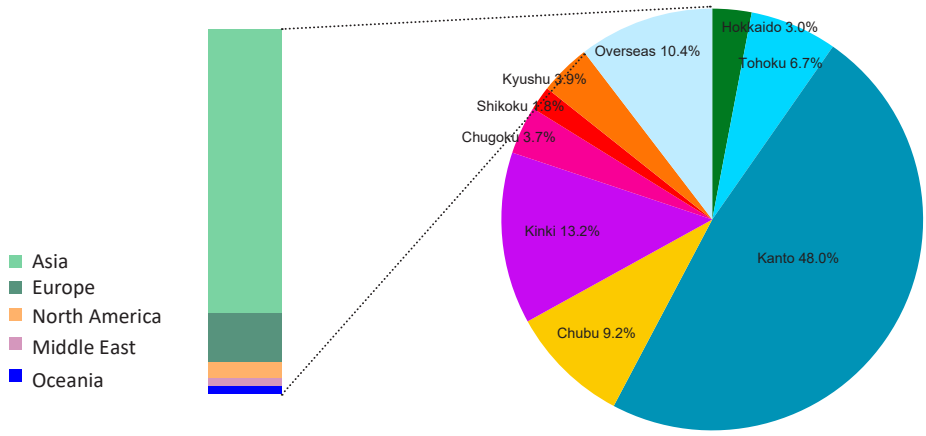

Figure 10: Regional distribution of the spokespersons of proposals accepted in FY2014. We corrected the pie chart on 2019/09/02.

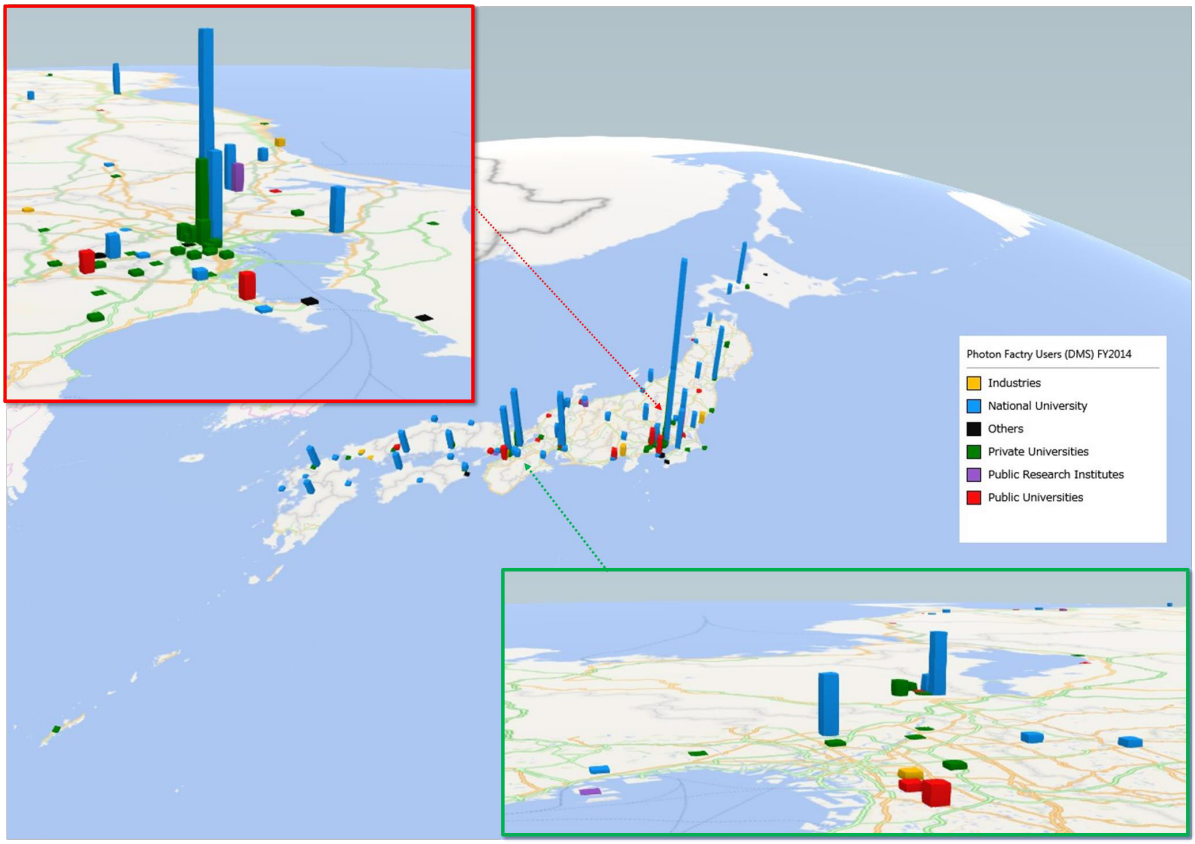

Figure 11: Geographical distribution of Photon Factory users in FY 2014 (domestic users only).

3 Accelerator Updates

3-1 Upgrade of Insertion Devices

In the PF ring, two variable polarized undulators (U#13, U#28) were installed in February 2015, and were commissioned in April 2015.

U#13 provides soft X-rays from 50 to 2000 eV for surface chemistry users. Above 270 eV, U#13 can operate in horizontal, vertical, and elliptical polarization modes. The specifications of U#13 are listed in Table 1 and its calculated spectral brilliance is shown in Fig. 1. A photograph of U#13 in the PF ring is shown in Fig. 2.

U#28 is devoted to users of high-resolution angle-resolved photoelectron spectroscopy. The photon energy from 30 to 300 eV is covered by the first harmonics of the undulator radiation. U#28 can operate in both horizontal and vertical polarization modes. The specifications of U#28 are listed in Table 2 and its calculated spectral brilliance is shown in Fig. 3. A photograph of U#28 in the PF ring is shown in Fig. 4.

Table 1: Specifications of undulator U#13.

Period length (mm)	76.0
Number of periods	47
Total length (mm)	3572
Minimum Gap (mm)	23.0
Maximum Ky (Kx) value	5.28 (3.65)
Maximum field By (Bx) (T)	0.74 (0.51)

Table 2 : Specifications of undulator U#28.

Period length (mm)	160
Number of periods	22
Total length (mm)	3520
Minimum Gap (mm)	27
Maximum Ky (Kx) value	4.93(4.93)
Maximum field By (Bx) (T)	0.33(0.33)

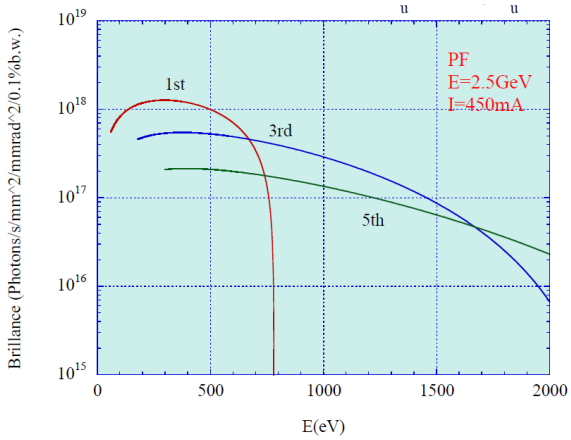

Figure 1: Spectral curves in an elliptical polarization mode of Bx/By=1/2.

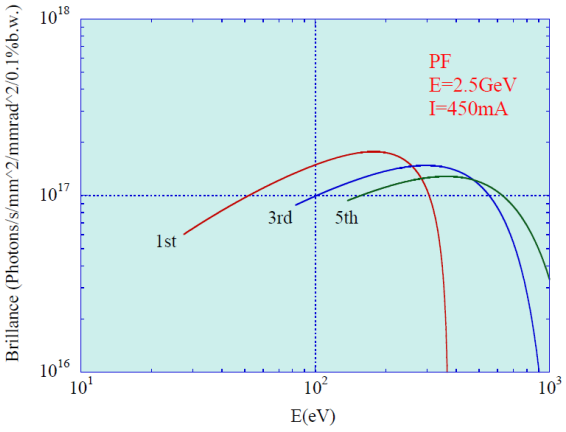

Figure 3: Spectral curves in both a horizontal and a vertical polarization mode.

Figure 2: U#13 in the PF ring.

Figure 4: U#28 in the PF ring.

3-2 Upgrade of Beam Position Monitor Circuit of PF-AR

The existing beam position monitor (BPM) circuits have been in use for more than thirty years since the construction of the PF-AR. Four detection circuits were placed at four different locations in the north, south, east, and west areas. Signals from four pick-up electrodes of the BPM were collected by switching coaxial relays connected to the electrodes. Thus, it took 10–20 s for a one-orbit measurement by the BPM system, making it impractical to apply the BPM system to various beam orbit adjustments. Moreover, in the BPM system, it was impossible to make an orbit correction during the acceleration period from 3 GeV to 6.5 GeV.

In FY2013, the BPM circuit was upgraded and a one-to-one connection between the signal circuit and one of the four electrodes of the BPM was adopted. All the new circuits were installed by August 2014 and operations commenced in October 2014. A component of the new BPM circuit is shown in Fig. 5. Figure 6 shows an example of measurement of the dispersion function; the horizontal axis corresponds to the location of the BPM, and beam position signals, which are proportional to the energy deviation, from all the 83 BPM units are displayed.

The one-orbit measurement time of 100 ms by the new BPM system is a significant improvement over that of the old system, which had a measurement time of 10–20 s. In other words, the new system is more than 100 times faster than the old one, enabling orbit correction to be made during the acceleration period. At present, the new system works efficiently during user operation, so synchrotron users benefit by obtaining a stable light source position.

Figure 5: A part of the new beam position circuits installed into the standard rack.

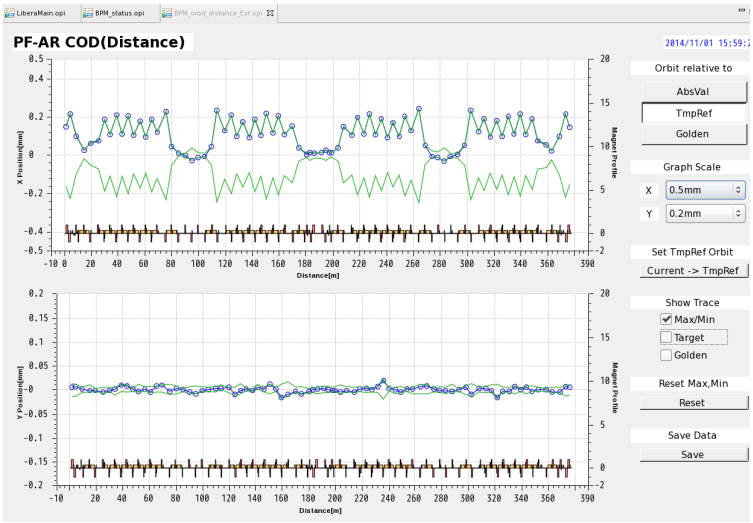

Figure 6: The graphical user interface (GUI) of the new BPM system. The horizontal axis indicates the location of the BPM along the entire ring circumference and the vertical axis indicates the measured beam position. The upper and lower graphs express the horizontal and vertical beam positions, respectively. The blue line with circles denotes the latest beam position, updated every 0.1 s, while the green line denotes the minimum and maximum orbit deviations during the measurement. The GUI can switch an absolute measurement mode into a relative one for a reference orbit. The figure shows an example of orbit measurement; the relative beam position just before and after the RF frequency change represents the dispersion function of the ring.

4 Research Groups and Beamline Updates

4-1 Overview

The Photon Factory (PF) is an outstanding research facility that harnesses accelerator technology to provide bright light for users. The facility utilizes the light so researchers can see the fundamental structure, composition and behavior of materials, on scales ranging from the atomic to the macroscopic with a level of detail, speed and accuracy not possible using conventional laboratory-based equipment. The PF supports a broad range of high-quality research and leads to major advances in energy production, environmental remediation, nanotechnology, new materials and medicine. Our advanced techniques and dedicated staff contribute directly to scientific advances and industrial innovations.

The PF has carried out the beamline refurbishment program since 2006, in which the main strategy is to concentrate investments mainly on insertion-device beamlines. With the upgrade of the 2.5-GeV PF ring for extending straight sections, the long and medium straight sections have been lengthened so that state-of-the-art insertion devices can be installed to cover the vacuum ultraviolet and soft X-ray regions. In addition, four short straight sections have been newly produced for allowing the installation of short-period and small-gap undulators to supply well-focused hard X-rays.

Beamline developments over the past year have mainly focused on the above-mentioned beamlines for improving the reliability, speed of operation, quality of data acquired, and the ability to reach new areas of scientific impact. Despite continuous improvements in efficiency, demand for beamtime exceeds supply on some beamlines, which reflects the continued expansion of our researcher community. There is a great need to expand the range of techniques to meet the oversubscribing demands of the user community.

At our facility, it is the expertise and dedication of all of our staff that maximizes the productivity from highly specialized equipment. Our people are a diverse group with expert skills in such areas as high-level research and development in materials and biological sciences including R&D projects for future light sources, beamline engineering and technical support, computing and control systems, user safety, user liaison and public relations (Table 1). The current status and future prospects of the groups at the PF are summarized below.

Table 1: Research groups in synchrotron radiation I and II (see Fig. 2 in p.114).

Group Name	Group Leader	Group Description
Electronic Structure	H. Kumigashira	This Group is studying the electronic structures of materials to reveal the origins of the properties of those materials and to design their functionalities by using photoelectron spectroscopic techniques such as photoemission spectroscopy and X-ray absorption spectroscopy. In order to conduct state-of-the-art research, we are developing high-performance beamlines and instruments with high brightness insertion devices in the VUV and soft X-ray regions.
Condensed Matter	H. Nakao	This Group is investigating the static structure of materials by means of precise X-ray crystal structural analysis, resonant X-ray scattering, magnetic X-ray scattering, and X-ray imaging. In addition, we are studying the dynamic structure of materials via a pump-and-probe experiment that uses a synchrotron radiation pulse. Our research has expanded from fundamental high-pressure properties to Earth and planetary science by a combination of high-pressure X-ray measurements. In addition to our research, we are optimizing beamlines and experimental devices to promote our research and are developing research methods that use next-generation light sources

Group Name	Group Leader	Group Description
Materials Chemistry	M. Kimura	This Group is developing and providing the observational technology required for chemistry that contributes to the production of materials and substances that improve daily life, and expanding the research and use of this technology in other fields. Taking into consideration next-generation light sources, we are conducting research that uses observational technology, including X-ray absorption fine structure (XAFS) spectroscopy and scattering and chemical-state imaging, in collaboration with industry, academia, and the government. Currently, we are involved in various projects such as “structural materials for innovation” under the Cross-ministerial Strategic Innovation Promotion Program (SIP) by the Cabinet Office and Accelerated Innovation Research Initiative Turning Top Science and Ideas into High-Impact Values (ACCEL) of Japan Science and Technology Agency (JST).
Life Sciences	T. Senda	This Group is conducting life science researches with synchrotron radiation in the fields of 1) structural biology, 2) X-ray imaging, and 3) radiology. These activities range from atomic to organ level researches and reveal connections between the structures and functions of biological components.
Slow Positron	T. Hyodo	The positron is the anti-particle of the electron. This Group uses a slow positron beam created by a dedicated 55-MeV linac for researches in solid state, surface, and atomic and molecular physics. The stations in operation are for positronium negative ion research, positronium-time-of-flight spectroscopy, and total-reflection high-energy positron diffraction (TRHEPD) for the surface structure
Beamline Engineering, Technical Service & Safety	N. Igarashi	The mission of this Group is to develop and construct advanced synchrotron radiation instrumentation and use it safely. Specific tasks are: 1) Development and construction of synchrotron radiation beamlines 2) R&D Study of experimental apparatus and detectors 3) R&D Study of beamline control system 4) Safety control for synchrotron radiation experiment
User Support and Dissemination	K. Hyodo	This Group works as the liaison to users and public relations. The major missions are: 1) Management of the whole peer-review process of the research proposals. 2) Analysis of the statistics related to user activities. 3) Dissemination of research outputs to public.
Advanced Detector R&D Working Group	S. Kishimoto	This Group aims to develop new detectors for materials structure science: 1) a high spatial-resolution and high-speed readout area detector for synchrotron X-rays, 2) an ultra-high-speed high-time-resolution X-ray detector, and 3) a pulse-counting detector with a fast response in the soft X-ray region with position and energy resolutions.
Ultrafast Dynamics Working Group	J. Adachi	This Group is pursuing the possibility of utilizing short-pulse X-rays which will be produced by the future light source, and is conducting R&D on establishing the technical platform for ultrafast dynamics experiments in the femtosecond time domain. To achieve this purpose, we are conducting time-resolved experiments at the PF and PF-AR, and carrying out R&D.

4-2 Electronic Structure Group

4-2-1. Construction of new wide-energy range VUV & SX beamline BL-2 "MUSASHI"

The new beamline BL-2 (MUSASHI: Multiple Undulator beamline for Spectroscopic Analysis on Surface and Hetero Interface) is designed for wide energy-range spectroscopic analysis including X-ray photoelectron spectroscopy, angle-resolved photoemission spectroscopy, and X-ray absorption spectroscopy. The new BL-2 has two types of undulators in tandem alignment; one is designed for the vacuum ultraviolet (VUV) region (30–300 eV), and the other for the soft X-ray (SX) region (250–2000 eV). Consequently, relatively wide energy-range light while maintaining high brilliance and high energy resolution will be available in this beamline by the combination of the two undulators and a variable-included-angle varied-line-spacing plane-grating monochromator (VLS-PGM). Moreover, in BL-2B, an additional double-crystal monochromator (DXM) is built into this branch beamline to have the energy range of 2000–4000 eV available using the wiggler mode of the SX undulator.

At the end of FY2013, a new VUV undulator was installed (Fig. 1) and the operation of both SX and VUV optics was available from FY2014. Figure 2(a) shows a photoabsorption spectrum of N_2 molecules obtained with the SX undulator and optics. The fitting result by Voigt functions, with Gaussian width of 29 meV and Lorentzian width of 117 meV, indicates that the SX optics of the new BL-2 beamline achieve a resolving power of more than 10,000 that of the old BL-2C beamline [1]. In addition, Fig. 2(b) shows a photoionization spectrum of double excited He obtained with the VUV undulator and optics. The minimum peak width of 3.0 meV in the $(2,0)_{18}$ resonance peak is obtained, indicating that the VUV optics of the BL-2 beamline achieve a resolving power of more than 20,000, which is comparable to VUV undulator beamline BL-28 [2]. Thus, we can perform spectroscopic experiments using both VUV and SX light with high energy resolution at the new BL-2 MUSASHI. The completed version of this beamline will be opened for users in FY2015.

REFERENCES

[1] M. Watanabe, A. Toyoshima, Y. Azuma, T. Hayaishi, Y. Yan, A. Yagishita, *Proc. SPIE* **3150**, 58 (1997).
[2] http://pfwww.kek.jp/users_info/station_spec/bl28/bl28a.html

Figure 1: Photograph of two undulators U#02-1 (for SX) and U#02-2 (for VUV) for BL-2.

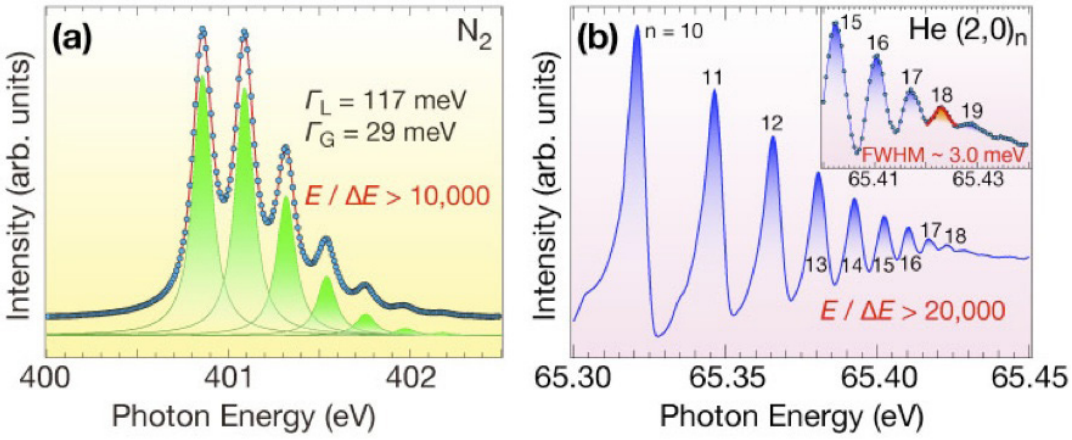

Figure 2: (a) 1sσ→π* photoabsorption spectrum of N_2 molecules and the fitting result by Voigt functions. (b) The photoionization spectrum of autoionizing resonance state $(2,0)_n$ of double excited He.

4-2-2. BL-13A/B: Variable polarization beamlines for VSX spectroscopy

An APPLE-II undulator was installed for BL-13A/B in February 2015. User experiments using horizontally linear and elliptically polarized SR began in May 2015. Vertically linear and circularly polarization modes will be available in the near future. Figure 3 shows typical undulator spectra in the horizontally linear polarization mode with the ρ/2 parameter of 0 mm measured at BL-13A. Photon intensity increases by about one order of magnitude in comparison with the BL-13A with the previous undulator.

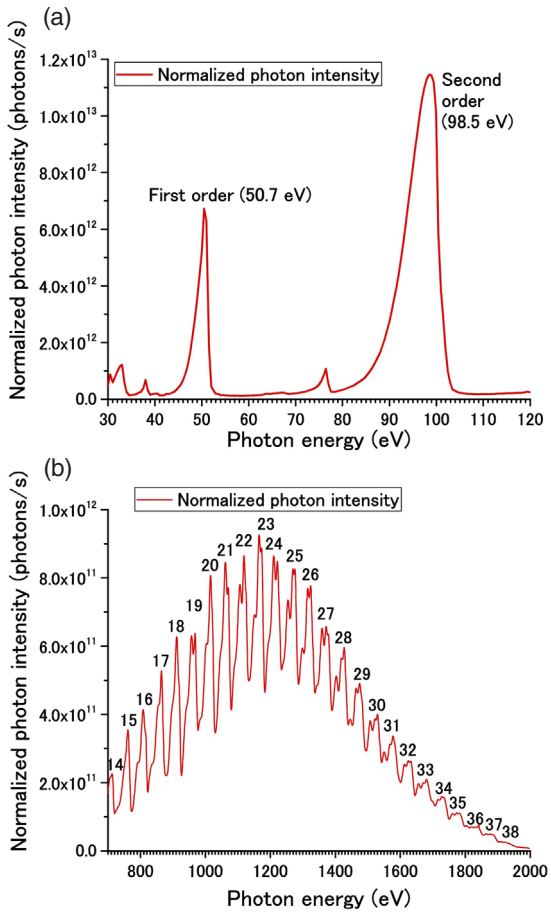

Figure 3 (a), (b): Typical undulator spectra in the horizontally linear polarization mode with the ρ/2 parameter of 0 mm measured at BL-13A. The small peaks at 33, 38, and 76.5 eV derive from higher order harmonics.

4-2-3. Upgrade of an undulator in beamline BL-28 for polarization-dependent angle-resolved photoemission spectroscopy

The optics of BL-28 were reconstructed as a high-performance spectroscopic beamline dedicated to angle-resolved photoelectron spectroscopy (ARPES) in the vacuum ultraviolet (VUV) region in 2006. At the end of FY2014, the undulator of BL-28 was replaced with a new one having six variable rows of magnetic arrays. The new undulator provides linear-horizontal, linear-vertical, and circular polarization states of radiation in the VUV energy region from 30 eV to 300 eV (Fig. 4). These variable polarization modes enable us to perform a state-of-the-art polarization-dependent ARPES, which will be available step-by-step for users from FY2015.

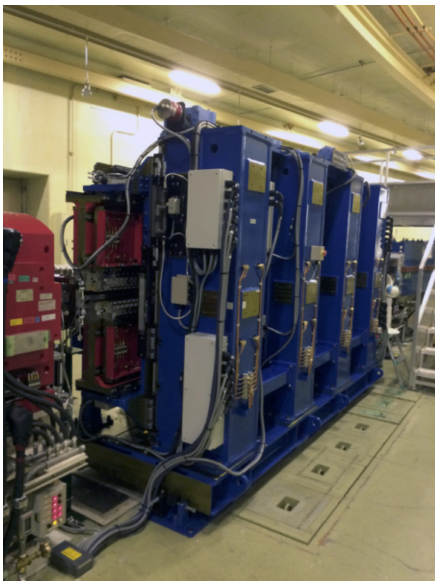

Figure 4: Photograph of the new undulator installed at BL-28.

4-3 Condensed Matter Group

4-3-1. Development of an in-vacuum diffractometer for resonant soft X-ray scattering

The strong correlation between electrons in solids plays very important roles in the electric and magnetic properties of the ordering states of orbital, charge, and spin degrees of freedom. The study of these electronic ordering states is essential to understand phenomena microscopically. Resonant X-ray scattering (RXS) at the *K*-edge is a powerful tool for observing the spatial ordering of charge and orbital degrees of freedom in 3*d* transition metal oxides. The RXS signal at the *K*-edge reflects the 4*p* electronic state. On the other hand, the RXS at the $L_{2,3}$-edge can probe the 3*d* electronic state directly, and the signal of resonant magnetic scattering is strongly observed at the $L_{2,3}$-edge in *d* electron systems. Moreover, the RXS at the *K*-edges of O, S, and P ions, which play a key role in itinerancy through hybridization with the metal ion, also becomes observable using soft X-rays.

We have developed a new in-vacuum diffractometer as shown in Fig. 5 to carry out Resonant Soft X-ray Scattering (RSXS) experiments. We have succeeded in drastically improving the signal-to-noise ratio of the RSXS signals using a slit and silicon drift detector with good energy resolution in a large vacuum chamber as shown in Fig. 5(b). The diffractometer was installed in the beamlines BL-16A and BL-11B at the Photon Factory, and was commissioned. Utilizing the dif-

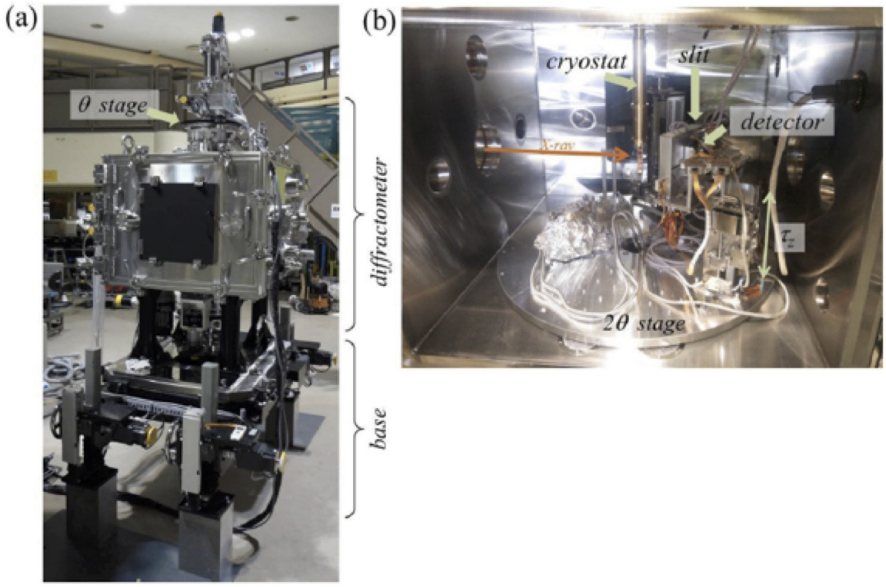

Figure 5: (a) New in-vacuum diffractometer and the alignment base. (b) Inside of the vacuum chamber. The stages, cryostat, and detector system are shown.

fractometer, not only RXS but also X-ray absorption spectroscopy measurements have been carried out to elucidate the electronic states, and the ordering of the charge, spin, and orbital states in strongly correlated electron systems such as transition metal oxides. We have also constructed a soft X-ray diffractometer with a 7.5-T superconducting magnet in order to study ordered electronic structures under high magnetic field. This diffractometer was used to detect the RSXS signals of $(LaMnO_3)_3(SrMnO_3)_3$ superlattice with a remarkable negative magnetoresistance effect under a 7 T magnetic field. We have succeeded in observing the difference of RSXS spectra corresponding to reversal of the Mn 3*d* magnetic moment.

4-3-2. Condensed Matter Research Center (CMRC)

The CMRC pursues cutting-edge research on condensed matter science through the comprehensive use of multiple probes: synchrotron light, neutron, muon, and slow positron. The Condensed Matter Group is partly involved in the CMRC, and is producing crucial scientific outputs mainly using synchrotron light. The CMRC consists of four groups: the correlated electron matter group, the surface/interface group, the matter under extreme conditions group, and the soft matter group. These groups have been promoting nine bottom-up projects: 1. Hybridized Orbital Ordering, 2. Geometrical Correlation, 3. Molecular Crystals, 4. Oxide Heterostructures, 5. Surface/interface Magnetism, 6. Extreme Conditions, 7. Soft Matter, 8. Hydrogen, and 9. Surface Structure and Electronic States. In addition, the CMRC is conducting two types of Ministry of Education, Culture, Sports, Science and Technology (MEXT) project: the Element Strategy Initiative to Form a Core Research Center, and the Photon and Quantum Basic Research Coordinated Development Program. In these national projects, the CMRC members are focusing on the Element Strategy Initiative for Electronic and Magnetic Materials, and Tribology with Muons and Neutrons.

4-4 Materials Chemistry Group

4-4-1. Status of beamlines managed by MCG

Our group operates the beamlines and experimental stations of BL-9A, BL-9C, BL-12C, BL-15A1, AR-NW10A, and AR-NW2A. These BLs are mainly dedicated to XAFS experiments, and are widely available for academic and industrial users. In addition, we support BL-4A for XRF experiments, which are operated by the microbeam XRF users group. The following experimental apparatuses have been recently installed at the BLs: an automated in situ experimental condition setup system (auto in situ system) at BL-9C, automatic 100 samples measurement system at BL-12C, and 21-element Ge pixel array detector (21Ge-PAD) at AR-NW10A. The auto in situ system at BL-9C enables us to set measurement conditions such as gas atmosphere, temperature and heating speed. H_2, O_2, CO, and NO gases are available with N_2 and He as balance gases. With the automatic 100 samples measurement system at BL-12C, we can measure up to 100 samples sequentially without sending any commands. Fluorescence yield measurements with the 21Ge-PAD at AR-NW10A enable us to study samples containing diluted elements of relatively high-energy absorption edges, especially higher than 18 keV. These apparatuses will attract researchers at corporations, not only in academia.

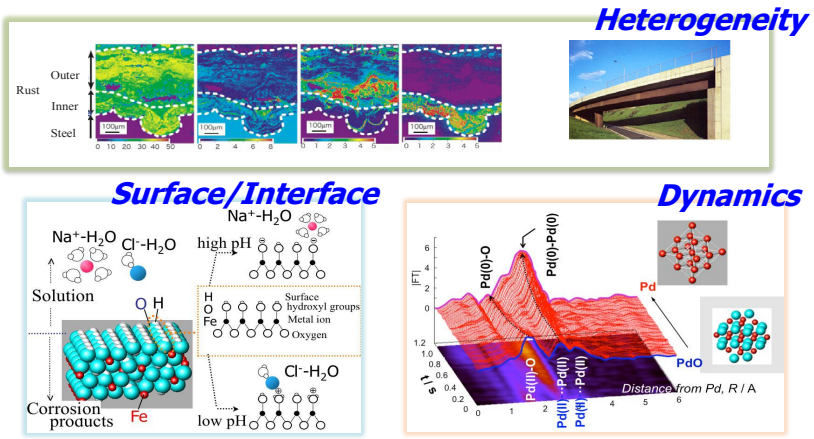

Figure 6: Target of the Materials Chemistry Group.

One of our most important missions is to develop experimental methods and to perform cutting-edge science, in addition to the maintenance and improvement of BLs as outlined above. Recently, we designated three important fields of science: heterogeneity, dynamics, and surface/interface (Fig. 6). BL-15A1 creates a semi-micro beam (ca. 20 μm) for mapping of chemical states using X-ray Absorption Spectroscopy (XAS) and crystal structures using XRD, and is suitable for studying the heterogeneity of various samples. Also, we plan to install a scanning transmission X-ray microscope (STXM). STXM at BL-15A1 enables us to observe samples with a spatial resolution of ca. 30–200 nm for elements with edges of between ~2–15 keV. Quick XAFS (QXAFS) measurement systems are available at each BL except AR-NW2A. The dispersive XAFS (DXAFS) measurement system is available at AR-NW2A, and we intend to promote dynamic studies by improving the DXAFS system. We have developed the laser pump–DXAFS probe method, paving the way for a new field of dynamics research. We have also developed a new surface-sensitive XAFS measurement method, the named Kramers-Kronig reflection XAFS (KK-XAFS) method. This is a relatively easy way to obtain surface-sensitive XAFS spectra by detecting signals of total reflection. The reflection spectra are transformed to “absorption” spectra based on Kramers-Kronig relations. The method is useful for studying the evolution of surface states during chemical reactions. The method can be combined with the DXAFS system, and thus fast dynamics studies of surfaces in the hard X-ray energy region will emerge.

4-5 Life Sciences Group

4-5-1. Structural Biology Research Center (SBRC)

The SBRC is playing a major role in a national project of structural biology, Platform for Drug Discovery, Informatics, and Structural Life Science (PDIS), which was launched with the support of MEXT in FY2012. The platform consists of three cores, “Structural Analysis”, “Regulation”, and “Informatics”. The SBRC has been leading the Structural Analysis core. With the support of the PDIS project, the SBRC has improved BL-1A for sulfur-based single-wavelength anomalous diffraction (S-SAD), which is a new phasing method in protein crystallography. We are also developing a standard experimental protocol for S-SAD data collection. For small-angle X-ray scattering (SAXS) experiments, a solution sample changer was installed in BL-15A2 and a new program for SAXS experiments, SAngler, has been developed. BL-17A for protein crystallography was extensively upgraded in FY2014 with supplementary budget. The optical layout was modified and a new X-ray detector, Pilatus S6M, was installed. Pilatus S6M, which is a pixel array detector with a large active area (423.6 × 434.6 mm^2), has short readout time (2.03 msec) and a high frame rate (25 Hz at maximum), enabling us to perform shutterless data collection and fine-phi slice data collection.

4-5-2. Upgrade of macromolecular crystallography beamline, BL-17A

BL-17A is one of the macromolecular crystallography beamlines at the Photon Factory. The beamline was constructed as the first short-gap undulator beamline at the Photon Factory in 2006, and thanks to this light source and dedicated optics, BL-17A was characterized as a beamline for diffraction experiments with small crystals [1]. Since the beamline was opened to general users, it has contributed to a large number of significant achievements on important biological problems. However, the recent trend in macromolecular crystallography is moving to much more difficult targets, and so users’ demands for the beamline have become much higher. In 2014, we upgraded the beamline to deliver a much more highly focused beam at the sample position and installed a new diffractometer and detector in the end station.

For this upgrade, the optical layout needed to be changed in order to achieve a more focused beam at the sample position. Several layout plans were con-

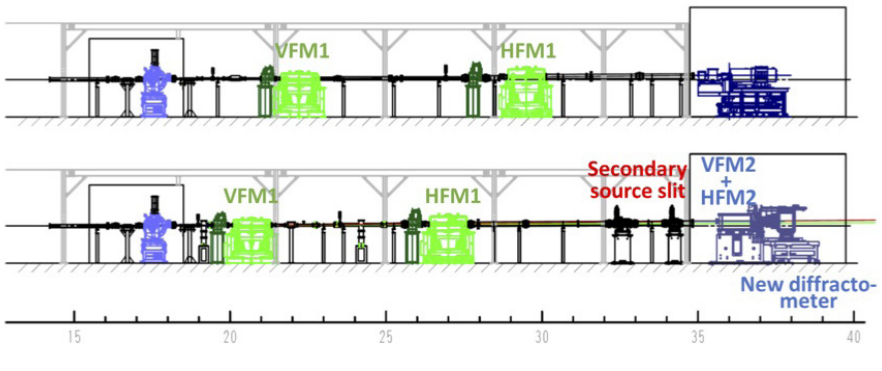

Figure 7: Optical layout of BL-17A before (upper) and after (lower) the upgrade.

sidered and we finally decided to employ a secondary source approach (Fig. 7) [2]. In this plan, the existing two mirrors which were used to focus the X-ray beam to the sample position vertically and horizontally, respectively, are moved upstream to make the secondary sources upstream of the end station. New bimorph KB mirrors are installed just upstream of the sample position to focus the beam from the secondary source to the sample position. Ray-trace simulation suggested that the beam size becomes much smaller with reasonable divergence (Fig. 8).

As the beam size decreases, the stability of each optical component becomes more important. Any small movements in the optical components may affect the beam intensity at the sample position, and therefore great care was taken to ensure the stability of the optical components. All newly installed devices have heavy granite base tables to damp the vibration transmitted from the floor. Particular sections of the experimental floor where the monochromator and mirrors are installed, were dug up and refilled with thicker reinforced concrete (Fig. 9).

The changing of optical layouts and installation of new devices will be finished in April 2015. After the

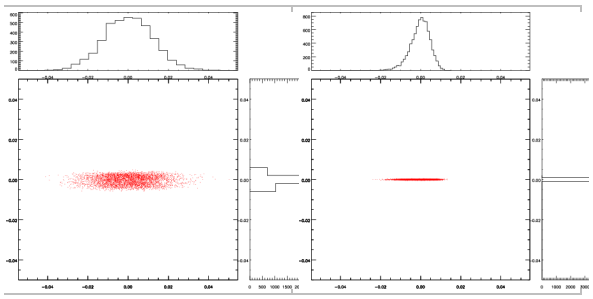

Figure 8: Ray-trace simulation of BL-17A with optical layouts (a) before and (b) after the upgrade. The beam sizes and divergences (H × V) are 284 × 52 μm^2 and 0.39 × 0.096 mrad^2, respectively, before the upgrade and 86 × 8.4 μm^2 and 1.47 × 0.7 mrad^2, respectively, after the upgrade.

beamline is commissioned, which is scheduled to be performed in May 2015, the beamline will be opened for general academic and industrial users in June 2015.

REFERENCES

[1] N. Igarashi, N. Matsugaki, Y. Yamada, M. Hiraki, A. Koyama, K. Hirano, T. Miyoshi, and S. Wakatsuki, *AIP Conference Proceedings*, **879**, 812 (2007).

[2] J. L. Smith, R. F. Fischetti, and M. Yamamoto, *Curr. Opin. Struct. Biol.*, **22**, 602 (2012).

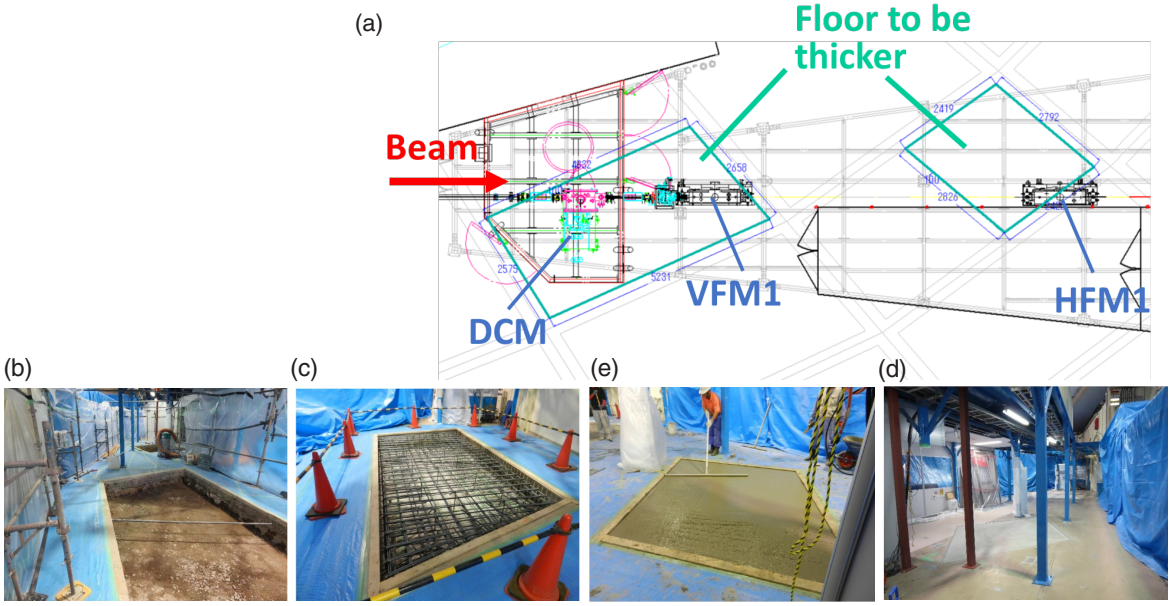

Figure 9: Reinforcement of experimental floor. (a) Sections of the experimental floor to be reinforced. (b)–(e) photographs of the reinforcement work.

4-5-3. New BL-10C: The result of commissioning

BL-10C is a small-angle X-ray scattering (SAXS) beamline. This beamline has been used for over 30 years from 1984. In FY2013, we scrapped and rebuilt it to replace almost all the components [1]. We then optimized and aligned the components in May 2015. We saw the first beam on the fluorescence screen monitor after the renewal on May 16 (Fig. 10). Figure 11(a) shows the photon flux at the sample position. Users can basically use X-ray energies from 6.5 to 14 keV. It is necessary to change the glancing angle of the focusing mirror to use energies below 6.5 keV because of the cutoff of the higher-order X-rays. Since the beam position moves only 0.03 mm in this energy range when changing the X-ray energy, users can easily change the energy without tuning by using the GUI software [Fig. 12(b)]. The energy is calibrated at 1.488 Å (Ni-K edge) as before. Figure 12 shows the beam shape at the focal position. The beam size is V0.18 × H0.63 mm (FWHM). The theoretical value of the beam size is V0.15 × H0.59 mm by raytracing. Therefore, the beam size is almost identical to that calculated by raytracing. Figure 13 shows the scattering pattern of a standard sample, silver behenate, measured at the condition of 1.488 Å and 1 m camera length. BL-10C was opened to users in June 2014.

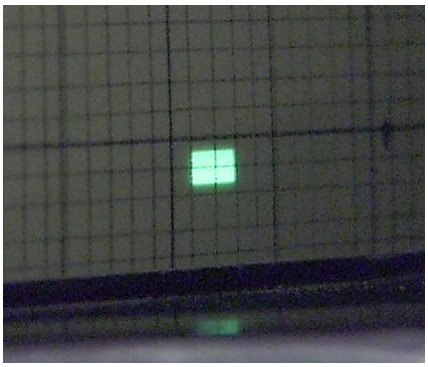

Figure 10: The first beam seen behind the monochromator.

REFERENCE

[1] *Photon Factory Activitiy Report 2013* **#31**, A 70 (2014).

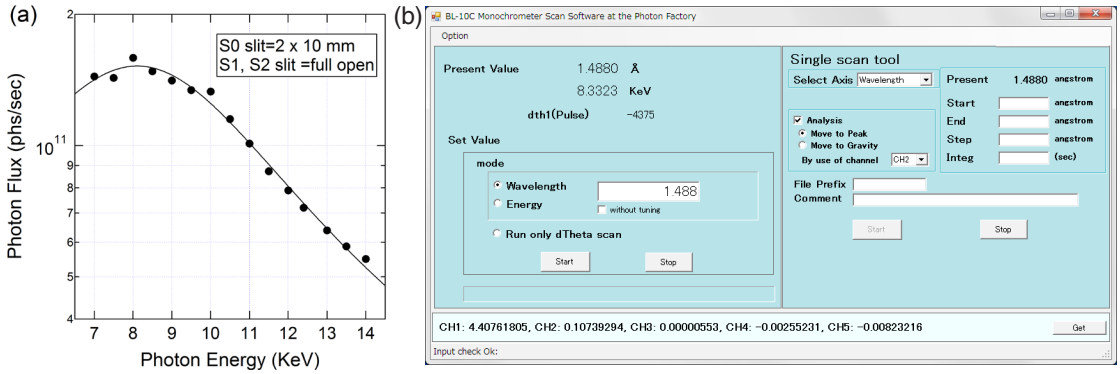

Figure 11: (a) Photon flux at the sample position, (b) GUI software for changing the measurement X-ray energy developed.

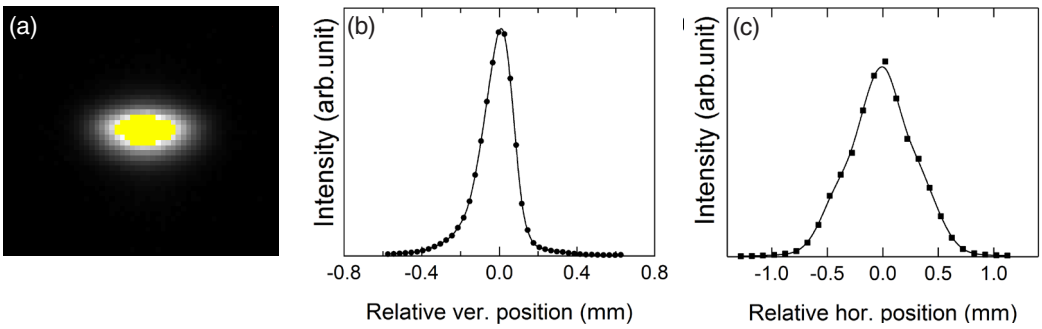

Figure 12: (a) Beam shape at the focal position recorded on the flat-panel detector (C10013SK, Hamamatsu). The X-ray beam was attenuated by 0.1 mm of Cu, (b) and (c) The line profiles in the vertical and horizontal directions, respectively. These profiles were calculated with the results of one-direction scanning of the slit blade.

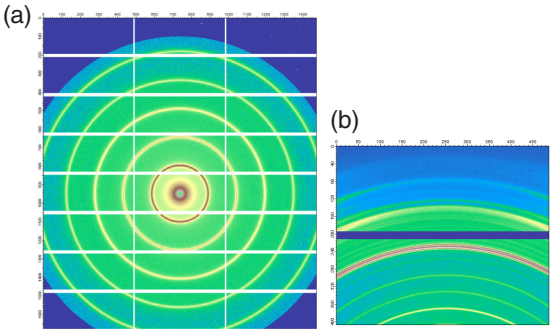

Figure 13: The scattering pattern of silver behenate (d = 58.38 Å). (a) SAXS, (b) WAXD.

4-6 Life Sciences and Materials Chemistry Groups

4-6-1. BL-15A, dedicated to semi-microbeam XAFS/XRF/XRD and high-brilliance SAXS/GISAXS studies

As reported previously, the construction of the new undulator beamline BL-15A was completed in FY2013. This beamline has a tandem beamline arrangement for both XAFS/XRF/XRD studies using semi-microfocus beams (station A1) and SAXS/GISAXS experiments using collimated softer and hard X-rays (station A2). At station A1, the semi-microfocus beams available in a wide range of photon energies (2.1–15 keV) allow analysis of the local structures of the elements and valence for inhomogeneous samples in the fields of environmental science and new energy source science. A new simultaneous XAFS/XRF/XRD measurement system was developed for grid-pattern element mapping and in situ experiments with the combined use of XAFS/XRF and XRD [Fig. 14(a)]. At station A2, the collimated beams are used for structural studies of functional membranes, large hierarchical structure analysis of soft matter and high-throughput solution structure determination of biological systems. Two experimental stages, a conventional SAXS/WAXS stage and a low-energy GISAXS stage, are placed in tandem in the station and a vacuum-compatible X-ray area detector, PILATUS3 2M, is equipped [Fig. 14(b, c)]. The detector is directly connected to the GISAXS stage and low-energy GISAXS experiments of up to 2.1 keV can be performed without any filter in a vacuum environment.

The first beams were introduced into both stations in FY2013. We subsequently started the alignment of beamline optics and the characterization of beam performance. The beam profiles at the three focal points, 32.8 m, 36.75 m and 42.75 m from the source, are shown in Fig. 15. The undulator spectra and the photon flux were measured and the results are almost consistent with the ray-tracing simulation. Next, we conducted commissioning experiments in the spring of 2014. Figure 16 shows some results of these experiments, XANES mapping analysis of the reduction of sintered ores at the Fe K-edge (station A1), the diffraction pattern from a dried chicken tendon and the GISAXS image from diblock PS/PMMA copolymers in a vacuum environment (station A2). The results were promising. After the commissioning experiments, BL-15A was opened to users in the autumn of 2014.

REFERENCE

[1] N. Igarashi, N. Shimizu, A. Koyama, T. Mori, H. Ohta, Y. Niwa, H. Nitani, H. Abe, M. Nomura, T. Shioya, K. Tsuchiya, and K. Ito, *J. Phys: Conf. Ser.*, **425** (2013) 072016.

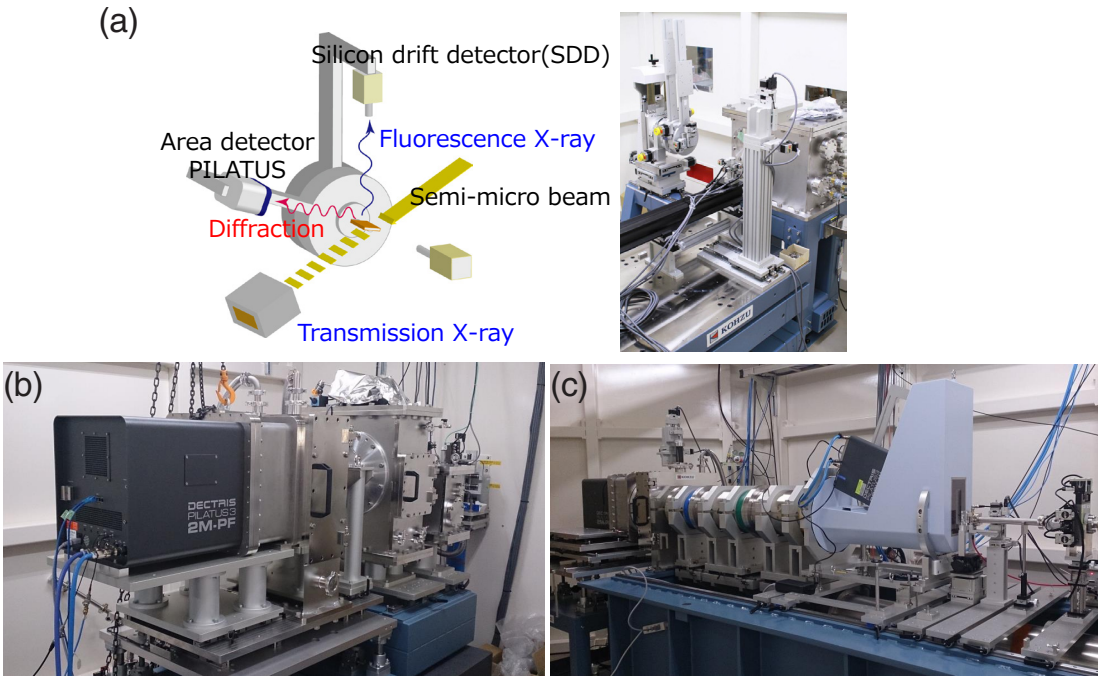

Figure 14: (a) Measurement geometry and simultaneous XAFS/XRF/XRD measurement system in station A1. (b) Low-energy GISAXS stage in the upstream of station A2. (c) Conventional SAXS/WAXS stage in the downstream of station A2.

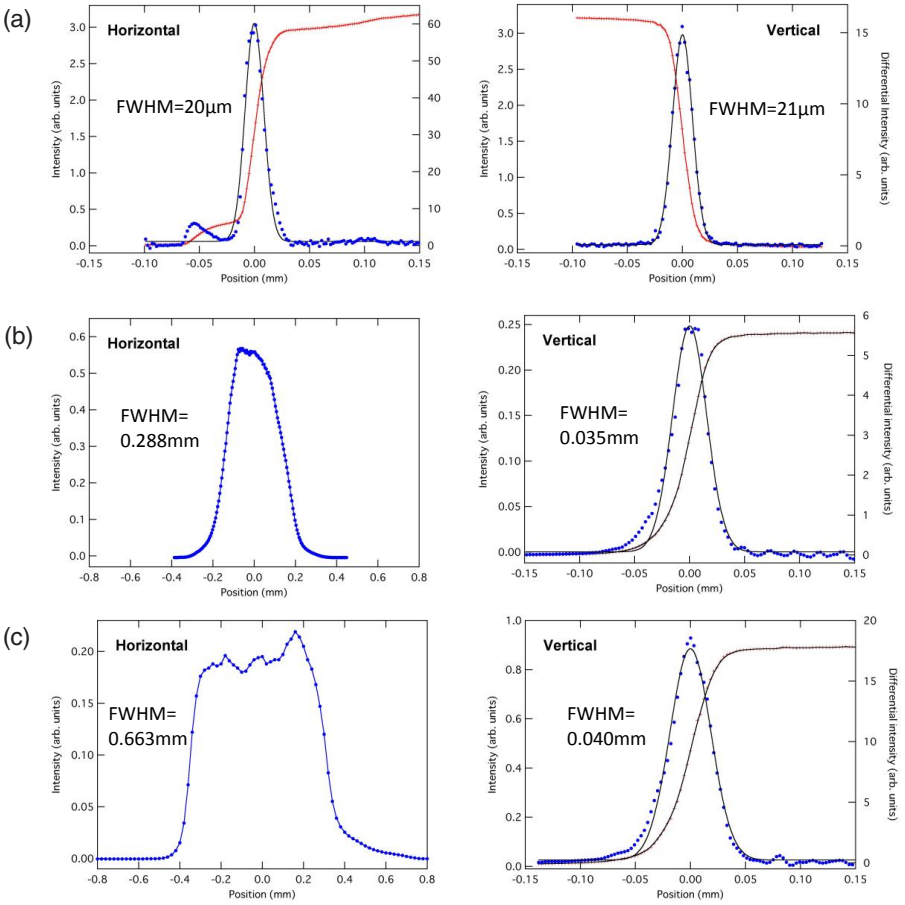

Figure 15: Beam profiles at three focal positions (10.4 keV, 0.1 mm width of the secondary light source): (a) Station A1 at 32.8 m, (b) GISAXS stage at 36.75 m and (c) SAXS/WAXS stage at 42.75 m.

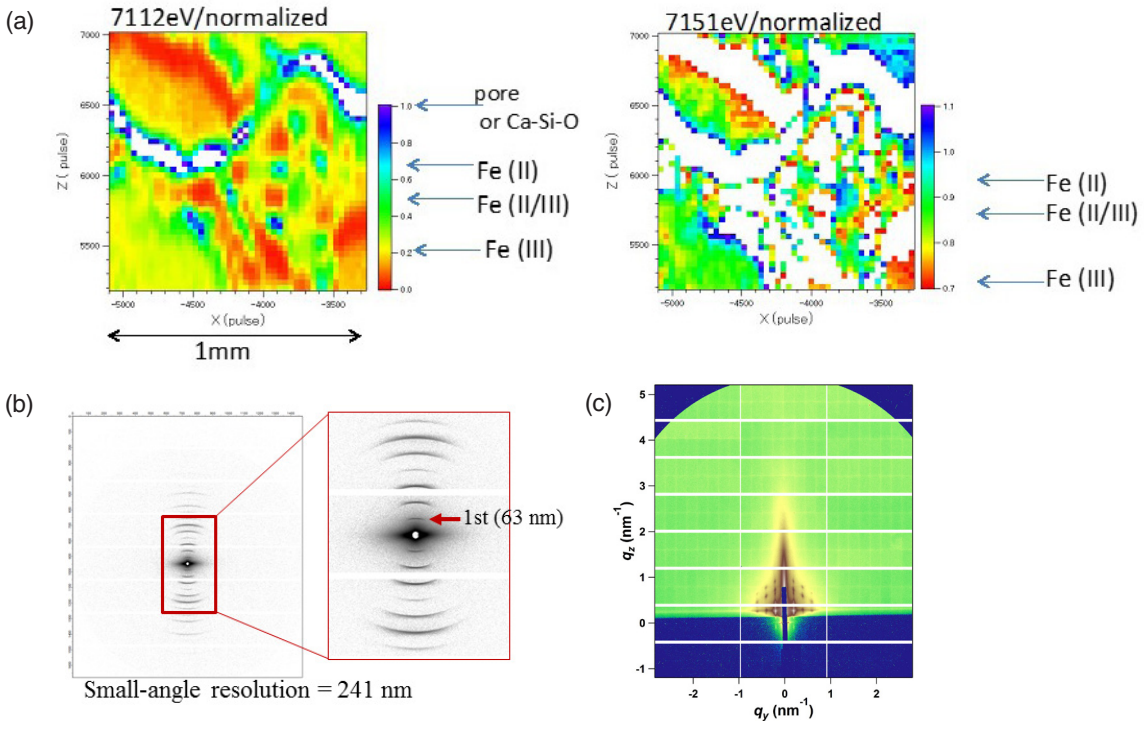

Figure 16: Commissioning experiments. (a) Station A1: XANES mapping analysis of reduction of sintered ore at the Fe K-edge in transmission mode (courtesy of Dr. Reiko Murao, Nippon Steel & Sumitomo Metal Corporation). The beam size is 20 μm square and the step size is 40 μm. (b) Diffraction pattern from a dried chicken tendon. The X-ray energy is 10.4 keV and the sample–detector distance is 3657 mm. (c) GISAXS image from diblock PS/PMMA copolymers. The X-ray energy is 3.6 keV and the sample–detector distance is 825 mm.

5 cERL

5-1 Introduction

KEK established an Energy Recovery Linac (ERL) Project Office in April 2006. Because a GeV-class ERL machine had not been constructed anywhere in the world, it was necessary to first construct a compact ERL (cERL) with an energy of 35 MeV that could be used for the development of several critical accelerator components such as a high-brilliance DC photocathode electron gun and superconducting cavities for the injector and main accelerator. In FY2013, the components of cERL were successfully installed in an ERL test facility and the energy recovery beam operation was successfully demonstrated. Figure 1 shows the bird's eye view of the cERL and Fig. 2 shows a photograph of the cERL accelerator in radiation shielding.

The following three targets were set for FY2014. First, with regard to beam development, a small emittance should be maintained during operation; two, achieving beam current operation at 100 μA, and three, production of the laser Compton scattering (LCS) X-ray system with the collaboration between KEK and JAEA.

Beam development was carried out from May until the end of June 2014. It was possible to maintain normalized beam emittance below 0.17 μm rad at 0.02 pC/bunch, and 0.8 μm rad at 7.7 pC/bunch at the injector part. At the recirculation loop of the ERL operation, normalized beam emittance was obtained as 0.14 μm rad at 14 fC/bunch. Therefore, beam development at the small bunch charge was successfully demonstrated during FY2014. Beam development at a high bunch charge is set as a target for FY2015. During the beam operation from January to March of 2015, higher beam current operation of ~80 μA was carried out without any issues regarding radiation safety until March 2015 (the end of FY2014) as shown in Fig. 3. For FY2015, the beam current will be increased gradually up to 1 mA. Beamline and laser systems for LCS production were installed between July and December 2014. The LCS signal was successfully obtained by mid-February and the application of the LCS on X-ray imaging was demonstrated. In the following sections, the above-mentioned topics will be discussed in detail.

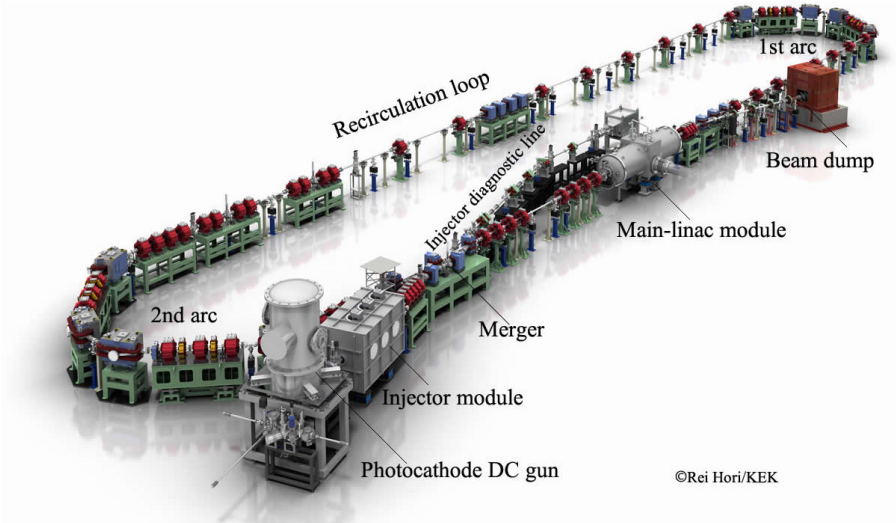

Figure 1: Bird's eye view (CG) of the cERL.

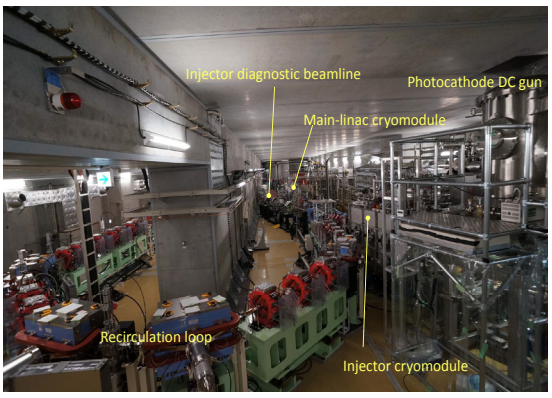

Figure 2: cERL accelerator in the radiation shielding.

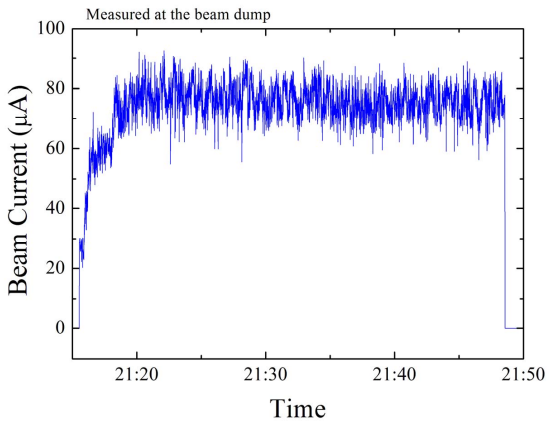

Figure 3: Successful demonstration of a beam current of ~80 μA.

Another important milestone of FY2014 was that the "Foundation for High Energy Accelerator Science" presented the "Suwa Award" to the cERL accelerator construction team for the "Construction and beam acceleration demonstration of performance by the test accelerator aimed at core technology establishment of energy recovery linac" [1]. Figure 4 shows the picture of the members of the team present at the award ceremony.

Figure 4: Picture of a part of the cERL construction team members at the "Suwa Award" ceremony in mid-February 2015.

5-2 Recirculation and Beam Tuning in the cERL

5-2-1 Overview of the operation of the cERL

The principal parameters of the cERL are given in Table 1. Figure 5 shows the statistics of beam operation time, (the time for which the beam was on) during FY2013–2014 [2]. The first continuous-wave (CW) beams of 20 MeV were successfully transported through the recirculation loop in February 2014 [3, 4]. After the commissioning of operation, various accelerator studies have been carried out. They include the establishment of start-up tuning, correction of beam optics, study on beam losses [5], and measurements of beam emittances in a recirculating loop. In the summer of 2014, the authorities requested a change in the maximum beam current (from 10 μA to 100 μA), and the approval was received in September.

Table 1: The principal parameters of the cERL.

	Design	In operation
Beam energy	35 MeV	20 MeV
Injector energy	5 MeV	2.9-6 MeV
Normalized emittance	0.1 μm rad@7.7 pC 1 μm rad@77 pC	under study
Beam current	10 mA	80 μA

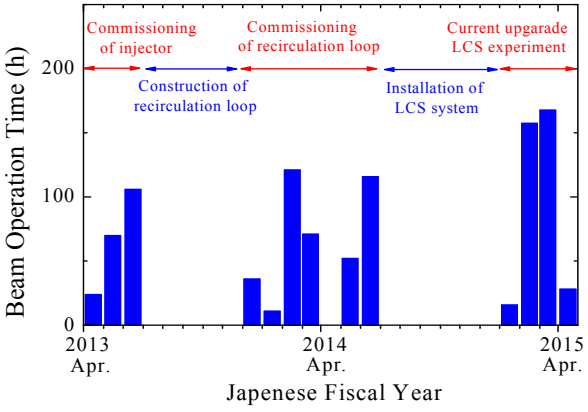

Figure 5: Statistics of beam operation time per month.

From September to December 2014, an LCS system was installed. The LCS system aims to demonstrate technology for future high-flux γ-ray sources [6, 7] and to develop advanced X-ray imaging technology using compact accelerators [8, 9]. The LCS system consists of an optical cavity resonator, a 1064 nm drive laser, an X-ray beamline, and an experimental hut. The LCS system was operated from February to April 2015. Accelerator issues related to the LCS system are reported in Sec. 2-4. The commissioning results of the LCS system are primarily reported in [7, 9].

5-2-2 Beam Development

A layout of the cERL is shown in Fig. 6. Thirty fluorescent screens are used to measure both the positions and profiles of beams at low average currents. Forty-five stripline beam position monitors (BPMs) are used to measure beam positions non-invasively. Beam currents are measured at the beam dump point and at the gun power supply by subtracting offset currents. They can also be measured using three movable Faraday cups along the beamline.

During machine tuning, low-intensity macropulse beams were produced by the photocathode DC gun with a cathode voltage of 390 kV. The typical parameters of the beam pulses were as follows: macropulse width of 1.2 μs, macropulse repetition rate of 5 Hz, and bunch frequency of 1.3 GHz.

First, we set up the injector beams. The RF phases in three injector cavities were adjusted to on-crest acceleration while a buncher cavity was turned off. The beams were steered at the centers of two solenoids and of the first injector cavity. The total energy of the injector beams was adjusted to 2.9 MeV. Next, we steered beams through a three-dipole merger and main linac (ML) cavities. The RF phases in ML cavities were then adjusted to on-crest acceleration, which yielded total beam energy of 19.9 MeV.

We transported beams through the first arc, the south straight section, and the second arc. The beams were steered at approximately the centers of major quadrupoles while changing the strength of each quadrupole and monitoring the beam positions downstream. The recirculated beams passed further through an injection chicane where a dipole kick due to a merger dipole is canceled by the other two dipoles. We set the momentum ratio of the recirculated beam to the injected beam to be 7:1. The momentum ratio should be larger than 6:1 because of the finite aperture in the injection chicane.

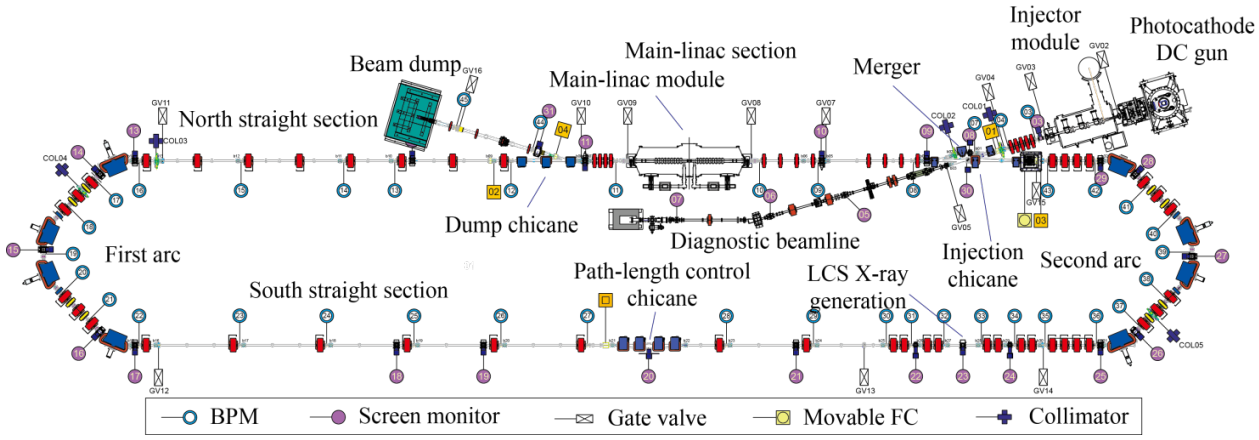

Figure 6: Layout of the cERL. The blue and red symbols denote dipole and quadrupole magnets, respectively.

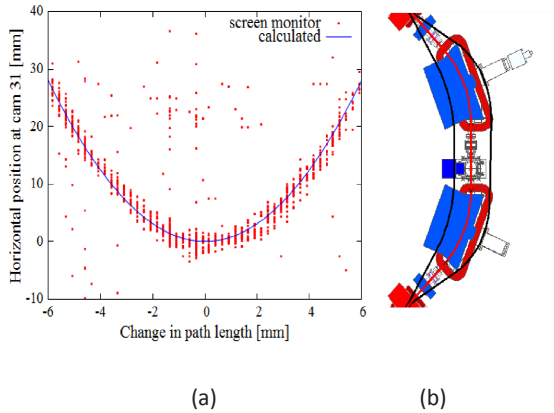

Figure 7: Tuning of decelerating phase. (a) Horizontal beam positions at the dump line as a function of the path length and (b) path length control in the second arc.dipole and quadrupole magnets, respectively.

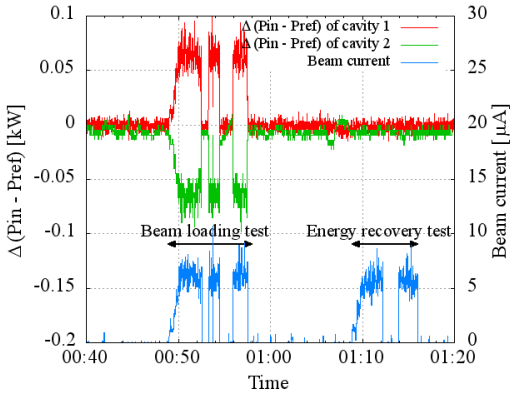

Figure 8: Demonstration of energy recovery in the ML cavities. Differences in the input and reflected RF powers are shown for the ML cavity 1 (red) and 2(green).

Both injected and recirculated bunches pass through the ML section between the injection chicane and the dump chicane while they are separated longitudinally by approximately half a RF wavelength. We measured the beam positions using four BPMs to ensure non-invasive measurements. The signals were detected at 1.3 GHz, and the signals from the two beams were separated using their timing difference by a beam-recirculation time of 300 ns. We steered beams in this section using corrector magnets located upstream the injection chicane because the use of correctors in the main linac section affected both beams. This procedure required delicate tuning of beam recirculation.

The recirculated beams decelerated when they passed through the ML cavities. We adjusted an RF phase of deceleration by changing the path length of the recirculation loop, as shown in an example in Fig. 7. The path length was changed by an orbit bump in the second arc section, shown in Fig. 7(b). The corresponding momenta of decelerated beams were measured at a screen in the dump line. The path length was adjusted so that the momenta require a minimum value. The path length can be changed by ±10 mm in each arc, and by ±5 mm in a path-length control chicane. The former method was mainly used because the latter chicane produced some hysteresis in the beam orbit. We found that an initial path length was very close (within a few mm) to the optimum one.

Figure 8 shows a demonstration of energy recovery in the ML cavities under CW operation. First, we conducted a non-ERL operation by reversing an RF phase in the downstream (ML2) cavity. A 2.9-MeV beam was accelerated and decelerated in ML1 and ML2 cavities, respectively, and was transported directly to the dump. Under this operation, both positive and negative beam loadings were observed in the ML1 and ML2 cavities, respectively. However, under the usual ERL operation, we observed little beam loading in these cavities.

Beam emittances were measured using the quadrupole-scan method. We varied the field strength of a single quadrupole located upstream a screen and measured beam sizes. Measurements at four locations showed that the normalized emittances could be preserved through the ML and the first arc at low bunch charges. For example, horizontal and vertical normalized emittances were both 0.14 μm rad just after the first arc at a bunch charge of 14 fC/bunch (macropulse beam). At a medium bunch charge of 0.5 pC, the normalized emittances of ε_{nx} = 0.41 μm rad (horizontal) and ε_{ny} = 0.3 μm rad (vertical) were obtained after several tunings [10].

5-2-3 100 μA beam current operation

Small beam losses are essential to realize the high-current operation. To this end, careful beam tuning and optics matching were carried out. To control beam losses, beam collimators were used. There are five collimators, and each of them has four movable copper rods cooled by water. A collimator at a merger section (E = 2.9 MeV, η_x= 0.23 m) was found to be very effective to eliminate beam tails or halos with a modest increase in radiation. To avoid problems caused by large beam losses, we used a fast interlock system for stopping the gun laser when large signals were detected at the beam loss monitors [11].

At the end of FY2014, we succeeded in transporting the maximum beam current of 80 μA to the beam dump. Operational parameters included beam energies of 19.9 MeV at the loop and 2.9 MeV at the merger, a bunch repetition rate of 162.5 MHz, a bunch charge of 0.5 pC, and beam optics for the LCS experiment.

5-2-4 Tuning for Laser Compton Scattering (LCS)

In an operation for the LCS experiment, electron beams are focused to a very small size (typically, 30 μm rms) at an interaction point (IP) where the electron bunches collide with laser pulses. Beam losses in the LCS section should be minimized to avoid undesirable background radiation to detectors. Therefore, there is a tradeoff between small beam size and small beam losses close to the IP. Figure 9 shows an example of low-β optics in the LCS section. In this design, beam sizes at the IP are expected to be σ_x^* = 21 μm (horizontal) and σ_y^* = 33 μm (vertical) using measured normalized emittances of ε_{nx} = 0.47 μm rad and ε_{ny} = 0.39 μm rad at a bunch charge of 0.5 pC.

The tuning procedure established for the beam optics in the LCS section is as follows. First, we designed K-values of quadrupoles containing some errors. After the optics matching before the LCS section, we scanned the K-value of quadrupole QMLC04, shown in Fig. 9, and measured beam sizes using a screen monitor at the IP. While observing the response curves, we adjusted the K-values of QMLC03 so that both horizontal and vertical beam sizes (σ_x, σ_y) had waists at the same K-value as QMLC04. The latter was determined so that both σ_x and σ_y took minima. After the tuning, we obtained beam sizes of σ_x^* = 13 μm and σ_y^* = 25 μm at the IP, which were estimated from the Q-scan measurement.

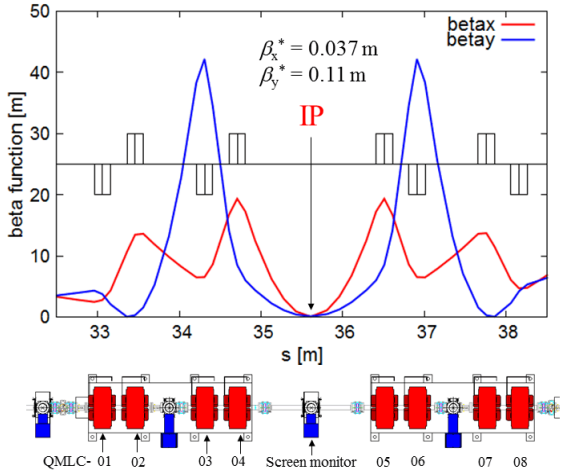

Figure 9: Design of low-β optics in the LCS section.

Using the "LCS optics" mentioned above, we succeeded in transporting the beam to the dump with small beam losses. We used a bunch repetition frequency of 162.5 MHz that was matched to the frequency of the LCS laser. After we adjusted both the positions and the phases of laser pulses, we succeeded in colliding the electron bunches with laser pulses at a bunch charge of 0.5 pC in CW operation and found that an average current value was approximately 80 μA. As a result, we observed a 6.9 keV X-ray signal at the end of the X-ray beamline using a detector [8, 10]. The typical count rate was 1200 counts/s in a detector with a diameter of 4.66 mm at a beam current of 58 μA at the experimental hut, located far from the IP of 16.6 m as shown in Fig. 10. The success of sustained collision between beam and laser demonstrated both high quality and high stability of cERL beams.

The LCS X-ray imaging was carried out by the setup shown in Fig. 11(a). The resulting X-ray image is shown in Fig. 11(b). This image was obtained by 10 min accumulation to achieve sufficient statistics. Due to the small source size of LCS X-rays, it is possible to perform refraction contrast imaging [12] that allows enhancing the edges of X-ray imaging. The detector was positioned 2.5 m from the specimen. Since the transmittance of a 7 keV X-ray in the air is low, the tube filled with He gas was placed between the beryllium window and the detector. The transmittance of the 7 keV X-rays in He is almost 100%. Therefore, it was possible to obtain the high contrast X-ray image shown in Fig. 11(b).

5-3 Conclusion

Various accelerator studies are in progress in the cERL. We have achieved the maximum beam current of 80 μA in CW operation. The successful beam-laser collisions demonstrated both high quality and high stability of cERL beams. In FY2015, we will study lower-emittance operation at high bunch charges, higher beam currents, bunch compression, and higher X-ray flux in the LCS experiment.

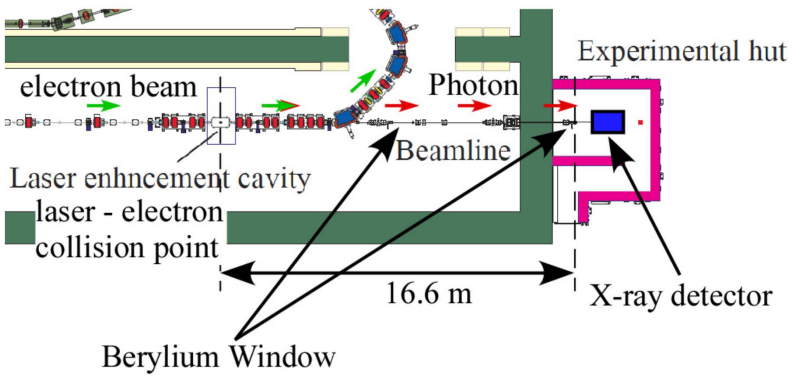

Figure 10: Schematic view of the layout of the LCS beamline.

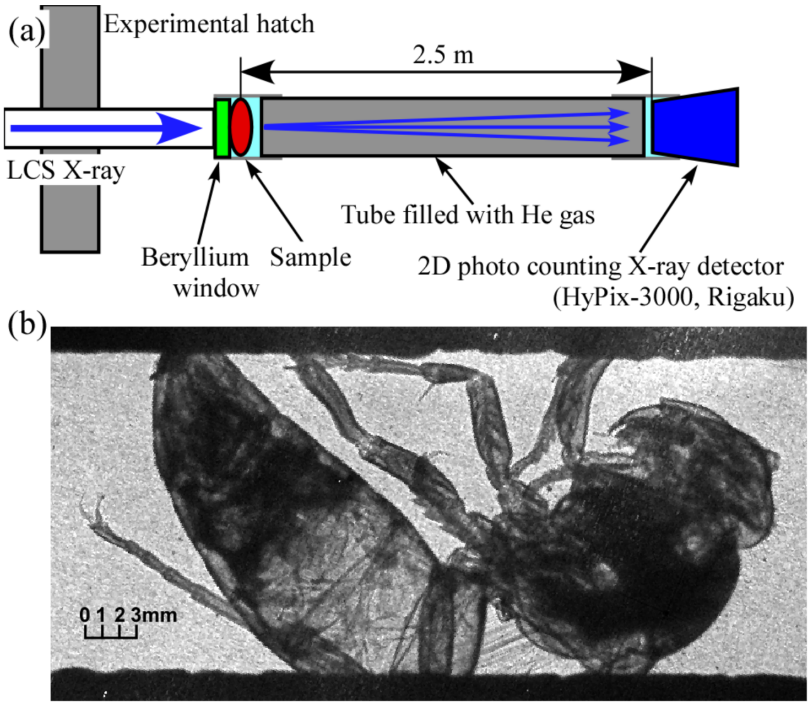

Figure 11: (a) Schematic layout of the LCS X-ray imaging experimental setup and (b) the LCS X-ray hornet imaging.

REFERENCES

[1] http://www.heas.jp/award/h26zyusyou.html (10 March, 2015, in Japanese)
[2] S. Sakanaka, *et al.* , *Proc. of IPAC'*15, TUBC1(2015).
[3] N. Nakamura, *et al.*, *Proc. of IPAC'14*, 353 (2014).
[4] S. Sakanaka, *et al.*, *Proc. of LINAC'14*, 599 (2014).
[5] O. Tanaka, *et al.*, *Proc. of IPAC'*15 ,TUPWA068 (2015).
[6] R. Nagai, *et al.*, *Proc. of IPAC'*14, 1940 (2014).
[7] R. Nagai, *et al.*, *Proc. of IPAC'*15, TUPJE002 (2015).
[8] T. Akagi, *et al.*, *Proc. of IPAC'*14, 2072 (2014).
[9] A. Kosuge, *et al.*, *Proc. of IPAC'*15 ,TUPWA066 (2015).
[10] T. Miyajima, *et al.*, *Proc. of IPAC'*15, TUPWA067 (2015).
[11] R. Takai, *et al.*, *Proc. of IBIC* 2014, MOCYB2 (2014).
[12] S. W. Wilkins, T. E. Gureyev, D. Gao, A. Pogany, and A. W. Stevenson, *Nature* **384**, 335 (1996).

6 Graduate School Education

KEK is one of the basic organizations of the Graduate University for Advanced Studies (SOKENDAI), and has the School of High Energy Accelerator Science, which consists of three departments: Accelerator Science, Materials Structure Science, and Particle and Nuclear Physics. The majority of the PF staff members are in charge of giving lectures and supervising graduate students of the Department of Materials Structure Science. SOKENDAI offers a five-year PhD course for undergraduate students and a three-year PhD course for master's degree holders. The School of High Energy Accelerator Science held its "open campus day" for young researchers and undergraduate students at the Tsukuba campus on July 8, 2014 and half-day guidance meetings for potential young candidates in June 21, 2014 and March 7, 2015 at Tokyo. Figure 1 is a photo of Prof. Toshiya Senda of the PF, who explains what is "Structural Biology" by using synchrotron radiation at the guidance meeting in March 7, 2015. Another topic of FY2014 for SOKENDAI was that Dr. Renzhong Tai, who was graduated SOKENDAI at 1999 and now is a deputy director of Shanghai Syncrotron Radiation Facility (SSRF), visited at the Academic Exchange Sessions of SOKENDAI during the period of the graduation ceremony at March 24, 2015, After the session, Dr. R. Tai visited to the photon Factory and gave us the seminar talk about the "present status of SSRF". Figure 2 is a photo of Dr. R. Tai at the seminar.

Figure 1: A snapshot of a guidance.

Figure 2: A snapshot of a seminar.

The PF has also a system for Joint PhD (JPHD) students, who are accepted by the PF to pursue advanced studies under the supervision of PF staff members towards their PhD degrees in collaboration with their home universities. The numbers of graduate students of SOKENDAI and JPHD during the past fifteen years are listed in Table 1.

In addition to the SOKENDAI and JPHD graduate students, a number of doctoral theses were written based on research carried out at the PF. Figure 3 shows the statistics of such graduate students. We are afraid that the decrease of operation time may have some influence on the decline since 2011 (ref. p.79) of the number of students who obtain doctoral degrees based on scientific activities at the PF.

Table 1: Number of SOKENDAI and JPHD students at the PF over the period 2000-2014. Number of October 1 at each year.

FY	SOKENDAI	JPHD
2000	8	12
2001	10	8
2002	13	13
2003	15	7
2004	14	5
2005	13	6
2006	9	10
2007	6	13
2008	6	10
2009	6	9
2010	5	10
2011	4	5
2012	3	6
2013	4	7
2014	3	7

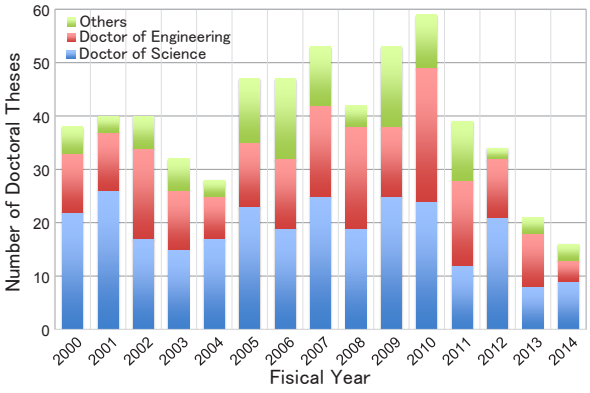

Figure 3: Number of students who obtained doctoral degrees based on scientific activities at the PF.

7 Projects

The Photon Factory is conducting a wide variety of national projects. This section outlines some of the currently running projects.

7-1 Elements Strategy Initiative to Form Core Research Center

The national project "Elements Strategy Initiative to Form Core Research Center" was started in 2012. The Photon Factory has especially been committed to two research fields of the Elements Strategy Initiative: electronic and magnetic materials. The project aims to develop entirely new materials that use ubiquitous elements. In the Elements Strategy Initiative for Electronic Materials, the aims are to develop materials based on successful experience though it is sometimes far away from conventional development policy, and to pioneer electronic materials to create new guidelines for material design using harmless elements to open up new fields of material science. The project members research the crystal, local, electronic, and magnetic structures of new functional materials using synchrotron radiation, muon and neutron sources. Meanwhile, the goals of the Elements Strategy Initiative Center for Magnetic Materials are: (1) laboratory-scale synthesis of mass-producible high-performance permanent magnets without using critical rare-earth elements for the next generation and (2) framework-building and provision of basic science and technology for industrial R&D. To achieve these goals, the project members focus on theoretical research and mining of new permanent magnet materials, and simultaneously pursue various processing technologies to improve the existing high-performance permanent magnet materials through cooperative activities in the three research fields of computer physics, structural and property characterization, and material processing.

7-2 Platform for Drug Discovery, Informatics, and Structural Life Science (PDIS)

Crystallography with synchrotron X-ray has been the most successful method for determining the high-resolution structures of proteins and their complexes. In Japan, the Photon Factory (PF) and Structural Biology Research Center (SBRC) have played leading roles in structural life science and have supported a number of scientific achievements, including two structural genomics projects since 2002. The SBRC has now been leading the third national project in the field.

The Platform for Drug Discovery, Informatics, and Structural Life Science (PDIS) has been supported by the Ministry of Education, Culture, Sports, Science & Technology (MEXT) and then the supporting organization was taken over by the Japan Agency for Medical Research and Development (AMED) in April 2015 (http://www.pford.jp/). In the project, all life scientists, both in academia and industry, have a chance to be supported by leading scientists with a variety of expertise through a single proposal if it is approved. They can also use facilities such as the PF and SPring-8. The plan is for the PDIS to become a critical research hub for all researchers who are interested in using structural information in their own research projects.

The platform is composed of three cores: structural analysis (Kaiseki), control (Seigyo), and information (Joho). The structural analysis core covers bioinformatics, protein production, and structural analysis. The core office has been located in the SBRC since April 2015 and the Center has also organized the structural analysis core. The Center has supported users through a pipeline with a high throughput crystallization system, synchrotron X-ray beamlines for structure determination as well as consulting for users' structural biology projects. It has also been developing a state-of-the-art environment for optimal data collection and data processing in protein crystallography and in small-angle X-ray scattering.

The Center is actively utilizing other structural biology techniques such as NMR and electron microscopy to collect as much structural and dynamic information as possible. The Center will work together in order to establish and support a better research environment for structural life science in Japan.

7-3 Cross-Ministerial Strategic Innovation Promotion Program (SIP)

The Cross-ministerial Strategic Innovation Promotion Program (SIP) [1] was established by the Council for Science, Technology and Innovation (CSTI) of the Cabinet Office in order to realize scientific and technological innovation strategically under its initiative in 2014. SM^{4}I (Structural Materials for Innovation) [2] is one of the 10 R&D subjects of the SIP that is planned

for the period from October 2014 to March 2019, with the participation of 72 major research groups in the field (industry: 27, university: 35, public (non-profit) institutions: 10 in FY2014). The TIA-nano consortium of AIST, NIMS, Univ. of Tsukuba and KEK joined the SM^{4}I project as Unit D66 - Innovative measurement and analysis for structural materials (SIP-IMASM), in which advanced analytical techniques are being researched and developed for structural materials for aerospace in the following four areas: (1) stress and cracks, (2) light and additional elements, (3) interfaces and microstructures, and (4) defects.

Members of IMSS of KEK take advantage of analytical techniques using synchrotron radiation and positron beams to characterize structural materials for aerospace such as ceramic coating, steel, nickel-alloy, and fiber-reinforced polymer (FRP). We focus on revealing the heterogeneity in microstructures and chemical states simultaneously using various techniques such as X-ray absorption fine structures (XAFS), X-ray diffraction (XRD), scanning transmission X-ray microscopy (STXM), and computed tomography (CT), and nano-scale defects using positron annihilation. We also plan to install an X-ray transmission microscope (XTM) in the PF-AR for 3D observation of microstructures and chemical states simultaneously with a special resolution as small as 50 nm. We aim to establish a new approach to enable detection of the initiation and propagation of degradation of structural materials for aerospace three-dimensionally using these advanced analytical techniques, through collaboration of the members of SM^{4}I (Fig. 1).

REFERENCES

[1] SIP: http://www.jst.go.jp/sip/index.html
[2] SM^{4}I: http://www.jst.go.jp/sip/k03.html

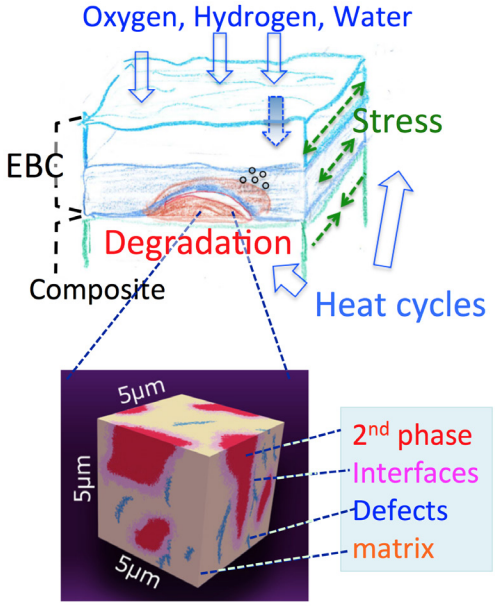

Figure 1: 3D characterization of degradation in structural materials in semi-nano scale.

7-4 Accelerated Innovation Research Initiative Turning Top Science and Ideas into High-Impact Values (ACCEL)

The Photon Factory has taken part in one of the projects of the Accelerated Innovation Research Initiative Turning Top Science and Ideas into High-Impact Values (ACCEL) of the Japan Science and Technology Agency (JST): “Materials Science and Application of Electrides”, which is led by Prof. Hideo Hosono (Tokyo Inst. Tech., JST-ACCEL) and managed by Prof. Toshiharu Yokoyama (JST-ACCEL, Tokyo Inst. Tech.). New electrides have been synthesized by Prof. Hosono’s group, and show low work functions together with thermal and chemical stabilities. The project seeks to apply the functions to develop new electronic and catalytic materials. As for catalysts, the main target is to develop a new process of ammonia synthesis, which works in a relatively mild atmosphere. The Photon Factory staff involved in this project have carried out experiments to characterize the catalysts and to provide feedback to the members synthesizing the catalysts.

7-5 Photon Beam Platform

This program aims to accelerate industrial innovation and enhance the academic activities of Japan through the shared use of advanced research facilities. MEXT has promoted this program since 2005, and deployed two platforms as a part of it since 2013, i.e., the Photon Beam Platform [1] and the NMR Platform.

In this program, the Photon Factory has been actively engaged in two tasks: one is the Trial Use that offers free-of-charge use of the beamlines to introduce new industrial users to the PF, and the other is to chair the Photon Beam Platform as a representative institute. Under the Photon Beam Platform, six synchrotron facilities and two large-scale laser facilities collaborate with each other to offer better services to users, set up general coordinators, conduct public relations campaigns, improve the ease of using the service, and investigate new technologies through the collaboration (Fig. 2).

REFERENCE

[1] http://photonbeam.jp/

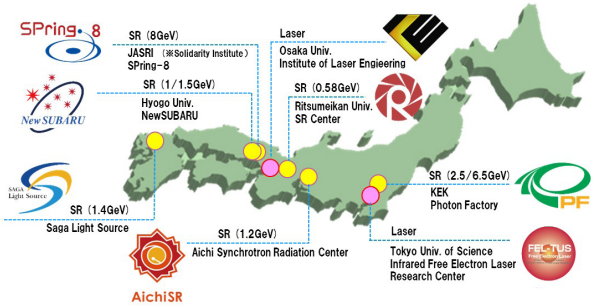

Figure 2: Framework of Photonebeam Platform.

7-6 Nanotech Career-Up Alliance (Nanotech CUPAL)

One of the most crucial missions of the synchrotron facility is to enhance the development of human resources actively involved in the synchrotron radiation community, especially the younger generation. In this context, the Photon Factory has joined the Nanotech Career-up Alliance (Nanotech CUPAL), which was established based on the MEXT projects in 2014.

The Nanotech CUPAL project was originally launched as a ten-year project in collaboration with the Tsukuba Innovation Arena for nanotechnology (TIA-nano) and Kyoto University's Nanotechnology Hub (KUNH) for enhancing the careers of young researchers in the nanotechnology field and improving the mobility of human resources. The alliance comprises "A Institutions", which are responsible for the training of human resources (KUNH and four organizations constituting TIA-nano in the Tsukuba area (National Institute of Advanced Industrial Science and Technology (AIST), National Institute for Materials Science (NIMS), KEK, and University of Tsukuba)) and "B Institutions", ten universities dispatching young researchers to the "A Institutions". The targets are mainly postdoctoral fellows, fixed-term assistant professors, and PhD students who belong to the alliance organizations. Researchers outside the alliance can also join the program by covering part of the costs by themselves.

The "A Institutions" provide various types of training courses related to state-of-the-art nanotechnologies such as ultrafine fabrication processes, micro/nano electro-mechanical systems (MEMS), electron microscope techniques. As a member of TIA-nano, the PF offers opportunities for training on basic synchrotron radiation techniques (X-ray absorption fine structure, small-angle X-ray scattering, powder diffraction and phase-contrast imaging) through on-the-job training at the beamlines. In 2014, four researchers joined the first course, and more participants are expected in the next term (Fig. 3).

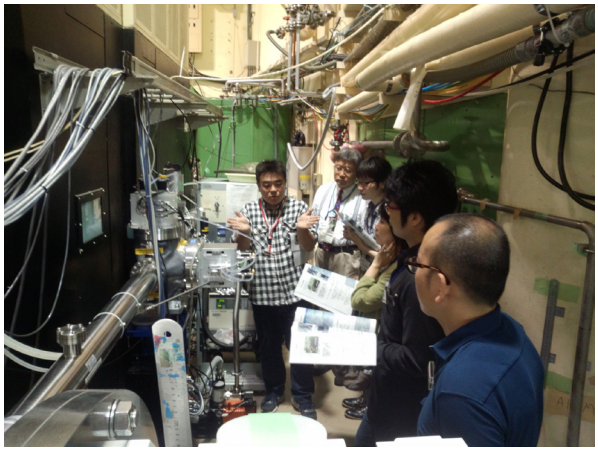

Figure 3: Practice scene of SAXS at BL-10C.

8 International and Domestic Collaboration

8-1 Overview

Since the user community of synchrotron radiation spreads across national boundaries, international discussion and collaboration are becoming more and more important. The Photon Factory has a history of collaborating internationally since the early 1980s, including the successful operation of Australian and Indian beamlines at the PF. The Australian National beamline BL-20B was constructed at the PF by the Australian Nuclear Science and Technology Organization (ANSTO) and was operated from 1992 to 2013. The major activity of the beamline at the PF has now been moved to the Australian Synchrotron in Melbourne, Australia. The Indian beamline BL-18B was leased from the Photon Factory to the Department of Science and Technology (DST), India, and has been operational since 2009. Part of the beamtime is open for domestic users as well. The PF is also collaborating with international synchrotron radiation communities through meetings, workshops, and schools. On the other hand, since KEK was originally established as the first inter-university research institute, collaboration with domestic universities and institutes is one of the major missions of KEK. Based on the supporting funding by KEK, mutual collaboration projects between the PF and domestic organizations are also ongoing.

8-2 Indian Beamline

The Indian beamline BL-18B is leased from the PF to DST, and has been operational since FY2009. This international collaboration between India and Japan has been strongly supported by the leaders of both countries. The Prime Minister of Japan, Mr. Shinzo Abe, and the Prime Minister of India, Dr. Manmohan Singh, signed a Letter of Intent on Scientific and Technological Cooperation between the DST and KEK as a part of the "Joint Statement on the Roadmap for New Dimensions to the Strategic and Global Partnership between Japan and India", which was announced in New Delhi on August 22, 2007. Based on the Letter of Intent, the DST and KEK agreed to set up an Indian beamline at the Photon Factory in 2008, with the Saha Institute of Nuclear Physics (SINP) as a nodal institute of India.

After the Memorandum of Understanding on Scientific and Technological Cooperation was signed in October 2008, the Indian BL office was started at KEK in March 2010. The BL was opened for Indian general users in October 2011, and also opened for non-Indian users in April 2014. The beamline enables various synchrotron radiation measurements including powder diffraction at low and high temperatures, X-ray reflectivity, diffuse scattering from solid and liquid interfaces, and X-ray diffraction of on-line growth and structural characterization of thin films and nanostructures. The numbers of proposals and unique users are gradually increasing as shown in Table 1. Scientific outputs based on BL-18B experiments have been published in refereed journals.

8-3 Cooperation with the SESAME Project

There are over 60 synchrotron radiation facilities in the world, but none in the Middle East. SESAME, which is a major synchrotron radiation facility under construction near Amman (Jordan), will not only be the first light-source in the Middle East, but also the region's first true international center of excellence. Since the SESAME-JSPS Collaboration funding was terminated in FY2013, the commitment from KEK to SESAME was mainly attendance at the SESAME Council meeting in FY2014. The SESAME Council meeting was held in December 2014, and Executive Director of KEK attended the meeting. The Council approved renewed plans for the construction of SESAME which was lost in 2014, due to the collapse of the roof in December 2013 as a result of unusually heavy snowfall in Jordan. The revised plan foresees commissioning starting in mid-2016 with two of the radio frequency cavities and two of the 'day-one' beamlines; the other two cavities and the two other 'day-one' beam lines will be added in 2017 (three more Phase 1 beamlines will be added later).

Table 1: The numbers of proposals and unique users of Indian beamline (BL-18B).

Fiscal year		Number of proposals	Unique users
2009	Jan. 2010 - Mar. 2010	4	7
2010	Apr. 2010 - Mar. 2011	12	18
2011	Oct. 2011 - Mar. 2012	16	26
2012	Apr. 2012 - Mar. 2013	20	38
2013	Apr. 2013 - Feb. 2014	25	45
2014	Apr. 2014 - Dec. 2014	28	51
	total	105	185

8-4 Domestic Collaborations

KEK has a wide variety of collaborations with domestic organizations. Among them, two collaboration meetings related to the PF and domestic organizations were held in FY2014.

Firstly, the 6th collaboration symposium between KEK and Hokkaido University was held in Sapporo on January 28, 2015. The main topics of the symposium were materials science and quantum beams. Speakers from Hokkaido University gave talks on photocatalytic reactions of TiO_2, and newly-designed fluorescence materials. Three speakers from the Institute of Materials Structure Science introduced techniques for materials science using quantum beams such as scanning transmission X-ray microscopy (STXM), neutron inelastic scattering, and muon spin resonance. Applications of novel quantum-beam techniques to brand-new materials developed at Hokkaido University were discussed in the symposium.

Secondly, a collaboration meeting among KEK, the University of Tokyo, and the National Institute of Advanced Industrial Science and Technology (AIST) was held at AIST West Campus in Tsukuba on February 20, 2015 (Fig. 1). The main topics of the meeting were enhancing the careers of young researchers especially in the nanotechnology field. Five young PhD students and postdoctoral fellows from the University of Tokyo and Photon Factory presented their research by talks and posters, and two senior researchers from AIST introduced new research programs at AIST. Young students and postdocs actively joined discussions with each other and with researchers at AIST. KEK and AIST are members of the Tsukuba Innovation Arena for nanotechnology (TIA-nano), seeking various types of collaborations in the field of nanotechnology in Tsukuba, and the secretary general of TIA-nano also briefly introduced the outline of the TIA-nano project.

Figure 1: Snapshot of the poster session in the collaboration meeting among KEK, University of Tokyo, and AIST.

9 Workshops and Seminars

9-1 IMSS Science Festa

The Institute of Materials Structure Science (IMSS) SCIENCE FESTA was held on March 17-18, 2015 at the EPOCHAL Tsukuba with the support of the user community and KEK.

Following two invited talks, entitled “Combination of Nice Cooking and Its Material” by Professor J. Akimitsu and “Molecular and Material Design Strategy for Flexible and Tough Polymers” by Professor K. Ito, three Parallel Sessions and a Poster Session were held on the first day of the FESTA. There were 233 poster presentations from users, with research results presented from 13 S-type and 3 T-type proposals. There were more than 75 presentations from the staff of the Accelerator Laboratory of KEK, Neutron Science Division and Muon Science Division of IMSS, MLF (J-PARC Materials and Life Science Experimental Facility) and the PF staff, resulting in a total of more than 334 poster presentations.

The 32nd PF symposium, the annual users’ meeting, the 6th MLF symposium and the Muon Science Laboratory (MSL) workshop were held simultaneously on March 18, the second day of the FESTA. The FESTA provided an excellent opportunity to exchange a broad range of knowledge in such fields as synchrotron, neutron and muon science and MLF, and was attended by more than 570 users and IMSS staff.

The main purpose of the PF symposium is to discuss the present status and future projects of the PF, and to encourage networking among users and PF staff through scientific presentations and discussions. At the start of the PF symposium, PF staff reported on the recent progress of the facility, including rearrangement of beamlines. We also had a discussion session on PF operation, especially regarding beamtime for users and future light sources.

9-2 PF Workshops

The proceedings of PF workshops and a KEK workshop on synchrotron-radiation research were published as shown in the following list. Please refer to the following URLs for more details. Anyone can propose such a workshop, which then freely discusses a specific scientific topic in synchrotron-radiation research and its related application fields.

Proceedings of the 28th Workshop on Radiation Detectors and Their Uses, KEK Proceedings 2014-11
KEK Proceedings 2014-10 (in Japanese)
KEK Proceedings 2014-9 (in Japanese)
KEK Proceedings 2014-8 (in Japanese)
KEK Proceedings 2014-1 (in Japanese)
http://www-lib.kek.jp/lists/publistall-e.html
http://www-lib.kek.jp/cgi-bin/kiss_prepri.v8?KN=201425%25&TI=&AU=&AF=&CL=&RP=&YR=

9-3 Seminars

The seminars hosted by each scientific project in the Institute of Materials Structure Science (IMSS) were arranged as seminars hosted by IMSS, called “IMSS Colloquium” and “IMSS Danwakai”. These seminars provide an opportunity to exchange a broad range of knowledge in such fields as synchrotron, neutron and muon science. IMSS Colloquium invites leading scientists in each scientific field. Please refer to the following URL for more details.
http://www.kek.jp/en/Conference/

Appendices

1. Site and Organization

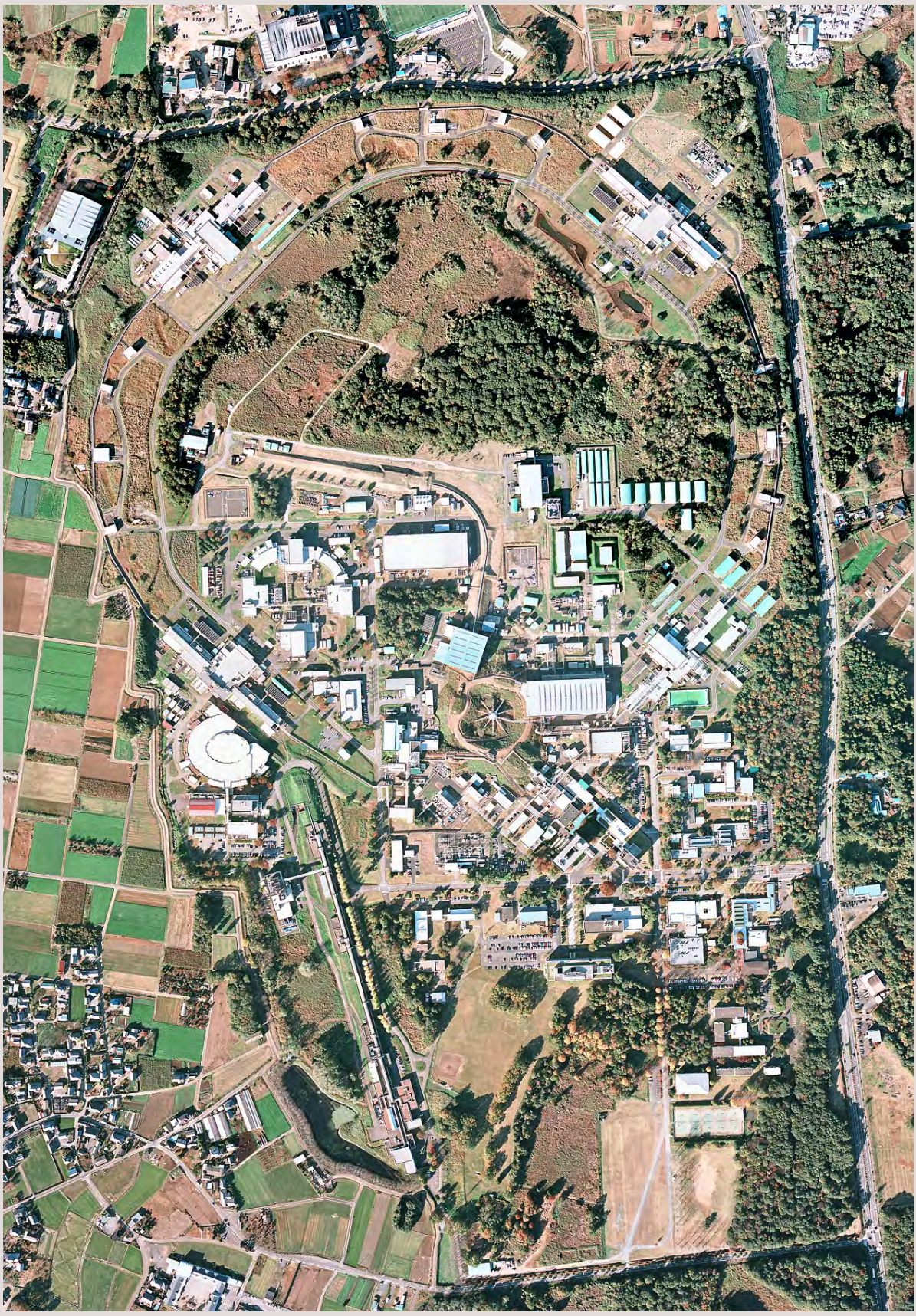

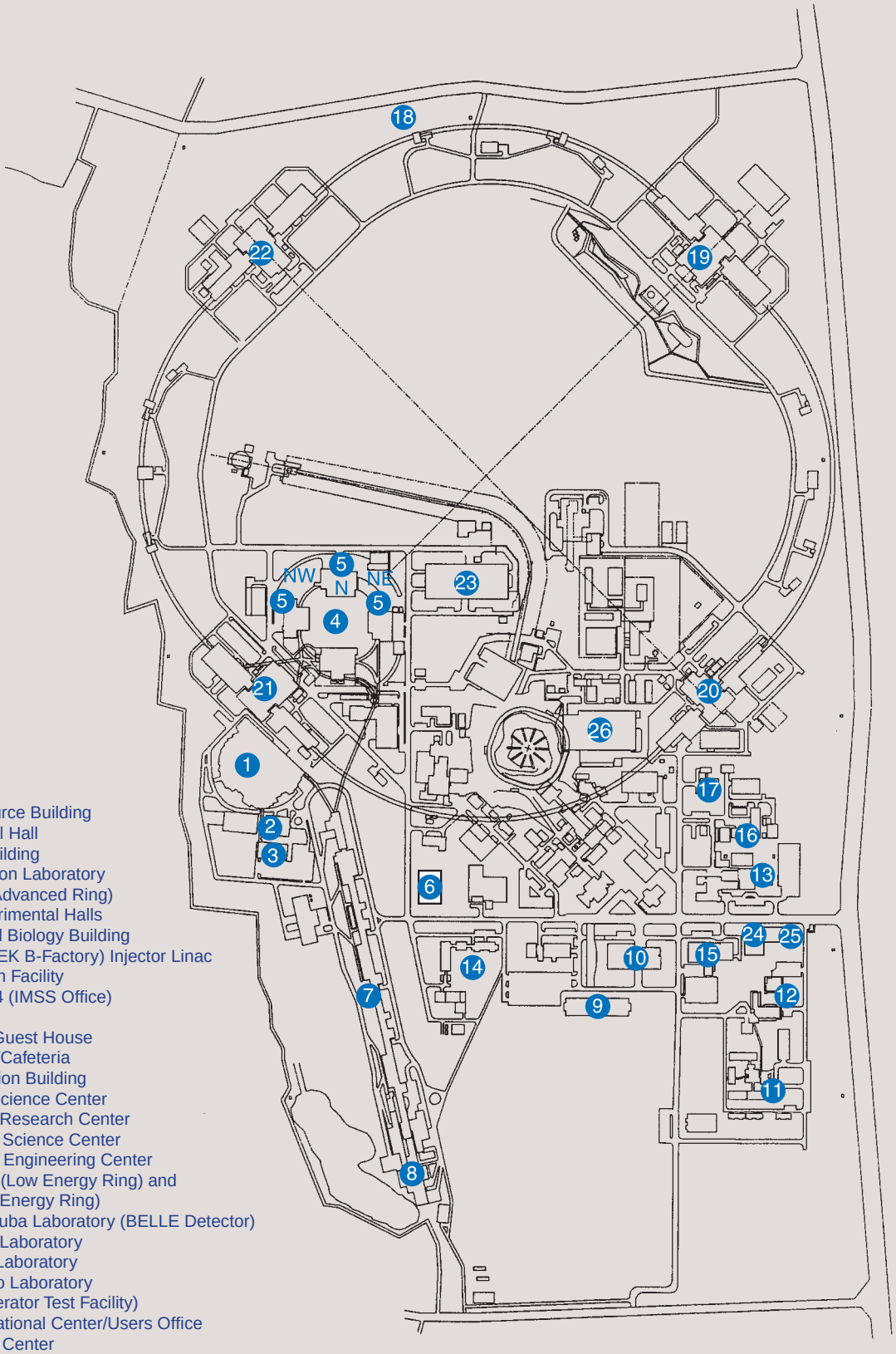

1. PF Light Source Building
   Experimental Hall
2. PF Office Building
3. PF Preparation Laboratory
4. PF-AR (PF Advanced Ring)
5. PF-AR Experimental Halls
6. PF Structural Biology Building
7. PF/KEKB (KEK B-Factory) Injector Linac
8. Slow Positron Facility
9. Building No.4 (IMSS Office)
10. Library
11. Dormitory/Guest House
12. Restaurant/Cafeteria
13. Administration Building
14. Radiation Science Center
15. Computing Research Center
16. Cryogenics Science Center
17. Mechanical Engineering Center
18. KEKB LER (Low Energy Ring) and
    HER (High Energy Ring)
19. KEKB Tsukuba Laboratory (BELLE Detector)
20. KEKB Oho Laboratory
21. KEKB Fuji Laboratory
22. KEKB Nikko Laboratory
23. ATF (Accelerator Test Facility)
24. KEK International Center/Users Office
25. Information Center
26. ERL Test Facility

KEK consists of four research institutions, i.e., the Institute of Materials Structure Science (IMSS), the Institute of Particle and Nuclear Studies (IPNS), the Accelerator Laboratory (AL), and the Applied Research Laboratory. As shown in Fig. 1, the IMSS constitutes the Synchrotron Radiation Divisions I and II, the Neutron Science Division, the Muon Science Division, the Structural Biology Research Center, and the Condensed Matter Research Center. Table I shows a list of the members of the Advisory Committee of the IMSS.

Photon Factory (PF) consists of two divisions of the IMSS (the Synchrotron Radiation Divisions I and II) and the Accelerator Division VII of the AL as shown in the organization chart of Fig. 2. The staff members of the PF list in Table 2. Synchrotron Radiation Science Divisions I and II consist of seven groups such as “Electronic Structure”, “Structural Material Science”, “Materials Chemistry”, “Life Sciences”, “Beamline Engineering, Technical Services & Safety”, “User Support and Dissemination”. The Accelerator Division VII has six groups, which are named Light Source Group I to VI. The missions of each group are as follows: Group I is in charge of orbits, magnets, and insertion devices, Group II of RF, SC cavities and so on, Group III mainly of vacuum, Group IV mainly of beam diagnostics and accelerator control, Group V of front-end, safety and so on, and Group VI mainly of electron guns.

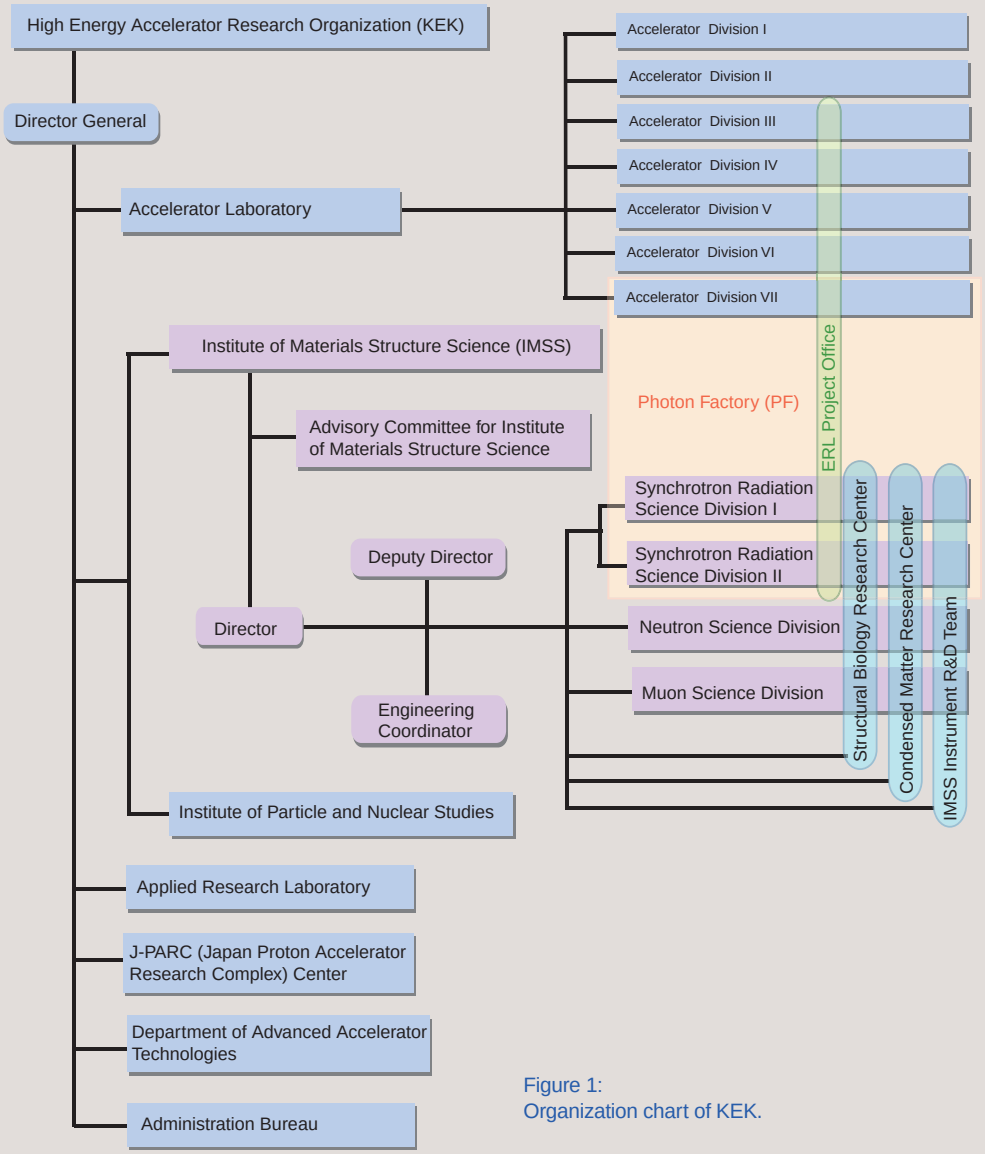

Figure 1:
Organization chart of KEK.

Table 1: The members of the Advisory Committee for Institute of Materials Structure Science.

ADACHI, Shin-ichi	Photon Factory, IMSS, KEK
AKIMITSU, Jun	Aoyama Gakuin University
AMEMIYA, Yoshiyuki**	The University of Tokyo
FUJII, Yasuhiko	Comprehensive Research Organization for Science and Society
KADONO, Ryosuke	Muon Science Division, IMSS, KEK
KANAYA, Toshiji	Kyoto University
KATAOKA, Mikio	Nara Institute of Science and Technology
KAWATA, Hiroshi	Photon Factory, IMSS, KEK
KOBAYASHI, Yukinori	Photon Factory, Accelerator Laboratory, KEK
KUMAI, Reiji	Photon Factory, IMSS, KEK
KUMIGASHIRA, Hiroshi	Photon Factory, IMSS, KEK
MIYAKE, Yasuhiro	Muon Science Division, IMSS, KEK
MIZUKI, Jun'ichiro	Kwansei Gakuin University
MURAKAMI, Youichi	Photon Factory, IMSS, KEK
OSHIMA, Masaharu	The University of Tokyo
OTOMO, Toshiya	Neutron Science Division, IMSS, KEK
SAITO, Naohito	Institute of Particle and Nuclear Studies, KEK
SASAKI, Shinichi	Applied Research Laboratory, KEK
SATO, Mamoru	Yokohama City University
SETO, Hideki*	Neutron Science Division, IMSS, KEK
SENDA, Toshiya	Photon Factory, IMSS, KEK
TAKATA, Masaki	RIKEN/SPring-8
TORIKAI, Eiko	University of Yamanashi
YAMAGUCHI, Seiya	Accelerator Laboratory, KEK

* Chairperson ** Vice-Chairperson

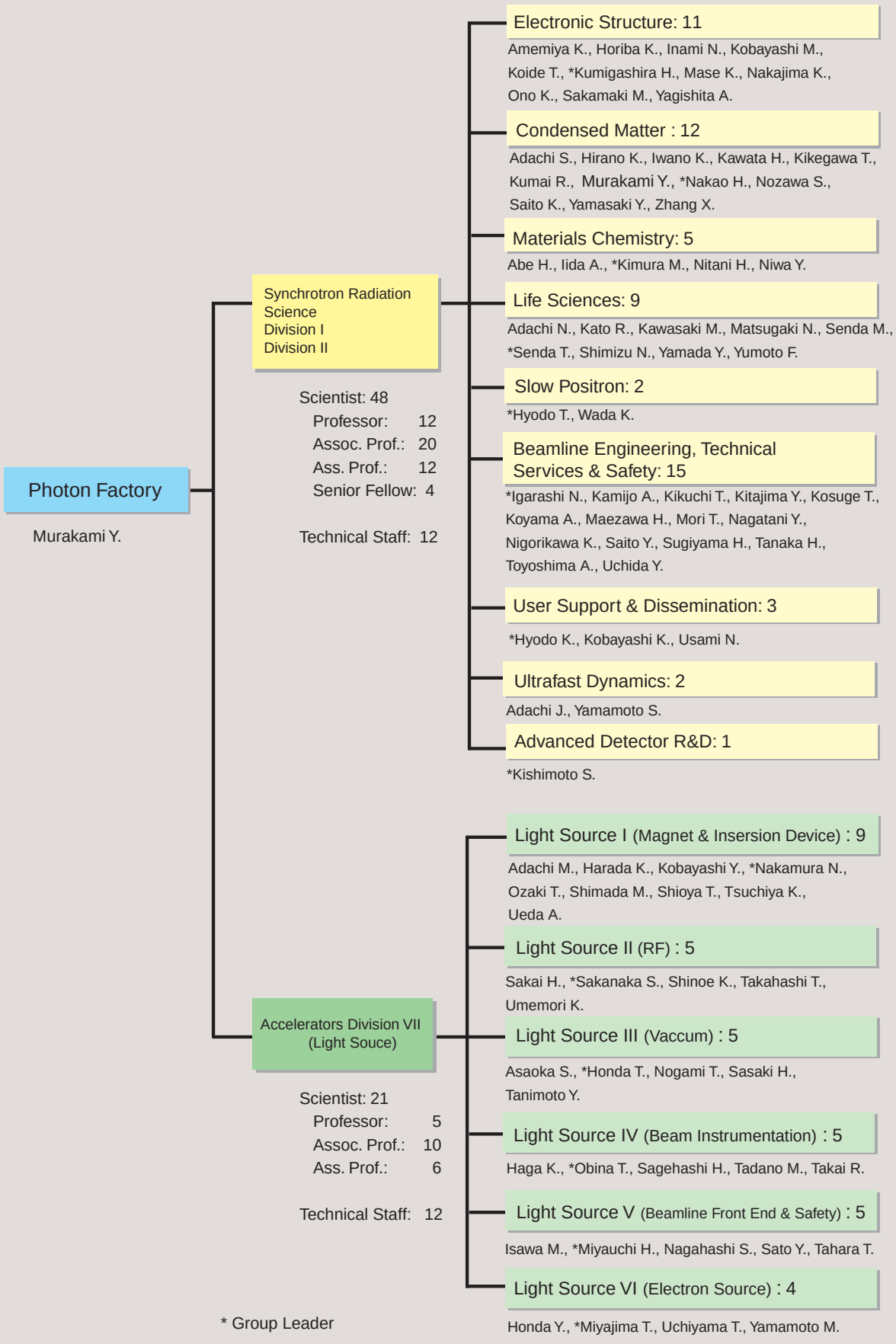

Figure 2:
Organization chart of PF (as of March 31, 2014) .

Table 2: Staff members of the Photon Factory.

Name	Group*
Research Staff	
Director	
MURAKAMI, Youichi	CM
Synchrotron Radiation Science Division I & II	
ABE, Hitoshi	MC
ADACHI, Jun-ichi	UD *(ES)*
ADACHI, Naruhiko	LS
ADACHI, Shinichi	CM *(UD, AD)*
AMEMIYA, Kenta	ES *(BETSS, AD, UD)*
HIRANO, Keiichi	CM
HORIBA, Koji	ES
HYODO, Kazuyuki	USD *(LS)*
HYODO, Toshio	SPF
IGARASHI, Noriyuki	BETSS *(LS, AD)*
IIDA, Atsuo	MC
INAMI, Nobuhito	ES *(AD)*
IWANO, Kaoru	CM
KAMIJO, Ai	BETSS
KATO, Ryuichi	LS
KAWASAKI, Masato	LS
KAWATA, Hiroshi	CM
KIKEGAWA, Takumi	CM
KIKUCHI, Takashi	BETSS *(UD)*
KIMURA, Masao	MC
KISHIMOTO, Shunji	AD, CM *(UD)*
KITAJIMA, Yoshinori	BETSS *(ES)*
KOBAYASHI, Katsumi	USD
KOBAYASHI, Masaki	ES
KOIDE, Tsuneharu	ES
KOSUGE, Takashi	BETSS *(AD)*
KOYAMA, Atsushi	BETSS
KUMAI, Reiji	CM *(AD)*
KUMIGASHIRA, Hiroshi	ES
MAEZAWA, Hideki	BETSS
MASE, Kazuhiko	ES
MATSUGAKI, Naohiro	LS
MORI, Takeharu	BETSS
NAGATANI, Yasuko	BETSS
NAKAJIMA, Kyo	ES
NAKAO, Hironori	CM *(UD)*
NIGORIKAWA, Kazuyuki	BETSS *(AD)*
NITANI, Hiroaki	MC
NIWA, Yasuhiro	MC (*BETSS,UD*)
NOZAWA, Shunsuke	CM *(UD)*
ONO, Kanta	ES *(AD)*
SAITO, Kotaro	CM
SAITO, Yuuki	BETSS
SAKAMAKI, Masako	ES *(AD)*
SENDA, Miki	LS
SENDA, Toshiya	LS
SHIMIZU, Nobutaka	LS *(BETSS)*
SUGIYAMA, Hiroshi	BETSS (*CM*)

	Name	Group*
	TANAKA, Hirokazu	BETSS *(UD)*
	TOYOSHIMA, Akio	BETSS *(UD)*
	UCHIDA, Yoshinori	BETSS
	USAMI, Noriko	USD (*LS*)
	WADA, Ken	SPF
	YAGISHITA, Akira	ES
	YAMADA, Yusuke	LS
	YAMAMOTO, Shigeru	UD
	YAMASAKI, Yuichi	CM *(UD)*
	YUMOTO, Fumiaki	LS
	ZHANG, Xiaowei	CM
Accelerator Division VII		
	ADACHI, Masahiro	Light Source I
	ASAOKA, Seiji	Light Source III
	HAGA, Kaiichi	Light Source IV
	HARADA, Kentaro	Light Source I
	HONDA, Tohru	Light Source III
	HONDA, Yosuke	Light Source VI
	ISAWA, Masaaki	Light Source V
	KOBAYASHI, Yukinori	Light Source I
	MIYAJIMA, Tsukasa	Light Source VI
	MIYAUCHI, Hiroshi	Light Source V
	NAGAHASHI, Shinya	Light Source V
	NAKAMURA, Norio	Light Source I
	NOGAMI, Takashi	Light Source III
	OBINA, Takashi	Light Source IV
	OZAKI, Toshiyuki	Light Source I
	SAGEHASHI, Hidenori	Light Source IV
	SAKAI, Hiroshi	Light Source II
	SAKANAKA, Shogo	Light Source II
	SASAKI, Hiroyuki	Light Source III
	SATO, Yoshihiro	Light Source V
	SHIMADA, Miho	Light Source I
	SHINOE, Kenji	Light Source II
	SHIOYA, Tatsuro	Light Source I
	TADANO, Mikito	Light Source IV
	TAHARA, Toshihiro	Light Source V
	TAKAHASHI, Takeshi	Light Source II
	TAKAI, Ryota	Light Source IV
	TANIMOTO, Yasunori	Light Source III
	TSUCHIYA, Kimichika	Light Source I
	UCHIYAMA, Takashi	Light Source VI
	UEDA, Akira	Light Source I
	UMEMORI, Kensei	Light Source II
	YAMAMOTO, Masahiro	Light Source VI
Guest Professor		
	ASAKURA, Kiyotaka	(Hokkaido Univ.)
	HAJIMA, Ryoichi	(JAEA)
	ISHIHARA, Sumio	(Tohoku Univ.)
	KAMIKUBO, Hironari	(Nara Institute of Science and Technology)
	KATOH, Masahiro	(UVSOR)

Name	Group*
KONDO, Tadashi	(Osaka Univ.)
KOSHIHARA, Shinya	(Tokyo Institute of Technology)
MORITOMO, Yutaka	(Univ. of Tsukuba)
OHKUMA, Haruo	(SPring-8)
TAKAHASHI, Yoshio	(Hiroshima Univ.)
YAO, Min	(Hokkaido Univ.)

Postdoctoral Fellow

SAKAI, Enju
TAKEICHI, Yasuo

The Graduate University for Advanced Studies

HARADA, Ayaka
INOUE, Keisuke
MATSUBARA, Haruki
WU, Yanlin

* Synchrotron Radiation Science Division

ES	Electronic Strucuture
CM	Condensed Matter
MC	Materials Chemistry
LS	Life Sciences
SPF	Slow Positron Facility
BETSS	Beamline Engineering, Technical Services and Safety
USD	User Support and Dissemination
UD	Ultrafast Dynamics
AD	Advanced Detector R&D

Italic: the additional post

Appendices (Web only)

2. Awards

The Japan Society for Bioscience, Biotechnology, and Agrochemistry Award for Young Scientists in 2014
NUMATA Tomoyuki (AIST)
“He Revealed the Post-Transcriptional tRNA Modification Mechanisms, by Using Crystallographic and Biochemical Analyzes, which also Elucidated a Part of Decoding Mechanism of the Genetic Code Essential for Life”

The Commendation for Science and Technology by the Minister of Education, Culture, Sports, Science and Technology, Research Category of Prizes for Science and Technology
OSHIMA Masaharu (The Univ. of Tokyo)
“Study on Synchrotron Radiation Nano Spectroscopy and Operando Electronic State Analysis”

The Commendation for Science and Technology by the Minister of Education, Culture, Sports, Science and Technology, Research Category of Prizes for Science and Technology
KOSHIHARA Shinya (Tokyo Inst. of Tech.)
“Experimenatl Studies on Photoinduced Phase Transition and Related Phenomena”

The Commendation for Science and Technology by the Minister of Education, Culture, Sports, Science and Technology, The Young Scientists’ Prize
KAGAWA Fumitaka (RIKEN)
“Reserach on Strongly Coorelated Electrons in Molecular Solids”

The Commendation for Science and Technology by the Minister of Education, Culture, Sports, Science and Technology, The Young Scientists’ Prize
YABUUCHI Naoaki (Tokyo Denki Univ.)
“Study on New Insertion Materials for Rechargeable Batteries”

2014 RESONATE AWARD, Resnick Institute, CALTECH, USA
KOMABA Shinichi (Tokyo Univ. of Science)
“Research and Development of New Electrode Materials for Next Generation Batteries”

The 2014 Japan Society of Coordination Chemistry Research Encouragement Award
SATO Sota (Tohoku Univ.)
“Development of Biomolecular Interfaces Constructed on the Frameworks of Huge, Hollow Spherical Complexes”

Award of Japan Society for Molecular Science
NISHIKAWA Keiko (Chiba Univ.)
“Molecular Science of Complex Condensed Systems Probed by Fluctuation”

The Crystallographic Society of Japan Award
SENDA Toshiya (KEK-PF)
“Structural Biology Studies of CagA from *Helicobacter pylori* and Histone Chaperone CIA/ASF1”

The Crystallographic Society of Japan, Progress Prize
KOTARO FUJII (Tokyo Inst. of Tech.)
“Reaction Mechanism in Organic Crystals and Development of Inorganic Oxide-Ion Conductor Using ab initio Powder Diffraction Analysis”

Surface Science Society Award of The Surface Science Society of Japan
UOSAKI Kohei (NIMS)
“Creation of Functional Materials Based on Understanding and Control of In situ Real-time Monitoring of Geometric, Electronic, and Molecular Structures at Solid/Liquid Interfaces”

Academic Encouragement Award (The Pharmaceutical Society of Japan, Kyushu Branch)
YAMAGUCHI Yoshihiro (Kumamoto Univ.)
“Structural-Functional Analysis and Developing Inhibitors of metallo-β-lactamases Conferring Drug Resistance in Bacteria”

Young Chemist Award of the Chemical Society of Japan Hokkaido Branch
MASUBUCHI Yuji (Hokkaido Univ.)
“Study on Characteristic Crystal Structure Induced by Coexisting of Oxygen and Nitrogen in Inorganic Oxynitride Materials”

The Foundation for High Energy Accelerator Science, Suwa Prize, 2014
The Construction Team of the Compact ERL (A Representative; KAWATA Hiroshi)
“Establishment on the Fundamental ERL Accelerator Tecnologies and their Examination Studies.”

Japan Society for the Promotion of Science Prize
KOMABA Shinichi (Tokyo Univ. of Science)
“Research and Development of New Electrode Materials for Next Generation Batteries”

Sawamura Awards: Best Papers Published in the Iron and Steel Institute of Japan International in Vol.13
KIMURA Masao[1] and MURAO Reiko[2] ([1]KEK, [2]Nippon Steel & Sumitomo Metal Corp.)
“Continuous Cooling Transformation (CCT) Concept for Iron Ore Sintering using In Situ Quick X-Ray Diffraction and Confocal Laser Microscope”

The 56th Japan Institute of Metals and Materials Industrial Achievement Award
ISHIYAMA Shintaro (JAEA)
“R&D on High Performacnce of Lithium Target for Boron Nuetron Chapture Theraphy”

Young Scientist Award of the Physical Society of Japan
SUMINO Yutaka (Tokyo Univ. of Science)
“Experimental and Theoretical Studies on Spontaneous Motion in None Quilibrium Soft Matter”

Award of Catalysis Society of Japan
YAMASHITA Hiromi (Osaka Univ.)
“Design of Functional Nano Materials Using Single-Site Photocatalysts”

School of Science Research Encouragement Award (Doctor), The Univ. of Tokyo
WAKABAYASHI Daisuke (The Univ. of Tokyo)
“Phase-Transition-Like Change in the Density and Viscosity of Silicate Melt Inferred from the Behavior of SiO_2 Glass under High Pressure”

2014 Encouraging Prize of Japanese Society of Enzyme Engineering
ARAI Ryoichi (Shinshu Univ.)
“Structural Analysis of a Binary Pattern-Designed de Novo Protein and its Application to Construction of Nano-Architectures”

Poster, Presentation Awards & Others

Highly Cited Researchers 2014 by Thomson Reuters (Physics)
TAKAHASHI Takashi (Tohoku Univ.)

Highly Cited Researchers 2014 by Thomson Reuters (Physics)
SATO Takafumi (Tohoku Univ.)

Protein Science Society of Japan 2014 Young Poster Award
MATSUZAWA Jun (The Univ. of Tokyo)
“Redox-Dependent Interaction between Terminal Oxygenase and Ferredoxin Components of Carbazole 1,9a-Dioxygenase”

The 1st Workshop of 3D Active Site Science Best Poster Award
MASUDA Takuya (NIMS)
“In Situ Studies of Electrochemical Processes at Solid Liquid Interfaces using Synchrotron Light Sources”

The 34th Annual Meeting of the Surface Science Society of Japan Best Presentation Award for Young Researcher
MASUDA Takuya (NIMS)
“Adsorption / Desorption Behavior of Nafion on Au and Pt Electrode Surfaces”

CENIDE-CNMM-TIMS Joint Symposium Poster Award
TAKACHI Masamitsu (Univ. of Tsukuba)
“Diffusion Constant of Li+/Na+ in Prussian Blue Analogues”

---

3. Ph. D Theses

List of doctoral theses, which were written based on the PF experiments. 2014FY (*registered by 2015. Jul. 1)

LAI, Kwing To (Osaka Univ.)
“Evolution of the Electronic Phase Diagram for Iron-Based Superconductor $LaFeP_{1-x}As_xO_{1-y}F_y$ (y=0-0.1)” (8A and 8B)

ZHANG, Shuijun (Dr of Science, Chinese Academy of Sciences)
“The Mechanism of NK Cell Receptors Interacting with their Ligand” (5A)

KIM, Kyoung Hoon (Dr of Biochemistry, Seoul National Univ.)
“Structural and Functional Studies of Tpa1 from *Saccharomyces cerevisiae*, a Component of the Messenger Ribonucleoprotein Complex” (AR-NW12A)

NISHIKAWA, Yosuke (Osaka Univ.)
“Structural Studies on the Stalk Region of the Dynein Motor Domain” (17A, 5A, 1A, and AR-NW12A)

WU, Yanlin (SOKENDAI / The Graduate University for Advanced Studies)
“Development of High-Contrast X-Ray Imaging Method with Multiple-Times-Diffraction Enhanced Imaging. X-Ray Phase-Contrast Imaging Using Synchrotron Radiation” (14C)

FUJII, Yuki (Osaka Univ.)
“Development of a Novel and Versatile Affinity Tagging System using an Anti-Podoplanin Antibody NZ-1” (1A and 17A)

EMORI, Masato (Sophia Univ.)
“Electronic States and Excited Carrier Dynamics of Titania Photocatalyst” (3B, 11A, and 13B)

HORI, Mayumi (The Univ. of Tokyo)
“Elucidation of Reduction Process of Hexavalent Chromium in Environment and Application to Pollution Remediation ” (9A, 9C, and 12C)

YAMAGATA, Takehiro (The Univ. of Tokyo)
“Evaluation of Redox Conditions at Dredged Trenches in Tokyo Bay by the Concentrations and Chemical States of Elements in the Sediments ” (9A, 9C, and 12C)

SANO, Masami (Nagoya Univ.)
“Photoinduced Cooperative Orientational Switching of Different Hierarchical Architectures in Liquid Crystalline Block Copolymer Films ” (6A)

NAKANISHI, Yuko (Tokyo Inst. of Tech.)
“The Production of Pairs of H(2p) Atoms in the Photodissociation of H_2 ” (20A and 28B)

YAMADA, Hiroyuki (Nagoya Univ.)
“Structural Study of High-Energy Metastable Conformational Substates of Proteins using High-Pressure X-Ray Crystallography” (AR-NW12A)

TONGSAKUL, Duangta (Japan Advanced Institute of Science and Technology)
“Studies on the Development of Platinum-Based Nanoparticles by a Green Synthetic Method as Heterogeneous Catalyst for Selective Oxidation of Polyols into Value-Added Chemicals” (9C)

AIZAWA, Hideki (Univ. of Tsukuba)
“Structural Characterization of Nonionic Surfactant Micelles and Bile Salt Based Mixed Micelles by using Small Angle X-Ray Scattering” (10C)

HAMAJIMA, Yuki (Rikkyo Univ.)
“Structural Basis of the Pressure Adaptation of 3-Isopropylmalate Dehydrogenase from an Extremely Piezophilic Bacterium Shewanella Benthica” (AR-NW12A)

TSUTSUMI, Naotaka (Kyoto Univ.)
“Structural Analysis of the Proteins Related to TLR/IL-1R Signaling” (1A, 5A, and 17A)

4. Publication List

1A

S.Okada, T.Yamamoto, H.Watanabe, T.Nishimoto, H.Chaen, S.Fukuda, T.Wakagi and S.Fushinobu
Structural and Mutational Analysis of Substrate Recognition in Kojibiose Phosphorylase
FEBS J., **281** (2014) 778.

S.Yamashita, D.Takeshita and K.Tomita
Translocation and Rotation of tRNA during Template-Independent RNA Polymerization by tRNA Nucleotidyltransferase
Structure, **22** (2014) 315.

J.Kondo, T.Yamada, C.Hirose, I.Okamoto, Y.Tanaka and A.Ono
Crystal Structure of Metallo DNA Duplex Containing Consecutive Watson-Crick-Like T-Hg^{II}–T Base Pairs
Angew. Chem. Int. Ed., **53** (2014) 2385.

D.Matsui, D.-H.Im, A.Sugawara, Y.Fukuta, S.Fushinobu, K.Isobe and Y.Asano
Mutational and Crystallographic Analysis of L–Amino Acid Oxidase/Monooxygenase from Pseudomonas sp. AIU 813: Interconversion between Oxidase and Monooxygenase Activities
FEBS Open Bio, **4** (2014) 220.

S.Liu, L.-F.Tian, Y.-P.Liu, X.-M.An, Q.Tang, X.-X.Yan and D.-C.Liang
Structural Basis for DNA Recognition and Nuclease Processing by the Mre11 Homologue SbcD in Double- Strand Breaks Repair
Acta Cryst. D, **70** (2014) 299.

S.Niwa, L.-J.Yu, K.Takeda, Y.Hirano, T.Kawakami, Z.Y.Wang-Otomo and K.Miki
Structure of the LH1-RC complex from *Thermochromatium tepidum* at 3.0 Å
Nature, **508** (2014) 228.

T.Ito, K.Saikawa, S.Kim, K.Fujita, A.Ishiwata, S.Kaeothip, T.Arakawa, T.Wakagi, G.T.Beckham, Y.Ito, S.Fushinobu
Crystal Structure of Glycoside Hydrolase Family 127 β-L Arabinofuranosidase from *Bifidobacterium longum*
Biochem. Biophys. Res. Commun., **447** (2014) 32.

A.Kishimoto, A.Kita, T.Ishibashi, H.Tomita, Y.Yokooji, T.Imanaka, H.Atomi and K.Miki
Crystal Structure of Phosphopantothenate Synthetase from *Thermococcus kodakarensis*
Proteins **82** (2014) 1924.

Y.Sakamoto, Y.Suzuki, I.Iizuka, C.Tateoka, S.Roppongi, M.Fujimoto, H.Tanaka, M.Masaki, K.Ohta, H.Okada, T.Nonaka, Y.Morikawa, K.T.Nakamura, W.Ogasawara and N.Tanaka
S46 Peptidases are the First Exopeptidases to be Members of Clan PA
Scientific Reports, **4** (2014) 4977.

E.Tamai, H.Yoshida, H.Sekiya, H.Nariya, S.Miyata, A.Okabe, T.Kuwahara, J.Maki and S.Kamitori
X-Ray Structure of a Novel Endolysin Encoded by Episomal Phage PhiSM101 of *Clostridium perfringens*
Molecular Microbiology, **92** (2014) 326.

J.Fujita, Y.Maeda, C.Nagao, Y.Tsuchiya, Y.Miyazaki, M.Hirose, E.Mizohata, Y.Matsumoto, T.Inoue, K.Mizuguchi and H.Matsumura
Crystal Structure of FtsA from *Staphylococcus aureus*
FEBS Letters, **588** (2014) 1879.

K.J.Cho, K.W.Hong, S.-H.Kim, J.H.Seok, S.Kim, J.-H.Lee, X.Saelens, K.H.Kim
Insight into Highly Conserved H1 Subtype-Specific Epitopes in Influenza Virus Hemagglutinin
PLOS ONE, **9** (2014) e89803.

Y.Fujioka, S.W.Suzuki, H.Yamamoto, C.Kondo-Kakuta, Y.Kimura, H.Hirano, R.Akada, F.Inagaki, Y.Ohsumi and N.N.Noda
Structural Basis of Starvation-Induced Assembly of the Autophagy Initiation Complex
Nature Structural Molecular Biology, **21** (2014) 513.

X.Liu, Y.Yin, J.Wu and Z.Liu
Structure and Mechanism of an Intramembrane Liponucleotide Synthetase Central for Phospholipid Biosynthesis
Nature Communications, **5** (2014) 4244.

S.Sato, T.Yamasaki and H.Isobe
Solid-State Structures of Peapod Bearings Composed of Finite Single-Wall Carbon Nanotube and Fullerene Molecules
Proc. Natl. Acad. Sci. USA, **111** (2014) 8374.

S.Terawaki, H.Ootsuka, Y.Higuchi and K.Wakamatsu
Crystallographic Characterization of the C-Terminal Coiled-Coil Region of Mouse Bicaudal-D1(BICD1)
Acta Cryst. F, **70** (2014) 1103.

H.Niwa, J.Mikuni, S.Sasaki, Y.Tomabechi, K.Honda, M.Ikeda, N.Ohsawa, M.Wakiyama, N.Handa, M.Shirouzu, T.Honma, A.Tanaka and S.Yokoyama
Crystal Structures of the S6K1 Kinase Domain in Complexes with Inhibitors
J. Struct. Funct. Genomics, **15** (2014) 153.

E.H.Lee, G.-H.Kwak, M.-J.Kim, H.-Y.Kim and K.Y.Hwang
Structural Analysis of 1-Cys Type Selenoprotein Methionine Sulfoxide Reductase A
Arch. Biochem. Biophys., **545** (2014) 1.

V.Schaeffer, M.Akutsu, M.H.Olma, L.C.Gomes, M.Kawasaki and I.Dikic
Binding of OTULIN to the PUB Domain of HOIP Controls NF-κB Signaling
Mol. Cell, **54** (2014) 349.

H.Tsukagoshi, A.Nakamura, T.Ishida, K.K.Touhara, M.Otagiri, S.Moriya, M.Samejima, K.Igarashi, S.Fushinobu, K.Kitamoto and M.Arioka
Structural and Biochemical Analyses of Glycoside Hydrolase Family 26 β-Mannanase from a Symbiotic Protist of the Termite Reticulitermes speratus
J. Biol. Chem., **289** (2014) 10843

K.K.Touhara, T.Nihira, M.Kitaoka, H.Nakai and S.Fushinobu
Structural Basis for Reversible Phosphorolysis and Hydrolysis Reactions of 2-*O*-α-Glucosylglycerol Phosphorylase
J. Biol. Chem., **289** (2014) 18067.

K.Suzuki, A.Hori, K.Kawamoto, R.R.Thangudu, T.Ishida, K.Igarashi, M.Samejima, C.Yamada, T.Arakawa, T.Wakagi, T.Koseki and S.Fushinobu
Crystal Structure of a Feruloyl Esterase Belonging to the Tannase Family: A Disulfide Bond Near a Catalytic Triad
Proteins, **82** (2014) 2857.

D.Yamashita, T.Sugawara, M.Takeshita, J.Kaneko, Y.Kamio, I.Tanaka, Y.Tanaka and M.Yao
Molecular Basis of Transmembrane Beta-Barrel Formation of Staphylococcal Pore-Forming Toxins
Nature Communications, **5** (2014) 4897.

H.Zhao, G.Sheng, J.Wang, M.Wang, G.Bunkoczi, W.Gong, Z.Wei and Y.Wang
Crystal Structure of the RNA-Guided Immune Surveillance Cascade Complex in *Escherichia coli*
Nature, **515** (2014) 147.

C.J.Bruns, D.Fujita, M.Hoshino, S.Sato, J.F.Stoddart and M.Fujita
Emergent Ion-Gated Binding of Cationic Host-Guest Complexes within Cationic M_{12} L_{24} Molecular Flasks
J. Am. Chem. Soc., **136** (2014) 12027.

Q.Tang, Y-P.Liu, X-X.Yan, D-C.Liang
Structural and Functional Characterization of Cys4 Zinc Finger Motif in the Recombination Mediator Protein RecR
DNA Repair, **24** (2014) 10.

Q-F.Sun, S.Sato and M.Fujita
An M_{12} $(L^1)_{12}$ $(L^2)_{12}$ Cantellated Tetrahedron: A Case Study on Mixed-Ligand Self-Assembly
Angew. Chem. Int. Ed., **53** (2014) 13510.

H.Yoshida, A.Yoshihara, M.Teraoka, Y.Terami, G.Takata, K.Izumori and S.Kamitori
X-Ray Structure of a Novel L-Ribose Isomerase Acting on a Non-Natural Sugar L-Ribose as its Ideal Substrate
FEBS J., **281** (2014) 3150.

D.Takeshita, S.Yamashita and K.Tomita
Molecular Insights into Replication Initiation by Qβ Replicase Using Ribosomal Protein S1
Nucleic Acids Res., **42** (2014) 10809.

J.Lu, Y.Gu, J.Feng, W.Zhou, X.Yang and Y.Shen
Structural Insight into the Central Element Assembly of the Synaptonemal Complex
Scientific Reports, **4** (2014) 7059.

Z.Wang, X.Yang, S.Guo, Y.Yang, X.C.Su, Y.Shen and J.Long
Crystal Structure of the Ubiquitin-Like Domain-CUT Repeat-Like Tandem of Special AT-Rich Sequence Binding Protein 1 (SATB1) Reveals a Coordinating DNA-Binding Mechanism
J. Biol. Chem., **289** (2014) 27376.

G.Wang, Q.He, C.Feng, Y.Liu, Z.Deng, X.Qi, W.Wu, P.Mei and Z.Chen
The Atomic-Resolution Structure of Human Alkb Homolog 7 (ALKBH7), a Key Protein for Programmed Necrosis and Fat Metabolism
J. Biol. Chem., **289** (2014) 27924.

P.Zhou, Y.Liu, Q.Yan, Z.Chen, Z.Qin and Z.Jiang
Structural Insights into the Substrate Specificity and Transglycosylation Activity of a Fungal Glycoside Hydrolase Family 5 β-Mannosidase
Acta Cryst. D, **70** (2014) 2970.

T.Kimura, N.Tsutsumi, K.Arita, M.Ariyoshi, H.Ohnishi, N.Kondo, M.Shirakawa, Z.Kato and H.Tochio
Purification, Crystallization and Preliminary X-Ray Crystallographic Analysis of Human IL-18 and its Extracellular Complexes
Acta Cryst. F, **70** (2014) 1351.

N.Tsutsumi, T.Kimura, K.Arita, M.Ariyoshi, H.Ohnishi, T.Yamamoto, X.Zuo, K.Maenaka, E.Y.Park, N.Kondo, M.Shirakawa, H.Tochio and Z.Kato
The Structural Basis for Receptor Recognition of Human Interleukin-18
Nature Communications, **5** (2014) 5340.

C.Ma, C.Pathak, S.Jang, S.Lee, M.Nam, S.Kim, H.Im and B.J.Lee
Structure of *Thermoplasma volcanium* Ard1 Belongs to N-Acetyltransferase Family Member Suggesting Multiple Ligand Binding Modes with Acetyl Coenzyme A and Coenzyme A
Biochim. Biophys. Acta, **1844** (2014) 1790.

H.S.Kim, S.Y.Cha, C.H.Jo, A.Han and K.Y.Hwang
The Crystal Structure of Arginyl-tRNA Synthetase from *Homo sapiens*
FEBS Letters, **558** (2014) 2328.

Y.Nishikawa, T.Oyama, N.Kamiya, T.Kon, Y.Y.Toyoshima, H.Nakamura and G.Kurisu
Structure of the Entire Stalk Region of the Dynein Motor Domain
J. Mol. Biol., **426** (2014) 3232.

H.S.Kim, J.Kim, H.N.Im, D.R.An, M.Lee, D.Hesek, S.Mobashery, J.Y.Kim, K.Cho, H.J.Yoon, B.W.Han, B.I.Lee and S.W.Suh
Structural Basis for the Recognition of Muramyltripeptide by *Helicobacter Pylori* Csd4, a D,L-Carboxypeptidase Controlling the Helical Cell Shape
Acta Cryst. D, **70** (2014) 2800.

B.Gong, M.Shin, J.Sun, C.H.Jung, E.L.Bolt, J.V.D.Oost and J.S.Kim
Molecular Insights into DNA Interference by CRISPR Associated Nuclease-Helicase Cas3
Proc. Natl. Acad. Sci. USA, **111** (2014) 16359.

T.Matsui, X.Han, J.Yu, M.Yao and I.Tanaka.
Structural Change in FtsZ Induced by Intermolecular Interactions between Bound GTP and the T7 Loop
J. Biol. Chem., **289** (2014) 3501.

T.Fujiwara, W.Saburi, H.Matsui, H.Mori and M.Yao
Structural Insights into the Epimerization of Beta-1,4 Linked Oligosaccharides Catalyzed by Cellobiose 2-Epimerase, the Sole Enzyme Epimerizing Non-Anomeric Hydroxyl Groups of Unmodified Sugars
J. Biol. Chem., **289** (2014) 3405.

X.Shen,W.Saburi,Z.Q.Gai,K.Komoda, J.Yu, T.O.Kato, Y.Kido, H.Matsui, H.Mori and M.Yao
Crystallization and Preliminary X-Ray Crystallographic Analysis of α-Glucosidase HaG from *Halomonas* sp. Strain H11
Acta Cryst. F, **70** (2014) 464.

M.Hasegawa, S.T.Fukai, JD.Kim, A.Fukamizu and T.Shimizu
Protein Arginine Methyltransferase 7 has a Novel Homodimer-Like Structure Formed by Tandem Repeats
FEBS Letters, **588** (2014) 1942.

2A

Y.Shimazu, T.Okumura, A.Shimada, K.Tanabe, K.Tokiwa, E.Sakai, H.Kumigashira and T.Higuchi
Electronic Structure of V_2O_3 Thin Film Prepared by RF Magnetron Sputtering using Oxygen Radical and V- Metal
Jpn. J. Appl. Phys., **53** (2014) 06JG05.

S.Kawasaki, R.Takahashi, K.Akagi, J.Yoshinobu, F.Komori, K.Horiba, H.Kumigashira, K.Iwashina, A.Kudo and M.Lippmaa
Electronic Structure and Photoelectrochemical Properties of an Ir-Doped $SrTiO_3$ Photocatalyst
J. Phys. Chem. C, **118** (2014) 20222.

2C

Y.Tezuka, T.Sasaki, Y.Fujita, T.Iwamoto, H.Osawa, S.Nozawa, N.Nakajima, H.Sato and T.Iwazumi
Core Excitations in Resonant X-Ray Raman Scattering of Titanium Oxides: An Approach to Studying Electronic Structures
J. Phys. Soc. Jpn., **83** (2014) 014707.

M.Stener, P.Decleva, T.Mizuno, H.Yoshida and A.Yagishita
Off-Resonance Photoemission Dynamics Studied by Recoil Frame F1s and C1s Photoelectron Angular Distributions of CH_3F
J. Chem. Phys., **140** (2014) 044305.

T.Katayama, A.Chikamatsu, Y.Hirose, H.Kumigashira, T.Fukumura and T.Hasegawa
Metallic Conductivity in Infinite-Layer Strontium Iron Oxide Thin Films Reduced by Calcium Hydride
J. Phys. D: Appl. Phys., **47** (2014) 135304.

S.Nagira, J.Sonoyama, T.Wakita, M.Sunagawa, Y.Izumi, T.Muro, H.Kumigashira, M.Oshima, K.Deguchi, H.Okazaki, Y.Takano, O.Miura, Y.Mizuguchi, K.Suzuki, H.Usui, K.Kuroki, K.Okada, Y.Muraoka and T.Yokoya
Soft X-Ray Photoemission Study of New BiS_2 -Layered Superconductor $LaO_{1-x}F_xBiS_2$
J. Phys. Soc. Jpn., **83** (2014) 033703.

Y.Muraoka, H.Nagao, S.Katayama, T.Wakita, M.Hirai, T.Yokoya, H.Kumigashira and M.Oshima
Persistent Insulator-to-Metal Transition of a VO_2 Thin Film Induced by Soft X-Ray irradiation
Jpn. J. Appl. Phys., **53** (2014) 05FB09.

E.Sakai, K.Yoshimatsu, M.Tamamitsu, K.Horiba, A.Fujimori, M.Oshima and H.Kumigashira
Bandwidth-Controlled Metal-Insulator Transition in Epitaxial $PrNiO_3$ Ultrathin Films Induced by Dimensional Crossover
Appl. Phys. Lett., **104** (2014) 171609.

K.Usui, T.Okumura, E.Sakai, H.Kumigashira and T.Higuchi
Structural and Electronic Properties of Anatase $Ti_{1-x}Fe_xO_{2-\delta}$ Thin Film Prepared by RF Magnetron Sputtering
J. Phys.: Conf. Ser., **502** (2014) 012001.

Y.Shimazu, T.Okumura, E.Sakai, H.Kumigashira, M.Okawa, T.Saitoh and T.Higuchi
Growth of $TiO_{2-\delta}$ Thin Film by RF Magnetron Sputtering using Oxygen Radicals and Ti Metal
Jpn. J. Appl. Phys., **53** (2014) 06JG01.

T.Inoue, T.Okumura, Y.Shimazu, E.Sakai, H.Kumigashira and T.Higuchi
Electrical Conductivity of Sc-Doped TiO_2 Thin Film Prepared by RF Magnetron Sputtering
Jpn. J. Appl. Phys., **53** (2014) 06JG03.

T.Nagata, K.Kawajiri, S.Kosugi, N.Suzuki, M.Kemmotsu, T.Nandi, E.Sokell, Y.Azuma and F.Koike
Photoion Spectroscopy on Isolated Mn Atoms in the 2p→3d Excitation Region: I. Total Photoion-Yield Spectrum
J. Phys. B, **47** (2014) 185006.

S.Hosokawa, H.Sato, K.Mimura, Y.Tezuka, D.Fukunaga, K.Shimamura and F.Shimojo
Oxygen 2*p* Partial Density of States in a Typical Oxide Glass B_2O_3
J. Phys. Soc. Jpn., **83** (2014) 114601.

T.Nagata, K.Kawajiri, S.Kosugi, N.Suzuki, M.Kemmotsu, T.Nandi, E.Sokell, F.Koike and Y.Azuma Photoion Spectroscopy on Isolated Mn Atoms in the 2p→3d Excitation Region. II. Decay Processes of the Excited States
J. Phys. B, **47** (2014) 215002.

H.Wadati, J.Mravlje, K.Yoshimatsu, H.Kumigashira, M.Oshima, T.Sugiyama, E.Ikenaga, A.Fujimori, A.Georges, A.Radetinac, K.S.Takahashi, M.Kawasaki and Y.Tokura
Photoemission and DMFT Study of Electronic Correlations in $SrMoO_3$: Effects of Hund's Rule Coupling and Possible Plasmonic Sideband
Phys. Rev. B, **90** (2014) 205131.

S.Tsuru, M.Kazama, T.Fujikawa, J.Adachi and A.Yagishita
Geometric Effect on the Issue of Asymetric C 1*s* Photoelectron Angular Distributions Detected in Coincidence with the Fragment Ion Pairs of CO^+ - O^+ for CO_2 Molecules
J. Phys. B, **47** (2014) 071002.

S.Tsuru, M.Kazama, T.Fujikawa, J.Adachi, T.Mizuno and A.Yagishita
Site-Specific Fragmentation Probabilities Deduced from O^+ - CO^+ Molecular Frame Photoelectron Angular Distributions from CO_2
Chem. Phys. Lett., **608** (2014) 152.

M.Okawa, T.Yokobori, K.Konishi, R,Takei, K.Katayama, S.Oozono, T.Shinmura, T.Okuda, H.Wadati, E.Sakai, K.Ono, H.Kumigashira, M.Oshima, T.Sugiyama, E.Ikenaga, N.Hamada and T.Saitoh
Cu-O-Cr Hybridization Effects on the Electronic Structure of a Hole-Doped Delafossite Oxide $CuCr_{1-x}Mg_xO_2$
JPS Conf Proc., **3** (2014) 017027.

3A

A.Tsuchiyama, M.Uesugi, K.Uesugi, T.Nakano, R.Noguchi, T.Matsumoto, J.Matsuno, T.Nagano, Y.Imai, A.Shimada, A.Takeuchi, Y.Suzuki, T.Nakamura, T.Noguchi, M.Abe, T.Yada and A.Fujimura
Three-Dimensional Microstructure of Samples Recovered from Asteroid 25143 Itokawa: Comparison with LL5 and LL6 Chondrite Particles
Meteoritics and Planetary Science, **49** (2014) 172.

T.Noguchi, M.Kimura, T.Hashimoto, M.Konno, T.Nakamura, M.E.Zolensky, R.Okazaki, M.Tanaka, A.Tsuchiyama, A.Nakato, T.Ogami, H.Ishida, R.Sagae, S.Tsujimoto, T.Matsumoto, J.Matsuno, A.Fujimura, M.Abe, T.Yada, T.Mukai, M.Ueno, T.Okada, K.Shirai and Y.Ishibashi
Space Weathered Rims Found on the Surfaces of the Itokawa Dust Particles
Meteoritics and Planetary Science, **49** (2014) 188.

M.Kubota, H.Yamada, H.Nakao, J.Okamoto, Y.Yamasaki, A.Sawa and Y.Murakami
Magnetic and Electronic Properties of $(LaMnO_3)_5(SrMnO_3)_5$ Superlattice Revealed by Resonant Soft X-Ray Scattering
Jpn. J. Appl. Phys., **53** (2014) 05FH07.

P.Barpanda, G.Oyama, S.Nishimura, S.-C.Chung and A.Yamada
A 3.8-V Earth-Abundant Sodium Battery Electrode
Nature Communications, **5** (2014) 4358.

H.Morisaki, T.Koretsune, C.Hotta, J.Takeya, T.Kimura and Y.Wakabayashi
Large Surface Relaxation in the Organic Semiconductor Tetracene
Nature Communications, **5** (2014) 5400.

3B

K.Ozawa, Y.Mimori H.Kato, M.Emori H.Sakama, S.Imanishi, K.Edamoto and K.Mase
Shockley Surface State on α-Brass(111) and its Response to Oxygen Adsorption
Surf. Sci., **623** (2014) 6.

K.Ozawa, Y.Mimori, H.Kato, S.Imanishi, K.Edamoto and K.Mase
Photoelectron Spectroscopy Study of Interaction of Oxygen with the (111) Surface of a Cu-Zn Alloy
Surf. Sci., **623** (2014) 1.

K.Edamoto, S.Imanishi, S.Masuda, Y.Kakefuda and K.Ozawa
Angle-Resolved Photoemission Study of $Ni_2P(1010)$: Changea in the Surface Electronic Structure Induced by P Segregation
e-J. Surf. Sci. Nanotech., **12** (2014) 175.

M.Emori, A.Sakino, K.Ozawa and H.Sakama Polarization-Dependent ARPES Measurement for Valence Band of Anatase TiO_2
Solid State Commun., **188** (2014) 15.

X.Hao, S.Wang, W.Fu, T.Sakurai, S.Masuda and K.Akimoto
Novel Cathode Buffer Layer of Ag-Doped Bathocuproine for Small Molecule Organic Solar Cell with Inverted Structure
Organic Electronics, **15** (2014) 1773.

M.Yano, M.Endo, Y.Hasegawa, R.Okada, Y.Yamada and M.Sasaki
Well-Ordered Monolayers of Alkali-Doped Coronene and Picene: Molecular Arrangements and Electronic Structures
J. Chem. Phys., **141** (2014) 034708.

S.Hasegawa, S.Obara, F.Yoshida, Y.Azuma, F.Koike and T.Nagata
K-Shell Photoionization Spectra of Atomic Beryllium between $1s2s^2$ and $1s(2s2p^3P)4s$
Phys. Rev. A, **90** (2014) 032503.

3C

K.Hirano, Y.Takahashi and H.Sugiyama
Development and Application of Variable-Magnification X-Ray Bragg Magnifiers
Nucl. Instrum. Meth. Phys. Res. A, **741** (2014) 78.

K.Hirano, Y.Takahashi and H.Sugiyama
Application of Variable-Magnification X-Ray Bragg Magnifier to Analyzer-Based Phase-Contrast Computed Tomography
Jpn. J. Appl. Phys., **53** (2014) 040302.

K.Hiiragi, M.Naito, H.Watanabe, H.Maruyama and M.Ito
Estimation of Order Parameter and Spin Moment of Fe_3Pt by White X-Ray Diffraction Method
Key Engineering Materials, **596** (2014) 3.

T.Yamamoto, K.Hayashi, K.Suzuki and M.Ito
Detection of Structural Change of Pd-Cu-Ge Metallic Glass Thin Films upon Heat Treatment by using X-Ray Reflectivity
Jpn. J. Appl. Phys., **53** (2014) 05FH03.

S.Ji, K.Kojima, Y.Ishida, H.Yamaguchi, S.Saito, T.Kato, H.Tsuchida, S.Yoshida and H.Okumura
Characterization of the Defect Evolution in Thick Heavily Al-Doped 4H-SiC Epilayers
Materials Science Forum, **778-780** (2014) 151.

M.Ito, K.Suzuki, T.Tadenuma, R.Nagayasu, Y.Sakurai, Y.Onuki, E.Nishibori and M.Sakata
A study of Magnetic Moments of $CeRh_3B_2$ by X-Ray Magnetic Diffraction Experiments
J. Phys.: Conf. Ser., **502** (2014) 012018.

N.Watanabe
Development of X-Ray Differential Phase-Contrast Microscope using a Scanning Edge Filter and its Application to Phase Tomography
X-Ray Imaging Optics, **39** (2014) 1. (in Japanese).

S.Harada, Y.Yamamoto, S.Xiao, M.Tagawa and T.Ujihara
Surface Morphology and Threading Dislocation Conversion Behavior during Solution Growth of 4H-SiC using Al-Si Solvent
Materials Science Forum, **778-780** (2014) 67.

Y.Yamamoto, S.Harada, K.Seki, A.Horio, T.Mitsuhashi, D.Koike, M.Tagawa, and T.Ujihara
Low-Dislocation-Density 4H-SiC Crystal Growth Utilizing Dislocation Conversion during Solution Method
Appl. Phys. Express., **7** (2014) 065501.

S.Harada, Y.Yamamoto, K.Seki, A.Horio, M.Tagawa, and T.Ujihara
Different Behavior of Threading Edge Dislocation Conversion During the Solution Growth of 4H-SiC Depending on the Burgers Vector
Acta Mater., **81** (2014) 284.

4A

T.Kikugawa, Y.Abe, A.Nakamura and I.Nakai Investigation of Coloring Mechanism of Ancient Egyptian Copper-Red Glass and Consideration of the Manufacturing Process
BUNSEKI KAGAKU, **63** (2014) 31. (in Japanese).

N.Yamaguchi, T.Ohkura, Y.Takahashi, Y.Maejima and T.Arao
Arsenic Distribution and Speciation near Rice Roots Influenced by Iron Plaques and Redox Conditions of the Soil Matrix
Environ. Sci. Technol., **48** (2014) 1549.

A.Iida, I.Nishiyama and Y.Takanishi
Chiral Smectic Transition Phases Appearing near the Electric-Field-Induced Phase Transition Observed by Resonant Microbeam X-Ray Scattering
Phys. Rev. E, **89** (2014) 032503.

W.Satake, T.Mikouchi and M.Miyamoto
Redox States of Thirteen Shergottites as Inferred from Iron Micro X-Ray Absorption Near Edge Structure of Maskelynite
Geochemical Journal, **48** (2014) 85.

Y.Kimoto, A.Nishizawa, Y.Takanishi, A.Yoshizawa and J.Yamamoto
Layer Modulated Smectic-*C* Phase in Liquid Crystals with a Terminal Hydroxyl Group
Phys. Rev. E, **89** (2014) 042503.

T.Mikouchi, M.Komatsu, K.Hagiya, M.E.Zolensky, V.Hoffmann, J.Martinez, R.Hochleitner, M.Kaliwoda, Y.Terada, N.Yagi, M.Takata, W.Satake, Y.Aoyagi, A.Takenouchi, Y.Karouji, M.Uesugi and T.Yada
Mineralogy and Crystallography of Some Itokawa Particles Returned by the Hayabusa Asteroidal Sample Return Mission
Earth, Planets and Space, **66** (2014) 68.

Y.Takanishi, H.Yao, T.Fukasawa, K.Ema, Y.Ohtsuka, Y.Takahashi, J.Yamamoto, H.Takezoe and A.Iida
Local Orientational Analysis of Helical Filaments and Nematic Director in a Nano-Scale Phase Separation Composed of Rod-Like and Bent-Core Liquid Crystals using Small- and Wide-Angle X-Ray Microbeam Scattering
J. Phys. Chem. B, **118** (2014) 3998.

T.Sugiyama, M.Uo, T.Wada, T.Hongo, D.Omagari, K.Komiyama, H.Sasaki, H.Takahashi, M.Kusama and Y.Mori
Novel Metal Allergy Patch Test using Metal Nanoballs
Journal of Nanobiotechnology, **12** (2014) 51.

A.Matsuura and M.Kinebuchi
New Age Pathologists with the Synchrotron: How to Apply the Synchrotron-Based X-Ray Fluorescence Analysis to Pathological Diagnosis
J Nanomed Nanotechnol, **5** (2014) 121.

4B2

K.Fujii, Y.Esaki, K.Omoto, M.Yashima, A.Hoshikawa, T.Ishigaki, J.R.Hester
New Perovskite-Related Structure Family of Oxide-Ion Conducting Materials $NdBaInO_4$
Chem.Mater., **26** (2014) 2488.

M.Yashima, N.Kubo, K.Omoto, H.Fujimori, K.Fujii and K.Ohoyama
Diffusion Path and Conduction Mechanism of Protons in Hydroxyapatite
J. Phys. Chem. C, **118** (2014) 5180.

P.Barpanda, G.Oyama, S.Nishimura, S.-C.Chung and A.Yamada
A 3.8-V Earth-Abundant Sodium Battery Electrode
Nature Communications, **5** (2014) 4358.

G.Liu, S.Nishimura, S.C.Chung, K.Fuji, M.Yashima and A.Yamada
Defect Induced Sodium Disorder and Ionic Conduction Mechanism in $Na_{1.82}Mg_{1.09}P_2O_7$
J. Mater. Chem. A, **2** (2014) 18353.

K.Fujii and M.Yashima
Discovery of the New Structure Family of Oxide-Ion Conductor $NdBaIno_4$
Parity, **29(9)** (2014) 35. (in Japanese).

K.Fujii and M.Yashima
Discovery of the New Structure Family of Oxide-Ion Conducting Material
Ceramics, **49** (2014) 615. (in Japanese).

M.Yashima, K.Fujii, K.Omoto, U.Fumi, N.Kaneko, D.Haratake, K.Ueda, Y.Esaki, K.Hibino and S.Yamada
Crystal Structure Research on the Ceramic Materials for the Clean Energy using Overseas Facility
NSL News Letter, ISSP joint research on neutron scattering in facilities abroad, (2014) 12. (in Japanese).

K.Ueda, K.Omoto, K.Fujii, M.Yashima, T.Ishigaki, S.J.Kim and S.Lee
Crystal Structure and Electrical Conductivity of $LaSr_2Ga_{11}O_{20}$
NSL News Letter, ISSP Joint Research on Neutron Scattering in Facilities Abroad, (2014) 123. (in Japanese).

Y.Esaki, K.Fuji, K.Omoto, M.Yashima, T.Ishigaki, A.Hoshikawa and J.R.Hester
Crystal Structure and Electrical Conductivity of New Mixed Conductor $Nd_{2-x}Ba_xInO_{4.5-x/2}$
NSL News Letter, ISSP joint research on neutron scattering in facilities abroad, (2014) 124. (in Japanese).

4C

H.Nakao, H.Yamada, A.Sawa, K.Iwasa, J.Okamoto, T.Sudayama, Y.Yamasaki and Y.Murakami
Neutron Magnetic Scattering Study in Manganite Thin Film System
Solid State Commun., **185** (2014) 18.

H.Sakuma and J.Kawano
Structures of Mineral/Fluid Interfaces: Direct Observation by Surface X-Ray CTR Scattering Method
Chikyukagaku (Geochemistry), **48** (2014) 31. (in Japanese).

M.Kubota, H.Yamada, H.Nakao, J.Okamoto, Y.Yamasaki, A.Sawa and Y.Murakami
Magnetic and Electronic Properties of $(LaMnO_3)_5(SrMnO_3)_5$ Superlattice Revealed by Resonant Soft X-Ray Scattering
Jpn. J. Appl. Phys., **53** (2014) 05FH07.

K.Iwasa, M.Amano, H.Nakao and Y.Murakami
Structural Modulation of the Cage Lattice System DyB_6
JPS Conf. Proc., **3** (2014) 016026.

H.Morisaki, T.Koretsune, C.Hotta, J.Takeya, T.Kimura and Y.Wakabayashi
Large Surface Relaxation in the Organic Semiconductor Tetracene
Nature Communications, **5** (2014) 5400.

5A

Y.Yasutake, W.Kitagawa, M.Hata, T.Nishioka, T.Ozaki, M.Nishiyama, T.Kuzuyama and T.Tamura
Structure of the Quinoline N-Hydroxylating Cytochrome P450 RauA, an Essential Enzyme that Confers Antibiotic Activity on Aurachin Alkaloids
FEBS Letters, **588** (2014) 105.

S.Okada, T.Yamamoto, H.Watanabe, T.Nishimoto, H.Chaen, S.Fukuda, T.Wakagi and S.Fushinobu
Structural and Mutational Analysis of Substrate Recognition in Kojibiose Phosphorylase
FEBS J., **281** (2014) 778.

C.Iwasa, T.Tonozuka, M.Shinoda, Y.Sagane, K.Niwa, T.Watanabe, H.Yoshida, S.Kamitori, T.Takao, K.Oguma and A.Nishikawa
Purification, Crystallization and Preliminary X-Ray Analysis of an HA17-HA70(HA2-HA3) Complex from *Clostridium botulinum* Type C Progenitor Toxin
Acta Cryst. F, **70** (2014) 64.

T.Satoh, K.Suzuki, T.Yamaguchi and K.Kato
Structural Basis for Disparate Sugar-Binding Specificities in the Homologous Cargo Receptors ERGIC-53 and VIP36
PLOS ONE, **9** (2014) e87963.

T.Yokoyama, Y.Kosaka and M.Mizuguchi
Crystal Structures of Human Transthyretin Complexed with Glabridin
J. Med. Chem., **57** (2014) 1090.

Y.Shinohara, A.Miyanaga, F.Kudo and T.Eguchi
The Crystal Structure of the Amidohydrolase VinJ Shows a Unique Hydrophobic Tunnel for its Interaction with Polyketide Substrates
FEBS Letters, **588** (2014) 995

K.Kosami, I.Ohki, K.Hayashi, R.Tabata, S.Usugi, T.Kawasaki, T.Fujiwara, A.Nakagawa, K.Shimamoto and C.Kojima
Purification, Crystallization and Preliminary X-Ray Crystallographic Analysis of a Rice Rac/Rop GTPase, OsRac1
Acta Cryst. F, **70** (2014) 113.

S.Arai, Y.Yonezawa, M.Ishibashi, F.Matsumoto, M.Adachi, T.Tamada, H.Tokunaga, M.Blaber, M.Tokunaga and R.Kuroki
Structural Characteristics of Alkaline Phosphatase from the Moderately Halophilic Bacterium *Halomonas* sp.593
Acta Cryst. D, **70** (2014) 811.

D.Matsui, D.-H.Im, A.Sugawara, Y.Fukuta, S.Fushinobu, K.Isobe and Y.Asano
Mutational and Crystallographic Analysis of L-Amino Acid Oxidase/Monooxygenase from *Pseudomonas* sp. AIU 813: Interconversion between Oxidase and Monooxygenase Activities
FEBS Open Bio, **4** (2014) 220.

D.Takeshita, M.Kataoka, T.Miyakawa, K.Miyazono, S.Kumashiro, T.Nagai, N.Urano, A.Uzura, K.Nagata, S.Shimizu and M.Tanokura
Structural Basis of Stereospecific Reduction by Quinuclidinone Reductase
AMB express, **4** (2014) 6.

K.Sugimoto, M.Senda, D.Kasai, M.Fukuda, E.Masai and T.Senda
Molecular Mechanism of Strict Substrate Specificity of an Extradiol Dioxygenase, DesB, Derived from *Sphingobium* sp. SYK-6.
PLOS ONE, **9** (2014) e92249.

T.Ito, K.Saikawa, S.Kim, K.Fujita, A.Ishiwata, S.Kaeothip, T.Arakawa, T.Wakagi, G.T.Beckham, Y.Ito, S.Fushinobu
Crystal Structure of Glycoside Hydrolase Family 127 β-L-Arabinofuranosidase from *Bifidobacterium longum*
Biochem. Biophys. Res. Commun., **447** (2014) 32.

H.Unno, S.Goda and T.Hatakeyama
Hemolytic Lectin CEL-III Heptamerizes via a Large Structural Transition from α-Helices to a β-Barrel during the Transmembrane Pore-Formation Process
J. Biol. Chem., **289** (2014) 12805.

L.Wang, X.Yang, S.Li, Z.Wang, Y.Liu, J.Feng, Y.Zhu and Y.Shen
Structural and Mechanistic Insights into MICU1 Regulation of Mitochondrial Calcium Uptake
EMBO J., **33** (2014) 594.

T.Tsuda, M.Asami, Y.Koguchi and S.Kojima
Single Mutation Alters the Substrate Specificity of L-Amino Acid Ligase
Biochemistry, **53** (2014) 2650.

Y.Kanoh, S.Uehara, H.Iwata, K.Yoneda, T.Ohshima and H.Sakuraba
Structural Insight into Glucose Dehydrogenase from the Thermoacidophilic Archaeon *Thermoplasma volcanium*
Acta Cryst. D, **70** (2014) 1271.

C.Feng, Y.Liu, G.Wang, Z.Deng, Q.Zhang, W.Wu, Y.Tong, C.Cheng and Z.Chen
Crystal Structures of the Human RNA Demethylase Alkbh5 Reveal Basis for Substrate Recognition
J. Biol. Chem., **289** (2014) 11571.

Z.Deng, K.C.Lehmann, X.Li, C.Feng, G.Wang, Q.Zhang, X.Qi, L.Yu, X.Zhang, W.Feng, W.Wu, P.Gong, Y.Tao, C.C.Posthuma, E.J.Snijder, A.E.Gorbalenya and Z.Chen
Structural Basis for the Regulatory Function of a Complex Zinc-Binding Domain in a Replicative Arterivirus Helicase Resembling a Nonsense-Mediated mRNA Decay Helicase
Nucleic Acids Research, **42** (2014) 3464.

Y.Ishida, W.Tsuchiya, T.Fujii, Z.Fujimoto, M.Miyazawa, J.Ishibashi, S.Matsuyama, Y.Ishikawa and T.Yamazaki
Niemann-Pick Type C2 Protein Mediating Chemical Communication in the Worker Ant
Proc. Natl. Acad. Sci. USA, **111** (2014) 3847.

T.Maehara, Z.Fujimoto, H.Ichinose, M.Michikawa, K.Harazono and S.Kaneko
Crystal Structure and Characterization of the Glycoside Hydrolase Family 62 α-L –Arabinofuranosidase from *Streptomyces coelicolor*
J. Biol. Chem., **289** (2014) 7962.

N.Suzuki, Z.Fujimoto, Y.-M.Kim, M.Momma, N.Kishine, R.Suzuki, S.Suzuki, S.Kitamura, M.Kobayashi, A.Kimura and K.Funane
Structural Elucidation of the Cyclization Mechanism of α-1,6-Glucan by *Bacillus circulans* T-3040 Cycloisomaltooligosaccharide Glucanotransferase
J. Biol. Chem., **289** (2014) 12040.

A.Kishimoto, A.Kita, T.Ishibashi, H.Tomita, Y.Yokooji, T.Imanaka, H.Atomi and K.Miki
Crystal Structure of Phosphopantothenate Synthetase from *Thermococcus kodakarensis*
Proteins **82** (2014) 1924.

M.Elahi, M.M.Islam, K.Noguchi, M.Yohda, H.Toh, Y.Kuroda
Computational Prediction and Experimental Characterization of a ″Size Switch Type Repacking" during the Evolution of Dengue Envelope Protein Domain III (ED3)
BBA Protein and Proteomics **1833** (2014) 585.

T.Shimegi, T.Ooyama, T.Ohtsuki, G.Kurisu, M.Kusunoki and S.Ui
Crystallization and Preliminary X-Ray Diffraction Analysis of Domain-Chimeric L-(2*S*,3*S*)-Butanediol Dehydrogenase
Acta Cryst. F, **70** (2014) 461.

E.Tamai, H.Yoshida, H.Sekiya, H.Nariya, S.Miyata, A.Okabe, T.Kuwahara, J. Maki and S.Kamitori
X-Ray Structure of a Novel Endolysin Encoded by Episomal Phage PhiSM101 of *Clostridium perfringens*
Molecular Microbiology, **92** (2014) 326.

Y.Fujioka, S.W.Suzuki, H.Yamamoto, C.Kondo-Kakuta, Y.Kimura, H.Hirano, R.Akada, F.Inagaki, Y.Ohsumi and N.N.Noda
Structural Basis of Starvation-Induced Assembly of the Autophagy Initiation Complex
Nature Structural Molecular Biology, **21** (2014) 513.

X.Liu, Y.Yin, J.Wu and Z.Liu
Structure and Mechanism of an Intramembrane Liponucleotide Synthetase Central for Phospholipid Biosynthesis
Nature Communications, **5** (2014) 4244.

H.Yokoyama and S.Fujii
Structures and Metal-Binding Properties of *Helicobacter pylori* Neutrophil-Activating Protein with a Di-Nuclear Ferroxidase Center
Biomolecules, **4** (2014) 600.

S.Akai, H.Ikushiro, D.Sawai, H.Hayashi, N.Kamiya and I.Miyahara
Crystallographic Study of Homoserine Dehydrogenase from *Thermus thermophius* HB8
Vitamins, **88** (2014) 358. (in Japanese).

T.Mise, H.Matsunami, F.A.Samatey and I.N.Maruyama
Crystallization and Preliminary X-Ray Diffraction Analysis of the Periplasmic Domain of the *Escherichia coli* Aspartate Receptor Tar and its Complex with Aspartate
Acta Cryst. F, **70** (2014) 1219.

M.Kanagawa, Y.Liu, S.Hanashima, A.Ikeda, W.Chai, Y.Nakano, K.Kojima-Aikawa, T.Feizi and Y.Yamaguchi
Structural Basis for Multiple Sugar Recognition of Jacalin-Related Human ZG16p Lectin
J. Biol. Chem., **289** (2014) 16954.

S.Kamachi, K.Wada, M.Tamoi, S.Shigeoka and T.Tada
The 2.2 ÃResolution Structure of the Catalase- Peroxidase KatG from *Synechococcus elongatus* PCC7942
Acta Cryst. F, **70** (2014) 288.

H.Tsukagoshi, A.Nakamura, T.Ishida, K.K.Touhara, M.Otagiri, S.Moriya, M.Samejima, K.Igarashi, S.Fushinobu, K.Kitamoto and M.Arioka
Structural and Biochemical Analyses of Glycoside Hydrolase Family 26 *β*-Mannanase from a Symbiotic Protist of the Termite *Reticulitermes speratus*
J. Biol. Chem., **289** (2014) 10843.

K.K.Touhara, T.Nihira, M.Kitaoka, H.Nakai and S.Fushinobu
Structural Basis for Reversible Phosphorolysis and Hydrolysis Reactions of 2-*O*-α-Glucosylglycerol Phosphorylase
J. Biol. Chem., **289** (2014) 18067.

K.Suzuki, A.Hori, K.Kawamoto, R.R.Thangudu, T.Ishida, K.Igarashi, M.Samejima, C.Yamada, T.Arakawa, T.Wakagi, T.Koseki and S.Fushinobu
Crystal Structure of a Feruloyl Esterase Belonging to the Tannase Family: A Disulfide Bond Near a Catalytic Triad
Proteins, **82** (2014) 2857.

H.Zhao, G.Sheng, J.Wang, M.Wang, G.Bunkoczi, W.Gong, Z.Wei and Y.Wang
Crystal Structure of the RNA-Guided Immune Surveillance Cascade Complex in *Escherichia coli*
Nature, **515** (2014) 147.

Y.Itoh, M.J.Bröcker, S.Sekine, D.Söll and S.Yokoyama
Dimer-Dimer Interaction of the Bacterial Selenocysteine Synthase SelA Promotes Functional Active-Site Formation and Catalytic Specificity
J. Mol. Biol., **426** (2014) 1723.

A.Miyanaga, J.Cieślak, Y.Shinohara, F.Kudo and T.Eguchi
The Crystal Structure of the Adenylation Enzyme VinN Reveals a Unique β-Amino Acid Recognition Mechanism
J. Biol. Chem., **289** (2014) 31448.

M.Koyama, N.Shirai and Y.Matsuura
Structural Insights into How Yrb2p Accelerates the Assembly of the Xpo1p Nuclear Export Complex
Cell Reports, **9** (2014) 983.

T.Yokoyama, Y.Kosaka and M.Mizuguchi
Inhibitory Activities of Propolis and its Promising Component, Caffeic Acid Phenethyl Ester, against Amyloidogenesis of Human Transthyretin
J. Med. Chem, **57** (2014) 8928.

H.Yoshida, A.Yoshihara, M.Teraoka, Y.Terami, G.Takata, K.Izumori and S.Kamitori
X-Ray Structure of a Novel L-Ribose Isomerase Acting on a Non-Natural Sugar L-Ribose as its Ideal Substrate
FEBS J., **281** (2014) 3150.

K.Kosami, I.Ohki, M.Nagano, K.Furuita, T.Sugiki, Y.Kawano, T.Kawasaki, T.Fujiwara, A.Nakagawa, K.Shimamoto and C.Kojima
The Crystal Structure of the Plant Small GTPase OsRac1 Reveals its Mode of Binding to NADPH Oxidase
J. Biol. Chem., **289** (2014) 28569.

J.Lu, Y.Gu, J.Feng, W.Zhou, X.Yang and Y.Shen
Structural Insight into the Central Element Assembly of the Synaptonemal Complex
Scientific Reports, **4** (2014) 7059.

Z.Wang, X.Yang, S.Guo, Y.Yang, X.C.Su, Y.Shen and J.Long
Crystal Structure of the Ubiquitin-Like Domain-CUT Repeat-Like Tandem of Special AT-Rich Sequence Binding Protein 1 (SATB1) Reveals a Coordinating DNA-Binding Mechanism
J. Biol. Chem., **289** (2014) 27376.

J.P.Maianti, H.Kanazawa, P.Dozzo, R.D.Matias, L.A.Feeney, E.S.Armstrong, D.J.Hildebrandt, T.R.Kane, M.J.Gliedt, A.A.Goldblum, M.S.Linsell, J.B.Aggen, J.Kondo and S.Hanessian
Toxicity Modulation, Resistance Enzyme Evasion, and A-Site X-Ray Structure of Broad-Spectrum Antibacterial Neomycin Analogs
ACS Chemical Biology, **9** (2014) 2067.

J.Y.Kim, C.W.Kim, Y.K.Park, N.Y.Kang, N.H.Heo and K.Seff
First Successful Application of the Thallous Ion Exchange (TIE) Method. Preparation of Fully Indium- Exchanged Zeolite Y (FAU, Si/Al = 1.69)
J. Phys. Chem. C, **118** (2014) 24655.

G.Wang, Q.He, C.Feng, Y.Liu, Z.Deng, X.Qi, W.Wu, P.Mei and Z.Chen
The Atomic-Resolution Structure of Human Alkb Homolog 7 (ALKBH7), a Key Protein for Programmed Necrosis and Fat Metabolism
J. Biol. Chem., **289** (2014) 27924.

K.Ito, T.Honda, T.Suzuki, T.Miyoshi, R.Murakami, M.Yao and T.Uchiumi
Molecular Insights into the Interaction of the Ribosomal Stalk Protein with Elongation Factor 1α
Nucleic Acids Res., **42** (2014) 14042.

P.Zhou, Y.Liu, Q.Yan, Z.Chen, Z.Qin and Z.Jiang
Structural Insights into the Substrate Specificity and Transglycosylation Activity of a Fungal Glycoside Hydrolase Family 5 β-Mannosidase
Acta Cryst. D, **70** (2014) 2970.

Y.Kawaguchi, K.Yoneda, T.Torikata and T.Araki
Asp48 Function in the Hydrogen-Bonding Network Involving Asp52 of Hen Egg-White Lysozyme.
Biosci., Biotechnol., Biochem., **16** (2014) 1-9.

K.Inoue, Y.Usami, Y.Ashikawa, H.Noguchi, T.Umeda, A.Y.Ashikawa, T.Horisaki, H.Uchimura, T.Terada, S.Nakamura, K.Shimizu, H.Habe, H.Yamane, Z.Fujimoto and H.Nojiri
Structural Basis of the Divergent Oxygenation Reactions Catalyzed by the Rieske Nonheme Iron Oxygenase Carbazole 1,9a-Dioxygenase.
Appl. Environ. Microbiol., **80** (2014) 2821.

J.Matsuzawa, H.Aikawa, T.Umeda, Y.Ashikawa, C.S.Minakuchi, Y.Kawano, Z.Fujimoto, K.Okada, H.Yamane and H.Nojiri
Crystallization and Preliminary X-Ray Diffraction Analyses of the Redox-Controlled Complex of Terminal Oxygenase and Ferredoxin Components in the Rieske Nonhaem Iron Oxygenase Carbazole 1,9a-Dioxygenase
Acta Cryst. F, **70** (2014) 1406.

F.Hou, T.Miyakawa, M.Kataoka, D.Takeshita, S.Kumashiro, A.Uzura, N.Urano, K.Nagata, S.Shimizu and M.Tanokura
Structural Basis for High Substrate-Binding Affinity and Enantioselectivity of 3-Quinuclidinone Reductase AtQR.
Biochem. Biophys. Res. Commun., **446** (2014) 911.

A.Nishizawa, A.Harada, M.Senda, Y.Tachihara, D.Muramatsu, S.Kishigami, S.Mori, K.Sugiyama, T.Senda and S.Kimura
Complete Pyridine Nucleotide-Specificity Conversion of an NADH-Dependent Ferredoxin Reductase.
Biochem. J, **462** (2014) 257.

K.Ishibashi, Y.Kezuka, C.Kobayashi, M.Kato, T.Inoue, T.Nonaka, M.Ishikawa, H.Matsumura and E.Katoh
Structural Basis for the Recognition-Evasion Arms Rase between *Tomato Mosaic Virus* and the Resistance Gene *Tm*-1
Proc. Natl. Acad. Sci. USA, **111** (2014) 3486.

M.Nagae, K.M.Matsumoto, M.Kato, M.K.Kaneko, Y.Kato and Y.Yamaguchi
A Platform of C-Type Lectin-Like Receptor CLEC-2 for Binding *O*-Glycosylated Podoplanin and Nonglycosylated Rhodocytin
Structure, **22** (2014) 1711.

N.Takahashi, S.H.Nakahara, Y.Itoh, K.Takemura, A.Shimada, Y.Ueda, M.Kitamata, R.Matsuoka, K.H.Suetsugu, Y.Senju, M.X.Mori, S.Kiyonaka, D.Kohda, A.Kitao, Y.Mori and S.Suetsugu
TRPV4 Channel Activity is Modulated by Direct Interaction of the Ankyrin Domain to PI(4,5)P_2
Nature Communications, **5** (2014) 4994.

T.Tomita, T.Ozaki, K.Matsuda, M.Nishiyama and T.Kuzuyama
Crystallization and Preliminary X-Ray Diffraction Analysis of Cyclolavandulyl Diphosphate Synthase, a New Member of the *Cis*-Isoprenyl Diphosphate Synthase Superfamily
Acta Cryst. F, **70** (2014) 1410.

S.Tashiro, J.M.M.Caaveiro, C.X.Wu, Q.Q.Hoang and K.Tsumoto
Thermodynamic and Structural Characterization of the Specific Binding of Zn(II) to Human Protein DJ-1
Biochemistry, **53** (2014) 2218.

C.Han, A.K.Tachikawa, A.Shimizu, D.Zhu, H.Nakamura, E.Adachi, T.Kikuchi, M.Koga, T.Koibuchi, G.F.Gao, Y.Sato, A.Yamagata, E.Martin, S.Fukai, Z.L.Brumme and A.Iwamoto
Switching and Emergence of CTL Epitopes in HIV-1 Infection
RETROVIROLOGY, **11** (2014) 38.

Y.Nishikawa, T.Oyama, N.Kamiya, T.Kon, Y.Y.Toyoshima, H.Nakamura and G.Kurisu
Structure of the Entire Stalk Region of the Dynein Motor Domain
J. Mol. Biol., **426** (2014) 3232.

T.T.Thach and S.H.Lee
New Crystal Structures of Adenylate Kinase from *Streptococcus Pneumoniae* D39 in Two Conformations
Acta Cryst. F, **70** (2014) 1468.

H.S.Kim, J.Kim, H.N.Im, D.R.An, M.Lee, D.Hesek, S.Mobashery, J.Y.Kim, K.Cho, H.J.Yoon, B.W.Han, B.I.Lee and S.W.Suh
Structural Basis for the Recognition of Muramyltripeptide by *Helicobacter Pylori* Csd4, a D,L-Carboxypeptidase Controlling the Helical Cell Shape
Acta Cryst. D, **70** (2014) 2800.

T.T.Thach, T.T.Luong, S.H.Lee and D.K.Rhee
Adenylate Kinase from Streptococcus Pneumoniae Is Essential for Growth Through Its Catalytic Activity
FEBS Open Bio., **4** (2014) 672.

S.J.Lee, Y.S.Park, S.J.Kim, B.J.Lee and S.W.Suh
Crystal Structure of PhoU from *Pseudomonas aeruginosa*, a Negative Regulator of the Pho Regulon
J. Struct. Biol., **188** (2014) 22.

Y.Anami, T.Itoh, D.Egawa, N.Yoshimoto and K.Yamamoto
A Mixed Population of Antagonist and Agonist Binding Conformers in a Single Crystal Explains Partial Agonism against Vitamin D Receptor: Active Vitamin D Analogues with 22*R*-Alkyl Group
J. Med. Chem., **57** (2014) 4351.

K.Yamamoto, Y.Anami and T.Itoh
Development of Vitamin D Analogs Modulating the Pocket Structure of Vitamin D Receptor
Curr. Top. Med. Chem., **14** (2014) 2378.

T.Kudo, M.Ishizawa, K.Maekawa, M.Nakabayashi, Y.Watarai, H.Uchida, H.Tokiwa, T.Ikura, N.Ito, M.Makishima and S.Yamada
Combination of Triple Bond and Adamantane Ring on the Vitamin D Side Chain Produced Partial Agonists for Vitamin D Receptor
J. Med. Chem., **57** (2014) 4073.

T.Fujiwara, W.Saburi, H.Matsui, H.Mori and M.Yao
Structural Insights into the Epimerization of Beta- 1,4-Linked Oligosaccharides Catalyzed by Cellobiose 2- Epimerase, the Sole Enzyme Epimerizing Non-Anomeric Hydroxyl Groups of Unmodified Sugars
J. Biol. Chem., **289** (2014) 3405.

X.Shen, W.Saburi, Z.Q.Gai, K.Komoda, J.Yu, T.O.Kato, Y.Kido, H.Matsui, H.Mori and M.Yao
Crystallization and Preliminary X-Ray Crystallographic Analysis of α-Glucosidase HaG from *Halomonas* sp. Strain H11
Acta Cryst. F, **70** (2014) 464.

M.Hasegawa, S.T.Fukai, JD.Kim, A.Fukamizu and T.Shimizu
Protein Arginine Methyltransferase 7 has a Novel Homodimer-Like Structure Formed by Tandem Repeats
FEBS Letters, **588** (2014) 1942.

E.Yoo, D.Salunke, D.Sil, X.Guo, A.Salyer, A.Hermanson, M.Kumar, S.S.Malladi, R.Balakrishna, W.H.Thompson, H.Tanji, U.Ohto, T.Shimizu and S.A.David
Determinants of Activity at Human Toll-Like Receptors 7 and 8: Quantitative Structure-Activity Relationship (QSAR) of Diverse Heterocyclic Scaffolds
J. Med. Chem., **57** (2014) 7955.

6A

Y.Kawabata, K.Hayashi, T.Kanao and A.Ishikawa
Bilayer Structure of Ester-Amide-Type Cationic Surfactants in a Dilute Aqueous Solution
Colloids and Surfaces A: Physicochemical and Engineering Aspects, **441** (2014) 140.

T.Yamamoto, H.Okuda, K.Takeshita, N.Usami, Y.Kitajima and H.Ogawa
Grazing-Incidence Small-Angle X-Ray Scattering from Ge Nanodots Self-Organized on Si(001) Examined with Soft X-Rays
J. Synchrotron Rad., **21** (2014) 161.

H.Okuda, T.Horiuchi, T.Maruyama, M.Yamasaki, Y.Kawamura, K.Hagiwara and S.Kohara
Development of Microstructures of Long-Period Stacking Ordered Structures in $Mg_{85}Y_9Zn_6$ Alloys Annealed at 673 K(400^{o} C) Examined by Small-Angle X-Ray Scattering
Metallurgical and Materials Transactions A, **45** (2014) 147.

S.Duangjit, Y.Obata, H.Sano, Y.Onuki, P.Opanasopit, T.Ngawhirunpat, T.Miyoshi, S.Kato and K.Takayama
Comparative Study of Novel Ultradeformable Liposomes: Menthosomes, Transfersomes and Liposomes for Enhancing Skin Permeation of Meloxicam
Biol. Pharm. Bull, **37** (2014) 239.

K.Hemmi, G.Matsuba, H.Tsuji, T.Kawai, T.Kanaya, K.Toyohara, A.Oda and K.Endou
Precursors in Stereo-Complex Crystals of Poly($_{L}$-Lactic Acid)/Poly($_{D}$-Lactic Acid) Blends under Shear Flow
J. Appl. Cryst., **47** (2014) 14.

F.Kaneko, N.Seto, K.Sasaki and S.Sakurai
Multiple Site Occupation of Flexible Polymeric Compounds in Cocrystals of Syndiotactic Polystyrene
Chem. Lett., **43** (2014) 904.

G.Cui, M.Fujikawa, S.Nagano, M.Sano, H.Takase, T.Miyazaki, S.Sakurai and K.Yamamoto
Perpendicular Oriented Cylinders via Directional Coalescence of Spheres Embedded in Block Copolymer Films Induced by Solvent Annealing
Polymer, **55** (2014) 1601.

K.Yamamoto, K.Ohara, G.Cui, R.Tanaka, D.Shimada, S.Nagano, M.Sano, S.Sakurai, K.Shimokita and T.Miyazaki
Solvent Annealing Induced Perpendicular Orientation of Microdomains in Block Copolymer Thin Films
Kobunshi Ronbunshu, **71** (2014) 104. (*in Japanese*).

M.Hishida, K.Tanaka, Y.Yamamura and K.Saito
Cooperativity between Water and Lipids in Lamellar to Inverted-Hexagonal Phase Transition
J. Phys. Soc. Jpn., **83** (2014) 044801.

R.Hori, Y.Miwa, K.Yamamoto and S.Kutsumizu
Phase Structure and Phase Transition Mechanism for Light-Induced *Ia3d* Cubic Phase in 4'-*n*-Docosyloxy-3'-Nitrobiphenyl-4-Carboxlic Acid/Ethyl 4-(4'-*n*-Docosyloxyphenylazo)Benzoate Binary Mixture
J. Phys. Chem. B, **118** (2014) 3743.

H.Okuda, T.Horiuchi, M.Yamasaki, Y.Kawamura and S.Kohara
In Situ Measurements on Stability of Long-Period Stacking-Ordered Structures in $Mg_{85}Y_9Zn_6$ Alloys during Heating Examined by Multicolor Synchrotron Radiation Small-Angle Scattering
Scripta Materialia, **75** (2014) 66.

H.Okuda, T.Yamamoto, K.Takeshita, M.Hirai, K.Senoo, H.Ogawa and Y.Kitajima
Normalization of Grazing-Incidence Small Angle Scattering of Phospholipid Alloy Systems at the K Absorption Edge of Phosphorous: A Standard Sample Approach
Jpn. J. Appl. Phys., **53** (2014) 05FH02.

G.Cui, M.Fujikawa, S.Nagano, K.Shimokita, T.Miyazaki, S.Sakurai and K.Yamamoto
Macroscopic Alignment of Cylinders via Directional Coalescence of Spheres along Annealing Solvent Permeation Directions in Block Copolymer Thick Films
Macromolecules, **47** (2014) 5989.

A.B.Imran, K.Esaki, H.Gotoh, T.Seki, K.Ito, Y.Sakai and Y.Takeoka
Extremely Stretchable Thermosensitive Hydrogels by Introducing Slide-Ring Polyrotaxane Cross-Linkers and Ionic Groups into the Polymer Network
Nature Communications, **5** (2014) 5124.

F.Kaneko
Cocrystallization of Syndiotactic Polystyrene by a Guest Exchange Phenomenon: Investigation of the Mechanism and Preparation of Polymer Composites
Kobunshi Ronbunshu, **71** (2014) 540. (*in Japanese*).

Y.Maki, K.Furusawa, S.Yasuraoka, H.Okamura, N.Hosoya, M.Sunaga, T.Dobashi, Y.Sugimoto and K.Wakabayashi
Universality and Specificity in Molecular Orientation in Anisotropic Gels Prepared by Diffusion Method
Carbohydr. Polym., **108** (2014) 118.

M.Hishida, Y.Yamamura and K.Saito
Salt Effects on Lamellar Repeat Distance Depending on Head Groups of Neutrally Charged Lipids
Langmuir, **30** (2014) 10583.

M.Hishida
Correlation between Hydration States and Self-assembly Structures of Phospholipid and Surfactant
C & I Commun, **39** (2014) 17. (*in Japanese*).

M.Sano, S.Nakamura, M.Hara, S.Nagano, Y.Shinohara, Y.Amemiya and T.Seki
Pathways Toward Photoinduced Alignment Switching in Liquid Crystalline Block Copolymer Films
Macromolecules, **47** (2014) 7178.

I.Saito, T.Okamoto, K.Shimokita, T.Miyazaki and K.Yamamoto
Perpendicular Orientation of Cylindrical Microdomains of $FeCl_3$ Doped Polystyrene-*b*-poly(2-vinyl pyridine) Thin Films
Koubunshi Ronbunshu, **71** (2014) 586. (*in Japanese*).

Former 6A

D.Matsui, D.-H.Im, A.Sugawara, Y.Fukuta, S.Fushinobu, K.Isobe and Y.Asano
Mutational and Crystallographic Analysis of L-Amino Acid Oxidase/Monooxygenase from *Pseudomonas* sp. AIU 813: Interconversion between Oxidase and Monooxygenase Activities
FEBS Open Bio, **4** (2014) 220.

T.Ito, K.Saikawa, S.Kim, K.Fujita, A.Ishiwata, S.Kaeothip, T.Arakawa, T.Wakagi, G.T.Beckham, Y.Ito, S.Fushinobu
Crystal Structure of Glycoside Hydrolase Family 127 β-L-Arabinofuranosidase from *Bifidobacterium longum*
Biochem. Biophys. Res. Commun., **447** (2014) 32.

N.Suzuki, Z.Fujimoto, Y.-M.Kim, M.Momma, N.Kishine, R.Suzuki, S.Suzuki, S.Kitamura, M.Kobayashi, A.Kimura and K.Funane
Structural Elucidation of the Cyclization Mechanism of α-1,6-Glucan by *Bacillus circulans* T-3040 Cycloisomaltooligosaccharide Glucanotransferase
J. Biol. Chem., **289** (2014) 12040.

H.Yokoyama and S.Fujii
Structures and Metal-Binding Properties of *Helicobacter pylori* Neutrophil-Activating Protein with a Di-Nuclear Ferroxidase Center
Biomolecules, **4** (2014) 600.

Y.Ikehara, K.Arai, N.Furukawa, T.Ohno, T.Miyake, S.Fushinobu, M.Nakajima, A.Miyanaga and H.Taguchi The Core of Allosteric Motion in *Thermus caldophilus* L-Lactate Dehydrogenase
J. Biol. Chem., **289** (2014) 31550.

Z.Wang, L.Li and X.D.Su
Structural and Functional Characterization of a Novel α/β Hydrolase from Cariogenic Pathogen *Streptococcus Mutans*
Proteins, **82** (2014) 695.

6C

K.Fukuda and K.Kumagai
Dot-Like Formation of Metal Nanocrystals from Exfoliated Ruthenate Nanosheets
E-Journal. Surface Science and Nanotechnology, **12** (2014) 97.

S.Hosokawa, N.Happo, K.Hayashi, A.Ohnishi, M.Kitaura and M.Sasaki
An X-Ray Fluorescence Holographic Study on a $Bi_2Te_3Mn_{0.1}$ Topological Insulator
J. Phys.: Conf. Ser., **502** (2014) 012024.

M.Kimura
Synchrotron Radiation Shed Light to *In Situ* and Dynamic Observation of High-Temperature Processes e-J. Surf. Sci. Nanotech., **12** (2014) 1.

B.-W.Li, M.Osada, Y.Ebina, K.Akatsuka, K.Fukuda and T.Sasaki
High Thermal Robustness of Molecularly Thin Perovskite Nanosheets and Implications for Superior Dielectric Properties
ACS Nano, **8** (2014) 5449.

M.Okube and S.Sasaki
Site-Specific Electronic Structures of Ferrimagnetic Fe_3O_4 Measured by Resonant X-Ray Magnetic Scattering
J. Appl. Cryst., **47** (2014) 1387.

M.Okube and S.Sasaki
Resonant X-Ray Scattering and Crystal Structure Analyses
J. Cryst. Soc. Jpn., **56** (2014) 158. (in Japanese).

S.Sasaki
Magnetic Structure Examined by Synchrotron X-Rays
Crystallography in Japan (II), (2014) 99. (in Japanese).

S.Hosokawa, N.Happo, S.Senba, T.Ozaki, T.Matsushita, A.Koura, F.Shimojo and K.Hayashi
Local Clusters in a Distorted Rocksalt GeTe Crystal Found by X-Ray Fluorescence Holography
J. Phys. Soc. Jpn., **83** (2014) 124602.

M.Osada, S.Yoguchi, M.Itose, B.Li, Y.Ebina, K.Fukuda, Y.Kotani, K.Ono, S.Ueda and T.Sasaki
Controlled Doping of Semiconducting Titania Nanosheets for Tailored Spinelectronic Materials
Nanoscale, **6** (2014) 14227.

N.Happo, K.Hayashi, S.Senba, H.Sato, M.Suzuki and S.Hosokawa
Distorted and Undistorted Atomic Sites in a Ferromagnetic Semiconductor $Ge_{0.6}Mn_{0.4}Te$ Film Determined by X-Ray Fluorescence Holography
J. Phys. Soc. Jpn., **83** (2014) 113601.

K.Hayashi, N.Happo and S.Hosokawa
Applications of X-Ray Fluorescence Holography to Determine Local Lattice Distortions
J. Elec. Spec. Relat. Phenom., **195** (2014) 337.

7A

K.Amemiya, M.Sakamaki, M.Mizusawa and M.Takeda
Twisted Magnetic Structure in Ferromagnetic Ultrathin Ni Films Induced by Magnetic Anisotropy Interaction with Antiferromagnetic FeMn
Phys. Rev. B, **89** (2014) 054404.

S.Kaneko and M.Kiguchi
Investigation on the Pyrazine Molecular Junction Studied by Conductance Measurement and Near Edge X-Ray Absorption Fine Structure
Fullerenes, Nanotubes, and Carbon Nanostructures, **22** (2014) 166.

Y.Nanba, D.Asakura, M.Okubo, H.S.Zhou, K.Amemiya, K.Okada, P.-A.Glans, C.A.Jenkins, E.Arenholz and J.H.Guo
Anisotropic Charge-Transfer Effects in the Asymmetric $Fe(CN)_5NO$ Octahedron of Sodium Nitroprusside: a Soft X-Ray Absorption Spectroscopy Study
Phys. Chem. Chem. Phys., **16** (2014) 7031.

J.Takashiro, Y.Kudo, S.Kaneko, K.Takai, T.Ishii, T.Kyotani, T.Enoki and M.Kiguchi
Heat Treatment Effect on the Electronic and Magnetic Structures of Nanographene Sheets Investigated through Electron Spectroscopy and Conductance Measurements
Phys. Chem. Chem. Phys., **16** (2014) 7280.

Y.Kudo, M.Kiguchi, J.Takashiro, K.Takai and T.Enoki
Development of Edge State on Graphite Surface Induced by Ar^+ Irradiation Studied using Near-Edge X-Ray Absorption Fine Structure Spectroscopy
Carbon, **72** (2014) 152.

S.-J.Hao, V.L.J.Joly, S.Kaneko, J.Takashiro, K.Takai, H.Hayashi, T.Enoki and M.Kiguchi
Magnetic Edge-States in Nanographene, HNO_3 - Doped Nanographene and its Residue Compounds of Nanographene-Based Nanoporous Carbon
Phys. Chem. Chem. Phys., **16** (2014) 6273.

M.Sakamaki and K.Amemiya
Enhancement of Perpendicular Magnetic Anisotropy by Compressive Strain in Alternately Layered FeNi Thin Films
J. Phys.: Condens. Matter, **26** (2014) 166002.

M.Yoshida and H.Kondoh
In-Situ Observation of Model Catalysts under Reaction Conditions using X-Ray Core-Level Spectroscopy
Chem. Rec., **14** (2014) 806.

S.Kanai, M.Tsujikawa, Y.Miura, M.Shirai, F.Matsukura and H.Ohno
Magnetic Anisotropy in Ta/CoFeB/MgO Investigated by X-Ray Magnetic Circular Dichroism and First-Principles Calculation
Appl. Phys. Lett., **105** (2014) 222409.

H.Kondoh, Y.Higashi, M.Yoshida, Y.Monya, R.Toyoshima, K.Mase, K.Amemiya, F.Tsukioka, M.Nagasaka, Y.Iwasawa, H.Orita, K.Mukai and J.Yoshinobu
Structure and Photo-Induced Charge Transfer of Pyridine Molecules Adsorbed on TiO_2(110): A NEXAFS and Core-Hole-Clock Study
Electrochemistry, **82** (2014) 341.

J.Takashiro, Y.Kudo, S.J.Hao, K.Takai, D.N.Futaba, T.Enoki and M.Kiguchi
Preferential Oxidation-Induced Etching of Zigzag Edges in Nanographene
Phys. Chem. Chem. Phys., **16** (2014) 21363.

T.Miyanaga, K.Takasugi, T.Ohba, T.Aida and T.Okazaki
Magnetic and Local Structure Analysis for Fe/Cr Multilayer Films
J. Phys. Conf. Ser, **502** (2014) 012032.

7C

M.Morikawa, N.Ahmed, Y.Yoshida, Y.Izumi Photoconversion of Carbon Dioxide in Zinc-Copper- Gallium Layered Double Hydroxides: the Kinetics to Hydrogen Carbonate and Further to CO/Methanol
Appl. Catal. B, **144** (2014) 561.

R.Otsuka and H.Yoshitake
Different Modes of Adsorptions of Arsenate on Silica Grafted with Fe^{3+}-Coordinated Silanes
Journal of Colloid and Interface Science, **415** (2014) 143.

Y.Tezuka, T.Sasaki, Y.Fujita, T.Iwamoto, H.Osawa, S.Nozawa, N.Nakajima, H.Sato and T.Iwazumi
Core Excitations in Resonant X-Ray Raman Scattering of Titanium Oxides: An Approach to Studying Electronic Structures
J. Phys. Soc. Jpn., **83** (2014) 014707.

K.Oka, Y.Ogura and Y.Izumi
X-Ray Evaluation of the Boundary between Polymer Electrolyte and Platinum and Carbon Functionalization to Conduct Protons in Polymer Electrolyte Fuel Cells
J. Power Sources, **258** (2014) 83.

K.Ikeue, K.Watanabe, T.Minekishi, A.Imamura, T.Sato, Y.Nagao, Y.Nakahara and M.Machida
Fe-Substituted $10Al_2O_3{\cdot}2B_2O_3$ as a Multifunctional Support for Automotive Pd Catalysts
Appl. Catal. B, **146** (2014) 50.

T.Kawamata, K.Sugiyama, Y.Yokoyama and T.Fujita
Structural Study of Zr-Cu-Ag Bulk Metallic Glasses using the Anomalous X-Ray Scattering Method
J. Phys.: Conf. Ser., **502** (2014) 012027.

H.Arima, T.Kawamata, Y.Yokoyama and K.Sugiyama
Structure of $Al_{87}Y_8Ni_5$ Amorphous Alloy Analyzed by Anomalous X-Ray Scattering
JPS Conf. Proc., **1** (2014) 012107.

M.Morikawa, Y.Ogura, N.Ahmed, S.Kawamura, G.Mikami, S.Okamoto and Y.Izumi
Photocatalytic Conversion of Carbon Dioxide into Methanol in Reverse Fuel Cells with Tungsten Oxide and Layered Double Hydroxide Photocatalysts for Solar Fuel Generation
Catal. Sci. Technol., **4** (2014) 1644.

H.Abe, M.Sakamaki and K.Amemiya
Structures of Fe Magnetic Ultrathin Films on Cu(001) before and after CO Adsorption Revealed by EXAFS
J. Phys. Soc. Jpn., **83** (2014) 084603.

Y.Idemoto
Investigation into Properties of Highly Functional Oxides using Quantum Beam and Thermodynamic Measurement
J. Ceram. Soc. Jpn., **122** (2014) 839.

S.Nagashima, S.Furukawa, S.Kamiguchi, R.Kajio, H.Nagashima, A.Yamaguchi, M.Shirai, H.Kurokawa and T.Chihara
Catalytic Activity of Molecular Rhenium Sulfide Clusters $[Re_6S_8(OH)_{6-n}(H_2O)_n]^{(4-n)-}$ (n = 0, 2, 4, 6) with Retention of the Octahedral Metal Frameworks: Dehydrogenation and Dehydration of 1,4-Butanediol
J. Clust. Chem., **25** (2014) 1203.

R.Kaur, S.Gupta, S.K.Mehta, Y.Imai, T.Takiue, H.Matsubara and M.Aratono
Probing the Self-Aggregation Behavior and Counter Ion Distribution of a Copper Surfactant Complex
New J. Chem., **38** (2014) 3925.

B.Sarkar, C.Pendem, L.N.S.Konathala, T.Sasaki and R.Bal
Pt Nanoparticle Supported on Nanocrystalline CeO_2: Highly Selective Catalyst for Upgradation of Phenolic Derivatives Present in Bio-Oil
J. Mater. Chem. A, **2** (2014) 18398.

R.Tiwari, B.Sarkar, R.Tiwari, C.Pendem, T.Sasaki, S.Saran and R.Bal
Pt Nanoparticles with Tuneable Size Supported on Nanocrystalline Ceria for the Low Temperature Water- Gas-Shift (WGS) Reaction
J. Mol. Catal. A: Chem., **395** (2014) 117.

S.Acharyya, S.Ghosh, R.Tiwari, B.Sarkar, R.Singha, C.Pendem, T.Sasaki and R.Bal
Preparation of the $CuCr_2O_4$ Spinel Nanoparticles Catalyst for Selective Oxidation of Toluene to Benzaldehyde
Green Chem., **16** (2014) 2500.

B.Sarkar, C.Pendem, L.N.S.Konathala, T.Sasaki and R.Bal
Formation of Ilmenite-type $CoTiO_3$ on TiO_2 and its Performance in Oxidative Dehydrogenation of Cyclohexane with Molecular Oxygen
Catal. Commun., **56** (2014) 5.

T.Kamegawa, Y.Ishiguro, R.Kido and H.Yamashita Design of Composite Photocatalyst of TiO_2 and Y- Zeolite for Degradation of 2-Propanol in the Gas Phase under UV and Visible Light Irradiation
Molecules, **19** (2014) 16477.

8A

Y.Nakai, K.Honda, K.Yanagi, H.Kataura, T.Kato, T.Yamamoto and Y. Maniwa
Giant Seebeck Coefficient in Semiconducting Single-Wall Carbon Nanotube Film
Appl. Phys. Express, **7** (2014) 025103.

F.Kagawa, S.Horiuchi, N.Minami, S.Ishibashi, K.Kobayashi, R.Kumai, Y.Murakami and Y.Tokura Polarization
Switching Ability Dependent on Multidomain Topology in a UniaxialOrganic Ferroelectric
Nano Lett., **14** (2014) 239.

T.Sato, F.Kagawa, K.Kobayashi, K.Miyagawa, K.Kanoda, R.Kumai, Y.Murakami and Y.Tokura
Emergence of Nonequilibrium Charge Dynamics in a Charge-Cluster Glass
Phys. Rev. B, **89** (2014) 121102(R).

Y.Kurihara and Y.Moritomo
Electrochemical, Structural, and Electronic Properties of Mn-Co Hexacyanoferrates against Li Concentration
Jpn. J. Appl. Phys., **53** (2014) 067101.

Y.Takeichi, N.Inami, T.Ueno, K.Saito, H.Otori, R.Sagayama, R.Kumai and K.Ono
Micromanipulation and Pick-Up System for X-Ray Diffraction Characterization of Micrometer-Sized Single Particles
J. Phys.: Conf. Ser, **502** (2014) 012008.

R.Mitsuyama, S.Tadera, H.Kyakuno, R.Suzuki, H.Ishii, Y.Nakai, Y.Miyata, K.Yanagi, H.Kataura and Y.Maniwa
Chirality Fingerprinting and Geometrical Determination of Single-Walled Carbon Nanotubes: Analysis of Fine Structure of X-Ray Diffraction Pattern
Carbon, **75** (2014) 299.

K.T.Lai, A.Takemori, S.Miyasaka, S.Tajima, A.Nakao, H.Nakao, R.Kumai and Y.Murakami
Suppression of Superconductivity around x=0.5-0.7 in $LaFeP_{1-x}As_xO_{0.95}F_{0.05}$
JPS Conf. Proc., **1** (2014) 012104.

Y.Sekine, M.Nihei, R.Kumai, H.Nakao, Y.Murakami and H.Oshio
X-Ray-Induced Phase Transitions by Selective Excitation of Heterometal Ions in a Cyanide-Bridged Fe-Co Molecular Square
Chem. Comm., **50** (2014) 4050.

T.Matsumoto, G.N.Newton, T.Shiga, S.Hayami, Y.Matsui, H.Okamoto, R.Kumai, Y.Murakami and H.Oshio
Programmable Spin-State Switching in a Mixed Valence Spin-Crossover Iron Grid
Nature Communications, **5** (2014) 3865.

D.Choudhury, T.Suzuki, D.Okuyama, D.Morikawa, K.Kato, M.Takata, K.Kobayashi, R.Kumai, H.Nakao, Y.Murakami, M.Bremholm, B.B.Iversen, T.Arima, Y.Tokura and Y.Taguchi
Evolution of Magnetic and Structural Transitions and Enhancement of Magnetocaloric Effect in $Fe_{1-x}Mn_xV_2O_4$
Phys. Rev. B, **89** (2014) 104427.

T.Aree, H.-B.Bu¨rgi, D.Chernyshov and K.W.To¨rnroos
Dynamics and Thermodynamics of Crystalline Polymorphs. 3. γ-Glycine, Analysis of Variable-Temperature Atomic Displacement Parameters, and Comparison of Polymorph Stabilities
J. Phys. Chem. A, **118** (2014) 9951.

M.Hagiwara, M.Ikeda, T.Kida, K.Matsuda, S.Tadera, H.Kyakuno, K.Yanagi, Y.Maniwa and K.Okunishi
Haldane State Formed by Oxygen Molecules Encapsulated in Single-Walled Carbon Nanotubes
J. Phys. Soc. Jpn., **83** (2014) 113706.

A.Kobayashi, T.Ohba, E.Saitoh, Y.Suzuki, S.Noro, H.C.Chang and M.Kato
Flexible Coordination Polymers Composed of Luminescent Ruthenium(II) Metalloligands: Importance of the Position of the Coordination Site in Metalloligands
Inorg. Chem. **53**(2014) 2910.

K.Kobayashi, S.Horiuchi, S.Ishibashi, F.Kagawa, Y.Murakami and R.Kumai
Structure-Property Relationship of Supramolecular Ferroelectric [H-66dmbp][Hca] Accompanied by High Polarization, Competing Structural Phases, and Polymorphs
Chem. Eur. J., **20** (2014) 17515.

H.Ikemoto
The Structures and Properties of Tenanoparticles
Proceeding of the 26th Symposium on Phase Change Oriented Science (2014) 3.

T.Nakayama, T.Sakuraba, S.Tomita, A.Kaneko, E.Takai, K.Shiraki, K.Tashiro, N.Ishii, Y.Hasegawa, Y.Yamada, R.Kumai and Y.Yamamoto
Charge-Separated Fmoc-Peptide β-Sheets: Sequence-Secondary Structure Relationship for Arranging Charged Side Chains on Both Sides
Asian J. Org. Chem. **3** (2014) 1182.

T.Sato, F.Kagawa, K.Kobayashi, A.Ueda, H.Mori, K.Miyagawa, K.Kanoda, R.Kumai, Y.Murakami and Y.Tokura
Systematic Variations in the Charge-Glass-Forming Ability of Geometrically Frustrated theta-(BEDT-TTF)$_{2}$X Organic Conductors
J. Phys. Soc. Jpn. **83** (2014) 083602.

9A

M.Morikawa, N.Ahmed, Y.Yoshida, Y.Izumi Photoconversion of Carbon Dioxide in Zinc-Copper- Gallium Layered Double Hydroxides: the Kinetics to Hydrogen Carbonate and Further to CO/Methanol
Appl. Catal. B, **144** (2014) 561.

M.Tanaka, Y.S.Togo, N.Yamaguchi and Y.Takahashi
An EXAFS Study on the Adsorption Structure of Phenyl-Substituted Organoarsenic Compounds on Ferrihydrit
J. Colloid Interface Sci., **415** (2014) 13.

K.Oka, Y.Ogura and Y.Izumi
X-Ray Evaluation of the Boundary between Polymer Electrolyte and Platinum and Carbon Functionalization to Conduct Protons in Polymer Electrolyte Fuel Cells
J. Power Sources, **258** (2014) 83.

M.Katayama, K.Sumiwaka, R.Miyahara, H.Yamashige, H.Arai, Y.Uchimoto, T.Ohta, Y.Inada and Z.Ogumi
X-Ray Absorption Fine Structure Imaging of Inhomogeneous Electrode Reaction in $LiFePO_4$ Lithium-Ion Battery cathode
J. Power Sources, **269** (2014) 994.

M.Morikawa, Y.Ogura, N.Ahmed, S.Kawamura, G.Mikami, S.Okamoto and Y.Izumi
Photocatalytic Conversion of Carbon Dioxide into Methanol in Reverse Fuel Cells with Tungsten Oxide and Layered Double Hydroxide Photocatalysts for Solar Fuel Generation
Catal. Sci. Technol., **4** (2014) 1644.

R.Nakada, K.Ogawa, N.Suzuki, S.Takahashi and Y.Takahashi
Late Triassic Compositional Changes of Aeolian Dusts in the Pelagic Panthalassa: Response to the Continental Climatic Change
Paleogeography. Paleoclimatology. Paleoecology., **393** (2014) 61.

H.Uehara, Y.Uemura, T.Ogawa, K.Kono, R.Ueno, Y.Niwa, H.Nitani, H.Abe, S.Takakusagi, M.Nomura, Y.Iwasawa and K.Asakura
In Situ Back-Side Illumination Fluorescence XAFS(BI-FXAFS) Studies on Platinum Nanoparticles Deposited on a HOPG Surface as a Model Fuel Cell: a New Approach to the Pt-HOPG Electrode/Electrolyte Interface
Phys. Chem. Chem. Phys., **16** (2014) 13748.

K.Mori, Y.Iwata, M.Yamamoto, N.Kimura, A.Miyauchi, G.Okamoto, T.Toyoshima and H.Yamashita
An Efficient $Cu/BaO/La_2O_3$ Catalyst for the Simultaneous Removal of Carbon Soot and Nitrogen Oxides from Simulated Diesel Exhaust
J. Phys. Chem. C, **118** (2014) 9078.

Y.Idemoto
Investigation into Properties of Highly Functional Oxides using Quantum Beam and Thermodynamic Measurement
J. Ceram. Soc. Jpn., **122** (2014) 839.

R.Nakada, T.Shirai, S.Takahashi, N.Suzuki, K.Ogawa and Y.Takahashi
A Geochemical Constraint on the Formation Process of a Manganese Carbonate Nodule in the Siliceous Mudstone of the Jurassic Accretionary Complex in the Mino Belt, Japan
J. Asian Earth Sci., **96** (2014) 59.

Y.Hatakeyama, K.Asakura, S.Takahashi, K.Judai and K.Nishikawa
Microscopic Structure of Naked Au Nanoparticles Synthesized in Typical Ionic Liquids by Sputter Deposition
J. Phys. Chem. C, **118** (2014) 27973.

H.Abe
Direct Evidence of Calcium Oxalate Formation in Spinach
Chem. Lett., **43** (2014) 1841.

T.Sugiyama, M.Uo, T.Wada, T.Hongo, D.Omagari, K.Komiyama, H.Sasaki, H.Takahashi, M.Kusama and Y.Mori
Novel Metal Allergy Patch Test using Metal Nanoballs
Journal of Nanobiotechnology, **12** (2014) 51.

S.Hinokuma, H.Kogami, N,Yamashita, Y.Katsuhara, K.Ikeue and M.Machida
Subnano-Particle Ce Catalyst Prepared by Pulsed Arc- Plasma Process
Catal. Commun., **54** (2014) 81.

A.Ohta
Speciation Study of Cr in Geochemical Reference Material Sediment Series using Sequential Extraction and XAFS Spectroscopy
Geostandards and Geoanalytical Research, **39** (2014) 87.

T.Kashiwabara, Y.Oishi, A.Sakaguchi, T.Sugiyama, A.Usui and Y.Takahashi
Chemical Processes for the Extreme Enrichment of Tellurium into Marine Ferromanganese Oxides
Geochim. Cosmochim. Acta, **131** (2014) 150.

M.Kato, K.Kimijima, M.Shibata, H.Notsu, K.Ogino, K.Inokuma, N.Ohta, H.Uehara, Y.Uemura, N.Oyaizu, T.Ohba, S.Takakusagi, K.Asakura and I.Yagi
Deprotonation of a Dinuclear Copper Complex of 3,5-Diamino-1,2,4-Triazole for High Oxygen Reduction Activity
Phys. Chem. Chem. Phys., **17** (2014) 8638.

Y.Ogawa, R.Yamada, K.Shinoda, C.Inoue and N.Tsuchiya
The Fate of Arsenic in a River Acidified by Volcanic Activity and an Acid Thermal Water and Sedimentation Mechanism
ENVIRONMENTAL SCIENCE PROCESSES and IMPACTS, **16** (2014) 2325.

Q.H.Fan, Y.Takahashi, K.Tanaka and A.Sakaguchi
An EXAFS Study on the Effects of Natural Organic Matter and the Expandability of Clay Minerals on Cesium Adsorption and Mobility
Geochim. Cosmochim. Acta, **135** (2014) 49.

Q.Fan, N.Yamaguchi, M.Tanaka, H.Tsukada, and Y.Takahashi,
Relationship between the Adsorption Species of Cesium and Radiocesium Interception Potential in Soils and Minerals: an EXAFS Study
J. Environ. Radioact., **138** (2014) 92.

Y.Takahashi, K.Kondo, A.Miyaji, Y.Watanabe, Q.H.Fan, T.Honma and K.Tanaka
Recovery and Separation of Rare Earth Elements using Salmon Milt
PLOS ONE, **1371** (2014) 0114858.

T.Kamegawa, Y.Ishiguro, R.Kido and H.Yamashita Design of Composite Photocatalyst of TiO_2 and Y- Zeolite for Degradation of 2-Propanol in the Gas Phase under UV and Visible Light Irradiation
Molecules, **19** (2014) 16477.

9C

M.Morikawa, N.Ahmed, Y.Yoshida, Y.Izumi
Photoconversion of Carbon Dioxide in Zinc-Copper-Gallium Layered Double Hydroxides: the Kinetics to Hydrogen Carbonate and Further to CO/Methanol
Appl. Catal. B, **144** (2014) 561.

K.Oka, Y.Ogura and Y.Izumi
X-Ray Evaluation of the Boundary between Polymer Electrolyte and Platinum and Carbon Functionalization to Conduct Protons in Polymer Electrolyte Fuel Cells
J. Power Sources, **258** (2014) 83.

T.Ohkubo, M.Ushio, K.Urita, I.Moriguchi, B.Ahmmad, A.Itadani and Y.Kuroda
Nanospace-Enhanced Photoreduction for the Synthesis of Copper(I) Oxide Nanoparticles under Visible-Light Irradiation
J. Colloid Interface Sci., **421** (2014) 165.

J.Liu, T.Hisatomi, G.Ma, A.Iwanaga, T.Minegishi, Y.Moriya, M.Katayama, J.Kubota and K.Domen
Improving the Photoelectrochemical Activity of $La_5Ti_2CuS_5O_7$ for Hydrogen Evolution by Particle Transfer and Doping
Energy Environ. Sci., 7 (2014) 2239.

Y.Masubuchi, H.Sato, T.Motohashi and S.Kikkawa Magnetic Softening of Co Doped α''-$Fe_{16}N_2$ Containing Residual Fe-Co Alloy Prepared in Low Temperature Nitridation
Journal of the Ceramic Society of Japan, **122** (2014) 288.

T.Yanoh, A.Kurokawa, H.Takeuchi, S.Yano, K.Onuma, T.Kondo, K.Miike, T.Miyasaka, K.Mibu and Y.Ichiyanagi
Characterization of Magnetic and Dielectric Properties of $Bi_{1-x}Gd_xFeO_3$ Nanoparticles by Local Structure Analyses
J. Nanosci. Nanotechnol, **14** (2014) 2190.

Y.Kurihara and Y.Moritomo
Electrochemical, Structural, and Electronic Properties of Mn-Co Hexacyanoferrates against Li Concentration
Jpn. J. Appl. Phys., **53** (2014) 067101.
H.Kitagawa, N.Ichikuni, H.Okuno, T.Hara and S.Shimazu

XAFS and HAADF STEM Combined Characterization for Size Regulated Ni Nanocluster Catalyst and its Unique Size Dependence for Water Gas Shift Reaction
Appl. Catal. A, **478** (2014) 66.

H.Abe, Y.Niwa, H.Nitani and M.Nomura
Development of Surface Sensitive DXAFS Measurement Method by Applying Kramers-Kronig Relations to Total Reflection Spectra
J. Phys.: Conf. Ser., **502** (2014) 012035.

M.Morikawa, Y.Ogura, N.Ahmed, S.Kawamura, G.Mikami, S.Okamoto and Y.Izumi
Photocatalytic Conversion of Carbon Dioxide into Methanol in Reverse Fuel Cells with Tungsten Oxide and Layered Double Hydroxide Photocatalysts for Solar Fuel Generation
Catal. Sci. Technol., **4** (2014) 1644.

D.Tongsakul, S.Nishimura and K.Ebitani
Effect of Stabilizing Polymers on Catalysis of Hydrotalcite-Supported Platinum Nanoparticles for Aerobic Oxidation of 1,2-Propanediol in Aqueous Solution at Room Temperature
J. Phys. Chem. C, **118** (2014) 11723.

S.Takemura, S.Kawakami, M.Harada and M.Iida Solvation Structure of a Copper(II) Ion in Protic Ionic Liquids Comprising *N*-Hexylethylenediamine
Inorg. Chem., **53** (2014) 9667.

Y.Masubuchi, R.Miyazaki, H.Kikuchi, T.Motohashi and S.Kikkawa
Exfoliation of One-Dimensional TiO_5 Chain in K_2TiO_3
Dalton Trans., **43** (2014) 13751.

K.Ingle, K.R.Priolkar, A.Pal, V.P.S.Awana and S.Emura
Local Structural Distortions and their Role in Superconductivity in $SmFeAsO_{1-x}F_x$ Superconductors
Supercond. Sci. Technol., **27** (2014) 075010.

J.Ohyama, R.Kanao, A.Esaki and A.Satsuma
Conversion of 5-Hydroxymethylfurfural to a Cyclopentanone Derivative by Ring Rearrangement over Supported Au Nanoparticles
Chem. Comm., **50** (2014) 5633.

H.Choudhary, S.Nishimura and K.Ebitani
Tailored Design of Palladium Species Grafted on an Amino Functionalized Organozinc Coordination Polymer as a Highly Pertinent Heterogeneous Catalyst
J. Mater. Chem. A, **2** (2014) 18687.

H.Einaga, J.Kawarada, K.Kimura and Y.Teraoka
Preparation of Platinum Nanoparticles on TiO_2 from DNA-Protected Particles
Colloid. Surf. A: Physicochem. Eng. Aspects, **455** (2014) 179.

Y.Hatakeyama, K.Asakura, S.Takahashi, K.Judai and K.Nishikawa
Microscopic Structure of Naked Au Nanoparticles Synthesized in Typical Ionic Liquids by Sputter Deposition
J. Phys. Chem. C, **118** (2014) 27973.

A.Cho, H.Kim, A.Iino, A.Takagaki and S.T.Oyama
Kinetic and FTIR Studies of 2-Methyltetrahydrofuran Hydrodeoxygenation on Ni_2P/SiO_2
J. Catal., **318** (2014) 151.

Y.Yamamoto, S.Arai, A.Esaki, J.Ohyama, A.Satsuma and N.Tanaka
Statistical Distribution of Single Atoms and Clusters of Supported Au Catalyst Analyzed by Global High-Resolution HAADF-STEM Observation with Morphological Image-Processing Operation
Microscopy, **63** (2014) 209.

F.Hayashi, M.Tanaka, D.Lin and M.Iwamoto
Surface Structure of Yttrium-Modified Ceria Catalysts and Reaction Pathways from Ethanol to Propene
J. Catal., **316** (2014) 112.

T.Yumura, A.Oda, H.Torigoe, A.Itadani, Y.Kuroda, T.Wakasugi and H.Kobayashi
Combined Experimental and Computational Approaches to Elucidate the Structures of Silver Clusters Inside the ZSM-5 Cavity
J. Phys. Chem. C, **118** (2014) 23874.

B.Sarkar, C.Pendem, L.N.S.Konathala, T.Sasaki and R.Bal
Pt Nanoparticle Supported on Nanocrystalline CeO_2: Highly Selective Catalyst for Upgradation of Phenolic Derivatives Present in Bio-Oil
J. Mater. Chem. A, **2** (2014) 18398.

E.I.Naito, H.Hondoh, S.Ueno and K.Sato
Mixing Phase Behavior of 1,3-Dipalmitoyl-2-Oleoyl-*sn*-Glycerol (POP) and 1,2-Dipalmitoyl-3-Oleoyl-*rac*-Glycerol (PPO) in *n*-Dodecane Solution
J. Am Oil Chem Soc, **91** (2014) 1837.

H.Shintaku, K.Nakajima, M.Kitano, N.Ichikuni and M.Hara
Lewis Acid Catalysis of TiO_4 Tetrahedra on Mesoporous Silica in Water
ACS Catalysis, **4** (2014) 1198.

R.Tiwari, B.Sarkar, R.Tiwari, C.Pendem, T.Sasaki, S.Saran and R.Bal
Pt Nanoparticles with Tuneable Size Supported on Nanocrystalline Ceria for the Low Temperature Water- Gas-Shift (WGS) Reaction
J. Mol. Catal. A: Chem., **395** (2014) 117.

B.Sarkar, C.Pendem, L.N.S.Konathala, R.Tiwari, T.Sasaki and R.Bal
Cu Nanoclusters Supported on Nanocrystalline SiO_2- MnO_2: a Bifunctional Catalyst for the One-Step Conversion of Glycerol to Acrylic Acid
Chem. Comm., **50** (2014) 9707.

S.Acharyya, S.Ghosh, R.Tiwari, B.Sarkar, R.Singha, C.Pendem, T.Sasaki and R.Bal
Preparation of the $CuCr_2O_4$ Spinel Nanoparticles Catalyst for Selective Oxidation of Toluene to Benzaldehyde
Green Chem., **16** (2014) 2500.

B.Sarkar, C.Pendem, L.N.S.Konathala, T.Sasaki and R.Bal
Formation of Ilmenite-type $CoTiO_3$ on TiO_2 and its Performance in Oxidative Dehydrogenation of Cyclohexane with Molecular Oxygen
Catal. Commun., **56** (2014) 5.

S.Acharyya, S.Ghosh, S.Adak, T.Sasaki and R.Bal
Facile Synthesis of $CuCr_2O_4$ Spinel Nanoparticles: a Recyclable Heterogeneous Catalyst for the One Pot Hydroxylation of Benzene
Catal. Sci.Technol., **4** (2014) 4232.

A.Oda, H.Torigoe and Y.Kuroda
MFI-Type Zeolite Functioning as the Specific Field for the Zinc Ion Working as the Activation Site for H2, as Well as CH4, at around 300 K
Zeolite, **31** (2014) 88. (in Japanese).

Y.Kuroda
Novel Properties Derived from Inorganic Compounds with Nanometer-Sized Pores: Chemisorption (1)
Journal of the Japan Society of Colour Material, **87** (2014) 102. (in Japanese).

Y.Kuroda
Novel Properties Derived from Inorganic Compounds with Nanometer-Sized Pores: Chemisorption (2)
J. Jpn. Soc. Colour Mater, **87** (2014) 131. (in Japanese).

T.Zhuang, K.Hiraoka, M.Kurisu, K.Konishi, T.Kamimori and I.Nakai
Valence Fluctuation in $YbIn_{1-x}Cd_xCu_4$ Compounds Studied by XANES
JPS Conf. Proc., **3** (2014) 011069

9C（SAXS）

F.Kaneko, N.Seto, K.Sasaki and S.Sakurai
Multiple Site Occupation of Flexible Polymeric Compounds in Cocrystals of Syndiotactic Polystyrene
Chem. Lett., **43** (2014) 904.

G.Cui, M.Fujikawa, S.Nagano, M.Sano, H.Takase, T.Miyazaki, S.Sakurai and K.Yamamoto
Perpendicular Oriented Cylinders via Directional Coalescence of Spheres Embedded in Block Copolymer Films Induced by Solvent Annealing
Polymer, **55** (2014) 1601.

K.Yamamoto, K.Ohara, G.Cui, R.Tanaka, D.Shimada, S.Nagano, M.Sano, S.Sakurai, K.Shimokita and T.Miyazaki
Solvent Annealing Induced Perpendicular Orientation of Microdomains in Block Copolymer Thin Films
Kobunshi Ronbunshu, **71** (2014) 104. (in Japanese).

H.Takahashi
On Hydration Repulsive Forces between Various Phosphlipid Bilayers
JPS Conf. Proc., **1** (2014) 012041.

Y.Kawabata, A.Murakami and T.Kato
Electrolyte Effect on Lamellar Domain Morphology in a Nonionic Surfactant Solution below the Krafft Temperature
J. Phys. Chem. B, **118** (2014) 1022.

G.Cui, M.Fujikawa, S.Nagano, K.Shimokita, T.Miyazaki, S.Sakurai and K.Yamamoto
Macroscopic Alignment of Cylinders via Directional Coalescence of Spheres along Annealing Solvent Permeation Directions in Block Copolymer Thick Films
Macromolecules, **47** (2014) 5989.

F.Kaneko
Cocrystallization of Syndiotactic Polystyrene by a Guest Exchange Phenomenon: Investigation of the Mechanism and Preparation of Polymer Composites
Kobunshi Ronbunshu, **71** (2014) 540. (in Japanese).

10A

T.Kuribayashi, A.Sano-Furukawa and T.Nagase
Observation of Pressure-Induced Phase Transition of δ-AlOOH by using Single-Crystal Synchrotron X-Ray Diffraction Method
Phys. Chem. Mineral., **41** (2014) 303.

R.Simura and K.Sugiyama
Site Determination of Sr in $Sr_3YB_3O_9$ Crystals by Anomalous X-Ray Scattering
J. Phys.: Conf. Ser., **502** (2014) 012028.

A.Nakayama, Y.Onda, S.Yamada, H.Fujihisa, M.Sakata, Y.Nakamoto, K.Shimizu, S.Nakano, A.Ohmura, F.Ishikawa and Y.Yamada
Collapse of CuO Double Chains and Suppression of Superconductivity in High-Pressure Phase of $YBa_2Cu_4O_8$
J. Phys. Soc. Jpn., **83** (2014) 093601.

M.Okube and S.Sasaki
Site-Specific Electronic Structures of Ferrimagnetic Fe_3O_4 Measured by Resonant X-Ray Magnetic Scattering
J. Appl. Cryst., **47** (2014) 1387.

M.Okube and S.Sasaki
Resonant X-Ray Scattering and Crystal Structure Analyses
J. Cryst. Soc. Jpn., **56** (2014) 158. (in Japanese).

A.Nakatsuka
Crystal Chemistry of Earth's Interior Related Materials with Edge-Sharing Structures
Crystallography in Japan (II), (2014) 157. (in Japanese).

A.Nakatsuka
Mineralogical Crystallography as a Function of Temperature − Elucidation of Atomic Displacement Behavior −
J. Cryst. Soc. Jpn., **56** (2014) 150. (in Japanese).

S.Sasaki
Magnetic Structure Examined by Synchrotron X-Rays
Crystallography in Japan (II), (2014) 99. (in Japanese).

S.Sasaki
Synchrotron Radiation and Crystal-Structure Analysis in the 1980s
Crystallography in Japan (II), (2014) 29. (in Japanese).

10C

Y.Koide, H.Ikake, Y.Muroga and S.Shimizu
Relationship between Transparency and Morphology of Cast Films Composed of a Mixture of Poly-D-Lactic Acid and Poly-L-Lactic Acid
Kobunshi Ronbunshu, **71** (2014) 47. (in Japanese).

K.Hemmi, G.Matsuba, H.Tsuji, T.Kawai, T.Kanaya, K.Toyohara, A.Oda and K.Endou
Precursors in Stereo-Complex Crystals of Poly(L-Lactic Acid)/Poly(D-Lactic Acid) Blends under Shear Flow
J. Appl. Cryst., **47** (2014) 14.

K.Terao, N.Morihana and H.Ichikawa
Solution SAXS Measurements over a Wide Temperature Range to Determine the Unperturbed Chain Dimensions of Polystyrene and a Cyclic Amylose Derivative
Polymer Journal, **46** (2014) 155.

Y.Asai, K.Yamada, M.Yamada, A.Takano and Y.Matsushita
Formation of Tetragonally-Packed Rectangular Cylinders from ABC Block Terpolymer Blends
ACS Macro Lett., **3** (2014) 166.

T.Okuhara, A.Hashidzume, K.Terao and T.Sato Aggregation and Phase Separation of Hydrophilically Modified Poly(Dimethylsiloxane) in Methanol-Water Mixtures
Polymer Journal, **46** (2014) 264.

H.Takeno and Y.Kuribayashi
Structural Studies of 1,3:2,4-Dibenzylidene Sorbitol Gels
Advanced Materials Research, **896** (2014) 300.

K.Terao and T.Sato
Lyotropic Liquid Crystals of Rigid Polymers
Ekisho, **18** (2014) 108. (in Japanese).

S.Nakagawa, T.Tanaka, T.Ishizone, S.Nojima, K.Kamimura, K.Yamaguchi and S.Nakahama
Crystallization Behavior of Poly(ε-Caprolactone) Chains Confined in Lamellar Nanodomains
Polymer, **55** (2014) 4394.

A.B.Imran, K.Esaki, H.Gotoh, T.Seki, K.Ito, Y.Sakai and Y.Takeoka
Extremely Stretchable Thermosensitive Hydrogels by Introducing Slide-Ring Polyrotaxane Cross-Linkers and Ionic Groups into the Polymer Network
Nature Communications, **5** (2014) 5124.

N.Suzuki, S.Ban, E.Itoh, S.Chen, F.L.Imai, Y.Sawano, T.Miyakawa, M.Tanokura and N.Yonezawa
Calcium-Dependent Structural Changes in Human Reticulocalbin-1
J. Biochem., **155** (2014) 281.

T.Sumi, H.Imamura, T.Morita, Y.Isogai and K.Nishikawa
Model-Potential-Free Analysis of Small Angle Scattering of Proteins in Solution: Insights into Solvent Effects on Protein-Protein Interaction
Phys. Chem. Chem. Phys., **16** (2014) 25492.

S.Kudo, J.M.Caaveiro, S.Goda, S.Nagatoishi, K.Ishii, T.Matsuura, Y.Sudou, T.Kodama, T.Hamakubo and K.Tsumoto
Identification and Characterization of the X-Dimer of Human P-Cadherin: Implications for Homophilic Cell Adhesion
Biochemistry, **53** (2014) 1742.

R.Hijikawa, L.Huang, G.Kiyofuji, H.Marubayashi and S.Nojima
Crystallization Behavior of Poly(β-propiolactone)-*block*-polyethylene Copolymers with Varying Polyethylene Crystallinities
Polymer, **55** (2014) 6960.

Y.Maki, K.Furusawa, S.Yasuraoka, H.Okamura, N.Hosoya, M.Sunaga, T.Dobashi, Y.Sugimoto and K.Wakabayashi
Universality and Specificity in Molecular Orientation in Anisotropic Gels Prepared by Diffusion Method
Carbohydr. Polym., **108** (2014) 118.

I.Saito, T.Okamoto, K.Shimokita, T.Miyazaki and K.Yamamoto
Perpendicular Orientation of Cylindrical Microdomains of $FeCl_3$ Doped Polystyrene-*b*-poly(2-vinyl pyridine) Thin Films
Koubunshi Ronbunshu, **71** (2014) 586. (in Japanese).

H.Takeoka, N.Fukui, S.Sakurai, Y.Nakamura and S.Fujii
Nanomorphology Characterization of Sterically Stabilized Polypyrrole-Palladium Nanocomposite Particles
Polymer Journal, **46** (2014) 704.

C.Takahashi, S.Yoshihara, S.Kang, K.Sakajiri, J.Watanabe and M.Tokita
Decrease in the Isotropization Temperature and Enthalpy of Main-Chain Polymer Smectic Liquid Crystals as a Result of the Inclusion of Chain Ends
Polymer, **55** (2014) 2609.

M.Hasegawa, S.T.Fukai, JD.Kim, A.Fukamizu and T.Shimizu
Protein Arginine Methyltransferase 7 has a Novel Homodimer-Like Structure Formed by Tandem Repeats
FEBS Letters, **588** (2014) 1942.

11A

R.Ishikawa, A.R.Lupini, F.Oba, S.D.Findlay, N.Shibata, T.Taniguchi, K.Watanabe, H.Hayashi, T.Sakai, I.Tanaka, Y.Ikuhara and S.J.Pennycook
Atomic Structure of Luminescent Centers in High- Efficiency Ce-Doped *w*-AlN Single Crystal
Scientific Reports, **4** (2014) 3778.

S.Kitamoto, S.Ogawa, T.Komatsu, R.Umezu, J.Sugimoto, H.Suzuki, D.Nambu, H.Tsumura, H.Seta, A.Hoshino, S.Aikawa and Y.Niizuma
Estimation of Observation Possibility of the X-Ray Interferometer with an X-Ray Beam-Splitter
Proc. of SPIE, **9144** (2014) 70.

I.Shimoyama, Y.Baba and T.Sekiguchi
A Polarization Rule on Atomic Arrangements of Graphite-Like Boron Carbonitride
Carbon, **71** (2014) 1.

S.Shiki, M.Ukibe, N.Matsubayashi, N.Zen, M.Koike, Y.Kitajima and M.Ohkubo
Current Status of AIST X-Ray-Absorption-Spectroscopy (XAFS) Instrument with 100-Pixel Superconducting- Tunnel-Junction Array Detector
J. Low Temp. Phys., **176** (2014) 604.

T.Miyanaga, T.Azuhata, K.Nakajima, H.Nagoya, K.Hazu and S.F.Chichibu
Polaraized XAFS Study of Al *K*-Edge for *m*-Plane AlGaN Films
J. Phys. Conf. Ser,, **502** (2014) 012031.

W.B.K.Putri, D.H.Tran, O.Y.Lee, W.N.Kang, T.Miyanaga, D.S.Yang and B.Kang,
Effect of Different Thickness Crystalline SiC Buffer Layers on the Ordering of MgB_2 Films Probed by Extended X-Ray Absorption Fine Structure
J. Appl. Phys., **115** (2014) 093901.

11B

T.Yamamoto, H.Okuda, K.Takeshita, N.Usami, Y.Kitajima and H.Ogawa
Grazing-Incidence Small-Angle X-Ray Scattering from Ge Nanodots Self-Organized on Si(001) Examined with Soft X-Rays
J. Synchrotron Rad., **21** (2014) 161.

H.Okuda, T.Yamamoto, K.Takeshita, M.Hirai, K.Senoo, H.Ogawa and Y.Kitajima
Normalization of Grazing-Incidence Small Angle Scattering of Phospholipid Alloy Systems at the K Absorption Edge of Phosphorous: A Standard Sample Approach
Jpn. J. Appl. Phys., **53** (2014) 05FH02.

Y.Hashimoto, A.Takamoto, R.Kikkawa, K.Murakami and N.Yamaguchi
Formations of Hydroxyapatite and Inositol Hexakisphosphate in Poultry Litter during the Composting Period: Sequential Fractionation, P K-Edge XANES and Solution ^{31}P NMR Investigations
Environ. Sci. Technol., **48** (2014) 5486.

Y.Hashimoto and Y.Watanabe
Combined Applications of Chemical Fractionation, Solution ^{31}P-NMR and P K-Edge XANES to Determine Phosphorus Speciation in Soils Formed on Serpentine Landscapes
Geoderma, **230** (2014) 143.

H.Nakao, Y.Yamasaki, J.Okamoto, T.Sudayama, Y.Takahashi, K.Kobayashi, R.Kumai and Y.Murakami
Development of an In-Vacuum Diffractometer for Resonant Soft X-Ray Scattering
J. Phys.: Conf. Ser., **502** (2014) 012015.

Y.Takahashi, H.Nakao, R.Kumai, S.Ishibashi, S.Horiuchi, M.Kohyama, K.Kobayashi, Y.Yamasaki, J.Okamoto, T.Sudayama, Y.Murakami and Y.Tokura
Molecular Electronic States in Charge Transfer Complex Studied by X-Ray Absorption Spectroscopy
J. Phys.: Conf. Ser., **502** (2014) 012036.

T.Fujimori, Y.Nishimoto, K.Shiota and M.Takaoka
Contrasting Effects of Sulfur Dioxide on Cupric Oxide and Chloride during Thermochemical Formation of Chlorinated Aromatics
Environ. Sci. Technol., **48** (2014) 13644.

A.Takamoto and Y.Hashimoto
Assessment of Hedleys Sequential Extraction Method for Phosphorus Forms in Biosolids using P K-Edge X-Ray Absorption Near-Edge Structure Spectroscopy
Chem. Lett., **43** (2014) 1696.

T.Tanikawa, Y.Hashimoto, N.Yamaguchi, Y.Ito, S.Fukushima, K.Kanda, M.Uemura, T.Hasegawa, M.Takahashi and S.Yoshinaga
Sulfur Accumulation in Melanudands during Development by Upbuilding Pedogenesis since 14-15 cal.ka
Geoderma, **232** (2014) 609.

11D

S.Tanaka, Y.Takano, M.Okusawa and K.Mase
What Does the Angle-Integrated Photoelectron Spectrum Show? A Comparison between First-Principles Calculation and Experiments for Graphite
J. Phys. Soc. Jpn., **83** (2014) 084705.

K.Mase, K.Hiraga, S.Arae, R.Kanemura, Y.Takano, K.Yanase, Y.Ogashiwa, N.Shohata, N.Kanayama, T.Kakiuchi, S.Ohno, D.Sekiba, K.K.Okudaira, M.Okusawa and M.Tanaka
Decay Processes of Si $2s$ Core Holes in Si(111)-7×7 Revealed by Si Auger Electron Si $2s$ Photoelectron Coincidence Measurements
J. Phys. Soc. Jpn., **83** (2014) 094704.

T.Ejima, T.Hatano, K.Ohno, T.Fukayama, S.Aihara, M.Yanagihara and T.Tsuru
Multilayer Coated Grazing Incidence Condenser for Large Numerical Aperture Objective at Wavelength of 4.5 nm
Appl. Optics, **53** (2014) 6846.

T.Hatano and T.Harada
Multilayer Reflectometry and Quantitative Analysis of Higher Order Diffraction Impurities of Grating Monochromator
J. Elec. Spec. Relat. Phenom., **196** (2014) 156.

12C

M.Tanaka, Y.S.Togo, N.Yamaguchi and Y.Takahashi
An EXAFS Study on the Adsorption Structure of Phenyl-Substituted Organoarsenic Compounds on Ferrihydrit
J. Colloid Interface Sci., **415** (2014) 13.

S.Takenaka, H.Miyamoto, Y.Utsunomiya, H.Matsune and M.Kishida
Catalytic Activity of Highly Durable Pt/CNT Catalysts Covered with Hydrophobic Silica Layers for the Oxygen Reduction Reaction in PEFCs
J. Phys. Chem. C, **118** (2014) 774.

T.Kikugawa, Y.Abe, A.Nakamura and I.Nakai Investigation of Coloring Mechanism of Ancient Egyptian Copper-Red Glass and Consideration of the Manufacturing Process
BUNSEKI KAGAKU, **63** (2014) 31. (in Japanese).

T.Kashiwabara, R.Toda, K.Fujinaga, T.Honma, Y.Takahashi and Y.Kato
Determination of Host Phase of Lanthanum in Deep-Sea REY-Rich Mud by XAFS and μ-XRF Using High-Energy Synchrotron Radiation
Chem. Lett., **43** (2014) 199.

K.Oka, Y.Ogura and Y.Izumi
X-Ray Evaluation of the Boundary between Polymer Electrolyte and Platinum and Carbon Functionalization to Conduct Protons in Polymer Electrolyte Fuel Cells
J. Power Sources, **258** (2014) 83.

F.Mauriello, H.Ariga, N.Murata and K.Asakura,
New Prospects for the Characterization of Heterogeneous Catlasyts by using Slow Muon Spectroscopy
J. Phys. Soc. Jpn., **2** (2014) 010306.

M.Yoshida, T.Iida, T.Mineo, T.Yomogida, K.Nitta, K.Kato, H.Nitani, H.Abe, T.Uruga and H.Kondoh
Electrochromic Characteristics of a Nickel Borate Thin Film Investigated by In Situ XAFS and UV/Vis Spectroscopy
Electrochemistry, **82** (2014) 355.

M.Katayama, K.Sumiwaka, R.Miyahara, H.Yamashige, H.Arai, Y.Uchimoto, T.Ohta, Y.Inada and Z.Ogumi
X-Ray Absorption Fine Structure Imaging of Inhomogeneous Electrode Reaction in $LiFePO_4$ Lithium-Ion Battery cathode
J. Power Sources, **269** (2014) 994.

R.Nakada, K.Ogawa, N.Suzuki, S.Takahashi and Y.Takahashi
Late Triassic Compositional Changes of Aeolian Dusts in the Pelagic Panthalassa: Response to the Continental Climatic Change
Paleogeography. Paleoclimatology. Paleoecology., **393** (2014) 61.

M.Hashimoto, S.Okajima, T.Kondo, K.Hara and W.- J.Chun
Thin Film Structures of Metal-Organic Framework $[Cu_3 BTC)_2(H_2O)_3]_n$ on $TiO_2(110)$
Electrochemistry, **82** (2014) 335.

H.Suga, Q.Fan, Y.Takeichi, K.Tanaka, H.Kondo, V.V.Kanivets, A.Sakaguchi, K.Kato, N.Inami, K.Mase, K.Ono and Y.Takahashi
Characterization of Particulate Matters in the Pripyat River in Chernobyl Related to their Adsorption of Radiocesium with Inhibition Effect by Natural Organic Matter
Chem. Lett., **43** (2014) 1128.

R.Nakada, T.Shirai, S.Takahashi, N.Suzuki, K.Ogawa and Y.Takahashi
A Geochemical Constraint on the Formation Process of a Manganese Carbonate Nodule in the Siliceous Mudstone of the Jurassic Accretionary Complex in the Mino Belt, Japan
J. Asian Earth Sci., **96** (2014) 59.

M.Yoshida, N.Gon, S.Maeda, T.Mineo, K.Nitta, K.Kato, H.Nitani, H.Abe, T.Uruga and H.Kondoh
In Situ XAFS Study of the Photoinduced Potential Shift of a MnO_x Cocatalyst on a $SrTiO_3$ Photocatalyst
Chem. Lett., **43** (2014) 1725.

M.Yoshida, T.Yomogida, T.Mineo, K.Nitta, K.Kato, T.Masuda, H.Nitani, H.Abe, S.Takakusagi, T.Uruga, K.Asakura, K.Uosaki and H.Kondoh
Photoexcited Hole Transfer to a MnO_x Cocatalyst on a $SrTiO_3$ Photoelectrode during Oxygen Evolution Studied by In Situ X-Ray Absorption Spectroscopy
J. Phys. Chem. C, **118** (2014) 24302.

M.Yoshida and H.Kondoh
In-Situ Observation of Model Catalysts under Reaction Conditions using X-Ray Core-Level Spectroscopy
Chem. Rec., **14** (2014) 806.

Y.Li, B.Huliyageqi, W.Haschaolu, Z.Song, O.Tegus and I.Nakai
EXAFS Study of $Mn_{1.28}Fe_{0.67}P_{0.46}Si_{0.54}$ Compound with First-Order Phase Transition
J. Elec. Spec. Relat. Phenom., **196** (2014) 104.

Y.Hatakeyama, K.Asakura, S.Takahashi, K.Judai and K.Nishikawa
Microscopic Structure of Naked Au Nanoparticles Synthesized in Typical Ionic Liquids by Sputter Deposition
J. Phys. Chem. C, **118** (2014) 27973.

T.Sugiyama, M.Uo, T.Wada, T.Hongo, D.Omagari, K.Komiyama, H.Sasaki, H.Takahashi, M.Kusama and Y.Mori
Novel Metal Allergy Patch Test using Metal Nanoballs
Journal of Nanobiotechnology, **12** (2014) 51.

S.Hinokuma, H.Kogami, N,Yamashita, Y.Katsuhara, K.Ikeue and M.Machida
Subnano-Particle Ce Catalyst Prepared by Pulsed Arc- Plasma Process
Catal. Commun., **54** (2014) 81.

A.Ohta
Sepeciation Study on Cr in Geochemical Reference Material Sediment Series using Sequential Extraction and XAFS Spectroscopy
Geostandards and Geoanalytical Research **39** (2014) 87.

T.Kashiwabara, Y.Oishi, A.Sakaguchi, T.Sugiyama, A.Usui and Y.Takahashi
Chemical Processes for the Extreme Enrichment of Tellurium into Marine Ferromanganese Oxides
Geochim. Cosmochim. Acta, **131** (2014) 150.

K.Fujikawa, H.Ariga, S.Takakusagi, H.Uehara, T.Ohba and K.Asakura
Micro Reverse Monte Carlo Approach to EXAFS Analysis
e-J Surf.Sci.Nanotech, **12** (2014) 322.

N.Fukuda, M.Takaoka,, K.Oshita and T.Mizuno
Stabilizing Conditions of Metal Mercury in Mercury Sulfurization using a Planetary Ball Mill
J. Hazard. Mater., **276** (2014) 433.

D.N.Lobo, K.R.Priolkar, S.Emura and A.K.Nigam
Ferromagnetic Interactions and Martensitic Transformation in Fe Doped Ni-Mn-In Shape Memory Alloys
J. Appl. Phys., **18** (2014) 183903.

M.Kato, K.Kimijima, M.Shibata, H.Notsu, K.Ogino, K.Inokuma, N.Ohta, H.Uehara, Y.Uemura, N.Oyaizu, T.Ohba, S.Takakusagi, K.Asakura and I.Yagi
Deprotonation of a Dinuclear Copper Complex of 3,5-Diamino-1,2,4-Triazole for High Oxygen Reduction Activity
Phys. Chem. Chem. Phys., **17** (2014) 8638.

13A

S.Yoshimoto, K.Kameshima, T.Koitaya, Y.Harada, K.Mukai, J.Yoshinobu
Interface State and Energy Level Alignment of F_4-TCNQ Sandwiched between a Pentacene Film and the Ethylene-Terminated Si(100) Surface
Organic Electronics, **15** (2014) 356.

K.Ozawa, Y.Mimori, H.Kato, M.Emori, H.Sakama, S.Imanishi, K.Edamoto and K.Mase
Shockley Surface State on α-Brass(111) and its Response to Oxygen Adsorption
Surf. Sci. **623** (2014) 6.

K.Ozawa, Y.Mimori, H.Kato, S.Imanishi, K.Edamoto and K.Mase
Photoelectron Spectroscopy Study of Interaction of Oxygen with the (111) Surface of a Cu-Zn Alloy
Surf. Sci., **623** (2014) 1.

Y.Takeichi, N.Inami, H.Suga, K.Ono and Y.Takahashi
Development of a Compact Scanning Transmission X- Ray Microscope (STXM) at the Photon Factory
Chem. Lett., **43** (2014) 373.

R.Toyoshima, M.Shimura, M.Yoshida, Y.Monya, K.Suzuki, K.Amemiya, K.Mase, B.S.Mun and H.Kondoh
A Near-Ambient-Pressure XPS Study on Catalytic CO Oxidation Reaction over a Ru(1010) Surface
Surf. Sci., **621** (2014) 128.

M.Z.Hossain, M.B.A.Razak, S.Yoshimoto, K.Mukai, T.Koitaya, J.Yoshinobu, H.Sone, S.Hosaka and M.C.Hersam
Aqueous-Phase Oxidation of Epitaxial Graphene on the Silicon Face of SiC(0001)
J. Phys. Chem. C, **118** (2014) 1014.

Y.Moritomo, T.Sakurai, T.Yasuda, Y.Takeichi, K.Yonezawa, H.Kamioka, H.Suga, Y.Takahashi, Y.Yoshida, N.Inami, K.Mase and K.Ono
Molecular Mixing in Donor and Acceptor Domains as Investigated by Scanning Transmission X-Ray Microscopy
Appl. Phys. Express, **7** (2014) 052302.

Y.Takeichi, N.Inami, H.Suga, T.Ueno, S.Kishimoto, Y.Takahashi and K.Ono
Development of a Compact Scanning Transmission X-Ray Microscope
J. Phys.: Conf. Ser, **502** (2014) 012009.

R.Friedlein, A.Fleurence, K.Aoyagi, M.P.de Jong, H.V.Bui, F.B.Wiggers, S.Yoshimoto, T.Koitaya, S.Shimizu, H.Noritake, K.Mukai, J.Yoshinobu, Y.Yamada-Takamura
Core Level Excitations–A Fingerprint of Structural and Electronic Properties of Epitaxial Silicene
J. Chem. Phys., **140** (2014) 184704.

H.Suga, Q.Fan, Y.Takeichi, K.Tanaka, H.Kondo, V.V.Kanivets, A.Sakaguchi, K.Kato, N.Inami, K.Mase, K.Ono and Y.Takahashi
Characterization of Particulate Matters in the Pripyat River in Chernobyl Related to their Adsorption of Radiocesium with Inhibition Effect by Natural Organic Matter
Chem. Lett., **43** (2014) 1128.

Y.Yoshiike, H.Fukumoto, I.Kokubo, Y.Aoki, K.Nakatsuji and H.Hirayama
Regular Ripples at the Surfaces of Heteroepitaxially Grown Ag(111) Ultra-Thin Films on Si(111)$\sqrt{3}\times\sqrt{3}$-B Substrates
Appl. Phys. Lett., **104** (2014) 191605.

K.Ozawa, T.Kakubo, K.Shimizu, N.Amino, K.Mase, E.Ikenaga, T.Nakamura, T.Kinoshita and H.Oji
In situ Chemical State Analysis of Buried Polymer/Metal Adhesive Interface by Hard X-Ray Photoelectron Spectroscopy
Appl. Surf. Sci., **320** (2014) 177.

S.Yoshimoto, M.Furuhashi, T.Koitaya, Y.Shiozawa, K.Fujimaki, Y.Harada, K.Mukai and J.Yoshinobu
Quantitative Analysis of Chemical Interaction and Doping of the Si(111) Native Oxide Surface with Tetrafluorotetracyanoquinodimethane
J. Appl. Phys., **115** (2014) 143709.

Y.Nakayama, Y.Uragami, M.Yamamoto, S.Machida, H.Kinjo, K.Mase, K.R.Koswattage and H.Ishii
Determination of the Highest Occupied Molecular Orbital Energy of Pentacene Single Crystals by Ultraviolet Photoelectron and Photoelectron Yield Spectroscopies
Jpn. J. Appl. Phys., **53** (2014) 01AD03.

M.Yoshida and H.Kondoh
In-Situ Observation of Model Catalysts under Reaction Conditions using X-Ray Core-Level Spectroscopy
Chem. Rec., **14** (2014) 806.

H.Kondoh, Y.Higashi, M.Yoshida, Y.Monya, R.Toyoshima, K.Mase, K.Amemiya, F.Tsukioka, M.Nagasaka, Y.Iwasawa, H.Orita, K.Mukai and J.Yoshinobu
Structure and Photo-Induced Charge Transfer of Pyridine Molecules Adsorbed on TiO_2(110): A NEXAFS and Core-Hole-Clock Study
Electrochemistry, **82** (2014) 341.

R.Toyoshima, M.Yoshida, Y.Monya, K.Suzuki, K.Amemiya, K.Mase, B.S.Mun and H.Kondoh
High-Pressure-Induced Dense CO Overlayer on Pt(111) Surface: A Chemical Analysis with *In-Situ* Near Ambient Pressure XPS
Phys. Chem. Chem. Phys., **16** (2014) 23564.

Q.H.Fan, Y.Takahashi, K.Tanaka and A.Sakaguchi
An EXAFS Study on the Effects of Natural Organic Matter and the Expandability of Clay Minerals on Cesium Adsorption and Mobility
Geochim. Cosmochim. Acta, **135** (2014) 49.

Q.Fan, N.Yamaguchi, M.Tanaka, H.Tsukada, and Y.Takahashi,
Relationship between the Adsorption Species of Cesium and Radiocesium Interception Potential in Soils and Minerals: an EXAFS Study
J. Environ. Radioact., **138** (2014) 92.

Former 13A

L.Li, T.Nagai, T.Ishido, S.Motai, K.Fujino and S.Itoh
Formation of a Solid Solution in the $MgSiO_3$-$MnSiO_3$ Perovskite System
Phys. Chem. Minerals, **41** (2014) 431.

13B

X.Hao, S.Wang, W.Fu, T.Sakurai, S.Masuda and K.Akimoto
Novel Cathode Buffer Layer of Ag-Doped Bathocuproine for Small Molecule Organic Solar Cell with Inverted Structure
Organic Electronics, **15** (2014) 1773.

M.Yano, M.Endo, Y.Hasegawa, R.Okada, Y.Yamada and M.Sasaki
Well-Ordered Monolayers of Alkali-Doped Coronene and Picene: Molecular Arrangements and Electronic Structures
J. Chem. Phys., **141** (2014) 034708.

M.Z.Hossain, M.B.A.Razak, H.Noritake, Y.Shiozawa, S.Yoshimoto, K.Mukai, T.Koitaya, J.Yoshinobu and S.Hosaka
Monolayer Selective Methylation of Epitaxial Graphene on SiC(0001) Through Two-Step Chlorination- Alkylation Reactions
J. Phys. Chem. C, **118** (2014) 22096.

R.Toyoshima, M.Yoshida, Y.Monya, K.Suzuki, K.Amemiya, K.Mase, B.S.Mun and H.Kondoh
High-Pressure-Induced Dense CO Overlayer on Pt(111) Surface: A Chemical Analysis with *In-Situ* Near Ambient Pressure XPS
Phys. Chem. Chem. Phys., **16** (2014) 23564.

14A

Y.Sun, M.Koshimizu, N.Yahaba, F.Nishikido, S.Kishimoto, R.Haruki and K.Asai
High-Energy X-Ray Detection by Hafnium-Doped Organic-Inorganic Hybrid Scintillators Prepared by Sol- Gel Method
Appl. Phys. Lett., **104** (2014) 174104.

N.Yahaba, M.Koshimizu, Y.Sun, T.Yanagida, Y.Fujimoto, R.Haruki, F.Nishikido, S.Kishimoto and K.Asai
X-Ray Detection Capability of a Cs_2ZnCl_4 Single-Crystal Scintillator
Appl. Phys. Express., **7** (2014) 062602.

T.Miyoshi, M.I.Ahmed, Y.Arai, Y.Fujita, Y.Ikemoto, A.Takeda and K.Tauchi
SOI Monolithic Pixel Detector
J. Instrum., **9** (2014) C05044.

N.Ishizawa, K.Tateishi, S.Oishi and S.Kishimoto
Bond-Length Fluctuation in the Orthorhombic 3×3×1 Superstructure of $LiMn_2O_4$ Spinel
American Mineralogist, **99** (2014) 1528.

S.Kishimoto, T.Mitsui, R.Haruki, Y.Yoda, T.Taniguchi, S.Shimazaki, M.Ikeno, M.Saito and M.Tanaka
Nuclear Resonant Scattering Measurements on ^{57}Fe by Multichannel Scaling with a 64-Pixel Silicon Avalanche Photodiode Linear-Array Detector
Rev. Sci. Instrum., **85** (2014) 113102.

T.Fujiwara, Y.Mitsuya, H.Takahashi, T.Fushie, S.Kishimoto, B.Guerard and M.Uesaka
The Performance of Glass GEM
J. Instrum, **9** (2014) 11007.

14B

K.Hirano, Y.Takahashi and H.Sugiyama
Development and Application of Variable-Magnification X-Ray Bragg Magnifiers
Nucl. Instrum. Meth. Phys. Res. A, **741** (2014) 78.

K.Hirano, Y.Takahashi and H.Sugiyama
Application of Variable-Magnification X-Ray Bragg Magnifier to Analyzer-Based Phase-Contrast Computed Tomography
Jpn. J. Appl. Phys., **53** (2014) 040302.

Y.Kato, H.Umezawa and S.Shikata
X-Ray Topographic Study of a Homoepitaxial Diamond Layer on an Ultraviolet-Irradiated Precision Polished Substrate
Acta Physica Polonica A, **125** (2014) 969.

T.Miyoshi, M.I.Ahmed, Y.Arai, Y.Fujita, Y.Ikemoto, A.Takeda and K.Tauchi
SOI Monolithic Pixel Detector
Journal of Instrumentation, **9** (2014) C05044.

Y.Mokuno, Y.Kato, N.Tsubouchi, A.Chayahara, H.Yamada and S.Shikata
A Nitrogen Doped Low-Dislocation Density Free-Standing Single Crystal Diamond Plate Fabricated by a Lift-Off Process
Appl. Phys. Lett., **104** (2014) 252109.

14C

M.Ando, N.Sunaguchi, Y.Wu, S.Do, Y.Sung, A.Louissaint, T.Yuasa, S.Ichihara and R.Gupta
Crystal Analyser-Based X-Ray Phase Contrast Imaging in the Dark Field: Implementation and Evaluation using Excised Tissue Specimens
European Radiology, **24** (2014) 423.

T.Miyoshi, M.I.Ahmed, Y.Arai, Y.Fujita, Y.Ikemoto, A.Takeda and K.Tauchi
SOI Monolithic Pixel Detector
J. Instrum., **9** (2014) C05044.

H.Mimachi, S.Takeya, A.Yoneyama, K.Hyodo, T.Takeda, Y.Gotoh and T.Murayama
Natural Gas Storage and Transportation within Gas Hydrate of Smaller Particle: Size Dependence of Self-Preservation Phenomenon of Natural Gas Hydrate
Chem. Eng. Sci., **118** (2014) 208.

J.Ryu, S.Ahn, S.G.Kim, T.Kim and S.J.Lee
Interactive Ion-Mediated Sap Flow Regulation in Olive and Laurel Stems: Physicochemical Characteristics of Water Transport via the Pit Structure
PLOS ONE, **9** (2014) e98484.

S.Takeya, Y.Gotoh, A.Yoneyama, K.Ueda, K.Hyodo and T.Takeda
Nondestructive Imaging of the Clathrate Hydrate Grown at Interparticle Space
Proceedings of the 8th International Conference on Gas Hydrates (ICGH8-2014), (2014)

S.Ichihara, K.Mori, N.Sunaguchi, T.Yuasa, Y.Wu and M.Ando
Three-Dimensional Observation of Sclerosing Adenosis Involved by Lobular Carcinoma in Situ using Crystal Analyzer-Based X-Ray Phase Contrast CT
Virchows Archiv, **465** (2014) S100.

N.Sunaguchi, T.Yuasa and M.Ando
Iterative Reconstruction for X-Ray Dark Field Imaging CT: Artifacts Reduction for Hard and Soft Mixture Tissue
Proc. IASTED Biomedical Engineerging, **818** (2014) 030.

Former 15A

Y.Sageshima, A.Noro and Y.Matsushita
Structural Isomer Effects on the Morphology of Block Copolymer/Metal Salts Hybrids
Journal of Polymer Science, Part B: Polymer Physics, **52** (2014) 377.

G.Cui, M.Fujikawa, S.Nagano, M.Sano, H.Takase, T.Miyazaki, S.Sakurai and K.Yamamoto
Perpendicular Oriented Cylinders via Directional Coalescence of Spheres Embedded in Block Copolymer Films Induced by Solvent Annealing
Polymer, **55** (2014) 1601.

K.Nakagawa, Y.Yamada, Y.Matsumura, S.Tsukamoto, M.Yamamoto-Ohtomo, H.Ohtomo, T.Okabe, K.Fujiwara and M.Ikeguchi
Relationship between Chain Collapse and Secondary Structure Formation in a Partially Folded Protein
Biopolymers, **101** (2014) 651.

H.Takahashi
On Hydration Repulsive Forces between Various Phosphlipid Bilayers
JPS Conf. Proc., **1** (2014) 012041.

Y.Kawabata, A.Murakami and T.Kato
Electrolyte Effect on Lamellar Domain Morphology in a Nonionic Surfactant Solution below the Krafft Temperature
J. Phys. Chem. B, **118** (2014) 1022.

M.Hishida, K.Tanaka, Y.Yamamura and K.Saito
Cooperativity between Water and Lipids in Lamellar to Inverted-Hexagonal Phase Transition
J. Phys. Soc. Jpn., **83** (2014) 044801.

A.B.Imran, K.Esaki, H.Gotoh, T.Seki, K.Ito, Y.Sakai and Y.Takeoka
Extremely Stretchable Thermosensitive Hydrogels by Introducing Slide-Ring Polyrotaxane Cross-Linkers and Ionic Groups into the Polymer Network
Nature Communications, **5** (2014) 5124.

Y.Maki, K.Furusawa, S.Yasuraoka, H.Okamura, N.Hosoya, M.Sunaga, T.Dobashi, Y.Sugimoto and K.Wakabayashi
Universality and Specificity in Molecular Orientation in Anisotropic Gels Prepared by Diffusion Method
Carbohydr. Polym., **108** (2014) 118.

M.Hishida, Y.Yamamura and K.Saito
Salt Effects on Lamellar Repeat Distance Depending on Head Groups of Neutrally Charged Lipids
Langmuir, **30** (2014) 10583.

E.I.Naito, H.Hondoh, S.Ueno and K.Sato
Mixing Phase Behavior of 1,3-Dipalmitoyl-2-Oleoyl-*sn*-Glycerol (POP) and 1,2-Dipalmitoyl-3-Oleoyl-*rac*-Glycerol (PPO) in *n*-Dodecane Solution
J. Am Oil Chem Soc, **91** (2014) 1837.

15A2

I.Saito, T.Okamoto, K.Shimokita, T.Miyazaki and K.Yamamoto
Perpendicular Orientation of Cylindrical Microdomains of $FeCl_3$ Doped Polystyrene-*b*-poly(2-vinyl pyridine) Thin Films
Koubunshi Ronbunshu, **71** (2014) 586. (*in Japanese*).

15B1

Y.Tezuka, T.Sasaki, Y.Fujita, T.Iwamoto, H.Osawa, S.Nozawa, N.Nakajima, H.Sato and T.Iwazumi
Core Excitations in Resonant X-Ray Raman Scattering of Titanium Oxides: An Approach to Studying Electronic Structures
J. Phys. Soc. Jpn., **83** (2014) 014707.

K.Mizuno, K.Morikawa, H.Okamoto and E.Hashimoto Row of Dislocation Loops as a Vacancy Source in Ultrahigh-Purity Aluminum Single Crystals with a Low Dislocation Density
Trans. Mat. Res. Soc. Japan, **39** (2014) 169.

H.Koizumi, S.Uda, K.Fujiwara, M.Tachibana, K.Kojima and J.Nozawa
Enhancement of Crystal Homogeneity of Protein Crystals under Application of an External Alternating Current Electric Field
AIP Conf. Proc., **1618** (2014) 265.

H.Koizumi, S.Uda, K.Fujiwara, M.Tachibana, K.Kojima and J.Nozawa
Control of Subgrain Formation in Protein Crystals by the Application of an External Electric Field
Cryst. Growth Des., **14** (2014) 5662.

15B2

T.Shirasawa, W.Voegeli, T.Nojima, Y.Iwasawa, Y.Yamaguchi and T.Takahashi
Identification of the Structure Model of the Si(111)-(5x2)-Au Surface
Phys. Rev. Lett., **113** (2014) 165501.

T.Shirasawa, M.Sugiki, T.Hirahara, M.Aitani, T.Shirai, S.Hasegawa and T.Takahashi
Structure and Transport Properties of Cu-Doped Bi_2Se_3 Films
Phys. Rev. B, **89** (2014) 195311.

15C

S.Ji, K.Kojima, Y.Ishida, H.Yamaguchi, S.Saito, T.Kato, H.Tsuchida, S.Yoshida and H.Okumura
Characterization of the Defect Evolution in Thick Heavily Al-Doped 4H-SiC Epilayers
Materials Science Forum, **778-780** (2014) 151.

S.Harada, Y.Yamamoto, S.Xiao, M.Tagawa and T.Ujihara
Surface Morphology and Threading Dislocation Conversion Behavior during Solution Growth of 4H-SiC using Al-Si Solvent
Materials Science Forum, **778-780** (2014) 67.

Y.Yamamoto, S.Harada, K.Seki, A.Horio, T.Mitsuhashi, D.Koike, M.Tagawa, and T.Ujihara
Low-Dislocation-Density 4H-SiC Crystal Growth Utilizing Dislocation Conversion during Solution Method
Appl. Phys. Express., **7** (2014) 065501.

S.Harada, Y.Yamamoto, K.Seki, A.Horio, M.Tagawa and T.Ujihara
Different Behavior of Threading Edge Dislocation Conversion During the Solution Growth of 4H-SiC Depending on the Burgers Vector
Acta Mater., **81** (2014) 284.

16A

K.Amemiya, M.Sakamaki, M.Mizusawa and M.Takeda
Twisted Magnetic Structure in Ferromagnetic Ultrathin Ni Films Induced by Magnetic Anisotropy Interaction with Antiferromagnetic FeMn
Phys. Rev. B, **89** (2014) 054404.

Y.Hikosaka, P.Lablanquie, F.Penent, P.Selles, E.Shigemasa and K.Ito
Resonant Multiple Auger Decay after the $2p_{3/2}4$ Excitation in Ar Studied with a Multielectron Coincidence Method
Phys. Rev. A, **89** (2014) 023410.

Y.Takeichi, N.Inami, H.Suga, K.Ono and Y.Takahashi
Development of a Compact Scanning Transmission X-Ray Microscope (STXM) at the Photon Factory
Chem. Lett., **43** (2014) 373.

J.Okamoto, H.Nakao, Y.Yamasaki, H.Wadati, A.Tanaka, M.Kubota, K.Horigane, Y.Murakami and K.Yamada
Antiferromagnetic Order of the Co^{2+} High-Spin State with a Large Orbital Angular Momentum in $La_{1.5}Ca_{0.5}CoO_4$
J. Phys. Soc. Jpn., **83** (2014) 044705.

Y.Takeichi, N.Inami, H.Suga, T.Ueno, S.Kishimoto, Y.Takahashi and K.Ono
Development of a Compact Scanning Transmission X- Ray Microscope
J. Phys.: Conf. Ser, **502** (2014) 012009.

T.Koide, Y.Saitoh, M.Sakamaki, K.Amemiya, A.Iwase and T.Matsui
Change in Magnetic and Structural Properties of FeRh Thin Films by Gold Cluster Ion Beam Irradiation with the Energy of 1.67MeV/Atom
J. Appl. Phys., **115** (2014) 17B722.

M.Sakamaki and K.Amemiya
Enhancement of Perpendicular Magnetic Anisotropy by Compressive Strain in Alternately Layered FeNi Thin Films
J. Phys.: Condens. Matter, **26** (2014) 166002.

G.Shibata, K.Yoshimatsu, E.Sakai, V.R.Singh, V.K.Verma, K.Ishigami, T.Harano, T.Kadono, Y.Takeda, T.Okane, Y.Saitoh, H.Yamagami, A.Sawa, H.Kumigashira, M.Oshima, T.Koide and A.Fujimori
Thickness-Dependent Ferromagnetic Metal to Paramagnetic Insulator Transition in $La_{0.6}Sr_{0.4}MnO_3$ Thin Films Studied by X-Ray Magnetic Circular Dichroism
Phys. Rev. B, **89** (2014) 235123.

H.Nakao, Y.Yamasaki, J.Okamoto, T.Sudayama, Y.Takahashi, K.Kobayashi, R.Kumai and Y.Murakami
Development of an In-Vacuum Diffractometer for Resonant Soft X-Ray Scattering
J. Phys.: Conf. Ser., **502** (2014) 012015.

Y.Takahashi, H.Nakao, R.Kumai, S.Ishibashi, S.Horiuchi, M.Kohyama, K.Kobayashi, Y.Yamasaki, J.Okamoto, T.Sudayama, Y.Murakami and Y.Tokura
Molecular Electronic States in Charge Transfer Complex Studied by X-Ray Absorption Spectroscopy
J. Phys.: Conf. Ser., **502** (2014) 012036.

M.Kubota, H.Yamada, H.Nakao, J.Okamoto, Y.Yamasaki, A.Sawa and Y.Murakami
Magnetic and Electronic Properties of $(LaMnO_3)_5$ $(SrMnO_3)_5$ Superlattice Revealed by Resonant Soft X-Ray Scattering
Jpn. J. Appl. Phys., **53** (2014) 05FH07.

M.Yoshida and H.Kondoh
In-Situ Observation of Model Catalysts under Reaction Conditions using X-Ray Core-Level Spectroscopy
Chem. Rec., **14** (2014) 806.

S.Shiki, M.Ukibe, N.Matsubayashi, N.Zen, M.Koike, Y.Kitajima and M.Ohkubo
Current Status of AIST X-Ray-Absorption-Spectroscopy (XAFS) Instrument with 100-Pixel Superconducting- Tunnel-Junction Array Detector
J. Low Temp. Phys., **176** (2014) 604.

Y.Takahashi, T.Kadono, S.Yamamoto, V.R.Singh, V.K.Verma, K.Ishigami, G.Shibata, T.Harano, Y.Takeda, T.Okane, Y.Saitoh, H.Yamagami, M.Takano and A.Fujimori
Orbital Magnetic Moment and Coercivity of SiO_2 -Coated FePt Nanoparticles Studied by X-Ray Magnetic Circular Dichroism
Phys. Rev. B, **90** (2014) 024423.

16B

S.Hasegawa, S.Obara, F.Yoshida, Y.Azuma, F.Koike and T.Nagata
K-Shell Photoionization Spectra of Atomic Beryllium between $1s^2s(2)$ and $1s(2s2p^3P)4s$
Phys. Rev. A, **90** (2014) 032503.

17A

Y.Yasutake, W.Kitagawa, M.Hata, T.Nishioka, T.Ozaki, M.Nishiyama, T.Kuzuyama and T.Tamura
Structure of the Quinoline N-Hydroxylating Cytochrome P450 RauA, an Essential Enzyme that Confers Antibiotic Activity on Aurachin Alkaloids
FEBS Letters, **588** (2014) 105.

S.Okada, T.Yamamoto, H.Watanabe, T.Nishimoto, H.Chaen, S.Fukuda, T.Wakagi and S.Fushinobu
Structural and Mutational Analysis of Substrate Recognition in Kojibiose Phosphorylase
FEBS J., **281** (2014) 778.

Y.Sakamoto, Y.Suzuki, I.Iizuka, C.Tateoka, S.Roppongi, H.Okada, T.Nonaka, Y.Morikawa, K.T.Nakamura, W.Ogasawara and N.Tanaka
Crystallization and Preliminary X-Ray Crystallographic Studies of Dipeptidyl Aminopeptidase BII from *Pseudoxanthomonas mexicana* WO24
Acta Cryst. F, **70** (2014) 221.

S.Yamashita, D.Takeshita and K.Tomita
Translocation and Rotation of tRNA during Template-Independent RNA Polymerization by tRNA Nucleotidyltransferase
Structure, **22** (2014) 315.

Y.Hizukuri, T.Oda, S.Tabata, K.Tamura-Kawakami, R.Oi, M.Sato, J.Takagi, Y.Akiyama and T.Nogi
A Structure-Based Model of Substrate Discrimination by a Noncanonical PDZ Tandem in the Intramembrane-Cleaving Protease RseP
Structure, **22** (2014) 326.

D.Matsui, D.-H.Im, A.Sugawara, Y.Fukuta, S.Fushinobu, K.Isobe and Y.Asano
Mutational and Crystallographic Analysis of L-Amino Acid Oxidase/Monooxygenase from *Pseudomonas* sp. AIU 813: Interconversion between Oxidase and Monooxygenase Activities
FEBS Open Bio, **4** (2014) 220.

H.-P.-T.Ngo, N.M.F.S.A.Cerqueira, J.-K.Kim, M.-K.Hong, P.A.Fernandes, M.J.Ramos, L.-W.Kang
PLP Undergoes Conformational Changes during the Course of an Enzymatic Reaction
Acta Cryst. D, **70** (2014) 596.

Y.S.Cho, J.H.Yoo, S.M.Park and H.S.Cho
The Structures of the Kinase Domain and UBA Domain of MPK38 Suggest the Activation Mechanism for Kinase Activity
Acta Cryst. D, **70** (2014) 514.

T.Suzuki, H.Makyio, H.Ando, N.Komura, M.Menjo, Y.Yamada, A.Imamura, H.Ishida, S.Wakatsuki, R.Kato and M.Kiso
Expanded Potential of Seleno-Carbohydrates as a Molecular Tool for X-Ray Structural Determination of a Carbohydrate-Protein Complex with Single/Multi-Wavelength Anomalous Dispersion Phasing
Bioorganic and Medicinal Chemistry, **22** (2014) 2090.

S.Liu, L.-F.Tian, Y.-P.Liu, X.-M.An, Q.Tang, X.-X.Yan and D.-C.Liang
Structural Basis for DNA Recognition and Nuclease Processing by the Mre11 Homologue SbcD in Double- Strand Breaks Repair
Acta Cryst. D, **70** (2014) 299.

S.Niwa, L.-J.Yu, K.Takeda, Y.Hirano, T.Kawakami, Z.-Y.Wang-Otomo and K.Miki
Structure of the LH1-RC complex from *Thermochromatium tepidum* at 3.0 Å
Nature, **508** (2014) 228.

S.Nakano, S.Okazaki, H.Tokiwa and Y.Asano
Binding of NAD^+ and L-Threonine Induces Stepwise Structural and Flexibility Changes in *Cupriavidus necator* L-Threonine Dehydrogenase
J. Biol. Chem., **289** (2014) 10445.

D.Sen, C.W.Kim, N.H.Heo and K.Seff
Introducing Copper Ions into Zeolite Y by the Thallous Ion Exchange Method: Single Crystal Structure of $|Cu_{21.6}Tl_{39.2}|[Si_{121}Al_{71}O_{384}]$-FAU
J. Porous. Mater., **21** (2014) 321.

T.Ito, K.Saikawa, S.Kim, K.Fujita, A.Ishiwata, S.Kaeothip, T.Arakawa, T.Wakagi, G.T.Beckham, Y.Ito and S.Fushinobu
Crystal Structure of Glycoside Hydrolase Family 127 β-L-Arabinofuranosidase from *Bifidobacterium longum*
Biochem. Biophys. Res. Commun., **447** (2014) 32.

L.Wang, X.Yang, S.Li, Z.Wang, Y.Liu, J.Feng, Y.Zhu and Y.Shen
Structural and Mechanistic Insights into MICU1 Regulation of Mitochondrial Calcium Uptake
EMBO J., **33** (2014) 594.

T.Tsuda, M.Asami, Y.Koguchi and S.Kojima
Single Mutation Alters the Substrate Specificity of L-Amino Acid Ligase
Biochemistry, **53** (2014) 2650.

K.Yasukawa, S.Nakano and Y.Asano
Tailoring D-Amino Acid Oxidase from the Pig Kidney to R-Stereoselective Amine Oxidase and its Use in the Deracemization of α-Methylbenzylamine
Angew. Chem. Int. Ed., **53** (2014) 4428.

A.Kishimoto, A.Kita, T.Ishibashi, H.Tomita, Y.Yokooji, T.Imanaka, H.Atomi and K.Miki
Crystal Structure of Phosphopantothenate Synthetase from *Thermococcus kodakarensis*
Proteins **82** (2014) 1924.

T.Ohnuma, N.Umemoto, T.Nagata, S.Shinya, T.Numata, T.Taira and T.Fukamizo
Crystal Structure of a "Loopless" GH19 Chitinase in Complex with Chitin Tetrasaccharide Spanning the Catalytic Center
Biochim. Biophys. Acta, **1844** (2014) 793.

Y.Sakamoto, Y.Suzuki, I.Iizuka, C.Tateoka, S.Roppongi, M.Fujimoto, H.Tanaka, M.Masaki, K.Ohta, H.Okada, T.Nonaka, Y.Morikawa, K.T.Nakamura, W.Ogasawara and N.Tanaka
S46 Peptidases are the First Exopeptidases to be Members of Clan PA
Scientific Reports, **4** (2014) 4977.

M.Elahi, M.M.Islam, K.Noguchi, M.Yohda, H.Toh, Y.Kuroda
Computational Prediction and Experimental Characterization of a ″Size Switch Type Repacking" during the Evolution of Dengue Envelope Protein Domain III (ED3)
BBA Protein and Proteomics **1833** (2014) 585.

K.J.Cho, K.W.Hong, S.-H.Kim, J.H.Seok, S.Kim, J.- H.Lee, X.Saelens, K.H.Kim
Insight into Highly Conserved H1 Subtype-Specific Epitopes in Influenza Virus Hemagglutinin
PLOS ONE, **9** (2014) e89803.

Y.Fujioka, S.W.Suzuki, H.Yamamoto, C.Kondo-Kakuta, Y.Kimura, H.Hirano, R.Akada, F.Inagaki, Y.Ohsumi and N.N.Noda
Structural Basis of Starvation-Induced Assembly of the Autophagy Initiation Complex
Nature Structural Molecular Biology, **21** (2014) 513.

S.Terawaki, H.Ootsuka, Y.Higuchi and K.Wakamatsu
Crystallographic Characterization of the C-Terminal Coiled-Coil Region of Mouse Bicaudal-D1(BICD1)
Acta Cryst. F, **70** (2014) 1103.

T.Itoh, T.Hibi, I.Sugimoto, F.Suzuki, Y.Fujii, A.Taketo and H.Kimoto
Crystallization and Preliminary X-Ray Analysis of the Catalytic Domains of *Paenibacillus* sp. Strain FPU-7 Cell-Surface-Expressed Chitinase ChiW
Acta Cryst. F, **70** (2014) 350.

H.S.Kim, G.-H.Kwak, K.Lee, C.-H.Jo, K.Y.Hwang and H.-Y.Kim
Structural and Biochemical Analysis of a Type II Free Methionine-R-Sulfoxide Reductase from *Thermoplasma acidophilum*
Arch. Biochem. Biophys., **560** (2014) 10.

N.Shibayama, K.Sugiyama, J.R.H.Tame and S.-Y.Park
Capturing the Hemoglobin Allosteric Transition in a Single Crystal Form
J. Am. Chem. Soc., **136** (2014) 5097.

H.Yokoyama and I.Matsui
Crystal Structure of the Stomatin Operon Partner Protein from *Pyrococcus horikoshii* Indicates the Formation of a Multimeric Assembly
FEBS Open Bio, **4** (2014) 804.

M.-K.Hong, A.J.M.Ribeiro, J.-K.Kim, H.-P.-T.Ngo, J.Kim, C.H.Lee, Y.-J.Ahn, P.A.Fernandes, Q.Li, M.J.Ramos and L.-W.Kang
Divalent Metal Ion-Based Catalytic Mechanism of the Nudix Hydrolase Orf153(YmfB) from *Escherichia coli*
Acta Cryst. D, **70** (2014) 1297.

V.Schaeffer, M.Akutsu, M.H.Olma, L.C.Gomes, M.Kawasaki and I.Dikic
Binding of OTULIN to the PUB Domain of HOIP Controls NF-κB Signaling
Mol. Cell, **54** (2014) 349.

H.Tsukagoshi, A.Nakamura, T.Ishida, K.K.Touhara, M.Otagiri, S.Moriya, M.Samejima, K.Igarashi, S.Fushinobu, K.Kitamoto and M.Arioka
Structural and Biochemical Analyses of Glycoside Hydrolase Family 26 *β*-Mannanase from a Symbiotic Protist of the Termite *Reticulitermes speratus*
J. Biol. Chem., **289** (2014) 10843.

K.K.Touhara, T.Nihira, M.Kitaoka, H.Nakai and S.Fushinobu
Structural Basis for Reversible Phosphorolysis and Hydrolysis Reactions of 2-*O*-*α*-Glucosylglycerol Phosphorylase
J. Biol. Chem., **289** (2014) 18067.

K.Suzuki, A.Hori, K.Kawamoto, R.R.Thangudu, T.Ishida, K.Igarashi, M.Samejima, C.Yamada, T.Arakawa, T.Wakagi, T.Koseki and S.Fushinobu
Crystal Structure of a Feruloyl Esterase Belonging to the Tannase Family: A Disulfide Bond Near a Catalytic Triad
Proteins, **82** (2014) 2857.

H.Zhao, G.Sheng, J.Wang, M.Wang, G.Bunkoczi, W.Gong, Z.Wei and Y.Wang
Crystal Structure of the RNA-Guided Immune Surveillance Cascade Complex in *Escherichia coli*
Nature, **515** (2014) 147.

L.Guo, J.Ding, R.Guo, Y.Hou, D.-C.Wang and L.Huang
Biochemical and Structural Insights into RNA Binding by Ssh10b, a Member of the Highly Conserved Sac10b Protein Family in Archaea
J. Biol. Chem., **289** (2014) 1478.

S.Nakano, M.Dadashipour and Y.Asano
Structural and Functional Analysis of Hydroxynitrile Lyase from *Baliospermum montanum* with Crystal Structure, Molecular Dynamics and Enzyme Kinetics
Biochim. Biophys. Acta, **1844** (2014) 2059.

A.Killivalavan, N.Zhuang, Y.S.Park and K.H.Lee
Purification, Crystallization and Preliminary X-Ray Diffraction Studies of UDP-Glucose: Tetrahydrobiopterin *α*-Glucosyltransferase(BGluT) from *Synechococcus* sp. PCC 7942
Acta Cryst. F, **70** (2014) 203.

Q.Tang, Y-P.Liu, X-X.Yan, D-C.Liang
Structural and Functional Characterization of Cys4 Zinc Finger Motif in the Recombination Mediator Protein RecR
DNA Repair, **24** (2014) 10.

D.Takeshita, S.Yamashita and K.Tomita
Molecular Insights into Replication Initiation by Qβ Replicase Using Ribosomal Protein S1
Nucleic Acids Res., **42** (2014) 10809.

M.K.Kim, Y.J.An, J.M.Song, C.S.Jeong, M.H.Kang, K.K.Kwon, Y.H.Lee and S.S.Cha
Structure-Based Investigation into the Functional Roles of the Extended Loop and Substrate-Recognition Sites in an Endo-β-1, 4-D-Mannanase from the Antarctic Springtail, *Cryptopygus antarcticus*
Proteins, **82** (2014) 3217.

E.O.Balogun, D.K.Inaoka, T.Shiba, Y.Kido, C.Tsuge, T.Nara, T.Aoki, T.Honma, A.Tanaka, M.Inoue, S.Matsuoka, P.A.Michels, K.Kita and S.Harada
Molecular Basis for the Reverse Reaction of African Human Trypanosomes Glycerol Kinase
Mol. Microbiol., **94** (2014) 1315.

J.Lu, Y.Gu, J.Feng, W.Zhou, X.Yang and Y.Shen
Structural Insight into the Central Element Assembly of the Synaptonemal Complex
Scientific Reports, **4** (2014) 7059.

Z.Wang, X.Yang, S.Guo, Y.Yang, X.C.Su, Y.Shen and J.Long
Crystal Structure of the Ubiquitin-Like Domain-CUT Repeat-Like Tandem of Special AT-Rich Sequence Binding Protein 1 (SATB1) Reveals a Coordinating DNA-Binding Mechanism
J. Biol. Chem., **289** (2014) 27376.

S.Hanessian, O.M.Saavedra, M.A.Vilchis-Reyes, J.P. Maianti, H.Kanazawa, P.Dozzo, R.D.Matias, A.Serio and J.Kondo
Synthesis, Broad Spectrum Antibacterial Activity, and X-Ray Co-Crystal Structure of the Decoding Bacterial Ribosomal A-Site with 4'-Deoxy-4'-Fluoro Neomycin Analogs
Chemical Science, **5** (2014) 4621.

H.Yamaguchi, J.Sebera, J.Kondo, S.Oda, T.Komuro, T.Kawamura, T.Dairaku, Y.Kondo, I.Okamoto, A.Ono, J.V.Burda, C.Kojima, V.Sychrovsky and Y.Tanaka
The Structure of Metallo-DNA with Consecutive Thymine-Hg^{II}-Thymine Base Pairs Explains Positive Entropy for the Metallo Base Pair Formation
Nucleic Acids Res., **42** (2014) 4094.

D.Yang, T.Mori, T.Matsui, M.Hashimoto, H.Morita, I.Fujii and I.Abe
Expression, Purification, and Crystallization of a Fungal Type III Polyketide Synthase that Produces the Csypyrones
Acta Cryst. F, **70** (2014) 730.

L.Zhang, J.Chen, T.Mori, Y.Yan, W.Liu and I.Abe
Crystallization, and Preliminary X-Ray Diffraction Analysis of AntE, a Crotonyl-CoA Carboxylase/Reductase from *Streptomyces* sp. NRRL 2288
Acta Cryst. F, **70** (2014) 734.

Y.Arimura, K.Shirayama, N.Horikoshi, R.Fujita, H.Taguchi, W.Kagawa, T.Fukagawa, G.Almouzni and H.Kurumizaka
Crystal Structure and Stable Property of the Cancer- Associated Heterotypic Nucleosome Containing CENP-A and H3.3.
Scientific Reports, **4** (2014) 7115.

M.Shiina, K.Hamada, T.B.Inoue, M.Shimamura, A Uchiyama, S.Baba, K.Sato and K.Ogata
Crystallization of the Ets1-Runx1-CBFβ-DNA Complex Formed on the TCRα Gene Enhancer
Acta Cryst. F, **70** (2014) 1380.

E.Hwang, H.U.Cheong, A.U.Mushtaq, H.Kim, K.J.Yeo, E.Kim, W.C.Lee, K.Y.Hwang, C.Cheong and Y.H.Jeon
Structural Basis of the Heterodimerization of the MST and RASSF SARAH Domains in the Hippo Signalling Pathway
Acta Cryst. D, **70** (2014) 1944.

Y.Fu, Y.Kim, K.S.Jin, H.S.Kim, J.H.Kim, D.Wang, M.Park, C.H.Jo, N.H.Kwon, D.Kim, M.H.Kim, Y.H.Jeon, K.Y.Hwang, S.Kim and Y.Cho
Structure of the ArgRS-GlnRS-AIMP1 Complex and its Implications for Mammalian Translation
Proc. Natl. Acad. Sci. USA, **111** (2014) 15084.

K.Inoue, Y.Usami, Y.Ashikawa, H.Noguchi, T.Umeda, A.Y.Ashikawa, T.Horisaki, H.Uchimura, T.Terada, S.Nakamura, K.Shimizu, H.Habe, H.Yamane, Z.Fujimoto and H.Nojiri
Structural Basis of the Divergent Oxygenation Reactions Catalyzed by the Rieske Nonheme Iron Oxygenase Carbazole 1,9a-Dioxygenase.
Appl. Environ. Microbiol., **80** (2014) 2821.

A.Nishizawa, A.Harada, M.Senda, Y.Tachihara, D.Muramatsu, S.Kishigami, S.Mori, K.Sugiyama, T.Senda and S.Kimura
Complete Pyridine Nucleotide-Specificity Conversion of an NADH-Dependent Ferredoxin Reductase.
Biochem. J, **462** (2014) 257.

Z.Wang, L.Li, Y.H.Dong and X.D.Su
Structural and Biochemical Characterization of MdaB from Cariogenic *Streptococcus Mutans* Reveals an NADPH-Specific Quinone Oxidoreductase
Acta Cryst. D, **70** (2014) 912.

K.Kuroki, J.Wang, T.Ose, M.Yamaguchi, S.Tabata, N.Maita, S.Nakamura, M.Kajikawa, A.Kogure, T.Satoh, H.Arase and K.Maenaka
Structural Basis for Simultaneous Recognition of an *O*-Glycan and its Attached Peptide of Mucin Family by Immune Receptor PILRα
Proc. Natl. Acad. Sci. USA, **111** (2014) 8877.

M.Nagae, K.Soga, K.M.Matsumoto, S.Hanashima, A.Ikeda, K.Yamamoto and Y.Yamaguchi
Phytohemagglutinin from *Phaseolus vulgaris* (PHA-E) Displays a Novel Glycan Recognition Mode using a Common Legume Lectin Fold
Glycobiology, **24** (2014) 368.

M.Nagae, A.Ikeda, Y.Kitago, N.Matsumoto, K.Yamamoto, and Y.Yamaguchi
Crystal Structures of Carbohydrate Recognition Domain of Blood Dendritic Cell Antigen-2 (BDCA2) Reveal a Common Domain-Swapped Dimer
Proteins, **82** (2014) 1512.

T.Tomita, T.Ozaki, K.Matsuda, M.Nishiyama and T.Kuzuyama
Crystallization and Preliminary X-Ray Diffraction Analysis of Cyclolavandulyl Diphosphate Synthase, a New Member of the *Cis-Isoprenyl* Diphosphate Synthase Superfamily
Acta Cryst. F, **70** (2014) 1410.

Y.Nishikawa, T.Oyama, N.Kamiya, T.Kon, Y.Y.Toyoshima, H.Nakamura and G.Kurisu
Structure of the Entire Stalk Region of the Dynein Motor Domain
J. Mol. Biol., **426** (2014) 3232.

H.S.Kim, J.Kim, H.N.Im, D.R.An, M.Lee, D.Hesek, S.Mobashery, J.Y.Kim, K.Cho, H.J.Yoon, B.W.Han, B.I.Lee and S.W.Suh
Structural Basis for the Recognition of Muramyltripeptide by *Helicobacter Pylori* Csd4, a D,L-Carboxypeptidase Controlling the Helical Cell Shape
Acta Cryst. D, **70** (2014) 2800.

S.J.Lee, Y.S.Park, S.J.Kim, B.J.Lee and S.W.Suh
Crystal Structure of PhoU from *Pseudomonas aeruginosa*, a Negative Regulator of the Pho Regulon
J. Struct. Biol., **188** (2014) 22.

Y.Hanada, Y.Nishimiya, A.Miura, S.Tsuda and H.Kondo
Hyperactive Antifreeze Protein from an Antarctic Sea Ice Bacterium *Colwellia* sp. Has a Compound Ice-Binding Site Without Repetitive Sequences
FEBS J., **281** (2014) 3576.

N.Asano, A.Nakamura, K.Komoda, K.Kato, I.Tanaka and M.Yao
Crystallization and Preliminary X-Ray Crystallographic Analysis of Ribosome Assembly Factors: the Rpf2-Rrs1 Complex
Acta Cryst. F, **70** (2014) 1649.

T.Matsui, X.Han, J.Yu, M.Yao and I.Tanaka.
Structural Change in FtsZ Induced by Intermolecular Interactions between Bound GTP and the T7 Loop
J. Biol. Chem., **289** (2014) 3501.

Y.Liu, A.Nakamura, Y.Nakazawa, N.Asano, K.A.Ford, M.J.Hohn, I.Tanaka, M.Yao and D.Soll
Ancient Translation Factor is Essential for tRNA- Dependent Cysteine Biosynthesis in Methanogenic Archaea
Proc. Natl. Acad. Sci. USA, **111** (2014) 10520.

F.Mimoto, S.Kadono, H.Katada, T.Igawa, T.Kamikawa and K.Hattori
Crystal Structure of a Novel Asymmetrically Engineered Fc Variant with Improved Affinity for FcγRs
Molecular Immunology, **58** (2014) 132.

H.Suzuki, U.Ohto, K.Higaki, T.M.Barragan, M.A.Moncayo, C.O.Mellet, E.Nanba, J.M.G.Fernandez, Y.Suzuki and T.Shimizu
Structural Basis of Pharmacological Chaperoning for Human β-Galactosidase
J. Biol. Chem., **289** (2014) 14560.

18A

K.Shudo, T.Aoki, S.Ohno, K.Yamazaki, F.Nakayama, M.Tanaka, T.Okuda, A.Harasawa, I.Matsuda, T.Kakizaki and M.Uchiyama
Titanium-Induced Charge of Si(001) Surface Dependent on Local Configuration
J. Elec. Spec. Relat. Phenom., **192** (2014) 35.

Sh.Yamamoto, M.Taguchi, M.Fujisawa, R.Hobara, S.Yamamoto, K.Yaji, T.Nakamura, K.Fujikawa, R.Yukawa, T.Togashi, M.Yabashi, M.Tsunoda, S.Shin and I.Matsuda
Observation of a Giant Kerr Rotation in a Ferromagnetic Transition Metal by *M*-Edge Resonant Magneto-Optic Kerr Effect
Phys. Rev. B, **89** (2014) 064423.

18B

S.A.Mollick, D.Ghose, S.R.Bhattacharyya, S.Bhunia, N.R.Ray and M.Ranjan
Synthesis of SiGe Layered Structure in Single Crystalline Ge Substrate by Low Energy Si Ion Implantation
Vacuum, **101** (2014) 387.

C.Pannu, U.B.Singh, S.Kumar, A.Tripathi, D.Kabiraj and D.K.Avasthi
Engineering the Strain in Graphene Layers with Au Decoration
Appl. Surf. Sci., **308** (2014) 193.

S.Chandran, N.Begam, V.Padmanabhan and J.K.Basu
Confinement Enhances Dispersion in Nanoparticle- Polymer Blend Films
Nature Communications, **5** (2014) 3697.

S.Singh, S.W.D'Souza, K.Mukherjee, P.Kushwaha, S.R.Barman, S.Agarwal, P.K.Mukhopadhyay, A.Chakrabarti and E.V.Sampathkumaran
Magnetic Properties and Magnetocaloric Effect in Pt Doped Ni-Mn-Ga
Appl. Phys. Lett., **104** (2014) 231909.

M.Sharma, M.K.Sanyal, B.Satpati, O.H.Seeck and S.K.Ray
Anomalous X-Ray Scattering Study of the Growth of Inverted Quantum Hut Structures in a Si-Ge Superlattice Emitting Strong Photoluminescence
Phys. Rev. B, **89** (2014) 205304.

R.R.Juluri, A.Rath, A.Ghosh, A.Bhukta, R.Sathyavathi, D.N.Rao, K.Müller, M.Schowalter, K.Frank, T.Grieb, F.Krause, A.Rosenauer and P.V.Satyam
Coherently Embedded Ag Nanostructures in Si: 3D Imaging and their Application to SERS
Scientific Reports, **4** (2014) 4633.

E.T.Dias, K.R.Priolkar and A.K.Nigam
Effect of Carbon Content on Magnetostructural Properties of Mn_3 GaC
J. Magn. Magn. Mater., **363** (2014) 140.

S.Kumar, A.Tripathi, S.A.Khan, C.Pannuand D.K.Avasthi
Radiation Stability of Graphene under Extreme Conditions
Appl. Phys. Lett., **105** (2014) 133107.

S.Mitra, S.Chakraborty and K.S.R.Menon
Specular X-Ray Reflectivity Study of Interfacial SiO_2 Layer in Thermally Annealed NiO/Si Assembly
Appl. Phys. A, **117** (2014) 1185.

P.Bag, S.Singh, P.D.Babu, V.Siruguri and R.Rawat
Study of Antiferro-Ferromagnetic Phase Coexistence in Ta Doped $HfFe_2$
Physica B, **448** (2014) 50.

K.Dey, S.Majumdar and S.Giri
Ferroelectricity in Spiral Short-Range Ordered Magnetic State of Spinel $MnCr_2O_4$: Significance of Topological Frustration and Magnetoelastic Coupling
Phys. Rev. B, **90** (2014) 184424.

S.N.Guin, J.Pan, A.Bhowmik, D.Sanyal, U.V.Waghmare and K.Biswas
Temperature Dependent Reversible *p-n-p* Type Conduction Switching with Colossal Change in Thermopower of Semiconducting AgCuS
J. Am. Chem. Soc., **136** (2014) 12712.

J.Singh, N.Kaurav, N.P.Lalla and G.S.Okram
Naturally Self-Assembled Nickel Nanolattice
Journal of Materials Chemistry C, **2** (2014) 8918.

A.Malakar, B.Das, S.Sengupta, S.Acharya and S.Ray
ZnS Nanorod as an Efficient Heavy Metal Ion Extractor from Water
Journal of Water Process Engineering, **3** (2014) 74.

S.Chandran, N.Begam and J.K.Basu
Dispersion of Polymer Grafted Nanoparticles in Polymer Nanocomposite Films: Insights from Surface X-Ray Scattering and Microscopy
J. Appl. Phys., **116** (2014) 222203.

S.Singh, S.Pal and C.Biswas
Disorder Induced Resistivity Anomaly in $Ni_2 Mn_{1+x} Sn_{1-x}$
Journal of Alloys and Compounds, **616** (2014) 110.

18C

H.Abe, T.Takekiyo, N.Hatano, M.Shigemi, N.Hamaya and Y.Yoshimura
Pressure-Induced Frustration-Frustration Process in 1-Butyl-3-Methylimidazolium Hexafluorophosphate, a Room-Temperature Ionic Liquid
J. Phys. Chem. B, **118** (2014) 1138.

H.Abe, Y.Imai, T.Takekiyo, Y.Yoshimura and N.Hamaya
Low Temperature and High Pressure Crystals of Room Temperature Ionic Liquid: *N*, *N*-Diethyl-*N*-Methyl-*N*-(2-Methoxyethyl) Ammonium Tetrafluoroborate
IOP Conf. Series: Materials Science and Engineering, **54** (2014) 012003.

T.Onimaru, S.Tsutsui, M.Mizumaki, N.Kawamura, N.Ishimatsu, M.A.Avila, S.Yamamoto, H.Yamane, K.Suekuni, K.Umeo, T.Kume, S.Nakano and T.Takabatake
Simultaneous Pressure-Induced Magnetic and Valence Transitions in Type-I Clathrate $Eu_8Ga_{16}Ge_{30}$
J. Phys. Soc. Jpn., **83** (2014) 013701.

Y.Kawamura, T.Kawaai, T.Nakayama, J.Hayashi, K.Takeda, C.Sekine, T.Nishioka and Y.Ohishi
Synchrotron X-Ray Diffraction Study of $CeRu_2 Al_{10}$ under High Pressure and Low Temperature
JPS Conf. Proc., **3** (2014) 011029.

H.Yamawaki, H.Fujihisa, Y.Gotoh and S.Nakano
Phase Changes in Lithium Amide-Borohydride Complexes under High Pressure
Solid State Ionics, **262** (2014) 490.

A.Nakayama, Y.Onda, S.Yamada, H.Fujihisa, M.Sakata, Y.Nakamoto, K.Shimizu, S.Nakano, A.Ohmura, F.Ishikawa and Y.Yamada
Collapse of CuO Double Chains and Suppression of Superconductivity in High-Pressure Phase of $YBa_2Cu_4 O8$
J. Phys. Soc. Jpn., **83** (2014) 093601.

H.Hirai, H.Kadobayashi, T.Matsuoka, Y.Ohishi and Y.Yamamoto
High Pressure X-Ray Diffraction and Raman Spectroscopic Studies of the Phase Change of D_2O Ice VII at Approximately 11 GPa
High Pressure Res., **34** (2014) 289.

H.Hirai, T.Tanaka, T.Matsuoka, Y.Ohishi, T.Yagi, M.Ohtake and Y.Yamamoto
Phase Changes Induced by Guest Orientational Ordering of Filled Ice I_h Methane Hydrate under High Pressure and Low Temperature
J. Phys.: Conf. Ser., **500** (2014) 192006.

H.Yamawaki, H.Fujihisa, Y.Gotoh and S.Nakano
Structure of Intermediate Phase II of $LiNH_2$ under High Pressure
J. Phys. Chem. B, **118** (2014) 9991.

T.Tomita, M.Ebata, H.Soeda, H.Takahashi, H.Fujihisa, Y.Gotoh, Y.Mizuguchi, H.Izawa, O.Miura, S.Demura, K.Deguchi and Y.Takano
Pressure-Induced Enhancement of Superconductivity and Structural Transition in BiS_2 -Layered $LaO_{1-x}F_x BiS_2$
J. Phys. Soc. Jpn., **83** (2014) 063704.

A.Shinozaki, H.Kagi, N.Noguchi, H.Hirai, H.Ohfuji, T.Okada, S.Nakano and T.Yagi
Formation of SiH_4 and H_2 O by the Dissolution of Quartz in H_2 Fluid under High Pressure and Temperature
American Mineralogist, **99** (2014) 1265.

M.Einaga, A.Ohmura, F.Ishikawa, A.Nakayama, Y.Yamada, S.Nakano, A.Matsushita and K.Shimizu
Pressure-Induced Superconductivity in Non-Stoichiometric Bismuth Telluride $Bi_{35}Te_{65}$
J. Phys: Conf. Ser., **500** (2014) 192003.

K.Takeda, Y.Kawamura, K.Ito, J.Hayashi, K.Matsui, H.Nakane and C.Sekine
X-Ray Study with Synchrotron Radiation for New Filled Skutterudite $GdFe_4As_{12}$ at Ambient Pressure and High Pressures
JPS Conf. Proc., **3** (2014) 017019.

19A

R.Suzuki, M.Sakano, Y.J.Zhang, R.Akashi, D.Morikawa, A.Harasawa, K.Yaji, K.Kuroda, K.Miyamoto, T.Okuda, K.Ishizaka, R.Arita and Y.Iwasa
Valley-Dependent Spin Polarization in Bulk MoS_2 with Broken Inversion Symmetry
Nature Nanotechnology, **9** (2014) 611.

19B

D.-Y.Kim, S.Miyoshi, T.Tsuchiya and S.Yamaguchi
Electronic Defects Formation in Fe-Doped $BaZrO_3$ Studied by X-Ray Absorption Spectroscopy
Chem. Mater., **26** (2014) 927.

20A

K.Shigemura, M.Kitajima, M.Kurokawa, K.Toyoshima, T.Odagiri, A.Suga, H.Kato, M.Hoshino, H.Tanaka and K.Ito
Total Cross Sections for Electron Scattering from He and Ne at Very Low Energies
Phys. Rev. A, **89** (2014) 022709.

M.Kitajima, K.Shigemura, M.Kurokawa, T.Odagiri, H.Kato, M.Hoshino, H.Tanaka and K.Ito
Measurements of Ultra-Low-Energy Electron Scattering Cross Sections of Atoms and Molecules
AIP Conf. Proc., **1588** (2014) 78.

Y.Nakanishi, K.Hosaka, R.Kougo, T.Odagiri, M.Nakano, Y.Kumagai, K.Shiino, M.Kitajima and N.Kouchi
Angular Correlation of a Pair of Lyman-α Photons Produced in the Photodissociation of H_2
Phys. Rev. A, **90** (2014) 043405.

20B

S.Ji, K.Kojima, Y.Ishida, H.Yamaguchi, S.Saito, T.Kato, H.Tsuchida, S.Yoshida and H.Okumura
Characterization of the Defect Evolution in Thick Heavily Al-Doped 4H-SiC Epilayers
Materials Science Forum, **778-780** (2014) 151.

Y.Kato, H.Umezawa and S.Shikata
X-Ray Topographic Study of a Homoepitaxial Diamond Layer on an Ultraviolet-Irradiated Precision Polished Substrate
Acta Physica Polonica A, **125** (2014) 969.

S.Harada, Y.Yamamoto, S.Xiao, M.Tagawa and T.Ujihara
Surface Morphology and Threading Dislocation Conversion Behavior during Solution Growth of 4H-SiC using Al-Si Solvent
Materials Science Forum, **778-780** (2014) 67.

Y.Yamamoto, S.Harada, K.Seki, A.Horio, T.Mitsuhashi, D.Koike, M.Tagawa, and T.Ujihara
Low-Dislocation-Density 4H-SiC Crystal Growth Utilizing Dislocation Conversion during Solution Method
Appl. Phys. Express., **7** (2014) 065501.

S.Harada, Y.Yamamoto, K.Seki, A.Horio, M.Tagawa and T.Ujihara
Different Behavior of Threading Edge Dislocation Conversion During the Solution Growth of 4H-SiC Depending on the Burgers Vector
Acta Mater., **81** (2014) 284.

H.Koizumi, M.Tachibana, I.Yoshizaki, S.Fukuyama, K.Tsukamoto, Y.Suzuki, S.Uda and K.Kojima
Dislocations in High-Quality Glucose Isomerase Crystals Grown from Seed Crystals
Cryst. Growth Des., **14** (2014) 5111.

Y.Mokuno, Y.Kato, N.Tsubouchi, A.Chayahara, H.Yamada and S.Shikata
A Nitrogen Doped Low-Dislocation Density Free- Standing Single Crystal Diamond Plate Fabricated by a Lift-Off Process
Appl. Phys. Lett., **104** (2014) 252109.

Former 20B

J.N.G.Stanley, P.Benndorf, F.Heinroth, A.F.Masters and T.Maschmeyer
Probing Structure-Functionality Relationships of Catalytic Bimetallic Pt-Ru Nanoparticles Associated with Improved Sulfur Resistance
RSC Advances **4** (2014) 28062

27A

Y.Baba, I.Shimoyama, N.Hirao and T.Sekiguchi
Structure of Ultra-Thin Silicon Film on HOPG Studied by Polarization-Dependence of X-Ray Absorption Fine Structure
Chem. Phys. Lett., **594** (2014) 64.

I.Shimoyama, Y.Baba and T.Sekiguchi
A Polarization Rule on Atomic Arrangements of Graphite-Like Boron Carbonitride
Carbon, **71** (2014) 1.

Y.Baba, I.Shimoyama, N.Hirao and T.Sekiguchi
Structures of Quasi-Freestanding Ultra-Thin Silicon Films Deposited on Chemically Inert Surfaces
Chem. Phys., **444** (2014) 1.

R.Shinoda, N.Hirao, Y.Baba, A.Iwase and T.Matsui
Effect of Doping for Epitaxial $(Ba_{1-x}Yb_x)(Fe_{0.2}Zr_{0.8})O_{3-\delta}$ Thin Films with Yb
Mater. Transactions, **55** (2014) 1521.

S.Ishiyama, R.Fujii, M.Nakamura and Y.Imahori
3KeV H_2^+ Irradiation to Li/Pd/Cu Trilaminar Neutron Production Target for BNCT
Mater. Transactions, **55** (2014) 658.

M.Honda, M.Yanagida, L.Han and K.Miyano
Investigation of the Influence of Coadsorbent Dye upon the Interfacial Structure of Dye-Sensitized Solar Cells
J. Chem. Phys., **141** (2014) 174709.

M.Honda, Y.Baba, T.Sekiguchi, I.Shimoyama and N.Hirao
Electrochemical Immobilization of Biomolecules on Gold Surface Modified with Monolayered L-Cysteine
Thin Solid Films, **556** (2014) 307.

H.I.Sekiguchi and T.Sekiguchi
Molecular Ordering Effect of Regioregular Poly(3-hexylthiophene) using Sulfur K-Edge X-Ray Absorption Spectroscopy
Jpn. J. Appl. Phys., **53** (2014) 02BB07.

I.Shimoyama, N.Hirao, Y.Baba, T.Izumi, Y.Okamoto, T.Yaita, and S.Suzuki
Low-Pressure Sublimation Method for Cesium Decontamination of Clay Minerals
Clay Science, **18** (2014) 71.

R.Shinoda, A.Iwase and T.Matsui
Magnetic and Structural Properties of $Ba(Co_{1-x}Mn_x)O_3$ Using Synchrotron X-Ray Spectroscopy
J. Appl. Phys., **116** (2014) 243901.

S.Ishiyama, Y.Baba, R.Fujii, M.Nakamura and Y.Imahori
Surficial Chemical States of Li_3N Synthesized on Lithium Target for Boron Neutron Capture Therapy
Mater. Trans., JIM, **55** (2014) 539.

N.Hirao, Y.Baba, T.Sekiguchi and I.Shimoyama
Focusing of Soft X-Rays using Poly-Capillary with Precise Adjustment Mechanism and its Application to Quick Chemical-State Analysis
BUNSEKI KAGAKU, **63** (2014) 53. (in Japanese).

27B

M.Numakura, N.Sato, C.Bessada, A.Nezu, H.Akatsuka and H.Matsuura
Local Structural Analyses of Molten Thorium Fluoride in Mono- and Divalent Cationic Fluorides
Molten Salts Chemistry and Technology, **6.7** (2014) 459.

T.Kishino, R.Shinoda, K.Shimizu, Y.Saitoh, N.Ishikawa, Y.Okamoto, F.Hori, T.Matsui and A.Iwase
Effect of 10MeV Iodine Ion Irradiation on the Magnetic Properties and Lattice Structure of CeO_2
Jpn. J. Appl. Phys., **53** (2014) 05FC07.

A.Hashimoto, Y.Kaneno, S.Semboshi, H.Yoshizaki, Y.Saitoh, Y.Okamoto and A.Iwase
Microstructure Evolution and Hardness Change in Ordered Ni_3V Intermetallic Alloy by Energetic Ion Irradiation
Nucl. Instrum. Meth. Phys. Res. B, **338** (2014) 72.

R.Shinoda, A.Iwase and T.Matsui
Magnetic and Structural Properties of $Ba(Co_{1-x}Mn_x)O_3$ Using Synchrotron X-Ray Spectroscopy
J. Appl. Phys., **116** (2014) 243901.

28A

D.Ootsuki, T.Toriyama, S.Pyon, K.Kudo, M.Nohara, K.Horiba, M.Kobayashi, K.Ono, H.Kumigashira, T.Noda, T.Sugimoto, A.Fujimori, N.L.Saini, T.Konishi, Y.Ohta and T.Mizokawa
Te 5*p* Orbitals Bring Three-Dimensional Electronic Structure to Two-Dimensional $Ir_{0.95}Pt_{0.05}Te_2$
Phys. Rev. B, **89** (2014) 104506.

M.Sunagawa, T.Ishiga, K.Tsubota, T.Jabuchi, J.Sonoyama, K.Iba, K.Kudo, M.Nohara, K.Ono, H.Kumigashira, T.Matsushita, M.Arita, K.Shimada, H.Namatame, M.Taniguchi, T.Wakita, Y.Muraoka and T.Yokoya
Characteristic Two-Dimensional Fermi Surface Topology of High-T_c Iron-Based Superconductors
Scientific Reports, **4** (2014) 4381.

Y.Muraoka, H.Nagao, S.Katayama, T.Wakita, M.Hirai, T.Yokoya, H.Kumigashira and M.Oshima
Persistent Insulator-to-Metal Transition of a VO_2 Thin Film Induced by Soft X-Ray irradiation
Jpn. J. Appl. Phys., **53** (2014) 05FB09.

M.Nomura, S.Souma, A.Takayama, T.Sato, T.Takahashi, K.Eto, K.Segawa and Y.Ando
Relationship between Fermi Surface Warping and Out-of-Plane Spin Polarization in Topological Insulators: A View from Spin- and Angle-Resolved Photoemission
Phys. Rev. B, **89** (2014) 045134.

E.Ieki, K.Nakayama, Y.Miyata, T.Sato, H.Miao, N.Xu, X.-P.Wang, P.Zhang, T.Qian, P.Richard, Z.-J.Xu, J.S.Wen, G.D.Gu, H.Q.Luo, H.-H.Wen, H.Ding and T.Takahashi
Evolution from Incoherent to Coherent Electronic States and its Implications for Superconductivity in $FeTe_{1-x}Se_x$
Phys. Rev. B, **89** (2014) 140506(R).

K.Sawada, D.Ootsuki, K.Kudo, D.Mitsuoka, M.Nohara, T.Noda, K.Horiba, M.Kobayashi, K.Ono, H.Kumigashira, N.L.Saini and T.Mizokawa
Coexistence of Bloch Electrons and Glassy Electrons in $Ca_{10}(Ir_4As_8)(Fe_{2-x}Ir_xAs_2)_5$ Revealed by Angle-Resolved Photoemission Spectroscopy
Phys. Rev. B, **89** (2014) 220508(R).

T.Shimojima, T.Sonobe, W.Malaeb, K.Shinada, A.Chainani, S.Shin, T.Yoshida, S.Ideta, A.Fujimori, H.Kumigashira, K.Ono, Y.Nakashima, H.Anzai, M.Arita, A.Ino, H.Namatame, M.Taniguchi, M.Nakajima, S.Uchida, Y.Tomioka, T.Ito, K.Kihou, C.H.Lee, A.Iyo, H.Eisaki, K.Ohgushi, S.Kasahara, T.Terashima, H.Ikeda, T.Shibauchi, Y.Matsuda and K.Ishizaka
Pseudogap Formation above the Superconducting Dome in Iron Pnictides
Phys. Rev. B, **89** (2014) 045101.

T.Shimojima, Y.Suzuki, T.Sonobe, A.Nakamura, M.Sakano, J.Omachi, K.Yoshioka, M.Kuwata-Gonokami, K.Ono, H.Kumigashira, A.E.Bo¨hmer, F.Hardy, T.Wolf, C.Meingast, H.V.L¨ohneysen, H.Ikeda and K.Ishizaka
Lifting of *xz*/*yz* Orbital Degeneracy at the Structural Transition in Detwinned FeSe
Phys. Rev. B, **90** (2014) 121111.

K.Nakayama, Y.Miyata, G.N.Phan, T.Sato, Y.Tanabe, T.Urata, K.Tanigaki and T.Takahashi
Reconstruction of Band Structure Induced by Electronic Nematicity in an FeSe Superconductor
Phys. Rev. Lett., **113** (2014) 237001.

K.Terashima, J.Sonoyama, T.Wakita, M.Sunagawa, K.Ono, H.Kumigashira, T.Muro, M.Nagao, S.Watauchi, I.Tanaka, H.Okazaki, Y.Takano, O.Miura, Y.Mizuguchi, H.Usui, K.Suzuki, K.Kuroki, Y.Muraoka and T.Yokoya
Proximity to Fermi-Surface Topological Change in Superconducting $LaO_{0.54}F_{0.46}BiS_2$
Phys. Rev. B, **90** (2014) 220512(R).

M.Xia, J.Jiang, Z.R.Ye, Y.H.Wang, Y.Zhang, S.D.Chen, X.H.Niu, D.F.Xu, F.Chen, X.H.Chen, B.P.Xie, T.Zhang and D.L.Feng
Angle-Resolved Photoemission Spectroscopy Study on the Surface States of the Correlated Topological Insulator YbB_6
Scientific Reports, **4** (2014) 5999.

S.Ideta, T.Yoshida, M.Nakajima, W.Malaeb, H.Kito, H.Eisaki, A.Iyo, Y.Tomioka, T.Ito, K.Kihou, C.H.Lee, Y.Kotani, K.Ono, S.K.Mo, Z.Hussain, Z.X.Shen, H.Harima, S.Uchida and A.Fujimori
Electronic Structure of $BaNi_2P_2$ Observed by Angle- Resolved Photoemission Spectroscopy
Phys. Rev. B, **89** (2014) 195138.

H.Suzuki, T.Kobayashi, S.Miyasaka, T.Yoshida, K.Okazaki, L.C.C.Ambolode, S.Ideta, M.Yi, M.Hashimoto, D.H.Lu, Z.X.Shen, K.Ono, H.Kumigashira, S.Tajima and A.Fujimori
Strongly Three-Dimensional Electronic Structure and Fermi Surfaces of $SrFe_2(As_{0.65}P_{0.35})_2$: Comparison with $BaFe_2(As_{1-x}P_x)_2$
Phys. Rev. B, **89** (2014) 184513.

T.Yoshida, S.Ideta, T.Shimojima, W.Malaeb, K.Shinada, H.Suzuki, I.Nishi, A.Fujimori, K.Ishizaka, S.Shin, Y.Nakashima, H.Anzai, M.Arita, A.Ino, H.Namatame, M.Taniguchi, H.Kumigashira, K.Ono, S.Kasahara, T.Shibauchi, T.Terashima, Y.Matsuda, M.Nakajima, S.Uchida, Y.Tomioka, T.Ito, K.Kihou, C.H.Lee, A.Iyo, H.Eisaki, H.Ikeda, R.Arita, T.Saito, S.Onari and H.Kontani
Anisotropy of the Superconducting Gap in the Iron- Based Superconductor $BaFe_2(As_{1-x}P_x)_2$
Scientific Reports, **4** (2014) 7292.

M.Okawa, T.Yokobori, K.Konishi, R,Takei, K.Katayama, S.Oozono, T.Shinmura, T.Okuda, H.Wadati, E.Sakai, K.Ono, H.Kumigashira, M.Oshima, T.Sugiyama, E.Ikenaga, N.Hamada and T.Saitoh
Cu-O-Cr Hybridization Effects on the Electronic Structure of a Hole-Doped Delafossite Oxide $CuCr_{1-x}Mg_xO_2$
JPS Conf Proc., **3** (2014) 017027.

28B

Y.Nakanishi, K.Hosaka, R.Kougo, T.Odagiri, M.Nakano, Y.Kumagai, K.Shiino, M.Kitajima, and N.Kouchi
Angular Correlation of a Pair of Lyman-α Photons Produced in the Photodissociation of H_2
Phys. Rev. A, **90** (2014) 043405.

Former 28B

J.N.G.Stanley, P.Benndorf, F.Heinroth, A.F.Masters and T.Maschmeyer
Probing Structure-Functionality Relationships of Catalytic Bimetallic Pt-Ru Nanoparticles Associated with Improved Sulfur Resistance
RSC Advances **4** (2014) 28062.

NE1A

L.Li, T.Nagai, T.Ishido, S.Motai, K.Fujino and S.Itoh
Formation of a Solid Solution in the $MgSiO_3$-$MnSiO_3$ Perovskite System
Phys. Chem. Minerals, **41** (2014) 431.

D.Nishio-Hamane, T.Minakawa and H.Okada
Iwateite, $Na_2BaMn(PO_4)_2$, a New Mineral from the Tanohata Mine, Iwate Prefecture, Japan
Journal of Mineralogical and Petrological Sciences, **109** (2014) 34.

H.Yusa, F.Kawamura, T.Taniguchi, N.Hirao, Y.Ohishi and T.Kikegawa
High-Pressure Synthesis and Compressive Behavior of Tantalum Nitrides
J. Appl. Phys., **115** (2014) 103520.

K.Niwa, K.Suzuki, S.Muto, K.Tatsumi, K.Soda, T.Kikegawa and M.Hasegawa
Discovery of the Last Remaining Binary Platinum-Group Pernitride RuN_2
Chem. Eur. J., **20** (2014) 1.

K.Niwa and M.Hasegawa
Novel Material Synthesis using Laser−Heated Diamond Anvil Cell
The Review of High Pressure Science and Technology, **24** (2014) 178. (in Japanese).

H.Yusa, T.Tsuchiya, M.Akaogi, H.Kojitani, D.Yamazaki, N.Hirao, Y.Ohishi and T.Kikegawa
Postperovskite Phase Transition of $ZnGeO_3$: Comparative Crystal Chemistry of Postperovskite Phase Transition from Germanate Perovskites
Inorg. Chem., **53** (2014) 11732.

X.Lai, F.Zhu, Y.Wu, R.Huang, X.Wu, Q.Zhang, K.Yang and S.Qin
New High-Pressure Polymorph of In_2S_3 with Defect Th_3P_4-type Structure
J. Solid State Chem., **210** (2014) 155.

NE3A

Y.Yasutake, W.Kitagawa, M.Hata, T.Nishioka, T.Ozaki, M.Nishiyama, T.Kuzuyama and T.Tamura
Structure of the Quinoline N-Hydroxylating Cytochrome P450 RauA, an Essential Enzyme that Confers Antibiotic Activity on Aurachin Alkaloids
FEBS Letters, **588** (2014) 105.

S.Okada, T.Yamamoto, H.Watanabe, T.Nishimoto, H.Chaen, S.Fukuda, T.Wakagi and S.Fushinobu
Structural and Mutational Analysis of Substrate Recognition in Kojibiose Phosphorylase
FEBS J., **281** (2014) 778.

T.Satoh, K.Suzuki, T.Yamaguchi and K.Kato
Structural Basis for Disparate Sugar-Binding Specificities in the Homologous Cargo Receptors ERGIC-53 and VIP36
PLOS ONE, **9** (2014) e87963.

K.Miyazono, Y.Furuta, M.Watanabe-Matsui, T.Miyakawa, T.Ito, I.Kobayashi and M.Tanokura
A Sequence-Specific DNA Glycosylase Mediates Restriction-Modification in *Pyrococcus abyssi*
Nature Communications, **5** (2014) 3178.

D.Matsui, D.-H.Im, A.Sugawara, Y.Fukuta, S.Fushinobu, K.Isobe and Y.Asano
Mutational and Crystallographic Analysis of L-Amino Acid Oxidase/Monooxygenase from *Pseudomonas* sp. AIU 813: Interconversion between Oxidase and Monooxygenase Activities
FEBS Open Bio, **4** (2014) 220.

S.Wang, M.Ogata, S.Horita, J.Ohtsuka, K.Nagata and M.Tanokura
A Novel Mode of Ferric Ion Coordination by the Periplasmic Ferric Ion-Binding Subunit FbpA of an ABC-Type Iron Transporter from *Thermus thermophilus* HB8.
Acta Cryst. D, **70** (2014) 196.

H.M.Qin, A.Yamamura, T.Miyakawa, M.Kataoka, T.Nagai, N.Kitamura, N.Urano, S.Maruoka, J.Ohtsuka, K.Nagata, S.Shimizu and M.Tanokura
Structure of Conjugated Polyketone Reductase from *Candida parapsilosis* IFO 0708 Reveals Conformational Changes for Substrate Recognition upon NADPH Binding
Appl. Microbiol. Biotechnol., **98** (2014) 243.

S.Niwa, L.-J.Yu, K.Takeda, Y.Hirano, T.Kawakami, Z.-Y.Wang-Otomo and K.Miki
Structure of the LH1-RC Complex from *Thermochromatium Tepidum* at 3.0 Å
Nature, **508** (2014) 228.

S.Tagami, S.Sekine, L.Minakhin, D.Esyunina, R.Akasaka, M.Shirouzu, A.Kulbachinskiy, K.Severinov and S.Yokoyama
Structural Basis for Promoter Specificity Switching of RNA Polymerase by a Phage Factor
Genes and Development, **28** (2014) 521.

.Sugimoto, M.Senda, D.Kasai, M.Fukuda, E.Masai and T.Senda
Molecular Mechanism of Strict Substrate Specificity of an Extradiol Dioxygenase, DesB, Derived from *Sphingobium* sp. SYK-6.
PLOS ONE, **9** (2014) e92249.

T.Ito, K.Saikawa, S.Kim, K.Fujita, A.Ishiwata, S.Kaeothip, T.Arakawa, T.Wakagi, G.T.Beckham, Y.Ito, S.Fushinobu
Crystal Structure of Glycoside Hydrolase Family 127 β-L-Arabinofuranosidase from *Bifidobacterium longum*
Biochem. Biophys. Res. Commun., **447** (2014) 32.

T.Tsuda, M.Asami, Y.Koguchi and S.Kojima
Single Mutation Alters the Substrate Specificity of L-Amino Acid Ligase
Biochemistry, **53** (2014) 2650.

Y.Kanoh, S.Uehara, H.Iwata, K.Yoneda, T.Ohshima and H.Sakuraba
Structural Insight into Glucose Dehydrogenase from the Thermoacidophilic Archaeon *Thermoplasma volcanium*
Acta Cryst. D, **70** (2014) 1271.

C.Feng, Y.Liu, G.Wang, Z.Deng, Q.Zhang, W.Wu, Y.Tong, C.Cheng and Z.Chen
Crystal Structures of the Human RNA Demethylase Alkbh5 Reveal Basis for Substrate Recognition
J. Biol. Chem., **289** (2014) 11571.

Z.Deng, K.C.Lehmann, X.Li, C.Feng, G.Wang, Q.Zhang, X.Qi, L.Yu, X.Zhang, W.Feng, W.Wu, P.Gong, Y.Tao, C.C.Posthuma, E.J.Snijder, A.E.Gorbalenya and Z.Chen
Structural Basis for the Regulatory Function of a Complex Zinc-Binding Domain in a Replicative Arterivirus Helicase Resembling a Nonsense-Mediated mRNA Decay Helicase
Nucleic Acids Research, **42** (2014) 3464.

T.Satoh, Y.Saeki, T.Hiromoto, Y.-H.Wang, Y.Uekusa, H.Yagi, H.Yoshihara, M.Yagi-Utsumi, T.Mizushima, K.Tanaka and K.Kato
Structural Basis for Proteasome Formation Controlled by an Assembly Chaperone Nas2
Structure, **22** (2014) 731.

T.Maehara, Z.Fujimoto, H.Ichinose, M.Michikawa, K.Harazono and S.Kaneko
Crystal Structure and Characterization of the Glycoside Hydrolase Family 62 α-L-Arabinofuranosidase from *Streptomyces coelicolor*
J. Biol. Chem., **289** (2014) 7962.

N.Suzuki, Z.Fujimoto, Y.-M.Kim, M.Momma, N.Kishine, R.Suzuki, S.Suzuki, S.Kitamura, M.Kobayashi, A.Kimura and K.Funane
Structural Elucidation of the Cyclization Mechanism of α-1,6-Glucan by *Bacillus circulans* T-3040 Cycloisomaltooligosaccharide Glucanotransferase
J. Biol. Chem., **289** (2014) 12040.

A.Kishimoto, A.Kita, T.Ishibashi, H.Tomita, Y.Yokooji, T.Imanaka, H.Atomi and K.Miki
Crystal Structure of Phosphopantothenate Synthetase from *Thermococcus kodakarensis*
Proteins **82** (2014) 1924.

E.Tamai, H.Yoshida, H.Sekiya, H.Nariya, S.Miyata, A.Okabe, T.Kuwahara, J. Maki and S.Kamitori
X-Ray Structure of a Novel Endolysin Encoded by Episomal Phage PhiSM101 of *Clostridium perfringens*
Molecular Microbiology, **92** (2014) 326.

Y.Fujioka, S.W.Suzuki, H.Yamamoto, C.Kondo-Kakuta, Y.Kimura, H.Hirano, R.Akada, F.Inagaki, Y.Ohsumi and N.N.Noda
Structural Basis of Starvation-Induced Assembly of the Autophagy Initiation Complex
Nature Structural Molecular Biology, **21** (2014) 513.

X.Liu, Y.Yin, J.Wu and Z.Liu
Structure and Mechanism of an Intramembrane Liponucleotide Synthetase Central for Phospholipid Biosynthesis
Nature Communications, **5** (2014) 4244.

H.Yokoyama and S.Fujii
Structures and Metal-Binding Properties of *Helicobacter pylori* Neutrophil-Activating Protein with a Di-Nuclear Ferroxidase Center
Biomolecules, **4** (2014) 600.

Y.Ohta, Y.Hatada, Y.Hidaka, Y.Shimane, K.Usui, T.Ito, K.Fujita, G.Yokoi, M.Mori, S.Sato, T.Miyazaki, A.Nishikawa and T.Tonozuka
Enhancing Thermostability and the Structural Characterization of *Microbacterium saccharophilum* K-1 *β*-Fructofuranosidase
Appl. Microbiol. Biotechnol., **98** (2014) 6667.

H.P.Kokatla, D.Sil, H.Tanji, U.Ohto, S.S.Malladi, L.M.Fox, T.Shimizu and S.A.David
Structure-Based Design of Novel Human Toll-Like Receptor 8 Agonists
ChemMedChem, **9** (2014) 719.

K.Miyazono, K.Tsutsumi, Y.Ishino and M.Tanokura
Expression, High-Pressure Refolding, Purification, Crystallization and Preliminary X-Ray Analysis of a Novel Single-Strand-Specific 3'-5' Exonuclease PhoExo I from *Pyrococcus horikoshii* OT3
Acta Cryst. F, **70** (2014) 1076.

T.Mise, H.Matsunami, F.A.Samatey and I.N.Maruyama
Crystallization and Preliminary X-Ray Diffraction Analysis of the Periplasmic Domain of the *Escherichia coli* Aspartate Receptor Tar and its Complex with Aspartate
Acta Cryst. F, **70** (2014) 1219.

M.Kanagawa, Y.Liu, S.Hanashima, A.Ikeda, W.Chai, Y.Nakano, K.Kojima-Aikawa, T.Feizi and Y.Yamaguchi
Structural Basis for Multiple Sugar Recognition of Jacalin-Related Human ZG16p Lectin
J. Biol. Chem., **289** (2014) 16954.

K.Kashiwagi, T.Ito and S.Yokoyama
Crystal Structure of the Eukaryotic Translation Initiation Factor 2A from *Schizosaccharomyces pombe*
J. Struct. Funct. Genomics, **15** (2014) 125.

S.Kamachi, K.Wada, M.Tamoi, S.Shigeoka and T.Tada
The 2.2 Å Resolution Structure of the Catalase- Peroxidase KatG from *Synechococcus elongatus* PCC7942
Acta Cryst. F, **70** (2014) 288.

S.Kamachi, J.Nagao, M.Miyashita, Y.Nakagawa, H.Miyagawa and T.Tada
Crystallization and Preliminary X-Ray Diffraction Studies of La1 from *Liocheles australasiae*
Acta Cryst. F, **70** (2014) 915.

H.Tsukagoshi, A.Nakamura, T.Ishida, K.K.Touhara, M.Otagiri, S.Moriya, M.Samejima, K.Igarashi, S.Fushinobu, K.Kitamoto and M.Arioka
Structural and Biochemical Analyses of Glycoside Hydrolase Family 26 *β*-Mannanase from a Symbiotic Protist of the Termite *Reticulitermes speratus*
J. Biol. Chem., **289** (2014) 10843.

K.K.Touhara, T.Nihira, M.Kitaoka, H.Nakai and S.Fushinobu
Structural Basis for Reversible Phosphorolysis and Hydrolysis Reactions of 2-O-*α*-Glucosylglycerol Phosphorylase
J. Biol. Chem., **289** (2014) 18067.

K.Suzuki, A.Hori, K.Kawamoto, R.R.Thangudu, T.Ishida, K.Igarashi, M.Samejima, C.Yamada, T.Arakawa, T.Wakagi, T.Koseki and S.Fushinobu
Crystal Structure of a Feruloyl Esterase Belonging to the Tannase Family: A Disulfide Bond Near a Catalytic Triad
Proteins, **82** (2014) 2857.

C.J.Bruns, D.Fujita, M.Hoshino, S.Sato, J.F.Stoddart and M.Fujita
Emergent Ion-Gated Binding of Cationic Host-Guest Complexes within Cationic M_{12} L_{24} Molecular Flasks
J. Am. Chem. Soc., **136** (2014) 12027.

H.Itou, S.Muramatsu, Y.Shirakihara and H.Araki
Crystal Structure of the Homology Domain of the Eukaryotic DNA Replication Proteins Sld3/Treslin
Structure, **22** (2014) 1341.

T.Yokoyama, Y.Kosaka and M.Mizuguchi
Inhibitory Activities of Propolis and its Promising Component, Caffeic Acid Phenethyl Ester, against Amyloidogenesis of Human Transthyretin
J. Med. Chem, **57** (2014) 8928.

Q-F.Sun, S.Sato and M.Fujita
An M_{12} $(L^1)_{12}$ $(L^2)_{12}$ Cantellated Tetrahedron: A Case Study on Mixed-Ligand Self-Assembly
Angew. Chem. Int. Ed., **53** (2014) 13510.

H.Yoshida, A.Yoshihara, M.Teraoka, Y.Terami, G.Takata, K.Izumori and S.Kamitori
X-Ray Structure of a Novel L-Ribose Isomerase Acting on a Non-Natural Sugar L-Ribose as its Ideal Substrate
FEBS J., **281** (2014) 3150.

Z.Wang, X.Yang, S.Guo, Y.Yang, X.C.Su, Y.Shen and J.Long
Crystal Structure of the Ubiquitin-Like Domain-CUT Repeat-Like Tandem of Special AT-Rich Sequence Binding Protein 1 (SATB1) Reveals a Coordinating DNA-Binding Mechanism
J. Biol. Chem., **289** (2014) 27376.

L.Guan, H.Yabuki, M.Okai, J.Ohtsuka and M.Tanokura
Crystal Structure of the Novel Haloalkane Dehalogenase DatA from *Agrobacterium tumefaciens* C58 Reveals a Special Halide-Stabilizing Pair and Enantioselectivity Mechanism
Appl. Microbiol. Biotechnol., **98** (2014) 8573.

T.Miyakawa, K.Hatano, Y.Miyauchi, Y.Suwa, Y.Sawano and M.Tanokura
A Secreted Protein of the Plant-Specific DUF26 Family Functions as a Mannose-Binding Lectin that Exhibits Antifungal Activity
Plant Physiol., **166** (2014) 766.

K.Ito, T.Honda, T.Suzuki, T.Miyoshi, R.Murakami, M.Yao and T.Uchiumi
Molecular Insights into the Interaction of the Ribosomal Stalk Protein with Elongation Factor 1α
Nucleic Acids Res., **42** (2014) 14042.

J.Matsuzawa, H.Aikawa, T.Umeda, Y.Ashikawa, C.S.Minakuchi, Y.Kawano, Z.Fujimoto, K.Okada, H.Yamane and H.Nojiri
Crystallization and Preliminary X-Ray Diffraction Analyses of the Redox-Controlled Complex of Terminal Oxygenase and Ferredoxin Components in the Rieske Nonhaem Iron Oxygenase Carbazole 1,9a-Dioxygenase
Acta Cryst. F, **70** (2014) 1406.

A.Nishizawa, A.Harada, M.Senda, Y.Tachihara, D.Muramatsu, S.Kishigami, S.Mori, K.Sugiyama, T.Senda and S.Kimura
Complete Pyridine Nucleotide-Specificity Conversion of an NADH-Dependent Ferredoxin Reductase.
Biochem. J, **462** (2014) 257.

M.Nagae, K.Soga, K.M.Matsumoto, S.Hanashima, A.Ikeda, K.Yamamoto and Y.Yamaguchi
Phytohemagglutinin from *Phaseolus vulgaris* (PHA-E) Displays a Novel Glycan Recognition Mode using a Common Legume Lectin Fold
Glycobiology, **24** (2014) 368.

T.Tomita, T.Ozaki, K.Matsuda, M.Nishiyama and T.Kuzuyama
Crystallization and Preliminary X-Ray Diffraction Analysis of Cyclolavandulyl Diphosphate Synthase, a New Member of the Cis-Isoprenyl Diphosphate Synthase Superfamily
Acta Cryst. F, **70** (2014) 1410.

H.S.Kim, J.Kim, H.N.Im, D.R.An, M.Lee, D.Hesek, S.Mobashery, J.Y.Kim, K.Cho, H.J.Yoon, B.W.Han, B.I.Lee and S.W.Suh
Structural Basis for the Recognition of Muramyltripeptide by *Helicobacter Pylori* Csd4, a D,L-Carboxypeptidase Controlling the Helical Cell Shape
Acta Cryst. D, **70** (2014) 2800.

F.Mimoto, S.Kadono, H.Katada, T.Igawa, T.Kamikawa and K.Hattori
Crystal Structure of a Novel Asymmetrically Engineered Fc Variant with Improved Affinity for FcγRs
Molecular Immunology, **58** (2014) 132.

T.Oguri, T.Furuyama, T.Okuno, Y.Ishii, K.Tateda, R.A.Bonomo and A.S.Ibuka.
Crystal Structure of Mox-1, a Unique Plasmid-Mediated Class C β-Lactamase with Hydrolytic Activity Towards Moxalactam.
Antimicrob. Agents Chemother., **58** (2014) 3914.

E.Yoo, D.Salunke, D.Sil, X.Guo, A.Salyer, A.Hermanson, M.Kumar, S.S.Malladi, R.Balakrishna, W.H.Thompson, H.Tanji, U.Ohto, T.Shimizu and S.A.David
Determinants of Activity at Human Toll-Like Receptors 7 and 8: Quantitative Structure-Activity Relationship (QSAR) of Diverse Heterocyclic Scaffolds
J. Med. Chem., **57** (2014) 7955.

H.Suzuki, U.Ohto, K.Higaki, T.M.Barragan, M.A.Moncayo, C.O.Mellet, E.Nanba, J.M.G.Fernandez, Y.Suzuki and T.Shimizu
Structural Basis of Pharmacological Chaperoning for Human β-Galactosidase
J. Biol. Chem., **289** (2014) 14560.

NE5C

C.Yang, T.Inoue, A.Yamada, T.Kikegawa and J.Ando
Equation of State and Phase Transition of Antigorite under High Pressure and High Temperature
Physics of the Earth and Planetary Interiors, **228** (2014) 56.

S.Gr´eaux and A.Yamada
P-V-T Equation of State of $Mn_3 Al_2 Si_3 O_{12}$ Spessartine Garnet
Phys. Chem. Minerals, **41** (2014) 141.

K.Fuchizaki and N.Hamaya
Melting Curve of Molecular Crystal GeI_4
J. Phys. Soc. Jpn., **83** (2014) 074603.

R.Iizuka, K.Komatsu, H.Kagi, T.Nagai, A.Sano-Furukawa, T.Hattori, H.Gotou and T.Yagi
Phase Transitions and Hydrogen Bonding in Deuterated Calcium Hydroxide: High-Pressure and High-Temperature Neutron Diffraction Measurements
J. Solid State Chemistry, **218** (2014) 95.

C.Sekine, H.Kato, M.Kanazawa, Y.Kawamura, K.Takeda, M.Matsuda, K.Kihou, C.-H.Lee and H.Gotou
In-Situ Observation of Synthesizing Process of $Mm_xCo_4Sb_{12}$ Utilizing X-Ray Diffraction under High Temperatures and High Pressures
J. Phys.: Conf. Ser., **502** (2014) 012017.

NE7A

C.Yang, T.Inoue, A.Yamada, T.Kikegawa and J.Ando
Equation of State and Phase Transition of Antigorite under High Pressure and High Temperature
Physics of the Earth and Planetary Interiors, **228** (2014) 56.

A.M.Dymshits, K.D.Litasov, A.Shatskiy, I.S.Sharygin, E.Ohtani, A.Suzuki, N.P.Pokhilenko and K.Funakoshi
P-V-T Equation of State of Na-Majorite to 21 GPa and 1673 K
Physics of the Earth and Planetary Interiors, **227** (2014) 68.

Y.Sun, M.Koshimizu, N.Yahaba, F.Nishikido, S.Kishimoto, R.Haruki and K.Asai
High-Energy X-Ray Detection by Hafnium-Doped Organic-Inorganic Hybrid Scintillators Prepared by Sol-Gel Method
Appl. Phys. Lett., **104** (2014) 174104.

N.Doi, T.Kato, T.Kubo, M.Noda, R.Shiraishi, A.Suzuki, E.Ohtani and T.Kikegawa
Creep Behavior during the Eutectoid Transformation of Albite: Implications for the Slab Deformation in the Lower Mantle
Earth Planet. Sci. Lett., **388** (2014) 92.

Y.Nishihara, T.Ohuchi, T.Kawazoe, D.Spengler, M.Tasaka, T.Kikegawa, A.Suzuki and E.Ohtani
Rheology of Fine-Grained Forsterite Aggregate at Deep Upper Mantle Conditions
Journal of Geophysical Research: Solid Earth, **119** (2014) 1.

N.Yahaba, M.Koshimizu, Y.Sun, T.Yanagida, Y.Fujimoto, R.Haruki, F.Nishikido, S.Kishimoto and K.Asai
X-Ray Detection Capability of a Cs_2 $ZnCl_4$ Single-Crystal Scintillator
Appl. Phys. Express, **7** (2014) 062602.

A.Shinozaki, K.Mimura, H.kagi, K.Komatsu, N.Noguchi and H.Gotou
Pressure-Induced Oligomerization of Benzene at Room Temperature as a Precursory Reaction of Amorphization J. Chem. Phys., **141** (2014) 084306.

H.Ito, S.Matsushita, K.Hyodo, H.Tsurushima, Y.Sato and Y.Sakakibara
Focusing on Delayed Clearance for Identifying Small-Sized Metastatic Lung Tumors using Synchrotron Radiation Angiography with a Highly Sensitive Receiver Gen. Thorac. Cardiovasc. Surg., **62** (2014) 553.

A.M.Dymshits, K.D.Litasov, I.S.Sharygin, A.Shatskiy, E.Ohtani, A.Suzuki and K.Funakoshi
Thermal Equation of State of Majoritic Knorringite and Its Significance for Continental Upper Mantle
Journal of Geophysical Research **119** (2014) 8034.

NW2A

M.Katayama and Y.Inada
Time-Resolved X-Ray Absorption Spectroscopy by Dispersive XAFS Technique
Hyomen Kagaku, **35** (2014) 141. (in Japanese).

M.Katayama, K.Sumiwaka, R.Miyahara, H.Yamashige, H.Arai, Y.Uchimoto, T.Ohta, Y.Inada and Z.Ogumi
X-Ray Absorption Fine Structure Imaging of Inhomogeneous Electrode Reaction in $LiFePO_4$ Lithium-Ion Battery cathode
J. Power Sources, **269** (2014) 994.

H.Abe, Y.Niwa, H.Nitani and M.Nomura
Development of Surface Sensitive DXAFS Measurement Method by Applying Kramers-Kronig Relations to Total Reflection Spectra
J. Phys.: Conf. Ser., **502** (2014) 012035.

M.Kimura
Synchrotron Radiation Shed Light to *In Situ* and Dynamic Observation of High-Temperature Processes
e-J. Surf. Sci. Nanotech., **12** (2014) 1.

M.Kawano
X-Ray Direct Observation of Reactions and Labile Species on the Basis of Crystal Design
Bull. Chem. Soc. Jpn., **87** (2014) 577.

H.Uehara, Y.Uemura, T.Ogawa, K.Kono, R.Ueno, Y.Niwa, H.Nitani, H.Abe, S.Takakusagi, M.Nomura, Y.Iwasawa and K.Asakura
In Situ Back-Side Illumination Fluorescence XAFS(BI- FXAFS) Studies on Platinum Nanoparticles Deposited on a HOPG Surface as a Model Fuel Cell: a New Approach to the Pt-HOPG Electrode/Electrolyte Interface
Phys. Chem. Chem.Phys., **16** (2014) 13748.

T.Kojima, T.Yamada, Y.Yakiyama, E.Ishikawa, Y.Morita, M.Ebihara and M.Kawano
The Diversity of Zn(II) Coordination Networks Composed of Multi-Interactive Ligand $TPHAP^-$ *via* Weak Intermolecular Interaction
CrystEngComm, **16** (2014) 6335.

T.Kojima, W.Choi and M.Kawano
Single-Crystal Growth of Coordination Networks *via* the Gas Phase and Dependence of Iodine Encapsulation on the Crystal Size
Chem. Comm., **50** (2014) 13793.

H.Oyanagi, Y.Orimoto, K.Hayakawa, K.Hatada, Z.Sun, L.Zhang, K.Yamashita, H.Nakamura, M.Uehara, A.Fukano and H.Maeda
Nanoclusters Synthesized by Synchrotron Radiolysis in Concert with Wet Chemistry
Scientific Reports, **4** (2014) 7199.

A.Kobayashi, T.Ohba, E.Saitoh, Y.Suzuki, S.Noro, H.C.Chang and M.Kato
Flexible Coordination Polymers Composed of Luminescent Ruthenium(II) Metalloligands: Importance of the Position of the Coordination Site in Metalloligands
Inorg. Chem., **53** (2014) 2910.

A.Kobayashi, A.Sugiyama, T.Ohba, Y.Suzuki, H.C.Chang and M.Kato
Synthesis and Vapor-Adsorption Behavior of a Flexible Porous Coordination Polymer Built from a Bis(bipyridyl)-Cu(I) Metalloligand
Chem. Lett., **43** (2014) 1070.

K.Nakabayashi, S.Chorazy, D.Takahashi, T.Kinoshita, B.Sieklucka and S.Ohkoshi
Cesium Cyano-Bridged Co^{II}-M^{V} (M = Mo and W) Layered Frameworks Exhibiting High Thermal Durability and Metamagnetism
Cryst. Growth Des., **14** (2014) 6093.

NW10A

Y.Ogura, S.Okamoto, T.Itoi, Y.Fujishima, Y.Yoshida and Y.Izumi
A Photofuel Cell Comprising Titanium Oxide and Silver($_I$/0) Photocatalysts for Use of Acidic Water as a Fuel
Chem. Comm., **50** (2014) 3067.

H.Ikemoto and T.Miyanaga
Local Structure of Amorphous Tellurium Studied by EXAFS
J. Synchrotron Rad. **21** (2014) 409.

H.Duan, N.Yan, R.Yu, C.-R.Chang, G.Zhou, H.-S.Hu, H.Rong, Z.Niu, J.Mao, H.Asakura, T.Tanaka, P.J.Dyson, J.Li and Y.Li
Ultrathin Rhodium Nanosheets
Nature Communications, **5** (2014) 3093.

K.Kume, N.Kawasaki, H.Wang, T.Yamada, H.Yoshikawa and K.Awaga
Enhanced Capacitor Effects in Polyoxometalate/Graphene Nanohybrid Materials: a Synergetic Approach to High Performance Energy Storage
J. Mater. Chem. A, **2** (2014) 3801.

K.Oka, Y.Ogura and Y.Izumi
X-Ray Evaluation of the Boundary between Polymer Electrolyte and Platinum and Carbon Functionalization to Conduct Protons in Polymer Electrolyte Fuel Cells
J. Power Sources, **258** (2014) 83.

T.Ohkubo, M.Ushio, K.Urita, I.Moriguchi, B.Ahmmad, A.Itadani and Y.Kuroda
Nanospace-Enhanced Photoreduction for the Synthesis of Copper(I) Oxide Nanoparticles under Visible-Light Irradiation
J. Colloid Interface Sci., **421** (2014) 165.

T.Komanoya, H.Kobayashi, K.Hara, W.-J.Chun and A.Fukuoka
Kinetic Study of Catalytic Conversion of Cellulose to Sugar Alcohols under Low-Pressure Hydrogen
ChemCatChem, **6** (2014) 230.

Y.Masubuchi, H.Sato, T.Motohashi and S.Kikkawa
Magnetic Softening of Co Doped α"-$Fe_{16}N_2$ Containing Residual Fe-Co Alloy Prepared in Low Temperature Nitridation
Journal of the Ceramic Society of Japan, **122** (2014) 288.

J.Zhang, J.Teo, X.Chen, H.Asakura, T.Tanaka, K.Teramura and N.Yan
A Series of NiM(M = Ru, Rh, and Pd) Bimetallic Catalysts for Effective Lignin Hydrogenolysis in Water
ACS Catal., **4** (2014) 1574.

F.Mauriello, H.Ariga, N.Murata and K.Asakura,
New Prospects for the Characterization of Heterogeneous Catlasyts by using Slow Muon Spectroscopy
J. Phys. Soc. Jpn., **2** (2014) 010306.

T.Kawamata, K.Sugiyama, Y.Yokoyama and T.Fujita
Structural Study of Zr-Cu-Ag Bulk Metallic Glasses using the Anomalous X-Ray Scattering Method
J. Phys.: Conf. Ser., **502** (2014) 012027.

H.Arima, T.Kawamata, Y.Yokoyama and K.Sugiyama
Structure of $Al_{87}Y_8Ni_5$ Amorphous Alloy Analyzed by Anomalous X-Ray Scattering
JPS Conf. Proc., **1** (2014) 012107.

H.Kitagawa, N.Ichikuni, H.Okuno, T.Hara and S.Shimazu
XAFS and HAADF STEM Combined Characterization for Size Regulated Ni Nanocluster Catalyst and its Unique Size Dependence for Water Gas Shift Reaction
Appl. Catal. A, **478** (2014) 66.

M.Kimura
Synchrotron Radiation Shed Light to In Situ and Dynamic Observation of High-Temperature Processes
e-J. Surf. Sci. Nanotech., **12** (2014) 1.

J.Zhang, H.Asakura, J.V.Rijn, J.Yang, P.Duchesne, B.Zhang, X.Chen, P.Zhang, M.Saeys and N.Yan
Highly Efficient, NiAu-Catalyzed Hydrogenolysis of Lignin into Phenolic Chemicals
Green Chem., **16** (2014) 2432.

S.Muratsugu, S.Tajima and M.Tada
Dispersed RhMo Nanoclusters Prepared from Oxide- Supported Rh_2Mo Heterometallic Complexes as Catalysts for Alcohol Oxidation
Chem. Lett., **43** (2014) 1321.

H.Ikemoto
The Structures and Properties of Tenanoparticles
Proceeding of the 26th Symposium on Phase Change Oriented Science (2014) 3.

M.Machida, S.Minami, K.Ikeue, S.Hinokuma, Y.Nagao, T.Sato and Y.Nakahara
Rhodium Nanoparticle Anchoring on $AlPO_4$ for Efficient Catalyst Sintering Suppression
Chem. Mater., **26** (2014) 5799.

S.Hinokuma, H.Fujii, Y.Katsuhara, K.Ikeue and M.Machida
Effect of Thermal Ageing on the Structure and Catalytic Activity of Pd/CeO_2 Prepared using Arc-Plasma Process
Catalysis Science and Technology, **4** (2014) 2990.

H.Yamada, I.Saruwatari, N.Kuwata and J.Kawamura
Local Structure of Thermally Stable Super Ionic Conducting AgI Confined in Mesopores
J. Phys. Chem. C, **118** (2014) 23845.

S.Ghosh, S.Acharyya, S.Shankha, S.Adak, L.N.S.Konathala, T.Sasaki and R.Bal
Selective Oxidation of Cyclohexene to Adipic Acid Over Silver Supported Tungsten Oxide Nanostructured Catalysts
Green Chem., **16** (2014) 2826.

A.Nakamura, M.Narita, S.Narita, Y.Suzuki and T.Miyanaga
In-Situ XAFS Study of Ag Clusters in Ag-Type Zeolite- A
J. Phys. Conf. Ser,, **502** (2014) 012033.

NW12A

Y.Yasutake, W.Kitagawa, M.Hata, T.Nishioka, T.Ozaki, M.Nishiyama, T.Kuzuyama and T.Tamura
Structure of the Quinoline N-Hydroxylating Cytochrome P450 RauA, an Essential Enzyme that Confers Antibiotic Activity on Aurachin Alkaloids
FEBS Letters, **588** (2014) 105.

S.Okada, T.Yamamoto, H.Watanabe, T.Nishimoto, H.Chaen, S.Fukuda, T.Wakagi and S.Fushinobu
Structural and Mutational Analysis of Substrate Recognition in Kojibiose Phosphorylase
FEBS J., **281** (2014) 778.

T.Satoh, K.Suzuki, T.Yamaguchi and K.Kato
Structural Basis for Disparate Sugar-Binding Specificities in the Homologous Cargo Receptors ERGIC-53 and VIP36
PLOS ONE, **9** (2014) e87963.

J.Yu, D.Ogata, Z.Gai, S.Taguchi, I.Tanaka, T.Ooi and M.Yao
Structures of AzrA and of AzrC Complexed with Substrate or Inhibitor: Insight into Substrate Specificity and Catalytic Mechanism
Acta Cryst. D, **70** (2014) 553.

T.Yokoyama, Y.Kosaka and M.Mizuguchi
Crystal Structures of Human Transthyretin Complexed with Glabridin
J. Med. Chem., **57** (2014) 1090.

T.Tsurumura, H.Qiu, T.Yoshida, Y.Tsumori and H.Tsuge
Crystallization and Preliminary X-Ray Diffraction Studies of a Surface Mutant of the Middle Domain of PB2 from Human Influenza A(H1N1) Virus
Acta Cryst. F, **70** (2014) 72.

K.Kosami, I.Ohki, K.Hayashi, R.Tabata, S.Usugi, T.Kawasaki, T.Fujiwara, A.Nakagawa, K.Shimamoto and C.Kojima
Purification, Crystallization and Preliminary X-Ray Crystallographic Analysis of a Rice Rac/Rop GTPase, OsRac1
Acta Cryst. F, **70** (2014) 113.

J.Kondo, T.Yamada, C.Hirose, I.Okamoto, Y.Tanaka and A.Ono
Crystal Structure of Metallo DNA Duplex Containing Consecutive Watson-Crick-Like T-Hg^{II}-T Base Pairs
Angew. Chem. Int. Ed., **53** (2014) 2385.

S.Arai, Y.Yonezawa, M.Ishibashi, F.Matsumoto, M.Adachi, T.Tamada, H.Tokunaga, M.Blaber, M.Tokunaga and R.Kuroki
Structural Characteristics of Alkaline Phosphatase from the Moderately Halophilic Bacterium *Halomonas* sp.593
Acta Cryst. D, **70** (2014) 811.

D.Matsui, D.-H.Im, A.Sugawara, Y.Fukuta, S.Fushinobu, K.Isobe and Y.Asano
Mutational and Crystallographic Analysis of L-Amino Acid Oxidase/Monooxygenase from *Pseudomonas* sp. AIU 813: Interconversion between Oxidase and Monooxygenase Activities
FEBS Open Bio, **4** (2014) 220.

S.Wang, M.Ogata, S.Horita, J.Ohtsuka, K.Nagata and M.Tanokura
A Novel Mode of Ferric Ion Coordination by the Periplasmic Ferric Ion-Binding Subunit FbpA of an ABC-Type Iron Transporter from *Thermus thermophilus* HB8.
Acta Cryst. D, **70** (2014) 196.

H.M.Qin, A.Yamamura, T.Miyakawa, M.Kataoka, T.Nagai, N.Kitamura, N.Urano, S.Maruoka, J.Ohtsuka, K.Nagata, S.Shimizu and M.Tanokura
Structure of Conjugated Polyketone Reductase from *Candida parapsilosis* IFO 0708 Reveals Conformational Changes for Substrate Recognition upon NADPH Binding 508
Appl. Microbiol. Biotechnol., **98** (2014) 243.

T.Ito, K.Saikawa, S.Kim, K.Fujita, A.Ishiwata, S.Kaeothip, T.Arakawa, T.Wakagi, G.T.Beckham, Y.Ito and S.Fushinobu
Crystal Structure of Glycoside Hydrolase Family 127 β-L Arabinofuranosidase from *Bifidobacterium longum*
Biochem. Biophys. Res. Commun., **447** (2014) 32.

T.Tsuda, M.Asami, Y.Koguchi and S.Kojima
Single Mutation Alters the Substrate Specificity of L-Amino Acid Ligase
Biochemistry, **53** (2014) 2650.

Y.Kanoh, S.Uehara, H.Iwata, K.Yoneda, T.Ohshima and H.Sakuraba
Structural Insight into Glucose Dehydrogenase from the Thermoacidophilic Archaeon *Thermoplasma volcanium*
Acta Cryst. D, **70** (2014) 1271.

Y.Ishida, W.Tsuchiya, T.Fujii, Z.Fujimoto, M.Miyazawa, J.Ishibashi, S.Matsuyama, Y.Ishikawa and T.Yamazaki
Niemann-Pick Type C2 Protein Mediating Chemical Communication in the Worker Ant
Proc. Natl. Acad. Sci. USA, **111** (2014) 3847.

T.Maehara, Z.Fujimoto, H.Ichinose, M.Michikawa, K.Harazono and S.Kaneko
Crystal Structure and Characterization of the Glycoside Hydrolase Family 62 α-L-Arabinofuranosidase from *Streptomyces coelicolor*
J. Biol. Chem., **289** (2014) 7962.

N.Suzuki, Z.Fujimoto, Y.-M.Kim, M.Momma, N.Kishine, R.Suzuki, S.Suzuki, S.Kitamura, M.Kobayashi, A.Kimura and K.Funane
Structural Elucidation of the Cyclization Mechanism of α-1,6-Glucan by *Bacillus circulans* T-3040 Cycloisomaltooligosaccharide Glucanotransferase
J. Biol. Chem., **289** (2014) 12040.

A.Kishimoto, A.Kita, T.Ishibashi, H.Tomita, Y.Yokooji, T.Imanaka, H.Atomi and K.Miki
Crystal Structure of Phosphopantothenate Synthetase from *Thermococcus kodakarensis*
Proteins **82** (2014) 1924.

Y.Lee, Y.B.Ryu, H.-S.Youn, J.K.Cho, Y.M.Kim, J.- Y.Park, W.S.Lee, K.H.Park and S.H.Eom
Structural Basis of Sialidase in Complex with Geranylated Flavonoids as Potent Natural Inhibitors
Acta Cryst. D, **70** (2014) 1357.

T.Shimegi, T.Ooyama T.Ohtsuki, G.Kurisu, M.Kusunoki and S.Ui
Crystallization and Preliminary X-Ray Diffraction Analysis of Domain-Chimeric L-(2*S*,3*S*)-Butanediol Dehydrogenase
Acta Cryst. F, **70** (2014) 461.

E.Tamai, H.Yoshida, H.Sekiya, H.Nariya, S.Miyata, A.Okabe, T.Kuwahara, J. Maki and S.Kamitori
X-Ray Structure of a Novel Endolysin Encoded by Episomal Phage PhiSM101 of *Clostridium perfringens*
Molecular Microbiology, **92** (2014) 326.

Y.Fujioka, S.W.Suzuki, H.Yamamoto, C.Kondo-Kakuta, Y.Kimura, H.Hirano, R.Akada, F.Inagaki, Y.Ohsumi and N.N.Noda
Structural Basis of Starvation-Induced Assembly of the Autophagy Initiation Complex
Nature Structural Molecular Biology, **21** (2014) 513.

H.Yokoyama and S.Fujii
Structures and Metal-Binding Properties of *Helicobacter pylori* Neutrophil-Activating Protein with a Di-Nuclear Ferroxidase Center
Biomolecules, **4** (2014) 600.

Y.Ohta, Y.Hatada, Y.Hidaka, Y.Shimane, K.Usui, T.Ito, K.Fujita, G.Yokoi, M.Mori, S.Sato, T.Miyazaki, A.Nishikawa and T.Tonozuka
Enhancing Thermostability and the Structural Characterization of *Microbacterium saccharophilum* K-1 β-Fructofuranosidase
Appl. Microbiol. Biotechnol., **98** (2014) 6667.

S.Buchini, F.-X.Gallat, I.R.Greig, J.-H.Kim, S.Wakatsuki, L.M.G.Chavas and S.G.Withers
Tuning Mechanism-Based Inactivators of Neuraminidases: Mechanistic and Structural Insights
Angew. Chem. Int. Ed., **53** (2014) 3382.

M.Kanagawa, Y.Liu, S.Hanashima, A.Ikeda, W.Chai, Y.Nakano, K.Kojima-Aikawa, T.Feizi and Y.Yamaguchi
Structural Basis for Multiple Sugar Recognition of Jacalin-Related Human ZG16p Lectin
J. Biol. Chem., **289** (2014) 16954.

M.Naganuma, S.Sekine, Y.E.Chong, M.Guo, X.-L.Yang, H.Gamper, Y.-M.Hou, P.Schimmel and S.Yokoyama
The Selective tRNA Aminoacylation Mechanism Based on a Single G·U Pair
Nature, **510** (2014) 507.

S.Kamachi, J.Nagao, M.Miyashita, Y.Nakagawa, H.Miyagawa and T.Tada
Crystallization and Preliminary X-Ray Diffraction Studies of La1 from *Liocheles australasiae*
Acta Cryst. F, **70** (2014) 915.

M.Nakajima, R.Yoshida, A.Miyanaga and H.Taguchi
Crystallization and Preliminary X-Ray Diffraction Analysis of Lin1840, a Putative *β*-Glucosidase from *Listeria innocua*
Acta Cryst. F, **70** (2014) 1398.

H.Tsukagoshi, A.Nakamura, T.Ishida, K.K.Touhara, M.Otagiri, S.Moriya, M.Samejima, K.Igarashi, S.Fushinobu, K.Kitamoto and M.Arioka
Structural and Biochemical Analyses of Glycoside Hydrolase Family 26 *β*-Mannanase from a Symbiotic Protist of the Termite *Reticulitermes speratus*
J. Biol. Chem., **289** (2014) 10843.

K.K.Touhara, T.Nihira, M.Kitaoka, H.Nakai and S.Fushinobu
Structural Basis for Reversible Phosphorolysis and Hydrolysis Reactions of 2-O-α-Glucosylglycerol Phosphorylase
J. Biol. Chem., **289** (2014) 18067.

K.Suzuki, A.Hori, K.Kawamoto, R.R.Thangudu, T.Ishida, K.Igarashi, M.Samejima, C.Yamada, T.Arakawa, T.Wakagi, T.Koseki and S.Fushinobu
Crystal Structure of a Feruloyl Esterase Belonging to the Tannase Family: A Disulfide Bond Near a Catalytic Triad
Proteins, **82** (2014) 2857.

Y.Itoh, M.J.Bröcker, S.Sekine, D.So¨ll and S.Yokoyama
Dimer-Dimer Interaction of the Bacterial Selenocysteine Synthase SelA Promotes Functional Active-Site Formation and Catalytic Specificity
J. Mol. Biol., **426** (2014) 1723.

A.Miyanaga, J.Cie´slak, Y.Shinohara, F.Kudo and T.Eguchi
The Crystal Structure of the Adenylation Enzyme VinN Reveals a Unique *β*-Amino Acid Recognition Mechanism
J. Biol. Chem., **289** (2014) 31448.

T.Yokoyama, Y.Kosaka and M.Mizuguchi
Inhibitory Activities of Propolis and its Promising Component, Caffeic Acid Phenethyl Ester, against Amyloidogenesis of Human Transthyretin
J. Med. Chem, **57** (2014) 8928.

T.Zhu, T.Satoh and K.Kato
Structural Insight into Substrate Recognition by the Endoplasmic Reticulum Folding-Sensor Enzyme: Crystal Structure of Third Thioredoxin-Like Domain of UDP-Glucose:Glycoprotein Glucosyltransferase
Scientific Reports, **4** (2014) 7322.

H.Yoshida, A.Yoshihara, M.Teraoka, Y.Terami, G.Takata, K.Izumori and S.Kamitori
X-Ray Structure of a Novel L-Ribose Isomerase Acting on a Non-Natural Sugar L-Ribose as its Ideal Substrate
FEBS J., **281** (2014) 3150.

K.Kosami, I.Ohki, M.Nagano, K.Furuita, T.Sugiki, Y.Kawano, T.Kawasaki, T.Fujiwara, A.Nakagawa, K.Shimamoto and C.Kojima
The Crystal Structure of the Plant Small GTPase OsRac1 Reveals its Mode of Binding to NADPH Oxidase
J. Biol. Chem., **289** (2014) 28569.

M.Shiina, K.Hamada, T.B.Inoue, M.Shimamura, AUchiyama, S.Baba, K.Sato and K.Ogata
Crystallization of the Ets1-Runx1-CBFβ-DNA Complex Formed on the TCRα Gene Enhancer
Acta Cryst. F, **70** (2014) 1380.

L.Guan, H.Yabuki, M.Okai, J.Ohtsuka and M.Tanokura
Crystal Structure of the Novel Haloalkane Dehalogenase DatA from *Agrobacterium tumefaciens* C58 Reveals a Special Halide-Stabilizing Pair and Enantioselectivity Mechanism
Appl. Microbiol. Biotechnol., **98** (2014) 8573.

K.Ito, T.Honda, T.Suzuki, T.Miyoshi, R.Murakami, M.Yao and T.Uchiumi
Molecular Insights into the Interaction of the Ribosomal Stalk Protein with Elongation Factor 1α
Nucleic Acids Res., **42** (2014) 14042.

A.Sikdar, T.Satoh, M.Kawasaki and K.Kato
Crystal Structure of Archaeal Homolog of Proteasome-Assembly Chaperone PbaA
Biochem. Biophys. Res. Commun., **453** (2014) 493.

K.Inoue, Y.Usami, Y.Ashikawa, H.Noguchi, T.Umeda, A.Y.Ashikawa, T.Horisaki, H.Uchimura, T.Terada, S.Nakamura, K.Shimizu, H.Habe, H.Yamane, Z.Fujimoto and H.Nojiri
Structural Basis of the Divergent Oxygenation Reactions Catalyzed by the Rieske Nonheme Iron Oxygenase Carbazole 1,9a-Dioxygenase.
Appl. Environ. Microbiol., **80** (2014) 2821.

J.Matsuzawa, H.Aikawa, T.Umeda, Y.Ashikawa, C.S.Minakuchi, Y.Kawano, Z.Fujimoto, K.Okada, H.Yamane and H.Nojiri
Crystallization and Preliminary X-Ray Diffraction Analyses of the Redox-Controlled Complex of Terminal Oxygenase and Ferredoxin Components in the Rieske Nonhaem Iron Oxygenase Carbazole 1,9a-Dioxygenase
Acta Cryst. F, **70** (2014) 1406.

H.M.Qin, F.L.Imai, T.Miyakawa, M.Kataoka, N.Kitamura, N.Urano, K.Mori, H.Kawabata, M.Okai, J.Ohtsuka, F.Hou, K.Nagata, S.Shimizu and M.Tanokura
L-*allo*-Threonine Aldolase with H128Y/S292R Mutation from *Aeromonas jandaei* DK-39 Reveals the Structural Basis of Changes in Substrate Stereoselectivity
Acta Cryst. D, **70** (2014) 1695.

A.Nishizawa, A.Harada, M.Senda, Y.Tachihara, D.Muramatsu, S.Kishigami, S.Mori, K.Sugiyama, T.Senda and S.Kimura
Complete Pyridine Nucleotide-Specificity Conversion of an NADH-Dependent Ferredoxin Reductase.
Biochem. J, **462** (2014) 257.

K.Ishibashi, Y.Kezuka, C.Kobayashi, M.Kato, T.Inoue, T.Nonaka, M.Ishikawa, H.Matsumura and E.Katoh
Structural Basis for the Recognition-Evasion Arms Rase between *Tomato Mosaic Virus* and the Resistance Gene *Tm-1*
Proc. Natl. Acad. Sci. USA, **111** (2014) 3486.

A.Ochiai, H.Sugai, K.Harada, S.Tanaka, Y.Ishiyama, K.Ito, T.Tanaka, T.Uchiumi, M.Taniguchi and T.Mitsui
Crystal Structure of α-Amylase from *Oryza Sativa*: Molecular Insights into Enzyme Activity and Thermostability
Biosci., Biotechnol., Biochem., **78** (2014) 989.

M.Nagae, K.M.Matsumoto, M.Kato, M.K.Kaneko, Y.Kato and Y.Yamaguchi
A Platform of C-Type Lectin-Like Receptor CLEC-2 for Binding *O*-Glycosylated Podoplanin and Nonglycosylated Rhodocytin
Structure, **22** (2014) 1711.

H.Im, S.B.Jang, C.Pathak, Y.J.Yang, H.J.Yoon, T.K.Yu, J.Y.Suh and B.J.Lee
Crystal Structure of Toxin HP0892 from *Helicobacter pylori* with Two Zn(II) at 1.8 Å Resolution.
Protein Science, **23** (2014) 819.

T.Tomita, T.Ozaki, K.Matsuda, M.Nishiyama and T.Kuzuyama
Crystallization and Preliminary X-Ray Diffraction Analysis of Cyclolavandulyl Diphosphate Synthase, a New Member of the Cis-Isoprenyl Diphosphate Synthase Superfamily
Acta Cryst. F, **70** (2014) 1410.

C.Han, A.K.Tachikawa, A.Shimizu, D.Zhu, H.Nakamura, E.Adachi, T.Kikuchi, M.Koga, T.Koibuchi, G.F.Gao, Y.Sato, A.Yamagata, E.Martin, S.Fukai, Z.L.Brumme and A.Iwamoto
Switching and Emergence of CTL Epitopes in HIV-1 Infection
RETROVIROLOGY, **11** (2014) 38.

Y.Nishikawa, T.Oyama, N.Kamiya, T.Kon, Y.Y.Toyoshima, H.Nakamura and G.Kurisu
Structure of the Entire Stalk Region of the Dynein Motor Domain
J. Mol. Biol., **426** (2014) 3232.

S.J.Lee, Y.S.Park, S.J.Kim, B.J.Lee and S.W.Suh
Crystal Structure of PhoU from *Pseudomonas aeruginosa*, a Negative Regulator of the Pho Regulon
J. Struct. Biol., **188** (2014) 22.

K.Yamamoto, Y.Anami and T.Itoh
Development of Vitamin D Analogs Modulating the Pocket Structure of Vitamin D Receptor
Curr. Top. Med. Chem., **14** (2014) 2378.

S.H.Seok, H.Im, H.S.Won, M.D.Seo, Y.S.Lee, H.J.Yoon, M.J.Cha, J.Y.Park and B.J.Lee
Structures of Inactive CRP Species Reveal the Atomic Details of the Allosteric Transition that Discriminates Cyclic Nucleotide Second Messengers
Acta Cryst. D, **70** (2014) 1726.

T.Kudo, M.Ishizawa, K.Maekawa, M.Nakabayashi, Y.Watarai, H.Uchida, H.Tokiwa, T.Ikura, N.Ito, M.Makishima and S.Yamada
Combination of Triple Bond and Adamantane Ring on the Vitamin D Side Chain Produced Partial Agonists for Vitamin D Receptor
J. Med. Chem., **57** (2014) 4073.

Y.Hanada, Y.Nishimiya, A.Miura, S.Tsuda and H.Kondo
Hyperactive Antifreeze Protein from an Antarctic Sea Ice Bacterium Colwellia sp. Has a *Compound* Ice-Binding Site Without Repetitive Sequences
FEBS J., **281** (2014) 3576.

T.Fujiwara, W.Saburi, H.Matsui, H.Mori and M.Yao
Structural Insights into the Epimerization of Beta-1,4-Linked Oligosaccharides Catalyzed by Cellobiose 2- Epimerase, the Sole Enzyme Epimerizing Non-Anomeric Hydroxyl Groups of Unmodified Sugars
J. Biol. Chem., **289** (2014) 3405.

X.Shen, W.Saburi, Z.Q.Gai, K.Komoda, J.Yu, T.O.Kato, Y.Kido, H.Matsui, H.Mori and M.Yao
Crystallization and Preliminary X-Ray Crystallographic Analysis of α-Glucosidase HaG from *Halomonas* sp. Strain H11
Acta Cryst. F, **70** (2014) 464.

NW14A

M.Hoshino
Structure Visualization of Short-Lived Photoexcited Molecule by Single Crystal X-Ray Structure Analysis
J. Cryst. Soc. Jpn., **56** (2014) 115. (in Japanese).

M.Hoshino, E.Uchida, Y.Norikane, R.Azumi, S.Nozawa, A.Tomita, T.Sato, S.Adachi and S.Koshihara
Crystal Melting by Light: X-Ray Crystal Structure Analysis of an Azo Crystal Showing Photoinduced Crystal-Melt Transition
J. Am. Chem. Soc., **136** (2014) 9158.

A.Tomita, T.Sato, S.Nozawa, N.Shibayama and S.Adachi
Structural Dynamics Measurements of the Biological Molecule using Pump-Probe Technique
J. Cryst. Soc. Jpn., **56** (2014) 253. (in Japanese).

A.F.Mabied, S.Nozawa, M.Hoshino, A.Tomita, T.Sato and S.Adachi
Application of Singular Value Decomposition Analysis to Time-Dependent Powder Diffraction Data of an *in-situ* Photodimerization Reaction
J. Synchrotron Rad., **21** (2014) 554.

Y.Uemura, H.Uehara, Y.Niwa, S.Nozawa, T.Sato, S.Adachi, B.Ohtani, S.Takakusagi and K.Asakura
In Situ Picosecond XAFS Study of an Excited State of Tungsten Oxide.
Chem. Lett. **43** (2014) 977.

SPF-A3

Y.Fukaya, M.Maekawa, A.Kawasuso, I.Mochizuki, K.Wada, T.Shidara, A.Ichimiya and T.Hyodo
Total Reflection High-Energy Positron Diffraction: An Ideal Diffraction Technique for Surface Structure Analysis
Appl. Phys. Express **7** (2014) 056601.

Y.Fukaya, M.Maekawa, I.Mochizuki, K.Wada, T.Hyodo and A.Kawasuso
Reflection High-Energy Positron Diffraction Study on the First Surface Layer
J. Phys.: Conf. Ser. **505** (2014) 012005.

K.Wada
KEK Slow Positron Facility: Current Status and Recent Results
positron sciences, **3** (2014) 11. (in Japanese).

M.Maekawa, K.Wada, Y.Fukaya, A.Kawasuso, I.Mochizuki, T.Shidara and T.Hyodo
Brightness Enhancement of a Linac-Based Intense Positron Beam for Total-Reflection High-Energy Positron Diffraction (TRHEPD)
Eur. Phys. J. D, **68** (2014) 165.

T.Hyodo, Y.Fukaya, M.Maekawa, I.Mochizuki, K.Wada, T.Shidara, A.Ichimiya and A.Kawasuso
Total Reflection High-Energy Positron Diffraction (TRHEPD)
J. Phys.: Conf. Ser., **505** (2014) 012001.

SPF-B1

K.Wada
KEK Slow Positron Facility: Current Status and Recent Results
positron sciences, **3** (2014) 11. (in Japanese).

Y.Nagashima, K.Michishio, H.Terabe, R.H.Suzuki, S.Iida, T.Yamashita, R.Kimura, T.Tachibana, I.Mochizuki, K.Wada, A.Yagishita and T.Hyodo
Positronium and Positronium Negative Ion Emission From Alkali-Metal Coated Tungsten Surfaces
J. Phys.: Conf. Ser., **505** (2014) 012037.

Y.Nagashima, K.Michishio and H.Terabe
The Simplest Three Body System: Positronium Negative Ions
AIP Conf. Proc., **1588** (2014) 27.

K.Michishio and Y.Nagashima
Development of Energy-Tunable Positronium Beams Employing
the Photodetachment of Positronium Negative Ions
JJAP Conf. Proc., **2** (2014) 011303.

PHOTON FACTORY ACTIVITY REPORT 2014

#32 PART A

High Energy Accelerator Research Organization, KEK